Leprosy bacilli in British red squirrels *pp. 702 & 744*

Progress on precaution with emerging technologies *p. 710*

Fano features profiled in real time *pp. 734 & 738*

Science

$15
11 NOVEMBER 2016
sciencemag.org

AAAS

What really happened to the

GREENLAND NORSE

p. 696

CONTENTS

11 NOVEMBER 2016 • VOLUME 354 • ISSUE 6313

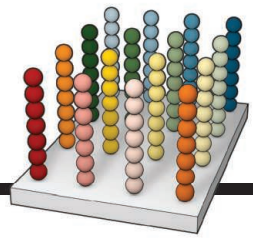

705 & 769
Decoding the noncoding genome

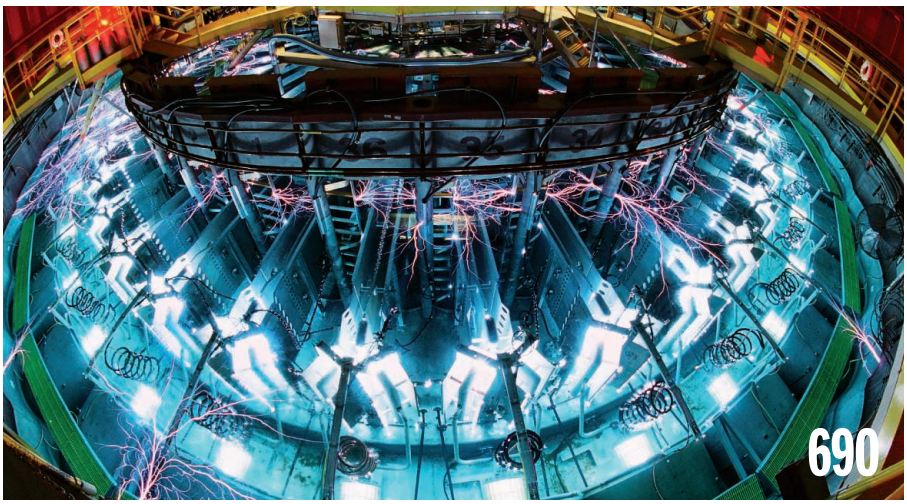

NEWS

IN BRIEF

IN DEPTH

FEATURES

INSIGHTS

PERSPECTIVES

POLICY FORUM

BOOKS *ET AL.*

LETTERS

PHOTO (BOTTOM RIGHT): CATHERINE CLARK

Published by AAAS

CONTENTS

11 NOVEMBER 2016 • VOLUME 354 • ISSUE 6313

RESEARCH

IN BRIEF

REVIEW

RESEARCH ARTICLES

REPORTS

DEPARTMENTS

ON THE COVER

Reconstruction of a 10th-century Norse church in Greenland. This replica, made of timber and turf, was built in 2000. Recent archaeological excavations and analyses in Greenland and elsewhere suggest a new solution to the medieval mystery of why the Norse colony in Greenland failed after 500 years. See page 696. For more on the process behind the cover image, see http://scim.ag/2foZdEL. *Photo: Bill Douthitt*

SCIENCE (ISSN 0036-8075) is published weekly on Friday, except the last week in December, by the American Association for the Advancement of Science, 1200 New York Avenue, NW, Washington, DC 20005. Periodicals mail postage (publication No. 484460) paid at Washington, DC, and additional mailing offices. Domestic individual membership and subscription (51 issues): $165 ($74 allocated to subscription). Domestic institutional subscription (51 issues): $1522; Foreign postage extra: Mexico, Caribbean (surface mail) $55; other countries (air assist delivery) $89. First class, airmail, student, and emeritus rates on request. Canadian rates with GST available upon request, GST #1254 88122. Publications Mail Agreement Number 1069624. **Printed in the U.S.A.**
Change of address: Allow 4 weeks, giving old and new addresses and 8-digit account number. **Postmaster:** Send change of address to AAAS, P.O. Box 96178, Washington, DC 20090–6178. **Single-copy sales:** $15.00 current issue, $20.00 back issue prepaid includes surface postage; bulk rates on request. *Science* is indexed in the *Reader's Guide to Periodical Literature* and in several specialized indexes.

Published by AAAS

Science
AAAS
1200 New York Avenue, NW, Washington, DC 20005
Clarendon House, Clarendon Road, Cambridge, UK CB2 8FH

SUBSCRIPTION SERVICES For change of address, missing issues, new orders and renewals, and payment questions: 866-434-AAAS (2227) or 202-326-6417, FAX 202-842-1065. Mailing addresses: AAAS, P.O. Box 96178, Washington, DC 20090-6178 or AAAS Member Services, 1200 New York Avenue, NW, Washington, DC 20005

INSTITUTIONAL SITE LICENSES 202-326-6730 **REPRINTS:** Author Inquiries 800-635-7181 **COMMERCIAL INQUIRIES** 803-359-4578 **PERMISSIONS** 202-326-6765, permissions@aaas.org **AAAS Member Services** 202-326-6417 or http://membercentral.aaas.org/discounts

Science serves as a forum for discussion of important issues related to the advancement of science by publishing material on which a consensus has been reached as well as including the presentation of minority of conflicting points of view. Accordingly, all articles published in *Science*—including editorials, news and comment, and book reviews—are signed and reflect the individual views of the authors and not official points of view adopted by AAAS or the institutions with which the authors are affiliated.

INFORMATION FOR AUTHORS See pages 624 and 625 of the 5 February 2016 issue or access www.sciencemag.org/authors/science-information-authors

EDITORIAL

Who should direct WHO?

Last week, member states of the World Health Organization (WHO) advanced another step in the nearly 1-year rigorous process of selecting its next director-general. Candidates for the position presented their vision of international health work and the role of this global health body. Having worked at WHO in a number of capacities in the area of infectious diseases, I know well that international health covers a wide breadth of issues. Add to that noncommunicable diseases and matters such as intellectual property and universal health coverage, and it becomes clear that the next director-general must be a jack of all trades, but also a master of one—leadership in public health. Leadership in this role is about conceiving and articulating a vision, staying faithful to that vision in the face of undue influence, and effectively engaging with not only governments, but with all stakeholders to gain their support and enable the vision to be realized.

"...leadership in public health...is about conceiving and articulating a vision..."

International health not only concerns the transborder spread of infectious diseases and epidemics, which have recently been high on the political and media agenda. It is much broader and includes many health challenges, ranging from antimicrobial resistance and hazards such as natural disasters, to war, nuclear accidents, and chemical spills. Noncommunicable disease risk factors such as poor nutrition, lack of physical exercise, and smoking also cross international borders—physically, as with the spread of chemical spills or nuclear fallout, and through advertising and marketing. They are therefore an important part of international health, although they attract less media interest. These factors are often driven by sectors outside of health, unlike infectious diseases, which are mostly naturally occurring and depend on government reporting and action. This complicates the landscape of those who must come to the table when problems are discussed.

In addition, public health decision-making by WHO must be safeguarded from undue influence. Thus, there are constraints on the director-general's interaction with nonstate actors. For example, on a day-to-day basis, the director-general must discuss international health problems with nongovernmental organizations and private companies that deal with pharmaceuticals, food, alcohol, and other goods. This adds even more complexity to the director-general's job, as the decisions made must be the right ones for public health.

WHO's focus on improving preparedness for public health emergencies, especially for infectious diseases with epidemic potential, must also be maintained. For example, its Research and Development Blueprint was initiated last year toward the end of the West Africa Ebola crisis. This year, proposals on technologies emerged, ranging from vaccines and immunotherapy to diagnostics. The next director-general must not only continue to encourage innovative thinking in preparedness, but must also draw the public and private sectors together to develop these global public goods and ensure equitable access for all who need them.

And finally, the WHO regional structure must be supported through constant interaction with the director-general. Each regional office has a director who is nominated by the WHO member states of the region—the same states that collectively decide on who will be director-general at the global level. It has often been said by senior staff at WHO that much more effort must be made to ensure that country, regional, and headquarters staffs work in harmony, compared to the effort spent on technical activities that support country needs.

On 1 July 2017, a new WHO director-general will take office. In the final decision-making steps, it will be important to identify the candidate who will be a technically sound leader with a deep understanding of politics and an ability to channel all stakeholders to the right outcome. This job takes boldness in vision, and the skills to bring others along with that vision.

—David L. Heymann

David L. Heymann is chair of the Health Protection Agency, United Kingdom; head of the Centre on Global Health Security at Chatham House, London; and professor of Infectious Disease Epidemiology at the London School of Hygiene and Tropical Medicine, United Kingdom. david.heymann@lshtm.ac.uk

10.1126/science.aal3456

PHOTOS: (INSET) WALLY SANTANA/ASSOCIATED PRESS; (TOP RIGHT) CHATHAM HOUSE

NEWS

> “Ralph was a … steadying presence … trying to keep scientists on track … sticking to the facts.”
>
> **National Academy of Sciences President Marcia McNutt**, on former President Ralph Cicerone, who died 5 November. An atmospheric scientist, Cicerone identified ozone layer threats from humanmade chemicals.

IN BRIEF

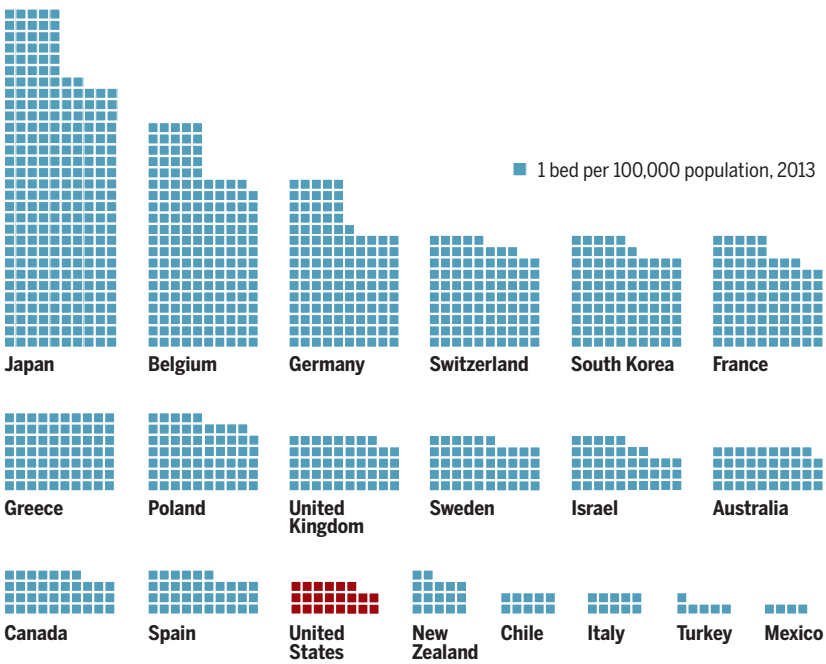

United States lags in mental hospital beds

Compared with many countries around the world, the United States has relatively few beds available to patients with psychiatric disorders, scientists noted last week in an editorial in the *Journal of the American Medical Association*. Of the 35 countries that participate in the intergovernmental Organisation for Economic Co-operation and Development (about half are represented in the graph above), the United States has among the fewest beds for its population, with only 22 per 100,000 people in 2013. Japan, Belgium, and Germany topped the list in 2013, with 267, 174, and 126 beds per 100,000 people, respectively. The United States's low numbers represent a 35% decrease from 1998, when there were 34 beds available per 100,000 people—and are a hallmark of an intensifying mental health crisis in the country, the researchers say. Most state-funded psychiatric beds are allocated to people in the criminal justice system, they note, and the country lacks “a safe minimum number” of beds to respond to suicide risk. Meanwhile, U.S. suicide rates are on the rise; in 2014, suicide was the second-leading cause of death in the country for people between 10 and 34 years old.

AROUND THE WORLD

Clinical trials go unpublished

OXFORD, U.K. | Advocates for transparency in the reporting of drug trial results have some new ammo. An analysis of clinical trial records released 3 November shows that results from nearly half the interventional clinical studies done in the last decade haven't been reported in a journal. The analysis comes from an automated system called TrialsTracker, created by researchers Anna Powell-Smith and Ben Goldacre of the University of Oxford in the United Kingdom, which regularly mines records from ClinicalTrials.gov and papers on PubMed. The first round of results turned up more than 25,000 trials completed between 2006 and 2014, of which 45.2% have no published results. Among major drug sponsors, Sanofi reported the fewest results, having published on only 34.5% of its 435 trials. The top 20 sponsors with unreported trials included other pharma giants—such as Bayer, Merck & Co., and Novartis—but also academic and government institutions such as the Mayo Clinic, Stanford University, and the National Cancer Institute.

Luxembourg eyes asteroid mining

LUXEMBOURG | The Grand Duchy of Luxembourg, one of Europe's smallest nations, is thinking big: It finalized a deal last week to invest €25 million in Planetary Resources, a startup company in Redmond, Washington, focused on asteroid mining. The deal, which makes the country a minority shareholder, gives a boost to the company's plan to launch its first asteroid-prospecting mission by 2020. Known as a financial powerhouse, Luxembourg has played a role in commercial communication satellites since the 1980s, and in February announced an initiative to establish laws and regulations for mining in space. (The United States took similar steps last year.) In May, the country also partnered with Mountain View, California–based Deep Space Industries (DSI), another startup, to help DSI develop its first spacecraft. That same month, DSI and Planetary Resources each established European headquarters in Luxembourg. Neither company

CREDITS: (GRAPHIC) JIA YOU/*SCIENCE*; (DATA) ORGANISATION FOR ECONOMIC CO-OPERATION AND DEVELOPMENT

is expected to conduct actual mining for asteroid metals or water anytime soon: Planetary Resources launched its first test satellite into Earth orbit last year, and in 2017 expects to launch Arkyd 6, an infrared-imaging test satellite.

Deadly fungus found in U.S.

ATLANTA | A dangerous infection caused by the fungus *Candida auris* has been reported for the first time in the United States. The Atlanta-based Centers for Disease Control and Prevention (CDC) published details last week on seven cases. The fungus was isolated from patients between May 2013 and August 2016 and six of the cases were identified retrospectively. A further six cases happened since August and are still being investigated, the agency said. *C. auris* was first described in 2009 in South Korea and has since been found in many countries around the world. The infection can be fatal and is often resistant to antimicrobials. In June, CDC asked hospitals to be on the lookout for the infection, which can only be identified with specialized lab equipment. Four of the first seven U.S. patients have since died, though it is not clear whether the infection was the cause. In two instances, one in Illinois and one in New Jersey, two patients were treated in the same hospital. The fungal genomes in both cases proved to be almost identical, suggesting the fungus may be spread in hospitals.

NEWSMAKERS

Court clears supplement sleuth

A dietary supplement company has lost its libel case against a physician—who, it claimed, had made inaccurate, damaging statements about its products in a research paper and to reporters. Seven months ago, Norcross, Georgia–based Hi-Tech Pharmaceuticals sued **Pieter Cohen**, an internist at Cambridge Health Alliance in Massachusetts, in a Massachusetts court. In 2015, Cohen wrote a paper in *Drug Testing and Analysis* that assessed whether certain dietary supplements contained a chemical stimulant called BMPEA, which the U.S. Food and Drug Administration said weeks later was illegal. The company claimed that the paper improperly included Hi-Tech supplements, and had harmed its reputation. Hi-Tech argued that its products actually contain a legal extract from *Acacia rigidula*, a shrub from the southwestern United States. A jury, however, backed Cohen, who has a long interest in revealing illegal ingredients in supplements (*Science*, 21 August 2015, p. 780).

Three Qs

On 14 November, National Geographic Channel will broadcast the big-budget TV series *MARS*. It's an unusual combination of documentary and dramatization: The real-life footage includes interviews with scientists and astronauts on traveling to the Red Planet, and chronicles the work of SpaceX to develop reusable rockets—crucial technology for a Mars landing. The fictional part follows the struggles of the Mars-bound crew of the spaceship Daedalus in 2033. *Science* spoke with executive producer **Ron Howard** about the new show. **http://scim.ag/_TVMARS**

Q: Why the mix of fact and fiction?
A: It's creative opportunism. It began as a documentary and we thought, "This could be a series." We began to delve and found such good storytellers. We realized this could be so cinematic: What would it feel like to be there? On a thematic level, it celebrates exploration in a visceral way.

Q: Space travel involves a lot of monotony. How have you made the journey exciting?
A: It's reality with the boring bits snipped out. We began with a great deal of research on coping with space. We selected a few [challenges] to dramatize. A lot of individuals are working on these problems. [NASA astronaut] Scott Kelly dedicated a year on the International Space Station to see what that could do to a human being.

Q: Is it a one-way trip for the crew?
A: It varies from person to person. They are colonizing and have terraforming in mind. The immediate imperative is to survive but they want to create sustainability, to begin to build.

The fictional crew of Daedalus lands on the Red Planet in the new series *MARS*.

FINDINGS

Early farmers expanded dogs' diet

As people began farming and shifted from a diet of game to starchy grains, their canine companions did the same. By 7000 years ago, thanks to the farmers' influence, dogs were consuming enough starch that their genomes changed to digest it more readily—just as early farmers' genomes changed for the same reason, says Morgane Ollivier, a paleogeneticist at the École Normale Supérieure de Lyon in France. Researchers learned 3 years ago that dogs have up to 20 copies of a gene for processing starch, whereas wolves have

PHOTO: NATIONAL GEOGRAPHIC CHANNELS

Comb jellies' ghostly glow brightens the polar twilight zone.

Strange creatures light up the polar 'twilight zone'

In the ocean's twilight zone, bioluminescent creatures like krill and comb jellies can outshine light filtered down from above—and in polar regions, the twilight zone may become much shallower in winter, new research shows. In most waters, the twilight zone stretches from 200 to 1000 meters beneath the surface. But during the nearly 4 months of Arctic "polar night"—a time of limited light during the long winter—the twilight zone and its denizens rise to just tens of meters deep. To study this phenomenon, marine ecologist Jørgen Berge of the University of Trømso - The Arctic University of Norway and colleagues first identified the bioluminescers in waters near Norway's Svalbard archipelago, using variations in intensity and duration of emitted light to identify distinct signals from seven of 17 tested species. Then they mapped total bioluminescence within the water column down to 120 meters. The brightest spot was 20 to 40 meters below the surface, they noted last week in *Scientific Reports*. Two layers of organisms dominated the watery light show, they found: microscopic dinoflagellates in the upper ranges and small crustaceans called copepods below.

BY THE NUMBERS

40%

Boost in performance of college basketball players in back-to-back games who answered questions on how they felt about death in the interim. Players who answered questions about basketball showed no boost (*Journal of Sport and Exercise Psychology*).

90%

Fraction of ivory samples that came from recently killed elephants—and therefore from poaching—rather than from old government stockpiles as was long suspected (*Proceedings of the National Academy of Sciences*).

40

Times that "rewritable paper," a flexible membrane made of tungsten oxide, can be printed and erased without losing resolution (*ACS Applied Materials & Interfaces*).

just two. So when did the dog genomes change? Ollivier and colleagues pulled out all the copies of the starch-processing gene from 13 dog bones and teeth found at archaeological sites in Eurasia. Four of the dogs had more than eight copies of the gene; those came from a 7000-year-old site in Romania and 5000-year-old sites in Turkey and France, Ollivier and his colleagues reported this week in *Royal Society Open Science*. These samples predate the development of dog breeds, ruling that out as the engine behind the change—instead, farmers' own changing diet was the likely driver. http://scim.ag/_dogdiet

Bhutan not immune to quakes

Although surrounded by countries regularly shaken by seismic activity, the kingdom of Bhutan has apparently been free of large temblors over the last 500 years. Some scientists thought the region may be truly aseismic; others, that the relative calm is simply an information gap about the country's geological history. Now, by piecing together historical and tectonic records, an international collaboration of European and Bhutanese researchers says it has solved this mystery. The team studied original historical texts written by monks and temple builders—and found several that mentioned a powerful quake apparently dating to about 4 May 1714. The researchers then gathered geological evidence to support the written records, digging trenches to look for tectonic faults that showed evidence of movement. Along one fault, the team found signs of a quake that occurred between 1642 and 1836 and was of magnitude 7.5 to 8.5, they reported last month in *Geophysical Research Letters*—comparable to the Nepal earthquake in 2015 that killed nearly 9000 people. http://scim.ag/BhutanEQ

Monks of Bhutanese monasteries wrote of a strong earthquake 300 years ago.

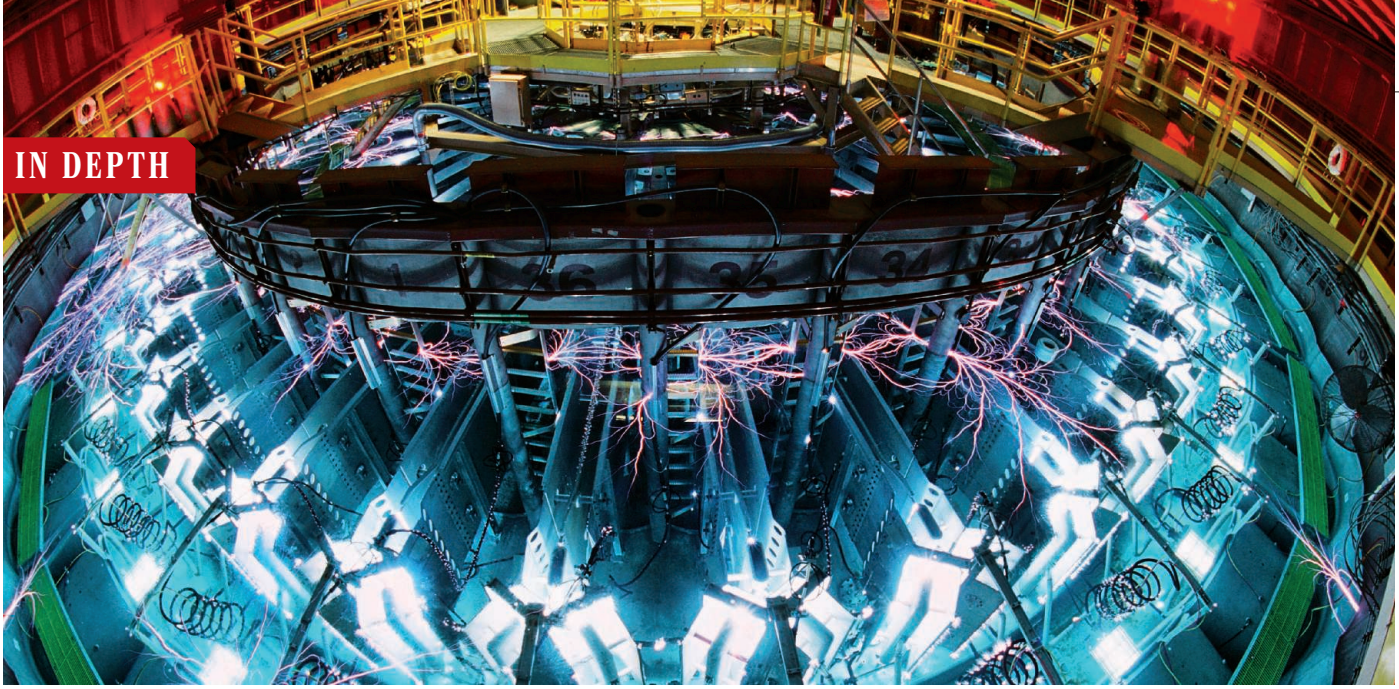

PLASMA PHYSICS

Fusion reactor fuels up with bomb ingredient

Radioactive tritium promises a bigger bang for Sandia's Z machine but poses safety issues

By **W. Wayt Gibbs**

Every time the plasma physicists at Sandia National Laboratories in Albuquerque, New Mexico, fire a shot on their fusion reactor, a big chunk of the hardware goes up in smoke. Their Z machine contains banks of capacitors that fill up with more electrical energy than a thousand lightning bolts. With the flip of a switch, 20 million amps surge toward a fuel-filled cylinder the size of a pencil eraser. The electrical current induces an overwhelming magnetic field, which pinches the tube so fast and furiously that hydrogen atoms inside fuse into helium, releasing a blast of high-energy neutrons and helium nuclei (known as α particles). The blast vaporizes the intricate hardware that holds the tiny tube—10 kilograms of solid metal. "We're basically delivering three sticks of dynamite worth of energy," says Mike Cuneo, a manager on the project. "After, there's a crater a foot wide."

The physicists are now preparing to make even bigger bangs by adding a precious fuel, used in thermonuclear weapons, that carries both risks and rewards. Calculations, simulations, and experimental results published in recent years suggest that Sandia's machine could offer a quicker and cheaper path to self-sustaining fusion than other approaches that blast the fuel with lasers or trap it in reactors called tokamaks. But so far the Z machine has unleashed its fury mainly on deuterium (a hydrogen with one neutron in its nucleus), which releases limited amounts of fusion energy. In August, however, researchers added a dash of tritium—hydrogen with two neutrons. Over the next 5 years, the tests will gradually ramp up to a 50-50 blend of deuterium and tritium (DT).

Fusion of 50-50 DT fuel releases 60 to 90 times as many neutrons as deuterium-only fusion does, and each of the neutrons and α particles ejected from DT fusion carries more than four times the energy of their deuterium-only counterparts. As tritium levels in the fuel rise toward 50%, energy yields should soar.

Other fusion efforts have followed the same path. In 1997, the Joint European Torus (JET), a tokamak in Abingdon, U.K., burned 50-50 DT to generate 16 megawatts of power, though for less than a second. That shot set a record for fusion power output that still stands today. But graphite in JET's reactor walls limited the output. "Carbon is like a sponge for tritium, so about 70% of the tritium we injected stuck to the wall," recalls Xavier Litaudon, who heads the ITER physics department in Oxford, U.K., and is now lobbying to extend JET's funding to include a new round of DT experiments in 2019. ITER, the overbudget and overdue international tokamak under construction near Cadarache in France, has staked its mission on eventually using DT to liberate far more power from fusion than is put in.

Unlike a tokamak, which uses magnetic fields to stabilize a wispy ring of hot plasma, the Z machine relies on inertia and a magnetic cage to contain the superheated fuel during microsecondlong shots. The approach, called magneto-inertial fusion, shares more in common with fusion efforts like that at the National Ignition Facility (NIF) at Lawrence Livermore National Laboratory in California, where trillion-watt lasers zap pellets of fuel to induce fusion. Sandia and NIF scientists

Adding fuel to the fire

Sandia's Z machine joins a small club of fusion reactors that have used deuterium-tritium (DT) fuel.

REACTOR	LOCATION	DT FUEL USED	NOTE
Tokamak Fusion Test Reactor	Princeton, New Jersey	1993–1997	Decommissioned
OMEGA	Rochester, New York	1995–present	DT systems stretch back to 1979
Joint European Torus	Abingdon, U.K.	1991–1997	New DT campaign planned for 2019
National Ignition Facility	Livermore, California	2010–present	Failed to achieve ignition with DT
ITER	Cadarache, in France	2035 (planned)	DT use delayed from 2021 to 2035

CREDITS: (PHOTO) RANDY MONTOYA; (DATA) W. WAYT GIBBS

The Z machine's electrical pulses create powerful magnetic fields that crush tubes of nuclear fuel.

don't have to worry about losing tritium into graphite because unlike tokamaks, their machines have no containing walls. Moreover, Cuneo says, unlike NIF, the Z machine's magnetic field can slow emerging α particles and trap them along field lines, funneling more energy into sustaining the fusion.

Sandia is one of only three fusion centers currently using DT (see table, p. 690). One issue is cost. Tritium costs tens of thousands of dollars a gram because there is no natural repository of the stuff; it is produced in nuclear reactors as a byproduct of fission.

Another issue is safety. "Tritium is mildly radioactive—it has a 12-year half-life—so regulations require you to handle it very carefully," says Rich Hawryluk, a researcher at the Princeton Plasma Physics Laboratory (PPPL) in New Jersey. What's more, the neutrons from DT fusion bang into steel parts and make them slightly radioactive. So when PPPL closed a reactor after its DT runs in the 1990s, the room-sized vessel was filled with concrete, sliced up, and buried at the Hanford nuclear reservation in Washington state.

In the presence of water, including humidity in the air, tritium can form tritiated water, which is at least ten thousand times more biologically hazardous than pure T_2 gas, Hawryluk says. That is a special concern at the Z machine, which insulates electrical components in pools of oil and water. "We do not want tritium to get into those," Cuneo says.

At NIF, tritium presents fewer hazards because it is contained within a tiny sphere during transport, and workers don't often enter the interior of the machine. Sandia's capsule, in contrast, is open at both ends, and the violent implosion mixes unburned tritium with vaporized metal that sprays everywhere. "People have to go in and completely replace the center of the accelerator after every shot," Cuneo says.

Sandia is nevertheless moving forward with tritium, in part because it generates extra neutrons that reveal what's happening in the hottest, densest part of the short-lived plasma, where the physics is not as well understood. In three planned shots next year, Cuneo says, they will remove a tritium containment system from around the target both to test an air-purging safety system and to get a clearer view of the neutrons.

"We're excited about the recent results, even though it's just a tenth of a percent tritium," he adds. "There was a barrier to belief that we could ever use tritium at all." ■

W. Wayt Gibbs is a freelance writer based in Seattle, Washington, and editorial director at Intellectual Ventures.

PHOTO: PAL S. SCHAATHUN

BIOMEDICINE

For chronic fatigue syndrome, a 'shifting tide' at NIH

New funding shows increased commitment to mystery illness, but not everyone trusts the agency's sincerity

By **Meredith Wadman**, *in Fort Lauderdale, Florida*

The most anticipated speaker late last month at an international conference devoted to the mysterious malady commonly known as chronic fatigue syndrome (CFS) was not a scientist with a hot new finding—although there was excitement about new research in the air. Rather, it was a National Institutes of Health (NIH) official bearing good news to a community that has long existed on the margins of the biomedical research establishment. Vicky Whittemore, the agency's CFS point person in Bethesda, Maryland, delivered on a promise that NIH Director Francis Collins made last year by announcing that NIH spending for research on the poorly understood disease should rise to roughly $15 million in 2017, doubling the estimated $7.6 million handed out in 2016.

What's more, the NIH emissary said to those gathered here, the biomedical agency will in December solicit CFS proposals from outside scientists to establish several collaborative centers for basic and clinical research, and another center to manage their data on the illness. The calls for applications, which will come with dedicated funds from the planned budget increase, are the first of their kind for CFS from the United States's major medical research funder since 2005. "There is a shifting tide at NIH with regard to ME/CFS," Whittemore told the conference, incorporating the term that many with the multisystem illness prefer. (ME stands for "myalgic encephalomyelitis," and the meeting was convened by the International Association for CFS/ME.)

Some scientists working on the disease agree. "The fact that there is a budget for it at all means that the agency is taking it seriously. And it's not coming only out of Francis Collins's discretionary fund, but from the individual NIH institutes," says Ian Lipkin, an immunologist at Columbia University, who serves on the Advisory Committee to the Director, Collins's key group of external advisers. Lipkin is also the principal investigator on a $766,000 grant from NIH's infectious diseases institute to collect samples from hundreds of patients and controls, looking for biomarkers that could be used to diagnose the disease and searching for clues to its causes.

It has been nearly 3 decades since a group of researchers led by the U.S. Centers for Disease Control and Prevention (CDC) coined the term "chronic fatigue syndrome" after an

A woman with chronic fatigue syndrome participates in a trial of rituximab, an antibody that has shown promise.

investigation of two outbreaks in the United States. Typified by exhaustion that commonly worsens with physical, mental, or emotional exertion, the condition is also often characterized by short-term memory and concentration problems and profound fatigue that sleep does not relieve. Sufferers may experience widespread muscle and joint pain, immune system problems, headaches, and many other symptoms. The onset of the disease frequently follows an infectious illness.

Ever since it was given a name, many researchers and physicians have viewed the malady, which has no Food and Drug Administration–approved treatment and no diagnostic test, as psychosomatic. Then, in 2015, the Institute of Medicine (IOM) dismissed the "misconception" of the disease as psychological in a report informed by a review of more than 9000 articles from 64 years of medical literature. "Remarkably little research funding has been made available to study the etiology, pathophysiology, and effective treatment of this disease, especially given the number of people affected," the authors noted. CDC estimates that ME/CFS affects more than 1 million Americans, a majority of them women.

The IOM report "had an unbelievable effect," because it validated patients' experiences—"it told them that they weren't crazy," says geneticist Ronald Davis, who directs the Genome Technology Center at Stanford University in Palo Alto, California, and was one of the report's 15 authors. Davis became a passionate advocate for ME/CFS research and shifted his own studies to the topic after his now 33-year-old son fell ill with ME/CFS in 2008; he is now bedridden. "It also did a lot to NIH and the CDC, who had been ignoring this disease."

A September protest called Millions Missing displayed shoes belonging to people with chronic fatigue syndrome/myalgic encephalomyelitis. This pair was among scores displayed in front of the Department of Health and Human Services in Washington, D.C.

Not long after the IOM report was published, NIH issued its own written assessment, concluding that research has neglected many of the biological factors behind ME/CFS and urging more basic science aimed at teasing out the mechanisms of the disease. Collins also announced a "strengthening" of the agency's ME/CFS effort. He moved oversight of the research out of the agency's small Office of Research on Women's Health and into the $1.7 billion National Institute of Neurological Disorders and Stroke (NINDS), and launched an intramural study that began enrolling people late last month. Forty patients who have developed the disease within the last 5 years, after an infection, will be run through a battery of exams at the Clinical Center, the NIH's research hospital. The assessments, from exercise stress tests to brain magnetic resonance imaging tests, will probe the biological and clinical characteristics of the disease—for which there is not even a broadly agreed-upon definition. For comparison, the study will also include healthy controls and people who have recovered from Lyme disease, which can cause similar symptoms.

Some ME/CFS patients remain skeptical that the NIH moves reflect a genuine commitment to research on the disease. They have criticized what they call the narrow eligibility criteria being used for the Clinical Center study, and they complain that even $15 million scarcely begins to the fund the research they say is needed. Critics such as Deborah Waroff, a retired Wall Street energy analyst who fell ill with ME/CFS in 1989, point, for instance, to multiple sclerosis, a similarly chronic, debilitating disease, which affects fewer than half as many Americans, according to one recent estimate. It received about 13 times as much NIH funding in 2016: $98 million. "ME still floats in space, belonging fully to no NIH institute and therefore having de jure claim to no budget," Waroff says. "The disease remains a beggar when it comes to budget."

Any goodwill won by Whittemore's appearance in Florida may have evaporated after anger erupted last week when ME/CFS patients learned NIH had invited Edward Shorter, a medical historian at the University of Toronto in Canada, to give a 9 November talk at the agency. Shorter last year called the IOM report affirming the biological basis of ME/CFS "valueless; junk science at its worst." He traces the disease to a 1970s "brew of toxic beliefs about being tired all the time."

Walter Koroshetz, the director of NINDS, defended the talk, writing in a letter to ME/CFS patients that "inclusion in the scientific conversation is not an endorsement." In an email to *Science*, he wrote that Shorter's talk was not "an official ME/CFS lecture. [An] announcement went out to the contrary. That was recalled. End of story."

Tangible scientific progress on unraveling ME/CFS might be the best medicine to heal the current divisions. A study published in the *Proceedings of the National Academy of Sciences* in August found depressed blood levels of scores of metabolites in people with the disease compared with healthy controls, suggesting that the disease may push the body into a low-energy state some have compared with hibernation. Scientists and patients are eagerly waiting for the results of a similar study by Lipkin's team. If replicated, the tantalizing finding could fit with an emerging theory that subpar function by mitochondria, the organelles that provide energy for cells, drives the disease.

Hints that the monoclonal antibody rituximab, a drug that destroys antibody-producing B cells, may help some people with ME/CFS have also sparked optimism. ME/CFS patients have a slightly elevated risk of developing B-cell lymphoma, and Norwegian researchers accidentally found that treating a woman who had both conditions with rituximab markedly improved her ME/CFS symptoms. The group went on to do a nonblinded study of the antibody in 29 ME/CFS patients, 18 of whom reported major or moderate improvements in their symptoms. The researchers are now running a larger, double-blind, randomized clinical trial of the drug in 152 patients, planning to evaluate its effectiveness next October.

Øystein Fluge, one of the Norwegian trial's leaders and an oncologist at the University of Bergen's Haukeland University Hospital in Norway, remains cautious. "Many places on the internet say this is an autoimmune disease. We haven't said that. We think some features fit, probably, with some autoimmune mechanism. But that's a hypothesis. We aren't sure." Only one thing is sure: After decades of frustration, the mysterious disease remains maddeningly elusive. ■

PHOTO: MEREDITH WADMAN

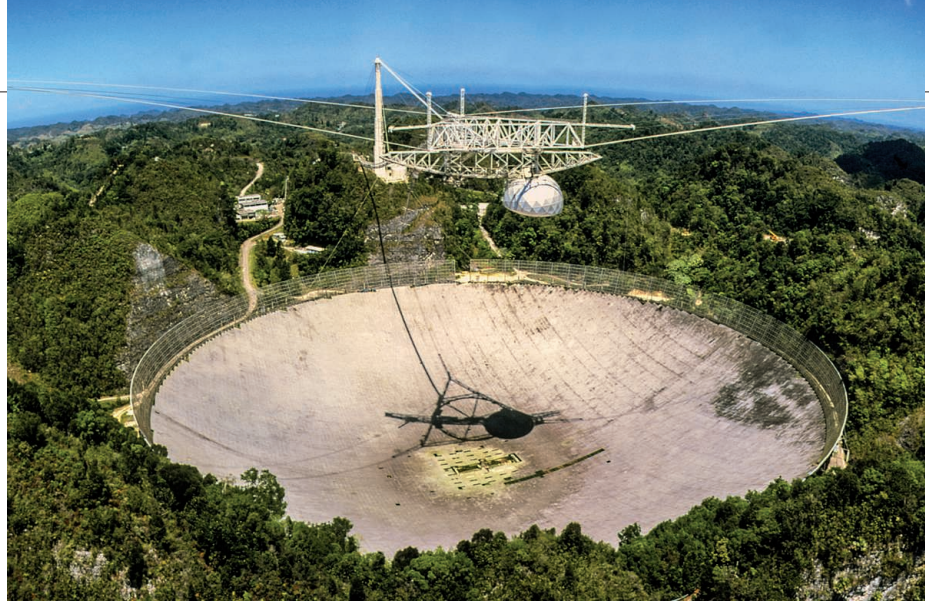

Caring for an endangered fern and reptile could add to the cost of dismantling the Arecibo radio telescope.

ASTRONOMY

NSF says: Out with the old telescopes, in with the new

Agency wants to shed ownership of iconic radio dishes

By **Daniel Clery**

Wanted: a good home for 10 used telescopes. Optical, radio, solar. Well-worn but cared for. Plenty of good years left.

The U.S. National Science Foundation (NSF) is carrying out an unprecedented yard sale of some older telescopes so that it can save $40 million annually and operate a new generation of observatories. It has already arranged to offload or share costs for five telescopes, saving $12 million a year (see table, below). But not enough bargain hunters have yet stepped forward to secure a future for two of its largest and most iconic telescopes, the giant radio dishes in Arecibo, Puerto Rico, and Green Bank, West Virginia. On 28 October, NSF released a draft environmental impact statement (EIS) for Arecibo, a first step in assessing the implications of offloading—or even closing—the telescope.

"We love these telescopes," says Jim Ulvestad, director of NSF's astronomy division in Arlington, Virginia. "We simply don't have the budget to run them all and push the frontier forward."

Already, the agency has a major new project to support: the Atacama Large Millimeter/submillimeter Array (ALMA), 66 dishes recently completed in Chile in collaboration with Europe and Japan. Soon it will have to operate the Daniel K. Inouye Solar Telescope in Hawaii and the Large Synoptic Survey Telescope (LSST) in Chile, due for completion in 2019 and 2021, respectively. NSF currently spends $140 million from its $250 million annual astronomy budget on telescope operations, leaving less than half its budget to support individual astronomers and medium-sized projects and instruments.

If the stable of telescopes does not shrink and there is no dramatic upturn in NSF funding, the two forthcoming telescopes will eat even more deeply into the division's research awards. "It's the combination of old and new coming together," says Jacqueline Hewitt, an astronomer at the Massachusetts Institute of Technology in Cambridge, who chaired a 2016 National Academies report that helped articulate the problem. "There's going to be a trainwreck."

Scientists who rely on the threatened telescopes say they are appalled by the prospect of closure. "It's mind-boggling that NSF doesn't see the merit of this facility," says Robert Kerr, who quit as Arecibo director in 2015 because of frustration with NSF funding cuts. Maura McLaughlin, an astronomer at West Virginia University (WVU) in Morgantown, is a member of the NANOGrav collaboration, which uses chunks of observing time at Arecibo and Green Bank to search for gravitational waves by monitoring the timing of pulsars—spinning stars that act as accurate cosmic clocks. "Frankly, I think it's crazy," she says. "We're very close to detecting gravitational waves. It would take $10 million per year to keep them open. But the NSF ship has sailed."

Yet in reports dating back to 2006, U.S. astronomers accepted that its future lay in observatories such as ALMA and LSST, and that

Telescopes for sale

The National Science Foundation (NSF) is trying to shed 10 aging telescopes to make way for new ones. So far, it has found partners for five of them, and $12 million in savings.

TELESCOPE ON OFFER	LOCATION	FIRST LIGHT	PARTNERS/STATUS	SAVING TO NSF
2.1-Meter Telescope	Kitt Peak in Arizona	1964	Caltech-led consortium	$0.5 million
Mayall Telescope	Kitt Peak in Arizona	1973	Taken over by U.S. Department of Energy	$4 million
Very Long Baseline Array	Various	1993	50% partnership with U.S. Navy	$4 million
Green Bank Telescope	Green Bank, West Virginia	2000	Breakthrough Listen, NANOGrav, West Virginia University	$2.5 million
SOLIS Telescope/GONG	Kitt Peak in Arizona	2003	NOAA sharing GONG operations costs	$1 million
WIYN Telescope	Kitt Peak in Arizona	1994	NASA providing new exoplanet instrument	
Dunn Solar Telescope	Sacramento Peak in New Mexico	1969	University consortium in development	
Arecibo Observatory	Arecibo, Puerto Rico	1963	Environmental review in process	
SOAR Telescope	Cerro Pachón, Chile	2003	Status review when collaboration ends in 2020	
McMath-Pierce Solar Telescope	Kitt Peak in Arizona	1962	Small user community presents few partner opportunities	

CREDITS: (PHOTO) DAVID PARKER/SCIENCE SOURCE; (TABLE) NSF

sacrifices have to be made. Some believe NSF has been slow to act, but the EIS has now planted a flag. Required for status changes at federally funded installations, the EIS lets NSF show it has considered all options and consulted all interested parties. For Arecibo, which was the largest single radio dish in the world until a Chinese telescope opened this year (*Science*, 30 September, p. 1488), the draft statement considers six possible futures: from do nothing to wipe the site clean.

Even closure will come with significant costs. The dish nestles in a hollow in lush, tropical terrain, and restoring the natural beauty of the site would be expensive. Although the EIS does not quantify costs, Ulvestad says that NSF's estimates for dismantling the dish and clearing the site start above $10 million, and could grow. An endangered fern as well as an endangered reptile, the Puerto Rican boa, live in the area; if they are found to be living under the dish, taking it apart while protecting their habitats could prove prohibitively expensive.

The real bargaining will begin around the end of the year when NSF will solicit bids from any partners willing to help support Arecibo. The agency currently spends $8.2 million per year on the telescope, split between astronomy and atmospheric research. (NASA is the Arecibo's other funder, chipping in $3.7 million for its work in identifying near-Earth asteroids.) NSF wishes to significantly reduce its contribution, says Ulvestad, who adds that the solicitation will contain further details about what the agency is willing to pay. A final decision on any offers will be made some time after next June, he says.

NSF is just starting an EIS for Green Bank, the world's largest steerable radio dish. But in some regards, Green Bank already points the way to an alternative future for Arecibo and other endangered telescopes. It is building up a smorgasbord of funding sources that could grow as NSF's support wanes. In addition to the $8.2 million Green Bank receives annually from NSF, the privately funded Breakthrough Listen project, which searches for extraterrestrial intelligence, contributes $2 million a year, and NANOGrav and WVU add smaller amounts. "We're trying to diversify as much as possible," says Karen O'Neil, director of the Green Bank Telescope.

Although Arecibo has had the threat of closure hanging over it for more than a decade, few offers of rescue have appeared so far. Breakthrough Listen made an offer similar to its one with Green Bank, but no deal has been made. Starting the EIS process and raising the specter of closure is focusing the minds of potential partners, Ulvestad says.

"There was no driver if people think [NSF] will solve the problem," he says. "People will only spend money if they have to." ■

NEUROSCIENCE

How the body learns to hurt

Glial cells turn up the volume on pain

By **Emily Underwood**

After 50 years, the neuroscience of pain has a new player. In 1966, researchers traced how the brain learns from repeated stimulation. They found that triggering neurons in one part of the hippocampus—a sliver of brain tissue key to memory—can make linked, distant neurons more likely to fire for many hours afterward, a phenomenon now known as long-term potentiation (LTP). LTP leaves its mark by strengthening some synapses--the connections between neurons—and not others. Now, researchers have found a new type of LTP that may explain how pain itself "teaches" the nervous system.

The pain-related LTP is driven not by neuronal activity, but by glia—nonneuronal cells that protect neurons from injury, among other duties. By releasing inflammatory molecules into cerebrospinal fluid, glia can dramatically strengthen the synapses among pain-sensing neurons in the spinal cord, the team reports online this week in *Science*. The involvement of glia "is an important novel insight that changes the current paradigm," says Niels Eijkelkamp, a neuroscientist at the University Medical Center Utrecht in the Netherlands. It could also help explain why people often experience chronic pain or heightened sensitivity far from the site of an injury.

It's known that traditional LTP can amplify pain in the spinal cord. But it spreads only micrometers from a synapse—not nearly far enough to account for the amped-up pain that some people experience after injury or opioid withdrawal. A growing body of evidence implicates glia in those conditions (*Science*, 4 November, p. 569), so Jürgen Sandkühler of the Medical University of Vienna and colleagues wondered whether glia might drive their own form of LTP. He and his team killed rats, then carefully removed a section of the dorsal horn of the spinal cord, where nerves that transmit pain signals from the extremities converge. To keep the cells alive, the team immersed the cords and attached nerve fibers in cold artificial cerebrospinal fluid. Then they inserted minute electrodes into the neurons to measure their activity.

When a real-life injury occurs, nerve cells release a flood of the cellular energy molecule adenosine triphosphate (ATP). Glia respond to the ATP by unleashing a barrage of inflammatory and other signaling molecules, which can travel long distances from where it is released. To simulate this effect, Sandkühler and colleagues added to the bath a synthetic form of ATP that binds only to two types of glia, microglia and astrocytes. The excited glia expelled inflammatory substances, and those in turn boosted LTP in the dorsal horn neurons by 50% to 150%—a level of amplification comparable to traditional, activity-driven LTP, he says.

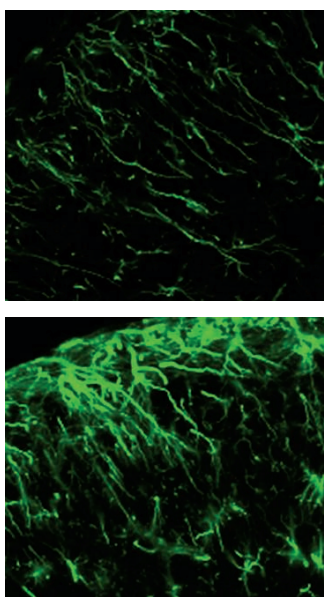

When activated (bottom panel), astrocytes pump out inflammatory molecules that trigger LTP.

Blocking the synthetic ATP from binding to glia eliminated the effect, as did interfering with the function of two molecules released by the cells: D-serine, an amino acid that helps regulate synaptic development, and tumor necrosis factor, an inflammatory protein. Subsequent experiments confirmed that glia-derived substances induced LTP in the spinal cords of live animals.

A key next step will be to pin down just how important specific molecules such as D-serine are to the response in living animals, says neuroscientist Cagla Eroglu at Duke University in Durham, North Carolina. Once the specific molecular actors are identified, it may be possible to develop drugs that block them to calm pain-sensing neurons, she says.

Sandkühler is skeptical that a single drug will be effective. "We have seen so many publications where blocking a single target abolished or reduced pain response in animals, but never worked in humans." Glia, he says, are just one part of a complex puzzle. ■

IMAGES: DEPT. OF NEUROPHYSIOLOGY/CENTER FOR BRAIN RESEARCH/MEDICAL UNIVERSITY OF VIENNA

A cystic fibrosis patient receives therapy to loosen the mucus in her lungs.

PHOTO: BSIP SA/ALAMY STOCK PHOTO

INFECTIOUS DISEASE

Study suggests hidden epidemic in CF patients

Dangerous *Mycobacterium* strains appear to be spreading

By **Kai Kupferschmidt**

Caused by a mutation, cystic fibrosis (CF) isn't contagious, but one serious complication definitely is: infection with *Mycobacterium abscessus*, an obscure agent related to the microbe that causes tuberculosis. Between 5% and 10% of CF patients become infected, and that number is growing. The bacterium thrives in the excess of thick mucus that builds up in the airways of CF patients—sometimes with fatal results.

Until recently, scientists believed that patients picked up the microbe at random, from the soil or water—making infection a case of bad luck. But an analysis of hundreds of bacterial genomes from patients around the world, published in this week's issue of *Science*, tells a different story. It suggests that the bacterium has adapted to humans and that several dangerous strains are spreading from one CF treatment center to the next, from country to country, and even between continents in a silent epidemic.

The researchers have no good explanation for this unexpected mobility, and not everyone is convinced. But other CF experts say the study shows that hospitals need to do more to reduce the infection risk for their patients. "This has huge implications for CF center isolation and cleansing protocols," says Brian O'Sullivan of the Geisel School of Medicine at Dartmouth College.

In CF a defect in a gene for a transporter protein involved in mucus production affects many organs and tissues, but its most serious effects are often seen in the lungs. The mucus-filled lungs are prone to infections, which lead to inflammation, which leads to more mucus production, worsening the disease or even suffocating the patient. *M. abscessus*, rare in healthy people, is notoriously difficult to treat because it is resistant to most antibiotics, O'Sullivan says. "Even when it seems to be gone it can resurface months or years later."

The first evidence that CF patients don't always pick up the microbe at random came in 2013. Researchers discovered that several patients at Papworth Hospital in Cambridge, U.K., were infected with bacteria that were almost identical genetically—something very unlikely to happen if the infections occurred independently. "That told us that there was transmission in one hospital and that was worrying enough," says geneticist Julian Parkhill of the Wellcome Trust Sanger Institute in Hinxton, U.K., who is an author on both the 2013 paper and the new one. "But it didn't answer two things: How widespread was that transmission? And was it just Papworth or was it happening elsewhere?"

To find the answers, the researchers collected more than a thousand *M. abscessus* isolates from 517 CF patients in the United States, the United Kingdom, Denmark, Sweden, the Netherlands, and Australia. They found that the microbial genomes from some patients differed widely from one another, just as you'd expect with environmental infections. But more than three-quarters of the study's patients had strains that belonged to "clusters" with very similar genomes—even though some of the patients lived far apart. "There are three major clones," says Parkhill, "and several others that are emerging and spreading."

The researchers found that bacteria forming part of a cluster were more likely to be taken up by human cells and to survive in them than the microbes without close relatives; the cluster strains also caused more severe disease in mice. This suggests that the microbes have adapted to cause more severe disease in humans, Parkhill says.

But though it's easy to envision spread within a single hospital—for instance through contaminated surfaces or droplets lingering in the air—how long-distance spread could happen is a mystery. CF patients don't travel much between centers, and equipment doesn't circulate widely, says study author Andres Floto of Papworth Hospital. It also seems unlikely that the bacteria are carried by an animal or some unknown environmental vehicle; many bacterial genomes are so similar that the spread must have been rapid. "Our most likely explanation (although we have no proof of this yet) is that healthy humans might be acting as vectors of transcontinental spread," Floto wrote in an email.

Erik Böttger, a medical microbiologist at the University of Zurich in Switzerland, says the paper makes a convincing case for spread within hospitals, which he says is important. But more evidence is needed about long-distance spread, Böttger says. He points out that the researchers didn't collect *M. abscessus* from the environment; patients in different countries may become infected with very similar bacteria because those are the most common in the environment worldwide, he argues. Parkhill admits that the lack of environmental samples is a weakness, but he points out that the big differences seen among bacterial genomes from patients who didn't belong to a cluster suggest that *M. abscessus* genomes in the environment vary widely.

Regardless of whether the clones are spreading globally or just locally, "we need to rethink infection control measures within CF centers," Floto says. At Papworth Hospital, room-cleaning protocols have already been improved, and the ventilation system in a new CF center has been redesigned to completely change the air once every 4 minutes. ■

THE LOST NORSE

Archaeologists have a new answer to the mystery of Greenland's Norse, who thrived for centuries and then vanished

By **Eli Kintisch**, *in Tasilikulooq, in Greenland*

Published by AAAS

Hvalsey Church was the site of a 1408 wedding, the last record of Norse life in Greenland.

CREDITS: (PHOTO) © PETER ESSICK/AURORA; (MAP) J. YOU/*SCIENCE*; (DATA) NABO AND C. MADSEN

In 1721, missionary Hans Egede sailed a ship called *The Hope* from Norway to Greenland, seeking Norse farmers whom Europeans hadn't heard from in 200 years in order to convert them to Protestantism. He explored iceberg-dotted fjords that gave way to gentle valleys, and silver lakes that shimmered below the massive ice cap. But when he asked the Inuit hunters he met about the Norse, they showed him crumbling stone church walls: the only remnants of 500 years of occupation. "What has been the fate of so many human beings, so long cut off from all intercourse with the more civilized world?" Egede wrote in an account of the journey. "Were they destroyed by an invasion of the natives … [or] perished by the inclemency of the climate, and the sterility of the soil?"

Archaeologists still wonder today. No chapter of Arctic history is more mysterious than the disappearance of these Norse settlements sometime in the 15th century. Theories for the colony's failure have included everything from sinister Basque pirates to the Black Plague. But historians have usually pinned most responsibility on the Norse themselves, arguing that they failed to adapt to a changing climate. The Norse settled Greenland from Iceland during a warm period around 1000 C.E. But even as a chilly era called the Little Ice Age set in, the story goes, they clung to raising livestock and church-building while squandering natural resources like soil and timber. Meanwhile, the seal-hunting, whale-eating Inuit survived in the very same environment.

Over the last decade, however, new excavations across the North Atlantic have forced archaeologists to revise some of these long-held views. An international research collective called the North Atlantic Biocultural Organisation (NABO) has accumulated precise new data on ancient settlement patterns, diet, and landscape. The findings suggest that the Greenland Norse focused less on livestock and more on trade, especially in walrus ivory, and that for food they relied more on the sea than on their pastures. There's no doubt that climate stressed the colony, but the emerging narrative is not of an agricultural society short on food, but a hunting society short on labor and susceptible to catastrophes at sea and social unrest.

Historian Poul Holm of Trinity College in Dublin lauds the new picture, which reveals that the Greenland Norse were "not a civilization stuck in their ways." To NABO archaeologist George Hambrecht of the University of Maryland in College Park, "The new story is that they adapted but they failed anyway."

Ironically, just as this new picture is emerging, climate change once again threatens Norse settlements—or what's left of them. Organic artifacts like clothing and animal bones, preserved for centuries in the deep freeze of the permafrost, are decaying rapidly as rising temperatures thaw the soil. "It's horrifying. Just at the time we can do something with all this data, it is disappearing under our feet," Holm says.

IN 1976, a bushy-bearded Thomas McGovern, then 26, arrived for the first time on the grassy shore of a fjord in southern Greenland, eager to begin work on his Ph.D. in archaeology. The basic Norse timeline had already been established. In the ninth century, the advances in seafaring technology that enabled Scandinavian Vikings to raid northern and central Europe also opened the way for the Norse, as they came to be known in their later, peaceful incarnations, to journey west to Iceland. If the unreliable Icelandic *Sagas*, written centuries later, are to be believed, an enterprising Icelander named Erik the Red led several ships to Greenland around 985 C.E. The Norse eventually established two settlements, with hundreds of farms and more than 3000 settlers at their peak. But by 1400, the settlement on the island's western coast had been abandoned, according to radiocarbon dates, and by 1450 the inhabitants in the Eastern Settlement on the island's southern tip were gone as well.

Data gathered in the 1980s by McGovern and others suggested that the colonies were doomed by "fatal Norse conservatism in the face of fluctuating resources," as McGovern, now at Hunter College in New York City, wrote at the time. The Norse considered themselves farmers, he and others thought, tending hay fields despite the short growing season and bringing dairy cows and sheep from Iceland. A 13th century Norwegian royal treatise called *The King's Mirror* lauds Greenland's suitability for farming: The sun has "sufficient strength, where the ground is free from ice, to warm the soil so that the earth yields good and fragrant grass."

Bone samples suggest that even small farms kept a cow or two, a sign of status

The Arctic frontier

Norse colonists established settlements in southern Greenland, often siting their farmsteads on fjords.

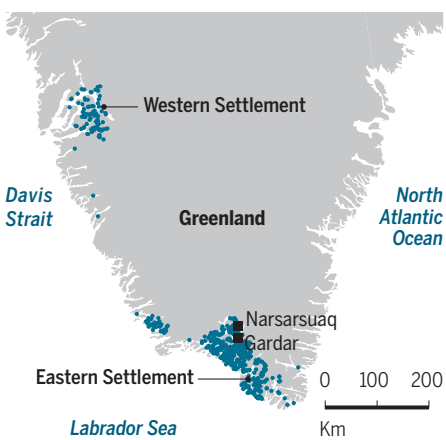

In the 10th and 11th centuries, the Norse crossed the stormy Atlantic to Greenland in vessels resembling this ninth century Viking ship found in Norway.

back in Norway, and written records mention dairy products including cheese, milk, and a yogurt called skyr as essential parts of the diet. "There were no activities more central to Norse identity than farming," archaeologist William Fitzhugh of the Smithsonian Institution's National Museum of Natural History (NMNH) in Washington, D.C., wrote in 2000.

Geographer Jared Diamond of the University of California, Los Angeles, popularized this view in his 2005 bestseller, *Collapse*. The Norse "damaged their environment" as they had done in Iceland, Diamond asserted, based on analyses of dust that suggested erosion caused by felling trees, agriculture, and turf cutting. While foolishly building churches with costly bronze bells, Diamond said, Greenland's Norse "refused to learn" Arctic hunting techniques from the Inuit, who hunted seals and fish year-round. He noted grisly evidence of calamity at a few sites in the Western Settlement: bones of pet dogs with cut marks on them, suggesting hunger; and the remains of insects that feast on corpses, suggesting too few survivors to bury their loved ones. "Every one of [the Norse] ended up dead," Diamond said in 2008.

This narrative held sway for years. Yet McGovern and others had found hints back in the 1980s that the Norse didn't entirely ignore Greenland's unique ecology. Even Diamond had noted that bones of seals comprised 60% to 80% of the bones from trash heaps, called middens, found at small Norse farms. (He believed, though, that only the poorer settlers ate seal meat.) Written sources reported that the Norse routinely rowed up to 1500 kilometers to walrus migratory grounds near Disko Bay in western Greenland. They returned with countless walrus snouts, whose ivory tusks they removed and prepared for trade with Europe. The Norse paid tithe to the Norwegian king and to the Catholic Church in ivory, and traded it with European merchants for supplies like iron, boat parts, and wood. But McGovern dismissed the walrus hunt as "a curious adjunct," he recalls, echoing the scholarly consensus that farming was central.

THREE DECADES LATER here at Tasilikulooq (TA-SEE-LEAK-U-LOCK), a modern Inuit farm of green pastures flanked by lakes, a couple of McGovern's students and others are busy exploring the remains of a medium-sized farm that once housed sheep, goats, horses, and a few cows. Two graduate students in rubber overalls hose 700-year-old soil off unidentified excavated objects near a midden downhill from a collapsed house. A brown button the size of a nickel emerges on the metal sieve. "They found one more of those buttons," says archaeologist Brita Hope of the University Museum of Bergen in Norway, smiling, when word makes it back to the farmhouse the nine-member team uses as a headquarters for the monthlong dig. "We could make a coat," a student jokes.

But the function of the button matters a lot less than what it's made of: walrus tooth. Several walrus face bones have also turned up at the farm, suggesting that the inhabitants hunted in the communal Disko Bay expedition, says excavation leader Konrad Smiarowski of the City University of New York in New York City. These finds and others point to ivory—a product of Greenland's environment—as a linchpin of the Norse economy.

One NABO dig in Reykjavik, for example, yielded a tusk, radiocarbon dated to about 900 C.E., which had been expertly removed from its skull, presumably with a metal tool. The find suggests that the early Icelandic Norse were "experienced in handling walrus ivory," NABO members wrote in a 2015 paper; it follows that the Greenlanders were, too. Although historians long assumed that the Norse settled Iceland and Greenland in search of new farmland, some researchers have recently suggested that the hunt for ivory instead drove the settlement of both islands. Walrus in Iceland were steadily extirpated after the Norse arrived there, likely hunted out by the settlers.

The high value that medieval Europe placed on walrus ivory would have provided plenty of incentive to pursue it in Greenland. Craftsmen used ivory in luxury ornaments and apparel, and in objects like the famous Lewis chess set, discovered in Scotland in 1831. In 1327, an 802-kilogram parcel of Greenland tusks was worth a small fortune—the equivalent of roughly

Fighting the big chill

Environmental data show that Greenland's climate worsened during the Norse colonization. In response, the Norse turned from their struggling farms to the sea for food before finally abandoning their settlements.

Temperature

Winter temperatures dropped below the long-term average by more than a degree halfway through the 5-century occupation, according to oxygen isotope data in cores taken from the Greenland Ice Sheet.

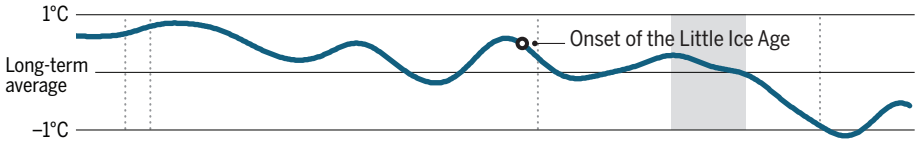

Storminess

Measurements of salt particles in ice cores suggest that storminess rose toward the end of the occupation, perhaps making voyages to hunt and trade walrus ivory even more dangerous.

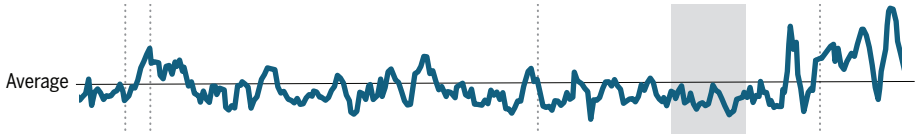

Proportion of marine food in diet

As conditions for farming worsened, the Norse shifted to a more marine diet, as shown by carbon isotopes in bones found in archaeological sites in the Eastern and Western settlements.

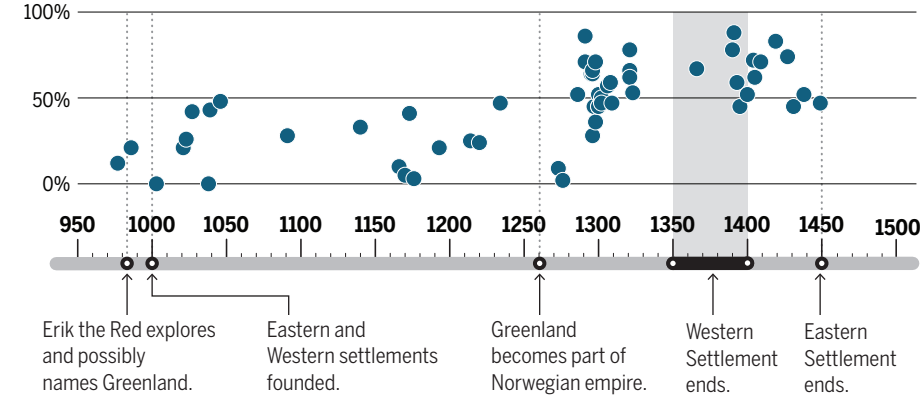

CREDITS: (PHOTO, OPPOSITE PAGE) © SWANNELL/AURORA PHOTOS; (GRAPHICS) J. YOU/*SCIENCE*; (DATA): [TEMPERATURE] CLIMATIC SIGNALS IN MULTIPLE HIGHLY RESOLVED STABLE ISOTOPE RECORDS FROM GREENLAND VINTHER *ET AL.* 3 NOVEMBER 2009; [STORMINESS] NORSE GREENLAND SETTLEMENT: DUNMORE *ET AL.*, 2007; [DIET] HUMAN DIET AND SUBSISTENCE PATTERNS IN NORSE GREENLAND AD C. 980–AD C.1450 ARNEBORG *ET AL.* 2012

Growing Greenland's archaeologists

By **Eli Kintisch**, *in Tasiilikulooq, in Greenland*

One warm afternoon at an ancient Norse site, now a modern Inuit sheep farm, archaeology graduate student Michael Nielsen lay on his stomach, contentedly sorting through thousands of tiny rocks and bones seeking artifacts. For archaeologists at a dig, the painstaking work known as picking is an everyday routine. What's unusual, however, is Nielsen's background: He is a native Greenlander.

"I just love the artifacts," he says. For Nielsen, born in the nearby town of Narsaq, an infatuation with archaeology started "from the first minute" he began working on a dig 3 years ago. Then an undergraduate at the University of Greenland in Nuuk, he enjoyed the physicality of the work. And the waves of occupation in Greenland—ancient indigenous populations who arrived then disappeared, followed by the Norse, and finally the Inuit—captured his interest.

Yet even as researchers comb Greenland for clues to the Norse disappearance (see main story, p. 696), only a handful of homegrown archaeologists are on hand to help; most research is done by outsiders from Denmark or other Western countries. The paucity of local experts may explain why much of the island's rich record has been overlooked, with hundreds of known archaeological sites unexcavated. "Having more homegrown archaeologists would be very important for Greenland so that they can set their own priorities," says Konrad Smiarowski, a graduate student at the City University of New York in New York City who leads the dig here. "The sites that have been excavated are those that the international community has prioritized, but you could see Greenlandic scientists targeting other ones, for example sites that are at risk of loss from climate change."

For now, budding archaeologists like Nielsen face challenges. The University of Greenland doesn't have an archaeology department. And parents and policymakers have other priorities, Nielsen says. "People want Greenlandic students to become doctors and lawyers."

All the same, "it's important for us to make our own research and write our own history," says Greenlander Mari Kleist, who got her Ph.D. in archaeology in Denmark in 2013 and is now based in Brussels. Both she and Nielsen intend to one day publish on Greenland archaeology in Greenlandic, an Inuit tongue. "Greenlanders don't know much about archaeology," Nielsen says. "I'd want to tell people about the prehistory of Greenland, the Norse, and the Inuit." ■

Greenlander Eva Luusi Marcussen-Mølgaard of the University of Greenland in Nuuk (left) washes soil off artifacts. She is one of a handful of students eager to study the archaeology of their homeland.

PHOTO: © ELI KINTISCH

780 cows or 60 tons of dried fish, according to tithing records analyzed in 2010 by University of Oslo archaeologist Christian Keller. "The Norse had found a cornucopia in the North Atlantic, a marine ecosystem just teeming with walruses and other animals," says historian Holm.

They exploited it not just for ivory, but also for food, Smiarowski says as he huddles in a dimly lit side room here to review recent finds. One bag contains bones collected from a layer dating to the 1350s. A long, thin, cow bone had been split open, probably to eat the marrow. But most of the bones are marine: scraps of whale bone, jaw and skull fragments of harp seals, a bit of inner ear of a hooded seal. These two species of seal migrate north along Greenland shores in the spring, and Smiarowski thinks the Norse likely caught them with boats and nets or clubs.

In 2012, NABO researchers clinched the case that the Greenlanders ate a marine diet by analyzing human bones in Norse graveyards. Animals that live in the sea have ratios of carbon and nitrogen isotopes that differ from those found in terrestrial animals, and this isotopic signature is passed on to the people who eat them. The Norse bones show that as the settlement developed from the 11th to the 15th century, their diet contained ever more marine protein (see graphic, p. 699). Far from clinging to livestock as temperatures fell, the Norse instead managed a successful subsistence system with "flexibility and capacity to adapt," wrote the author of the 2012 paper, Jette Arneborg from the National Museum of Denmark in Copenhagen.

Nor were the Norse incompetent farmers, as Diamond and others have suggested. Soil geographer Ian Simpson of the University of Stirling in the United Kingdom says previous studies overestimated the Norse contribution to erosion in Greenland. New pollen and soil data show that the Norse allowed fields and what little forest existed to recover after tilling and turf cutting. And in analyses of soil and lake sediment cores, researchers have found chemical and paleoecological clues indicating that Norse farmers skillfully maintained pastures with manure fertilizer and irrigation ditches.

Such findings, along with the ivory evidence, have transformed ideas about Norse society, says McGovern, whose beard is now white. "You start to see old data, like the seal bones in the middens, in a new light. It's exciting to get a chance to revise your old thinking before a younger colleague can," he says. "We used to think of Norse as farmers who hunted. Now, we consider them hunters who farmed."

It was a sustainable lifestyle for hundreds of years. But in the 13th century, economics and climate began to conspire against the Norse. After 1250, a cooling climate posed multiple threats to a marine-oriented society reliant on seal and walrus. (Global average temperature fell by about a degree during the Little Ice Age, although scientists have struggled to quantify local cooling.) Even before the big chill set in, *The King's Mirror* describes ships lost and men who perished in ice. Historians and climatologists agree that as the cold spell continued, ice would have clogged the seas farther south and for longer each year, disrupting voyages. And concentrations of salt particles in glacier cores indicate that seas became stormier in the 15th century. Norsemen hunting migratory seals or walrus on the high seas would have been at increasing risk. The nomadic Inuit, by contrast, hunted seal native to the fjords, and rarely embarked on open-ocean hunts or journeys.

Not only did the climate disrupt trade, but the market did, too. Around 1400, the value of ivory in Europe fell as tusks from Russian walrus and African elephants flowed into the continent.

Even as surviving from marine resources became more difficult, the growing season on land shortened, and the meager pastures yielded even less. But soil and sediment analyses show that the farmers, too, tried to adapt, Simpson said, often fertilizing and watering their pastures more intensively as temperatures dropped. "We went in with the view that they were helpless in the face of climate change and they wrecked the landscape," Simpson says. Instead, he says, these "pretty good managers" actively adapted to the cooling climate. In the end, however, their best efforts fell short.

AT THE GRAND BISHOP'S SEAT of Gardar, 35 kilometers away by boat from the modest farm at Tasilikulooq, grass grows around the ruins of a cathedral, the bishop's residence, and myriad other buildings probably built by stonemasons shipped in from Norway. Stone shelters here once housed more than 100 cows—a sign of power in medieval Scandinavia.

If the Greenland settlement was originally an effort to find and exploit the prized natural resource of ivory, rather than a collection of independent farmers, the society would have needed more top-down planning than archaeologists had thought, says Christian Koch Madsen of the Danish and Greenlandic National Museums in Copenhagen. His work and other research support that notion by revealing orchestrated changes in the settlement pattern as the climate worsened.

Madsen carefully radiocarbon dated organic remains like wood from the ruins of 1308 Norse farms. The dates show that Gardar, like other rich farms, was established early. But they also suggest that when the first hints of the Little Ice Age appeared around 1250, dozens of outlying farms were abandoned, and sometimes reestablished closer to the central manors. The bones in middens help explain why: As temperatures fell, people in the large farms continued to eat beef and other livestock whereas those in smaller farms turned to seal and caribou, as Diamond had suggested. To maintain their diet, Greenland's powerful had to expand labor-intensive practices like storing winter fodder and sheltering cows. He thinks that larger farms got the additional labor by establishing tenant farms.

Greenland was a key source of walrus ivory, which was carved into luxury goods such as the famous 12th century Lewis chessmen from Scotland.

PHOTO: © NATIONAL MUSEUMS SCOTLAND

The stresses mounted as the weather worsened, Madsen suspects. He notes that the average Norse farmer had to balance the spring- and summertime demands of his own farm with annual communal walrus and migratory seal hunts. "It was all happening at once, every year," Madsen says. Deprivation in lower societal strata "could eventually have cascaded up through the system," destabilizing large farms dependent on tithes and labor from small ones. The disrupted ivory trade, and perhaps losses at sea, couldn't have helped. The Greenland Norse simply could not hold on.

It adds up to a detailed picture that most archaeologists studying the Norse have embraced. But not everyone agrees with the entire vision. Fitzhugh of NMNH, for one, questions the reconception of the colony as an ivory-focused trading post and still thinks farming was more important. "They couldn't get enough ivory to maintain 5000 people in the Arctic," he says.

Fitzhugh does agree with Madsen and others on how the final chapter of the Greenland saga may have played out. Despite the signs of crisis at a few Western Settlement sites, those in the Eastern Settlement show no sign of a violent end. Instead, after farmhouses collapsed, remaining settlers scavenged the wood from them, suggesting a slow dwindling of population. The challenge for the average Greenlander to survive drove "a constant emigration" back to Iceland and Europe, Fitzhugh hypothesizes, "which could bring the Eastern [Settlement] to a close peacefully, without starvation or death by Inuit."

The NABO team hopes future grants will allow them to fill out that picture. They're eager to start new excavations in the Western Settlement, where artifacts could shed light on any contact between the Norse and Inuit, a historical possibility about which there are little hard data.

Time is running out. The Tasilikulooq excavation yielded well-preserved artifacts including wooden spoons, bowls, and a small wooden horse. But McGovern fears that its success may not be repeated. Thirty years ago most sites in the Eastern Settlement contained preserved bone, hair, feathers, and cloth. A NABO survey of 90 sites has found, however, that most organic samples "had pretty much turned to mush" as the permafrost thawed, Smiarowski says. Tasilikulooq was one of only three sites spared.

Hans Egede, the missionary, wrote that he went to Greenland 500 years ago to save its people from "eternal oblivion." Today's archaeologists fear a different oblivion—that Greenland's prehistory will be lost unless it is quickly unearthed. As pioneers who weathered climate change, the Greenland Norse may hold lessons for society today. But the very changes that make those lessons urgent could keep them from ever being fully deciphered. ■

Reporting for this story was supported by the Pulitzer Center on Crisis Reporting.

EPIDEMIOLOGY

Leprosy in red squirrels

Red squirrels are an unexpected reservoir of otherwise human-restricted leprosy bacilli

By **Timothy P. Stinear**[1] *and* **Roland Brosch**[2]

In 1873, the Norwegian doctor Armauer Hansen helped to lay the foundations of modern microbiology when he discovered that leprosy was an infectious disease, not an inherited condition. However, his attempts to cultivate the rod-shaped bacilli that he had observed in microscopic studies of tissues from leprosy patients were unsuccessful, emphasizing the unique growth requirements of these bacilli. Even today, *Mycobacterium leprae*, the causative organism of leprosy, cannot be grown on culture media, and many questions remain about its mode of transmission and epidemiology (*1*). The unexpected identification of red squirrels (*Sciurus vulgaris*) as an extant animal reservoir of leprosy bacilli by Avanzi *et al.* (*2*) on page 744 of this issue elucidates the host conditions that may allow leprosy bacilli to multiply and cause disease.

Despite the global implementation of effective multidrug therapy, more than 220,000 new cases of leprosy still occur each year (*2*). The disease is infamous for the terrible disfigurement and deformity that victims can experience, the result of peripheral nerve damage inflicted by slowly replicating leprosy bacilli. Leprosy was long considered to be an exclusively human infectious disease, mainly because most attempts to propagate the causative bacteria in diverse animal models failed.

The most commonly used experimental methods for multiplying leprosy bacilli are infection of nine-banded armadillos or inoculation of mouse footpads (*3*). Armadillo-grown *M. leprae* was crucial for obtaining the genetic material for the first whole-genome sequencing of *M. leprae* in 2001 (*4*). This project revealed that *M. leprae* has undergone extensive genome decay, associated with the loss of about half of its gene functions (*4*). This observation suggests that the pathogen has adapted to a specialized niche environment (human skin and nerve tissues), followed by very limited genetic diversification (*5*).

Avanzi *et al.* enrich this view by identifying a new wildlife reservoir for *M. leprae* besides the nine-banded armadillo in the southern United States (*6*). The authors further report that red squirrels can also harbor *Mycobacterium lepromatosis*. This recently discovered

[1]*Department of Microbiology and Immunology, Peter Doherty Institute for Infection and Immunity, University of Melbourne, Melbourne, VIC 3000, Australia.* [2]*Institut Pasteur, Unit for Integrated Mycobacterial Pathogenomics, 75015 Paris, France. Email: roland.brosch@pasteur.fr*

Red squirrels (*Sciurus vulgaris*) on Brownsea Island in southern England harbor leprosy bacilli of the same genotype as those that infected medieval humans.

species of leprosy bacilli can cause a severe and debilitating form of leprosy (lepromatous leprosy) in humans and shares many genomic characteristics with *M. leprae* (*7*).

However, it is Avanzi *et al.*'s discovery of *M. leprae* in endangered red squirrels on the island of Brownsea in southern England that is the most startling (see the figure). Using sophisticated enrichment techniques directly from infected tissues (*8*), the authors obtained sufficient bacterial DNA to sequence the entire genomes of the leprosy bacilli and show that Brownsea Island red squirrels are infected with the same genotype (3I) of *M. leprae* as were humans that inhabited southern England during the Middle Ages (see the figure). The same genotype has previously been found in *M. leprae*–infected armadillos in the southern United States (*6*). In both cases, an ancient human-to-animal transmission is the most plausible explanation of how leprosy may have appeared in these nonhuman mammalian hosts (*2, 6*).

This situation is reminiscent of the evolutionary pathway of another important group of pathogenic mycobacteria, the *Mycobacterium tuberculosis* complex. In this group of genomically very closely related strains, *M. tuberculosis* and *Mycobacterium africanum* represent seven lineages that are responsible for the millions of global human tuberculosis cases. In contrast, the animal pathogens are regrouped in a single sublineage that has branched off from the *M. africanum* lineage and evolved into different subtypes (*9*). The different members of this animal lineage cause tuberculosis-like disease in a range of nonhuman mammalian species, such as antelopes, badgers, cattle, deer, goats, mongooses, seals, and voles (*9*). In some cases, these mycobacteria have hijacked social communication behavior of the animals to further transmission; for example, transmission from the anal gland to the nasal planum in mongoose populations (*10*) causes skin lesions that roughly resemble the lepromatous lesions in red squirrels.

Another mycobacterial pathogen, *Mycobacterium ulcerans*, has a niche-adapted genomic signature similar to that of *M. leprae*. Small terrestrial mammals may also play a role in the ecology of this pathogen, which is the agent of the neglected tropical disease Buruli ulcer (*11, 12*).

It is remarkable that *M. leprae* has persisted for centuries undetected in wildlife populations of the British Isles. The possibility of an as-yet-undiscovered host diversity of mycobacterial pathogens existing under our noses must be taken into account for disease control. However, Avanzi *et al.* show that, in contrast to red squirrels, gray squirrels were not infected with leprosy bacilli. Thus, host susceptibility and immunity are of major importance for development of mycobacterial disease. The discovery of other environmental reservoirs remains critically important if we are to eradicate diseases like leprosy that have plagued humanity for too long. ■

Evolution of slow-growing mycobacteria

This simplified evolutionary model illustrates the relationships between different pathogenic mycobacteria, including *M. leprae*. Phylogenetic distances are approximate. MRCA, most recent common ancestor.

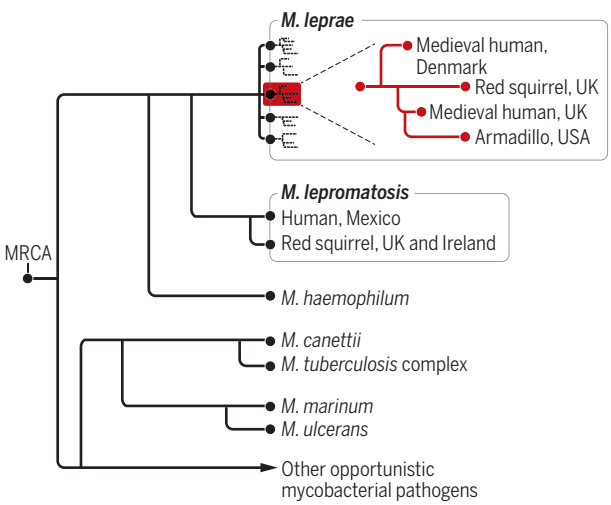

GRAPHIC: V. ALTOUNIAN/*SCIENCE*

REFERENCES AND NOTES

1. C. Franco-Paredes, A. J. Rodriguez-Morales, *Ann. Clin. Microbiol. Antimicrob.* **15**, 33 (2016).
2. C. Avanzi *et al.*, *Science* **354**, 744 (2016).
3. C. C. Shepard, *J. Exp. Med.* **112**, 445 (1960).
4. S. T. Cole *et al.*, *Nature* **409**, 1007 (2001).
5. M. Monot *et al.*, *Nat. Genet.* **41**, 1282 (2009).
6. R. W. Truman *et al.*, *N. Engl. J. Med.* **364**, 1626 (2011).
7. P. Singh *et al.*, *Proc. Natl. Acad. Sci. U.S.A.* **112**, 4459 (2015).
8. V. J. Schuenemann *et al.*, *Science* **341**, 179 (2013).
9. E. C. Boritsch *et al.*, *Mol. Microbiol.* **93**, 835 (2014).
10. K. A. Alexander *et al.*, *MBio* **7**, e00281 (2016).
11. J. A. Fyfe *et al.*, *PLOS Negl. Trop. Dis.* **4**, e791 (2010).
12. T. P. Stinear *et al.*, *Genome Res.* **17**, 192 (2007).

ACKNOWLEDGMENTS

T.P.S. is supported by a research fellowship from the National Health and Medical Research Council of Australia (1105525). R.B. is a member of the LabEx consortium IBEID at the Institut Pasteur and is supported by the Fondation pour la Recherche Médicale (grant DEQ20130326471).

10.1126/science.aal0145

TECHNOLOGY

Science of the World Wide Web

Web science must remain an interdisciplinary pursuit

By **James Hendler**[1] *and* **Wendy Hall**[2]

Ten years ago, Wikipedia was still in its infancy (and totally dismissed by the establishment), Facebook was still restricted to university users, Twitter was in beta testing, and improving search capabilities was the topic that dominated Web conference research agendas. There were virtually no smartphones, online surveillance of activity and data storage was largely unknown beyond security services, and no one knew that being a data scientist was one day going to be "the sexiest job in the world" (*1*).

In 2006, we and others argued for the need to create a field to explore the underlying science, engineering principles, and social impacts of the World Wide Web (*2*). Certainly, over the decade since "Creating a science of the Web" was published (*2*), society has become increasingly dependent on Internet technology for virtually all aspects of communication and handling information. The 2006 article and its follow-ons helped fuel the emergence of a field now known as "Web science," with dedicated academic programs, conferences, and research journals that are associated with this interdisciplinary specialty and community. Although this field is still in an early stage, it continues to lay the groundwork for future research that will be needed to ensure that this amazing information-age ecosystem that has been collectively built by society remains fit for purpose and especially for the betterment of humanity in the years to come.

In the past decade, new uses of the Web—the major means by which information is disseminated over the Internet—in both scientific and public discourse have grown, and shared data on the Web increasingly have become both a critical research resource and a challenge to manage technically and socially. Web science researchers have focused on several different aspects of the Web and

[1]*Department of Information Technology and Web Science, Rensselaer Polytechnic Institute, Troy, NY, USA.* [2]*Computer Science Department, University of Southampton, UK. Email: hendler@cs.rpi.edu; wh@ecs.soton.ac.uk*

We must continue to study the impact of the Web on society, and vice versa.

of its evolution. Much of the interest in data science today can be attributed to the vast stores of information, both structured (where metadata is organized into defined fields such as temperature or precipitation) and unstructured (documents, images, and videos), that have become available via the Web. The information available through mobile Web platforms, such as geolocation information from smartphones, now powers a growing segment of new industries such as Uber, Lyft, Airbnb, and other parts of what has become known as the sharing economy. Social media analysts look to understand, mathematically and socially, the trends being seen on the Web as reflected through information shared on social networking websites and mobile applications (indeed, apps may not appear to be like Web browsing, but they rely on the same Web architectures). Governments in cities and countries around the world now release a range of data on the Web in open formats, ranging from city bus locations to environmental pathogen reports (*3*). Open publishing is making journal and conference papers freely available to researchers, and online forums, such as PatientsLikeMe.com, are new sources of information for scientists and the wider community, too.

The emerging Internet of Things—the idea of networks of electronically enabled objects that collect and exchange data—promises to yield even more information, including much real-time data on the movement not just of people, but of energy and other resources needed for modern society. The growth of available information is also leading to increasing use of data analytics in many fields, and the intersection of network science, data science, and Web science is helping to bring new technologies to scientists and engineers who grapple with large-scale problems (*4*).

One of the goals of Web science is to track and explore trends and usages of the information space that abounds. To this end, a number of research groups in Web science laboratories around the world began a project in 2012 called the "Web Observatory" to collect and share data about Web utilization. Increasingly, the move is from static analyses to tracking changes in Web use in real time, and to improving predictive models for understanding the impacts of information use across the Internet. Repository metadata and lightweight standards (protocols and interface methods that dictate communication processes across the Web) have been developed, and information is now being tracked from 12 countries on five continents (*5*). The continued development of this global Web Observatory will enable researchers to study past patterns of Web usage and growth and develop forecasting models to help us better understand future impacts of emerging technologies.

Web science researchers are also studying what can be gleaned from data accrued through crowdsourcing, collective intelligence, and citizen science, endeavors that have been enabled by Web technologies. Websites such as Wikipedia are powered by an interaction of many people, in many roles, and increasingly, the growth of citizen science sites such as the Web portal Zooniverse (home to numerous citizen science projects) provide new ways for scientists to interact with volunteers over the Web (*6*, *7*). Such websites are harnessing the cognitive capacities of many millions of people, and the results are "social machines" that are powerful in their societal influence—Wikipedia alone reports billions of page views per month. Developing principles for the successful design and governance of such sites, and lowering the barriers of entry for scientists and others in creating them, remain active areas of Web science research (*8, 9*).

As information on the Web continues to grow, so will the tension between the privacy desires of data providers and potential use of the information for the social good. Issues such as Internet governance and policy, Web engineering principles, digital identity, digital literacy, and the privacy and ethical issues that society face as more of our lives are lived online are major analytic challenges for the future (*10*). Web scientists must address these issues using tools and methodologies whose development began over the past 10 years. These tools and approaches are being forged from the interdisciplinary perspectives needed to cover such a wide range of concerns.

As politicians and funding bodies emphasize the economic advantages of more students entering science, technology, engineering, and mathematics (STEM) areas of study, there is evidence of a concomitant tendency, seen in both developed and developing countries, to treat the social sciences and humanities as if they are somehow of lesser value. Yet, not only is the Web a network of machines, it is a network of billions of people throughout the world interacting together in ways not previously possible. Appreciating the impact of the Web's science and engineering on society, and conversely the impact that society has on the development of the Web and the Internet, requires a deep understanding of socio-technical systems. Web science therefore is, and must remain, an interdisciplinary pursuit, uniting the talents of a wide swath of researchers from many fields of physical and mathematical sciences, engineering, humanities, and social sciences. The World Wide Web will continue to bring people together and provide unimagined opportunities for society. The need for Web science is manifest, and indeed, as we wrote 10 years ago: "If we want to model the Web; if we want to understand the architectural principles that have provided for its growth; and if we want to be sure that it supports the basic social values of trustworthiness, privacy, and respect for social boundaries, then we must chart out a research agenda that targets the Web as a primary focus of attention" (*2*). ■

REFERENCES

1. T. H. Davenport, D. J. Patil, "Data scientist: The sexiest job of the 21st century," *Harvard Business Review* (October 2012).
2. T. Berners-Lee *et al.*, *Science* **313**, 769 (2006).
3. M. Janssen, Y. Charalabidis, A. Zuiderwijk, *Inf. Syst. Manag.* **29**, 258 (2012).
4. K. O'Hara *et al.*, S. Contractor, W. Hall, A. Hendler, N. Shadbolt, *Found. Trends Web Sci.* **4**, 103 (2013).
5. T. Tiropanis *et al.*, *IEEE Intell. Syst.* **28**, 100 (2013).
6. C. J. Lintott *et al.*, *Mon. Not. R. Astron. Soc.* **389**, 1179 (2008).
7. R. Simpson, K. R. Page, D. De Roure, in *Proceedings of the 23rd International Conference on World Wide Web* (Association for Computing Machinery, 2014), pp. 1049–1054.
8. J. Hendler, T. Berners-Lee, *Artif. Intell.* **174**, 156 (2010).
9. N. R. Shadbolt *et al.*, *Proceedings of the 22nd International Conference on World Wide Web* (Association for Computing Machinery, 2013).
10. L. Cranor *et al.*, https://arxiv.org/abs/1604.03160 (2016).

10.1126/science.aai9150

GENE REGULATION

Making the cut in the dark genome

CRISPR screens will reveal important regulatory elements in the noncoding genome

By **Jaclyn M. Einstein**[1,2] *and* **Gene W. Yeo**[1,2,3,4]

Noncoding elements encompass more than 98% of the human genome and have been linked to regulatory sequences that contribute to human health and disease (*1*). Since the publication of the human genome sequence, considerable effort has been made to annotate functional elements, including noncoding regulatory regions—i.e., cis-regulatory regions and noncoding RNAs (ncRNAs) that are involved in transcriptional regulation. Transcription factors often associate with hundreds to thousands of binding sites throughout the genome, and identifying which sites regulate gene expression often requires time-consuming and complex enhancer studies, or parallel assays in which short enhancer or promoter sequences are cloned into non-native contexts (*2*, *3*). A recent study by Sanjana *et al.* (*4*) and a report by Fulco *et al.* (*5*) on page 769 of this issue address this obstacle using clustered regularly interspaced short palindromic repeats (CRISPR) screens to functionally characterize noncoding elements in their native context.

Previously, large-scale biochemical efforts have discovered potential regulatory sequences that are targeted by hundreds of DNA-binding proteins. In particular, the development of methods to identify deoxyribonuclease I hypersensitive sites (DHSs) and large-scale chromatin immunoprecipitation–sequencing (ChIP-seq) profiling have enabled a genome-wide view of the protein-bound chromatin landscape (*2*, *3*). However, despite these advances, linking these molecular associations with functional regulation has remained challenging.

CRISPR screens offer a powerful approach for the unbiased removal of protein-coding genes using a pool of CRISPR vectors that target different genomic loci. The CRISPR system effectively generates mutations at specific genomic loci, guided by single guide RNAs (sgRNAs) that are homologous to genomic regions upstream of an NGG sequence (protospacer adjacent motif) in human cells (*6*, *7*). The first CRISPR "knockout" screens were on the genome scale, inducing full gene knockout, and overcame many limitations experienced in RNA interference screens—i.e., off-target effects and incomplete protein depletion (*8*, *9*) (see the figure).

Sanjana *et al.* used this system to investigate noncoding regulation of vemurafenib resistance in melanoma cells [vemurafenib is an inhibitor of the serine-threonine protein kinase domain of B-Raf (BRAF) proteins carrying the V600E mutation, in which valine at position 600 is substituted by glutamic acid]. Noncoding regions were targeted 5′ and 3′ of the major variants of resistance genes, neurofibromatosis type 1 (*NF1*), *NF2*, and cullin 3 (*CUL3*), using oligonucleotide arrays tiling across 713 kb of sequence. CRISPR-associated protein 9 nuclease (Cas9) from *Streptococcus pyogenes* (spCas9) generates frameshift, loss-of-function mutations by inducing double-stranded breaks in DNA and creating insertion and deletion (indel) mutations at loci guided by an sgRNA characterized by a CRISPR targeting RNA (crRNA)–trans-activating crRNA (tracrRNA) fusion (*6*, *7*). After infection and treatment with BRAF inhibitor, sgRNAs targeting CUL3 noncoding regions 5′ of the transcription start site were the most highly enriched compared with the control. Enriched sgRNAs occurred with *CUL3* depletion and were associated with regulatory regions that experienced chromatin looping, changes in posttranslational histone modifications, and disruptions in canonical transcription factor binding sites.

Fulco *et al.* used a proliferation-based CRISPR screen with sgRNAs tiling across 1.29 Mb of sequence in noncoding regions 5′ and 3′ of globin transcription factor 1 (*GATA1*)

CRISPR-Cas9 screening methods: dead or alive

Pooled screening approaches identify noncoding regulatory elements using CRISPR-mediated gene knockout methods that employ Cas9 nucleases exhibiting various levels of control.

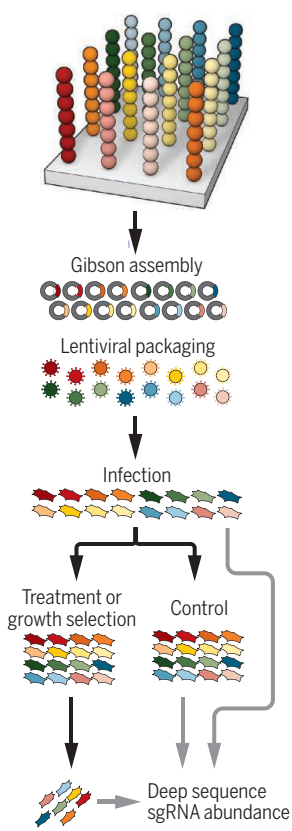

CRISPR screening method
Lentiviral vectors are created by cloning an oligonucleotide array containing sgRNA sequences into a lentiviral vector backbone. The cells are transduced and treatment selected, and sgRNA abundance is quantified by deep sequencing.

CRISPR-spCas9
A CRISPR-spCas9 vector backbone exhibiting constitutive spCas9 expression. Mutations are generated by double-strand breaks.

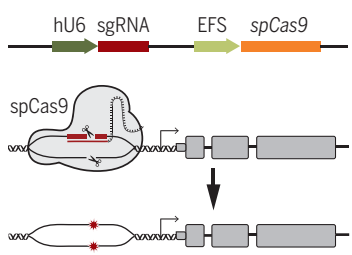

CRISPRi
A CRISPRi vector backbone exhibiting doxycycline-induced expression of dCas9-KRAB. The KRAB effector represses transcription of the target gene.

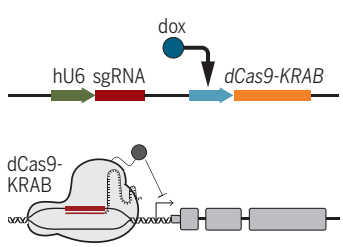

[1]Department of Cellular and Molecular Medicine, University of California, San Diego, La Jolla, CA 92093, USA. [2]Stem Cell Program and Institute for Genomic Medicine, University of California, San Diego, La Jolla, CA 92093, USA. [3]Department of Physiology, National University of Singapore, Singapore 117597. [4]Molecular Engineering Laboratory, A*STAR, Singapore 138673. Email: geneyeo@ucsd.edu

GRAPHIC: V. ALTOUNIAN/SCIENCE

and Myc proto-oncogene protein (*MYC*), which regulate proliferation of K562 erythroleukemia cells. The authors used the CRISPR interference (CRISPRi) method, which uses the catalytically inactive version of Cas9 (dCas9), providing an inducible system for RNA-guided DNA targeting without inducing mutations (*10*). When coupled to a Krüppel-associated box (KRAB) repressor domain, stable and effective transcriptional repression is achieved at specific loci guided by an sgRNA, characterized by crucial dCas9 and *S. pyogenes* terminator hairpins (*10*, *11*). After infection and doxycycline-induced dCas9 targeting, enriched sgRNAs corresponded to DHSs, which harbor binding sites for many transcription factors. More interestingly, dCas9 targeting of *GATA1* or histone deacetylase 6 (*HDAC6*) enhancers reduced HDAC6 expression, suggesting competition between genes for common enhancers. Identified *MYC* enhancers corresponded to alternative transcription start sites and CCCTC-binding factor (CTCF)–mediated chromatin loops, all of which likely affect cellular proliferation.

Whereas both CRISPR-spCas9 and CRISPRi screening methods were successful in identifying noncoding regulators, CRISPRi is limited to transcriptional repression, which often varies between genes. The studies of Sanjana *et al.* and Fulco *et al.* serve as specific cases that contribute to the larger goal of identifying all noncoding regulatory regions by laying the groundwork for generating genome-wide screens tiling all noncoding regions. In addition, specific CRISPR screens can be generalized to other disease-based phenotypic assays, as studies have confirmed that noncoding mutations causing small changes in gene expression can have large phenotypic effects (*12*). Although germline variants have been identified in genome-wide association studies, systematic studies that provide functional annotation of all noncoding regions will be exceedingly important for identifying disease-causing somatic variants. For example, specific somatic variants that include gain of transcription factor binding sites, fusion events due to genomic rearrangements, and variants caused by ncRNAs and pseudogenes have been identified in focused studies on the disease gene (*12*). ■

REFERENCES

1. M. Bulger, M. Groudine, *Cell* **144**, 327 (2011).
2. W. Akhtar *et al.*, *Cell* **154**, 914 (2013).
3. D. E. Dickel *et al.*, *Nat. Methods* **11**, 566 (2014).
4. N. Sanjana *et al.*, *Science* **353**, 1545 (2016).
5. C. P. Fulco *et al.*, *Science* **354**, 769 (2016).
6. P. Mali *et al.*, *Science* **339**, 823 (2013).
7. L. Cong *et al.*, *Science* **339**, 819 (2013).
8. O. Shalem *et al.*, *Science* **343**, 84 (2014).
9. T. Wang *et al.*, *Science* **343**, 80 (2014).
10. M. H. Larson *et al.*, *Nat. Protoc.* **8**, 2180 (2013).
11. L. A. Gilbert *et al.*, *Cell* **159**, 647 (2014).
12. E. Khurana *et al.*, *Nat. Rev. Genet.* **17**, 93 (2016).

10.1126/science.aak9849

EPIDEMIOLOGY

First flu is forever

A change in the properties of influenza virus in 1968 has left a profound mark on population immunity

By **Cécile Viboud**[1] *and* **Suzanne L. Epstein**[2]

Influenza is a threat that has been with humans throughout history, fueled by a constant race between host immunity and viral evolution. Control strategies rely on annual immunizations and require frequent updates of the vaccine, an expensive, cumbersome, and not always foolproof process. Efforts are therefore under way to develop vaccines that confer broadly cross-protective immunity to diverse influenza strains. Cross-immunity is pervasive in nature; in multistrain viral diseases such as influenza or dengue, response to a primary infection can profoundly influence response to the next strain encountered. Even unrelated viruses can be recognized by the same cross-reactive T cells. On page 722 of this issue (*1*), Gostic *et al.* show that severe infection with a bird flu virus depends on the individual's first encounter with influenza in childhood.

Gostic *et al.* dissected the age patterns of human infections with avian influenza A/H5N1 and A/H7N9 reported globally since 1997. These viruses represent two distinct types of hemagglutinin (HA), type 1 for A/H5N1 and type 2 for A/H7N9, which differ in genetic sequence. This HA difference parallels intriguing epidemiological differences: A/H5N1 cases are found mainly in children and young adults, whereas A/H7N9 cases are concentrated in older individuals. These contrasting age profiles have sparked several hypotheses, including the effect of age-specific contacts with infected birds for A/H7N9 (*2*) and previous immunity to the neuraminidase surface protein for A/H5N1 (*3*).

Gostic *et al.* offer a single explanation for the contrasting age profiles of A/H5N1 and A/H7N9 cases and for the abrupt change in infection risk around birth year 1968. The latter coincides with the emergence of a new influenza virus in human populations and a shift in circulating antigens from HA group 1 to group 2. A previously little-noted consequence of this event was an altered immune status of the population (see the figure).

Population immunity to bird flu depends on birth year

In 1968, there was a change in a major protective antigen of influenza, hemagglutinin (HA). This altered the type of flu virus that new birth cohorts first encountered in life. Gostic *et al.* show that resulting levels of broadly protective immunity differ by birth year and that these differences can predict the risk of severe infection with different types of bird flu.

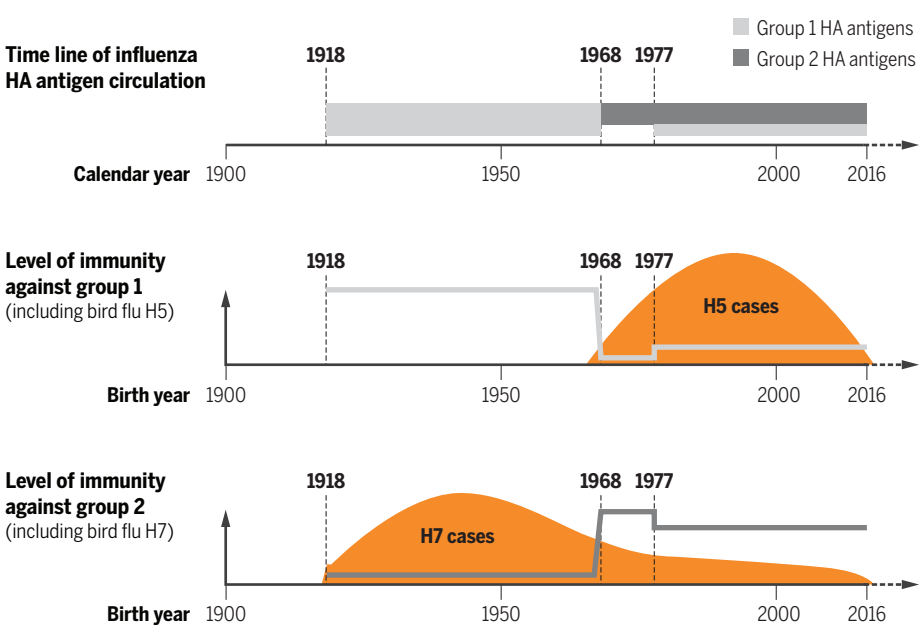

GRAPHIC: C. BICKEL/*SCIENCE*

Using historical influenza epidemiological records, Gostic *et al.* carefully reconstruct the susceptibility of each birth cohort based on the likelihood that their primary infection was with group 1 or 2 HA influenza, which they term "HA immune imprinting" (see the figure). Individuals born before 1968, likely had their first infection with a group 1 virus and appear protected against viruses of the same group, including A/H5N1. Conversely, primary infection with group 2 viruses, likely for those born after 1968, appears to protect against the group 2 virus A/H7N9. The more recent history of influenza circulation is muddled, because group 1 and 2 HAs have cocirculated since 1977 (see the figure). Despite these complexities, the reconstructed susceptibility profiles mirror the age patterns of reported cases, lending support to a lifelong effect of HA imprinting on immunity.

As for potential imprinting mechanisms, Gostic *et al.* favor the role of antibodies directed toward the base of the HA protein, called the HA stem, a structure conserved at the group level (*4*). It is hard to explain imprinting protection by antibody or T cell responses to other parts of the influenza virus because most did not change abruptly around 1968.

Others have observed that early childhood exposure may leave a persistent mark on influenza immunity (*5*–*7*). It remains unclear, however, whether the imprinting is specific to the first (or second) influenza infection or a result of the cumulative effect of lifelong exposure and boosting. On the one hand, there could be more boosting opportunities for immunological target sites of the first virus encountered in life relative to later ones. On the other hand, primary infection may play a unique role if subsequent infections are partially controlled via cross-protective mechanisms and thus less immunogenic. The latter scenario is plausible, because the available epidemiological data do not support double imprinting in individuals who lived through the group 1 and 2 HA eras (*1*).

Imprinting could have important consequences for vaccination efforts and pandemic risk assessment (*1*). New influenza viruses encounter populations with age-dependent levels of protective immunity to a myriad of conserved features of the influenza virus, which might mitigate pandemic potential. The ability of a new virus to spread would be influenced both by its HA group and by the local population history of previous influenza exposure. It is unknown to what extent cross-protective mechanisms such as HA imprinting reduce viral shedding and, hence, transmission potential, making projections of pandemic risk of a new virus uncertain.

A related issue is whether vaccination interferes with or promotes immune imprinting. Does only natural infection induce robust immunity? This question contributes to a larger debate on the adverse effects of repeat vaccination, given that large-scale routine pediatric immunization campaigns are being rolled out in the United States and United Kingdom (*8*). The populations studied by Gostic *et al.* likely had robust natural infections and minimal vaccination history, so their results cannot speak to this issue.

Gostic *et al.*'s analysis is rooted in epidemiological data but opens avenues for research in other disciplines. Animal models could be used to test the effect of different exposure histories but are limited by short life spans and differences in immunological development. Human cross-reactive HA antibodies could be measured in vaccinated and unvaccinated age cohorts. Previous studies of HA stem antibodies could be reanalyzed by birth year (*9*). It would also be useful to examine the age profile of individuals with mild versus severe zoonotic influenza infections (*1*). If HA imprinting protects against severe disease but does not completely prevent infection, mild cases should be found in all age groups.

Gostic *et al.*'s study builds on old and new work focused on the life course of immunity to influenza, from Francis's seminal work on the concept of original antigenic sin (*5*) to recent notions of antigenic seniority (*6*) and antibody landscapes (*7*). A growing body of epidemiological evidence points to the prolonged effects of cross-immunity, including competition between strains during seasonal and pandemic outbreaks, reduced risk of pandemic infection in those with previous seasonal exposure (*10*), and—as reported by Gostic *et al.*—lifelong protection against viruses of different subtypes but in the same HA homology group (*1*). Basic science efforts are now needed to fully validate the HA imprinting hypothesis. More broadly, further experimental and theoretical work should map the relationship between early childhood exposure to influenza and immune protection and the implications of lifelong immunity for vaccination strategies and pandemic risk. ■

REFERENCES

1. K. M. Gostic *et al.*, *Science* **354**, 722 (2016).
2. A. J. Kucharski, W. J. Edmunds, *Epidemiol. Infect.* **143**, 1119 (2015).
3. B. J. Cowling *et al.*, *Euro Surveill.* **18**, 20475 (2013).
4. D. C. Ekiert, I. A. Wilson, *Curr. Opin. Virol.* **2**, 134 (2012).
5. T. Francis Jr. *et al.*, *Trans. Assoc. Am. Physicians* **66**, 231 (1953).
6. A. J. Kucharski *et al.*, *PLOS Biol.* **13**, e1002082 (2015).
7. J. M. Fonville *et al.*, *Science* **346**, 996 (2014).
8. R. Bodewes *et al.*, *Lancet Infect. Dis.* **9**, 784 (2009).
9. W. Wang *et al.*, *J. Infect. Dis.* **213**, 403 (2016).
10. S. Sridhar, *Front. Immunol.* **7**, 195 (2016).

10.1126/science.aak9816

[1]*Fogarty International Center, National Institutes of Health, Bethesda, MD 20892, USA.* [2]*Center for Biologics Evaluation and Research, Food and Drug Administration, Silver Spring, MD 20993, USA. Email: viboudc@mail.nih.gov*

CHEMISTRY

Ammonia activation at a metal

A cationic molybdenum complex weakens the N–H bond of ammonia and generates H_2

By **Jessica Hoover**

Although ammonia (NH_3) is made on a vast scale for use in fertilizers, its use as a chemical feedstock or as an energy carrier is much more limited. Many reactions that occur easily with its substitution products (amines) are sluggish for NH_3, in part because of the difficulty of activating the N–H bond. For fuel cells, NH_3 is attractive because it does not generate greenhouse gases, as do methanol and methane (*1*), and is more easily stored than hydrogen (H_2). Amine-containing organic molecules are used in pharmaceutical and materials applications, and accessing these structures directly from ammonia could limit the generation of by-products during their synthesis (*2*). Bringing NH_3 up to speed for these applications will require both the development of catalysts that can activate the strong N–H bond of ammonia and a fundamental understanding of the N–H bond cleavage step. On page 730 of this issue, Bezdek *et al.* (*3*) report a molybdenum complex capable of weakening the N–H bond of NH_3 and releasing a H atom to generate H_2 under mild conditions.

"...a bond weakening of this magnitude...is unprecedented, as is the spontaneous formation of H_2."

The transfer of a H atom from a metal (M)–NH_3 species has not been reported previously, in part because this reaction must overcome the strong N–H bond of NH_3 (bond dissociation free energy = 99.5

Department of Chemistry, West Virginia University, Morgantown, WV 26506, USA. Email: jessica.hoover@mail.wvu.edu

kcal mol^{-1}) (*4*). Most transition-metal complexes react with NH_3 to form simple coordination complexes by binding through the lone electron pair of the N atom. Instead, the activation of the N–H bond usually proceeds either through deprotonation or oxidative addition. Deprotonation, the heterolytic cleavage of the N–H bond in the presence of a base, occurs with simultaneous reduction of the metal center or the loss of an anionic ligand and is typically favored for complexes that are positively charged or otherwise electron-poor. Conversely, the oxidative addition to the N–H bond involves formation of new M–N and M–H bonds with concomitant oxidation of the metal center by two electrons. However, because the bond-breaking and bond-forming processes are partnered with oxidation of the metal center, this mode of activation is most common for electron-rich metal centers.

Bezdek *et al.* have identified a favorable combination of these electronic features in their ammonia-bound terpyridine bis(phosphine) molybdenum(I) cation (see the figure). Because this species is both positively charged and electron-rich, a new H atom transfer reaction pathway is accessible. The N–H bond cleaves homolytically to form a H atom and a M–N bond with the one-electron oxidation of the metal center. Two H atoms then combine rapidly to generate H_2. Other researchers have previously shown that coordination of NH_3 (*5*) and amines (*6*) to a metal center weakens the corresponding N–H bond, yet a bond weakening of this magnitude (by 53.7 kcal mol^{-1}) is unprecedented, as is the spontaneous formation of H_2. The authors refer to these distinctive features as "nonclassical coordination."

A full understanding of this N–H bond–weakening effect and the transfer of a H atom of NH_3 will have implications not only for energy storage and the utilization of NH_3 for the synthesis of organic molecules, but potentially also for the development of new routes to synthesize NH_3. The industrial synthesis proceeds through the reaction of N_2 with H_2 over supported iron catalysts in the energy-intensive Haber-Bosch process that consumes 1 to 2% of the world's annual energy supply (*7*). In nature, the reduction of N_2 to NH_3 (nitrogen fixation) is conducted by the nitrogenase enzymes and occurs at an iron center in the iron-molybdenum cofactor, a cluster of iron and molybdenum atoms contained within the enzyme. This transformation requires eight protons and eight electrons and is driven by the energy from 16 equivalents of adenosine triphosphate as the energy source.

Thus, both the industrial and physiological nitrogen-reduction processes are high-energy processes. The need for a large driving force arises from the high-energy intermediates that are formed from stepwise protonation and electron-transfer steps. The ability to transfer H atoms (the combination of a proton and an electron) directly in a single step, without relying on sequential proton and electron transfers, has the potential to avoid these high-energy intermediates and lead to a more efficient NH_3 synthesis. Given the importance of energy storage and the challenges associated with the efficient generation of NH_3 from renewable resources, this striking new system will likely initiate the development of new complexes capable of efficient hydrogen atom transfer from NH_3 and other small molecules. ■

Three ways to bind ammonia

Ammonia could provide a way to carry hydrogen if its N–H bonds could be activated catalytically. Most metal complexes bind by either deprotonation with help by a base (left) (*8*) or bind hydrogen by oxidative addition (right) (*9*). The hydrogen-atom transfer route of Bezdek *et al.* (center) generates hydrogen atoms that combine to form H_2.

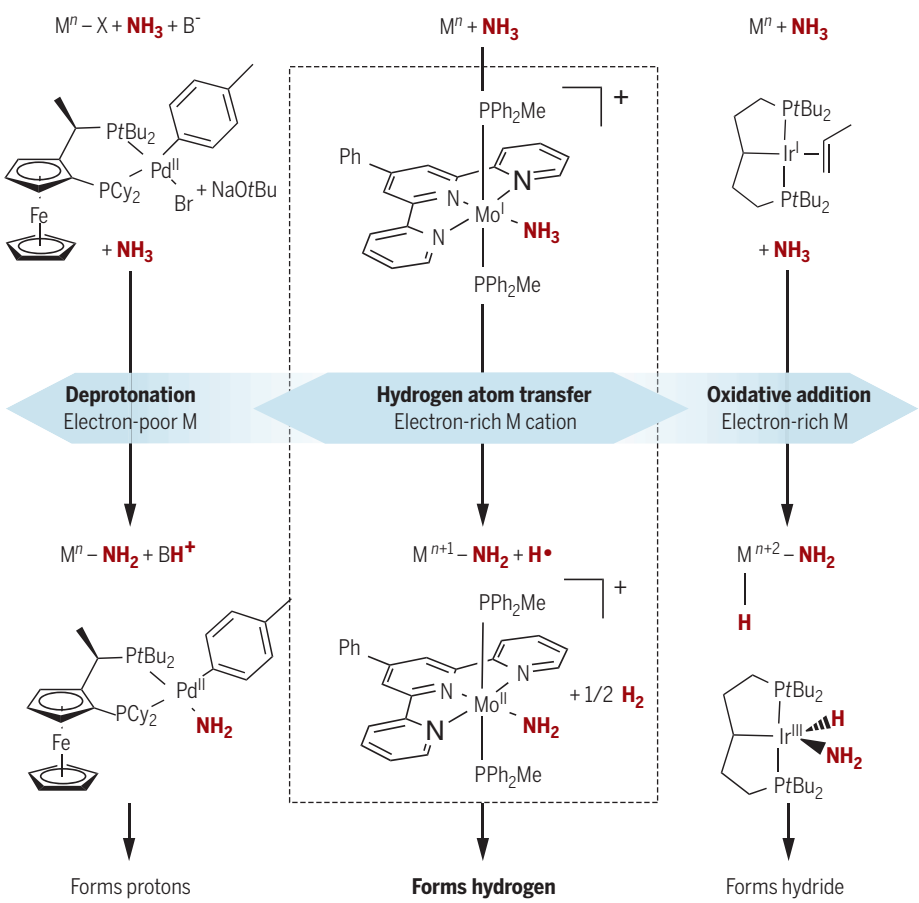

NH$_3$: ammonia H$_2$: hydrogen M: metal B: base
*t*Bu: *tert*-butyl Cy: cyclohexyl Ph: phenyl Me: methyl

GRAPHIC: K. SUTLIFF/*SCIENCE*

REFERENCES

1. A. Klerke, C. H. Christensen, J. K. Nørskov, T. Vegge, *J. Mater. Chem.* **18**, 2304 (2008).
2. J. L. Klinkenberg, J. F. Hartwig, *Angew. Chem. Int. Ed.* **50**, 86 (2011).
3. M. J. Bezdek, S. Guo, P. J. Chirik, *Science* **354**, 730 (2016).
4. J. J. Warren, T. A. Tronic, J. M. Mayer, *Chem. Rev.* **110**, 6961 (2010).
5. H. Fang, Z. Ling, K. Lang, P. J. Brothers, D. De Bruin, X. Fu, *Chem. Sci.* **5**, 916 (2014).
6. J. M. Mayer *Acc. Chem. Res.* **44**, 36 (2011).
7. Y. Tanabe, Y. Nishibayashi, *Coord. Chem. Rev.* **257**, 2551 (2013).
8. J. L. Klinkenberg, J. F. Hartwig, *J. Am. Chem. Soc.* **132**, 11830 (2010).
9. J. Zhao, J. S. Goldman, J. F. Hartwig, *Science* **307**, 1080 (2005).

10.1126/science.aaj2332

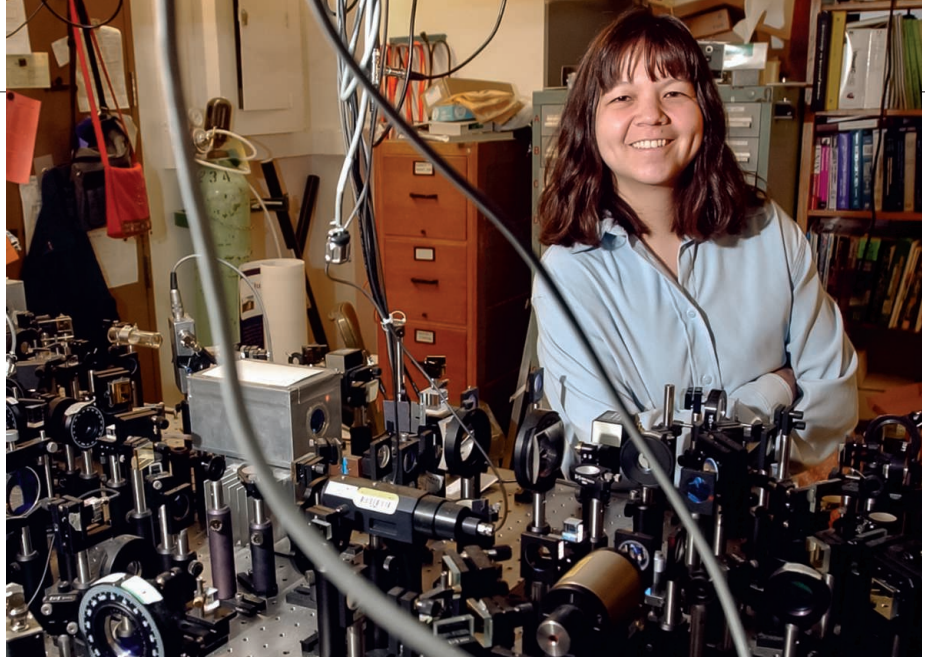

PHOTO: ANDY CROSS/THE DENVER POST VIA GETTY IMAGES

RETROSPECTIVE

Deborah S. Jin (1968–2016)

A pioneer of ultracold quantum physics also promoted women in science

By **Cindy Regal** *and* **Jun Ye**

Deborah S. Jin was a world leader in ultracold gases and a pioneering intellectual in quantum systems consisting of strongly interacting particles. She spent much of her career as a U.S. National Institute of Standards and Technology (NIST) physicist at JILA (formerly known as the Joint Institute for Laboratory Astrophysics) in Boulder, Colorado, where she undertook a string of challenging experiments, including the creation of the first Fermi gas of atoms and the formation of a condensate of paired fermions. She imbued all that she worked on with a sense of scientific vision, creativity, detail-oriented excellence, and old-fashioned hard work. Jin died of cancer on 15 September 2016 at the age of 47, a loss that leaves a void in the scientific community and is, for so many, the untimely loss of a colleague and friend.

The focus of Jin's work started early in her career. In her graduate work at the University of Chicago, she studied low-temperature materials and how exotic properties emerge from a collection of quantum particles. Throughout her career, she helped answer questions about the mechanisms behind superconductivity at anomalously high temperatures, how molecules and Cooper pairs (electrons or other fermions bound together at low temperatures) are related, and universal relations that connect microscopic properties to macroscopic thermodynamics in many-body quantum systems. Importantly, Jin not only studied and developed experimental answers to these questions, but she also created completely new ways of probing such problems using atomic physics. Her tools for studying Fermi gases of atoms and molecules have been widely adopted and will continue to answer the questions she pursued for years to come.

Jin received numerous honors for her work, including the American Physical Society's I. I. Rabi Prize, a John D. and Catherine T. MacArthur Fellowship (the "genius" award), the Samuel J. Heyman Service to America Medal, the Arthur S. Flemming Award, the Benjamin Franklin Medal in Physics, the L'Oréal-UNESCO Women in Science Award for North America, the U.S. National Academy of Sciences Comstock Prize in Physics, and the Institute of Physics Isaac Newton Medal. Jin traveled the world giving brilliant talks, and she championed clarity and simplicity in scientific writing and communication. Especially in recent years, she devoted herself to promoting women in physics and science through groups, talks, and advocacy.

Jin trained numerous graduate and undergraduate students, many of whom she worked with side by side in the laboratory. One had to think fast to keep up when working with her. She often taught by demonstrating and doing, as opposed to talking. She was reserved and known for being quiet in her early years, but one soon realized that behind this demeanor was a pioneering spirit and a fiercely honest force.

Her early scientific life was shaped by her undergraduate years at Princeton University, where she received a B.A. in physics in 1990. She then completed her Ph.D. work under Thomas Rosenbaum at the University of Chicago, where she worked on unconventional superconductors and measuring their dependences on pressure and magnetic field. After earning her doctoral degree in 1995, Jin moved to Boulder, Colorado, to join the efforts of Eric Cornell at JILA, a joint institute between NIST and the University of Colorado. With Cornell, she worked on newly created Bose-Einstein condensates composed of dilute atomic gases. Jin's methods and experimental techniques helped her quickly make contributions to this new field, including measurements of the collective-mode spectrum of a Bose-Einstein condensate. She started her own research efforts at JILA in 1997, thereby launching her longstanding successful work with fermionic atoms.

Jin's family had a substantial impact on her life. She was born in 1968 in Stanford, California, and grew up in Indian Harbour Beach, Florida. Her father was a professor of physics at the Florida Institute of Technology, and her mother was also a trained physicist. Growing up, Jin played the violin, was most drawn to mathematics, and was helped along in her scientific interests by discussions with her father. She met her husband, John Bohn, during her graduate work at the University of Chicago, and for many years they collaborated on studies of atomic collisions. Deborah arranged her scientific life around spending time with John, their daughter Jaclyn, and extended family.

Jin's most recently initiated scientific pursuit was the study of ultracold diatomic molecules. One of us (J.Y.) was fortunate to collaborate with her at JILA on this project for over a dozen years, pioneering cooling techniques and chemical reactions at ultralow temperatures. Indeed, Jin was poised to study a multitude of many-body quantum phenomena with polar molecules. This field of work in particular has lost one of its guiding forces all too soon. But her vision will be clearly manifest in the legacy of the ongoing work, and her collaborators will continue to be inspired by the enthusiasm she brought to the project.

Deborah Jin's work in defining the path of her institute, the field of ultracold matter, and her many students and postdocs will endure. ■

JILA, National Institute of Standards and Technology and University of Colorado, Boulder, CO 80309, USA. Email: regal@colorado.edu; ye@jila.colorado.edu

10.1126/science.aal2545

POLICY FORUM

TECHNOLOGY GOVERNANCE

Precaution and governance of emerging technologies

Precaution can be consistent with support of science

By **Gregory E. Kaebnick,[1] Elizabeth Heitman,[2] James P. Collins,[3] Jason A. Delborne,[4] Wayne G. Landis,[5] Keegan Sawyer,[6] Lisa A. Taneyhill,[7] David E. Winickoff[8,9]**

Precautionary approaches to governance of emerging technology call for constraints on the use of technology whose outcomes include potential harms and are characterized by high levels of complexity and uncertainty. Although articulated in a variety of ways, proponents of precaution often argue that its essential feature is to require more evaluation of a technology before it is put to use, which increases the burden of proof that its overall effect is likely to be beneficial. Critics argue that precaution reflects irrational fears of unproven risks—"risk panics" (*1*)—and would paralyze development and use of beneficial new technologies (*1*, *2*). Advocates give credence to this view when they suggest that precaution leads necessarily to moratoria (*3*). Progress in the debate over precaution is possible if we can reject the common assumption that precaution can be explained by a simple high-level principle and accept instead that what it requires must be worked out in particular contexts. The 2016 report from the U.S. National Academies of Science, Engineering, and Medicine (NASEM) on gene drive research (*4*) illustrates this position. The report shows both that precaution cannot be rejected out of hand as scaremongering and that meaningful precaution can be consistent with support for science.

Gene drives are a form of preferential inheritance that occur naturally and can be constructed in the laboratory using new genetic editing tools such as CRISPR-Cas9. Constructed drives could be used to alter, reduce, or eliminate populations of organisms in the environment; in principle, an entire species could be modified. Gene drives have considerable potential benefit, especially in the control of vector-borne diseases and the protection and restoration of environments threatened by nonindigenous organisms. Gene drives also might have harmful effects, especially to the environment. A drive designed to eliminate a non-native mouse population from an island to protect native species might pose threats to related species, to populations of the mouse elsewhere in the world, or to other species on the island that depend on the mouse population. The range of effects due to hybridization, geographic dispersal, and predator-prey interactions, for example, would need to be studied and the probabilities quantified. These are a few possible harms for one hypothetical use; given the present state of knowledge for gene drives, the outcomes and their probabilities are not yet well understood.

INTERPRETING PRECAUTION

At least four common objections to precaution underlie critics' claims that precaution is irrational and paralyzing. First, precaution is said to be too vague and ambiguous to provide useful guidance. In response, some advocates hold that precaution is not meant to provide a decision-making algorithm that is able to identify appropriate precautionary measures for each and every technology. Precaution is better described at a high level not as a principle but as an attitude or approach that consists in sharpening or broadening the scrutiny of a proposed project (*5*, *6*). Deciding whether precautionary measures are appropriate, and then determining what they are, depends on examining details of the technology and its potential impacts (*2*).

The NASEM report demonstrates this contextual approach to precaution. It starts from an understanding of the science, how the science might be used, and downstream effects of attempts to use it. Some general potential benefits and harms can be easily identified, but prospective uses involve multiple complex systems—genomic, environmental, and social—that add layers of uncertainty. For a given proposed gene drive, we may be uncertain about the probability of outcomes but also about how outcomes should be described and valued and about what all the possible outcomes are. The latter kinds of uncertainty can be distinguished from uncertainty about probability by referring to them as issues of ambiguity and ignorance (*6*).

The potential benefits of research on gene drives make prohibiting the research unjustifiable. The potential harms and uncertainties make a too-quick commitment to those uses unacceptable. The report therefore recommends research under four broad constraints:

[1]*The Hastings Center, Garrison, NY 10524, USA.* [2]*Vanderbilt University Medical Center, Nashville, TN 37232, USA.* [3]*Arizona State University, Tempe, AZ 85281, USA.* [4]*North Carolina State University, Raleigh, NC 27695, USA.* [5]*Western Washington University, Bellingham, WA 98225, USA.* [6]*National Academies of Sciences, Engineering, and Medicine, Washington, DC 20418, USA.* [7]*University of Maryland, College Park, MD 20742, USA.* [8]*University of California, Berkeley, CA 94720, USA.* [9]*Organization for Economic Cooperation and Development, 75775 Paris Cedex 16, France. Email: kaebnickg@thehastingscenter.org*

1. Any proposed release of a gene drive must be understood as raising issues related to values. Questions will arise about potential benefits and harms, the moral seriousness of the problem that the release is meant to address, the merits of other ways to address the problem, the distribution of benefits and harms, and control over decisions about the proposed release. Such questions can address economic, social, environmental, and health effects. Attention to them is itself an important aspect of precaution (*5*), and they frame discussion of other possible precautionary measures.

2. Any proposed release requires engagement with relevant publics, fostering attention to the values questions, broadening control over decisions beyond the community of scientists and engineers, creating an additional layer of review, and improving scientists' understanding of potential outcomes.

3. Researchers should follow a phased testing approach that provides a step-by-step framework from initial development of a research plan through to postrelease monitoring, with predefined, study-specific criteria for determining whether to transition to the next phase based on evidence regarding potential outcomes.

4. Proposed releases require ecological risk assessment as a basis for examining the probability of immediate and long-term environmental and health effects.

Missing from these recommendations are detailed substantive requirements—for example, performance goals for the evolutionary stability of a proposed drive or specific requirements for environmental or social outcomes. The constraints are instead process requirements: They offer strategies for thinking about proposed releases and identifying, characterizing, and evaluating outcomes. In carrying them out, substantive requirements specific to an application should emerge. For example, a high level of assurance that a drive will be geographically limited might be demanded. In effect, contextual development of precaution continues as researchers and oversight bodies examine specific applications.

ITERATIVE APPROACH TO UNCERTAINTY

Two other common objections to precaution are closely connected: Precaution sets epistemologically impossible demands because uncertainty about outcomes can never be fully resolved, and therefore, precaution simply means giving up on technological innovation and its potential benefits (*1*, *2*). However, precaution comes in more and less restrictive forms. Any precautionary position, whether developed as a high-level principle or with reference to a particular technology, has three components: a preliminary reason to suspect a possible harm, a preliminary reason to believe that there is uncertainty about the effects, and a recommendation (triggered by the first two components) for precautionary measures (*7*–*9*). The restrictiveness of precaution depends on how much potential harm and uncertainty are necessary to trigger precautionary measures and how severe the measures are.

The charge of epistemological impossibility is plausible if the presence of any uncertainty is a triggering condition. When precaution is formulated as a high-level principle, the language is inevitably vague, and extreme demands are more easily read into it. The NASEM report, however, taking a contextual approach, identifies fairly specific, concrete, and manageable triggers, such as that gene drives could have unwanted effects in the organism's genome, that a gene drive–modified organism may have unwanted effects on an ecosystem, and that what counts as "unwanted" may vary among different publics.

"[In] gene drive–modified organism…effects on an ecosystem, what counts as "unwanted" may vary…."

The charge that precaution means giving up on technology depends both on the triggers and the precautionary recommendations. Those opposed to a technology sometimes use precaution to argue for barricades to technology development—for example, general moratoria pending global enactment of very stringent oversight measures (*3*). The NASEM report, however, calls for targeted but meaningful measures. These measures will be familiar to many scientists, but, taken together, they encourage a broader range of perspectives on and questions about the technology; ensure that any proposed release receives robust and iterative assessment that can incrementally reduce uncertainty surrounding its outcomes and probabilities; raise the bar for demonstrations of efficacy and safety that those proposing a gene drive release must provide; and ensure that risks are acceptable to the relevant publics and are reduced to the greatest extent possible. The constraints would almost certainly bring some proposed releases to a halt. Yet their purpose is not to halt research but to establish conditions under which it can be successful. They constitute a path toward possible release of gene drives—a route with flashing red lights, checkpoints, and off ramps rather than barricades.

SCIENCE AND VALUES

A fourth common objection to precaution, implicit in the idea of a risk panic (*1*), is that precaution is grounded on emotion—fear of the unknown—rather than reason. This objection is not wholly mistaken. Risk panics might explain some precautionary policy positions. We should, however, seek input from a wide range of stakeholders, and although the values that stakeholders embrace should be subject to the critical examination of public deliberation, we should be wary at the outset about rejecting some as less rational than others (*10*, *11*).

There is another possible emotional response to new technologies: instead of a risk panic, an "innovation thrill." As Oppenheimer said, "When you see something that is technically sweet, you go ahead and do it and you argue about what to do about it only after you have had your technical success" (*12*). Although the primary rationale for releasing a gene drive would be human or environmental benefit, the thrill of understanding and engineering biological systems would be part of the motivation to undertake the basic science. That thrill could also generate an impulse to move the science from the laboratory to the field. The NASEM report aims to counteract that impulse. An innovation thrill is no better than a risk panic as a basis for policy on when and how to use gene drives. ■

REFERENCES AND NOTES

1. C. R. Sunstein, *Laws of Fear: Beyond the Precautionary Principle* (Cambridge Univ. Press, Cambridge, 2005).
2. J. B. Weiner, in *Human and Ecological Risk Assessment: Theory and Practice*, D. D. Paustenbach, Ed. (Wiley, Hoboken, NJ, 2007), chap. 32.
3. Friends of the Earth, International Center for Technology Assessment, and ETC Group, *The Principles for the Oversight of Synthetic Biology* (Friends of the Earth, Washington, DC, 2012).
4. NASEM, *Gene Drives on the Horizon: Advancing Science, Navigating Uncertainty, and Aligning Research with Public Values* (NASEM Washington, DC, 2016).
5. J. Wolff, *Hast. Cent. Rep.* **44** (suppl. 5), S27 (2014).
6. A. Stirling, *EMBO Rep.* **8**, 309 (2007).
7. E. C. Parke, M. A. Bedau, in *The Ethics of Protocells: Moral and Social Implications of Creating Life in the Laboratory*, M. A. Bedau, E. C. Parke, Eds. (MIT Press, Cambridge, MA, 2009), chap 5.
8. S. M. Gardiner, *J. Polit. Philos.* **14**, 33 (2006).
9. D. A. Kysar, *J. Land Use Environ. Law* **22**, 1 (2006).
10. D. M. Kahan, P. Slovic, D. Braman, J. Gastil, *Harv. Law Rev.* **119**, 1071 (2006).
11. A. Finkel, *Ann. N. Y. Acad. Sci.* **1128**, 121 (2008).
12. Atomic Energy Commission, "In the matter of J. Robert Oppenheimer: Transcripts of hearing before Personnel Security Board" (Government Printing Office, Washington, DC, 1954).

ACKNOWLEDGMENTS

The authors are some of the members and staff of the committee that authored the report discussed in this paper (*4*). The opinions in this essay are those of the authors and may not reflect the view of NASEM or all members of the National Academies committee on gene drive research in nonhuman organisms. G.E.K. was supported by NSF grant 1353433.

10.1126/science.aah5125

Genetically engineered "micropigs" were on display at the 2015 China Hi-Tech Fair in Shenzhen city.

GENETIC ENGINEERING

Tinkering with evolution

A comprehensive tome explores the far-reaching implications of genome editing

By **Adrian Woolfson**

We have an ambivalent relationship with nature. On the one hand, we acknowledge that it begat and nurtures us, while on the other, we are quick to denounce its shortcomings and sulk at the inconveniences of disease, mortality, and inadequacies of human existence.

That we should have attempted to improve our lot is unsurprising. Indeed, the history of humankind is a chronicle of deeply ingrained and incremental attempts to liberate ourselves from the embarrassments of the natural situation. The recent discovery that components of the bacterial immune system can be harnessed to edit genomes with great speed and precision, coupled with the emerging science of synthetic biology, has ratcheted these possibilities up to a new level. We have, as a result, reached a watershed in the history of our species and of life itself—a moment where critical issues pertaining to the relationship between natural and artificial, the sanctity of human nature, and the future of humankind must be addressed.

John Parrington's new book, *Redesigning Life*, is a comprehensive digest of the extraordinary scientific material relevant to this topic. Parrington presents himself as the trusted tour guide of the latest developments in this rapidly advancing area of investigation, lacing his accounts with a number of charming analogies and anecdotes. These include his description of bacterial CRISPR/Cas9 repeat sequences as "genetic sandwiches" and their display of bacteriophage sequence spacer fragments as a "molecular most-wanted gallery."

Redesigning Life
How Genome Editing Will Transform the World
John Parrington
Oxford University Press, 2016. 364 pp.

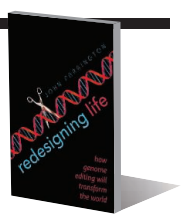

Although somewhat humdrum at times, the book achieves its stated aim, which is to provide readers with the basic factual information necessary to comprehend the enormity and potential effect of these unprecedented technologies. Parrington economically covers a huge swath of material, including a discussion of artificial genetic materials, and successfully communicates the excitement and relentless pace of the developments in this field. But there are some notable omissions, including the potential importance and effects of microbiome editing.

It was bacteria that provided the first basic tool kit for modifying genomes in the form of restriction enzymes, the catalytic proteins used to cut the DNA of invading viruses. Parrington gives an entertaining account of their discovery, weaving the story of American microbiologist Hamilton Smith's career with colorful descriptions of his moth-eaten sweaters and thick-rimmed glasses. Smith, we learn, was incredulous when he was informed that he had been awarded a Nobel Prize for his work, which he and others had viewed as esoteric and obscure. This provides a poignant reminder of how basic scientific investigations can deliver profound and unexpected insights of immense significance.

Parrington reminds us that humans have been indirectly modifying genomes for many thousands of years and that many aspects of our "natural" surroundings have arisen as a result of these activities. Cabbages, for example, were originally so toxic that they were only eaten in small quantities for their medicinal properties.

Using modifiable computer text as the metaphor for the genomic information of organisms, Parrington aspires to inform the reader of the risks and potential benefits of gene editing. It is disappointing, however, that he offers no framework or personal perspective on this critical issue.

Such is the speed of developments that the concerns about human germline editing expressed by Edward Lanphier and colleagues in March 2015 (*1*) are already being undermined by next-generation CRISPR/Cas9 gene-editing technologies that are more efficient, have fewer off-target effects, and have the potential to reduce genetic mosaicism (*2*). It is hard, then, to imagine why we would not want to edit the germ line to correct monogenic disease genes. The deep history of our formation and the tinkering nature of the evolutionary process have, however, riddled human nature with a host of interdependencies, paradoxes, inconsistencies, and constraints, making the results of complex interventions difficult to predict. As such, the repair of polygenic diseases is likely to be far more challenging.

The fact that many proteins perform more than one function does not make the prospect of redesign any easier. We have seen recently, for example, how variants of the complement protein C4 of the primitive immune system are implicated in the pathology of schizophrenia, most likely through their supplementary role in synaptic pruning (*3*).

The rate-limiting step in any grand design to reconfigure our genomes is likely to be the ability to model any proposed rewrites or edits. Equally important, however, will be the need to ensure that any changes align with our conception of what it means to be human. ■

REFERENCES

1. E. Lanphier, F. Urnov, S. E. Haeckler, M. Werner, J. Smolenski *Nature* **519**, 7544 (2015).
2. I. M. Slaymaker *et al.*, *Science* **351**, 6268 (2016).
3. A. Sekar *et al.*, *Nature* **530**, 177 (2016).

10.1126/science.aah5876

The reviewer is the author of The Intelligent Person's Guide to Genetics *(Overlook TP, New York, 2006).*
Email: adrianwoolfson@yahoo.com

PLANT SCIENCE

Crops on demand

A probing portrait of early plant-breeding technologies unearths surprising roots of genetic engineering efforts

By **Luis Campos**

Evolution Made to Order
Plant Breeding and Technological Innovation in Twentieth-Century America
Helen Anne Curry
University of Chicago Press, 2016. 295 pp.

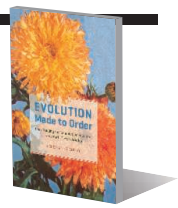

"X-rays speed up evolution over 1,000 per cent" proclaimed the *Science News-Letter* in 1927, in the wake of Hermann J. Muller's legendary artificial transmutation of the gene. Widespread claims of having accelerated evolution and manufactured new living things with these unusual rays ranged from sober to sensational. But x-rays were far from the only tool available to breeders and geneticists seeking to induce hereditary changes in the first part of the 20th century.

In *Evolution Made to Order*, Helen Anne Curry offers a fascinating foray into a mutated cornucopia of agricultural and horticultural products and the tools that made them. Viewing biological innovation as little different from "any other modern industrial product," Curry firmly plants her history of biological innovation within both the history of larger technological systems and the promissory realm that links scientific and commercial ingenuity, industrial efficiency, and democratic demand.

As some experimenters rolled mobile laboratory x-ray units around orchards in 1930, a variety of agricultural companies, commercial growers, and industrial researchers found ways to bring the field into the laboratory. Rather than view the admittedly "dismal outcomes of nearly all the early efforts at x-ray breeding" as failures, however, Curry notes that they serve as important indicators of how the quest to industrialize and make more efficient the haphazard processes of evolution surpassed not only any profit potential but even any particular set of tools.

Indeed, by the 1930s, much attention had turned to the possibilities made possible by the chemical mutagen colchicine. This newfound ability to alter chromosomes suggested a future in which organisms would be built to predictable biological and economic specifications by a "genetics engineer." As with x-rays, however, the spectacular futures envisioned by promoters contrasted notably with the "slow trickle of enhanced crops and flowers" that actually emerged, underscoring the continued need for substantive trial-and-error testing and further knowledge of basic genetics.

That did not stop a larger world of amateurs from being fascinated by the "wonder drug" colchicine and from continuing to tinker with it in their own gardens. Even if plants might not emerge from the backyard quite "made to order," the mere fact that new changes could be observed was fascination enough for many.

"Experimental control" kits containing treated and untreated seeds gave gardeners a sense of participation in atomic research.

After World War II, the availability of artificial radioisotopes brought still more hopes for biological innovation. Lofting a chunk of cobalt-60 high on a retractable pole at the center of their "gamma fields"—concentric circles planted with maize, tomatoes, corn, barley, and other crops—Brookhaven National Laboratory biologists sought to assess the effects of chronic rather than acute irradiation, for example.

Collaborations between the Atomic Energy Commission and the national laboratories also resulted in the introduction of nuclear techniques into long-established centers of U.S. agriculture. Although these efforts were not always successful—it wasn't enough to "just add radiation and stir," as one observer noted—the broader adoption of growing irradiated seeds popularized "atomic gardens" from Cleveland to Los Angeles by 1961.

Gardeners searched for valuable mutants among their flowers, and up to $50,000 awaited the lucky man or woman who discovered a blue rose. However, most who noticed any changes at all found "strange growths," malformations, or stunted and undesirable forms rather than improved plants. For still others, irradiated seeds raised atomic-era anxieties about what might be lurking in one's own plot of vegetables, whether a "man-eating rutabaga or sweet corn with teeth that bite back."

It is perhaps no small irony, then, that even as negative results were increasingly reported at home, radiation breeding efforts—emerging as part and parcel of Eisenhower's "atoms for peace" program—expanded their scope internationally under the auspices of the International Atomic Energy Agency. Radiation mutations programs were necessarily dependent, Curry convincingly argues, on an expanding atomic infrastructure that both demanded and produced innovation.

Although the promise of x-rays and colchicine had suggested a future of industrialized biological innovation where evolution could be accelerated and new species made at will by both commercial producers and tinkering amateurs alike, Curry concludes that the history of postwar mutation breeding efforts is best viewed through the mutually reinforcing roles of politics, scientific institutions, and entrenched infrastructures (both atomic and agricultural). Such varied and important insights into the history of biological innovation and its many aspirations seem as relevant as ever in our ongoing search for new tools to reshape living things to our goals, needs, and desires—and to envision life as it could be. ■

The reviewer is Baruch S. Blumberg NASA/Library of Congress Chair of Astrobiology and in the Department of History, University of New Mexico, Albuquerque, NM 87131, USA. Email: luiscampos@unm.edu

10.1126/science.aai8771

PHOTO: THE LIFE PICTURE COLLECTION

LETTERS

Edited by **Jennifer Sills**

The promise of negative emissions

IN THEIR PERSPECTIVE "The trouble with negative emissions" (14 October, p. 182), K. Anderson and G. Peters assert that negative-emissions technologies are an "unjust and high-stakes gamble." This characterization would sideline negative-emissions technologies and remove potentially important options from the portfolio for mitigating and ameliorating climate change.

As Anderson and Peters acknowledge, the remaining carbon budget is pitifully small; at the current rate, the world will blow through 600 Gt of CO_2 in 15 years. Dumping this much CO_2 in the atmosphere will almost certainly result in more than 1.5°C warming. Indeed, as advocates of a 350-ppm target point out, the remaining CO_2 budget could be negative.

Anderson and Peters provide no evidence that faith in negative-emissions technologies is to blame for a delay in implementing other mitigation plans or for the failure of countries to cut emissions. This failure is easily explained by the free-riding behavior of some countries (*1*), and taking negative-emissions technologies off the table would not make collective action any easier. Indeed, given that negative-emission technologies require financial contributions, not changes in behavior, their development and deployment may well be less vulnerable to free riding. Furthermore, we need a lot of arrows in the quiver to stand a chance of meeting the Paris targets. This was a key finding from the integrated assessment modelers (*2*).

Rather than dividing mitigation into competing strategies, an inclusive approach would focus on stopping climate change as fast as possible while minimizing risk to vulnerable populations and to societal stability. Negative-emission technologies are not unique in facing challenges, risks, and uncertainties. It is true that negative emissions may fall short of closing the gap, but to characterize them as a high-stakes gamble is not consistent with the facts and the plausibility of meeting the Paris goals without them. Throwing a life-preserver to a drowning victim may not assure a successful rescue, but it is not a high-stakes gamble. Offering the life-preserver is preferable to withholding it, even though it might reduce the victim's incentive for learning how to swim.

Klaus S. Lackner and 45 additional signatories*

School of Sustainable Engineering and the Built Environment, Arizona State, Univerity, Tempe, AZ 85287, USA. Email: Klaus.Lackner@asu.edu

*The full list of 46 authors and affiliations is available in the supplementary materials.

REFERENCES

1. S. Barrett, R. Stavins, *Int. Environ. Agreements* **3**, 349 (2003).
2. IPCC, *Climate Change 2014: Mitigation of Climate Change. Contribution of Working Group III to the Fifth Assessment Report of the Intergovernmental Panel on Climate Change*, O. Edenhofer *et al.*, Eds. (Cambridge Univ. Press, 2014).

SUPPLEMENTARY MATERIALS

www.sciencemag.org/content/full/354/6313/714.1/DC1
Full author list

10.1126/science.aal2432

At the current rate of carbon emissions, it will be difficult to meet climate goals.

Response

AS WE WROTE IN OUR Perspective, we agree with Lackner *et al.* that negative-emissions technologies should "be the subject of research, development, and potentially deployment." We support research on the technical, environmental, social, and economic viability of negative-emissions technologies. However, we stand by our conclusion that given the breadth and depth of fundamental uncertainties associated with negative-emissions technologies (*1*–*6*), a program of timely and deep mitigation in line with 2°C budgets should assume that they will not be deployed at a large scale.

A mitigation agenda that does not rely on future large-scale application of negative-emissions technologies will require a legislative environment that delivers profound social and behavioral change by high-emitters, rapid deployment of existing low-carbon energy technologies, and urgent research and development of new promising energy technologies, including negative-emissions technologies. If negative-emissions technologies do indeed prove to be successful, then a lower temperature rise can be subsequently pursued.

Lackner *et al.* claim that including negative-emissions technologies in assessments does not delay other mitigation tactics. On the contrary, evidence indicates that an assumption of negative-emissions success does delay conventional mitigation. Without negative-emissions technologies, much more ambitious and far reaching mitigation is required (*2*). The 2°C scenarios assessed by the IPCC that do not include negative emissions but do allow afforestation have considerably lower fossil-fuel consumption than scenarios that include negative emissions [e.g., Fig. S4 in (*7*)]. The "emissions gap" (*8*, *9*) between the necessary level of mitigation to deliver on the Paris goals and the collective proposition of governments (i.e., the sum of the Intended Nationally Determined Contributions) would be much larger if negative emissions were excluded.

We stand by our claim that postulating large-scale negative emissions in the future leads to much less mitigation today. Negative emissions facilitate the appealing option (*10*) of exceeding tight carbon budgets and assuming that the debt will be paid back later. If we cannot pay back our carbon debt because the negative-emissions technologies do not deliver as planned, then we have saddled the vulnerable and future generations with the

PHOTO: YOCAMON

temperatures we seek to avoid in the Paris Agreement. To use the analogy of Lackner *et al.*, we knowingly let someone jump into a raging torrent, telling them we may be able to save them with a technology we have yet to develop.

Kevin Anderson[1,2]* and Glen Peters[3]

[1]Tyndall Centre, University of Manchester, Manchester, M13 9PL, UK. [2]Centre for Sustainable Development, Uppsala University, 75236, Uppsala, Sweden. [3]Center for International Climate and Environmental Research—Oslo (CICERO), 0318, Oslo, Norway.

*Corresponding author. Email: kevin.anderson@manchester.ac.uk

REFERENCES

1. M. Tavoni, R. Socolow, *Clim. Change* **118**, 1 (2013).
2. L. Clarke *et al.*, in *Climate Change 2014: Mitigation of Climate Change. Contribution of Working Group III to the Fifth Assessment Report of the Intergovernmental Panel on Climate Change*, O. Edenhofer *et al.*, Eds. (Cambridge Univ. Press, 2014), pp. 413–510.
3. S. Fuss *et al.*, *Nat. Clim. Change* **4**, 850 (2014).
4. P. Smith *et al.*, *Nat. Clim. Change* **6**, 42 (2015).
5. P. Smith, *Global Change Biol.* **22**, 1315 .(2016).
6. P. Williamson, *Nature* **530**, 153 (2016).
7. G. P. Peters, *Nat. Clim. Change* **6**, 646 (2016).
8. UNEP, "The Emissions Gap Report 2015" (United Nations Environment Programme, Nairobi, 2015).
9. J. Rogelj *et al.*, *Nature* **534**, 631 (2016).
10. O. Geden, *Nature* **521**, 27 (2015).

10.1126/science.aal2610

Keeping creationism out of classrooms

IN HIS LETTER "Institutionalizing creationism" (*1*), Baltzley criticized the Western Interstate Commission for Higher Education's Interstate Passport Initiative—which will standardize curriculum objectives across a number of U.S. institutions—for including a reference to the 2014 debate between Bill Nye and Ken Ham about evolution. The faculty handbook to which Baltzley referred included the sentence, "Students evaluate the effectiveness of the use of scientific data in a debate, for example:…Students watch the Ken Hamm [*sic*]–Bill Nye evolution-creation science debate (available online) and evaluate the scientific evidence and arguments used by the participants." The program's proficiency criteria have now been revised to omit this example (*2*, *3*).

The Passport Initiative Natural Science faculty is to be praised for its decision. Contrary to T. Krabacher and P. Flatt's defense of the curriculum ("Passport Initiative fosters applied science," Letters, 19 August, p. 759), the National Center for Science Education agrees with Baltzley. It would be a disservice to students to present Ken Ham's young-Earth creationist views as if they were scientifically credible or even the subject of current scientific debate, and it would be a disservice to the scientific community to appear to confer any unearned scientific legitimacy to creationism. The Federation of American Societies for Experimental Biology, representing 125,000 researchers in the life sciences, agreed, urging the removal of the debate (*4*).

Glenn Branch

National Center for Science Education, Oakland, CA 94612–2922, USA. Email: branch@ncse.com

REFERENCES

1. M. Baltzley, *Science* **352**, 1285 (2016).
2. Interstate Passport, "Faculty handbook: Constructing your institute's Passport block" (2016), p. 43; www.wiche.edu/files/info/Faculty%20HB-CYIPB%20March%202016%20(REV%204-08-16).pdf.
3. Interstate Passport, "The Passport learning outcomes and proficiency criteria" (2016); www.wiche.edu/files/info/FINAL%20Matrix%20PLO-PC%20Natural%20Sciences%20October%202016.pdf.
4. FASEB, Letter to WICHE (2016); www.faseb.org/Portals/2/PDFs/opa/2016/WICHE%20Letter.pdf.

10.1126/science.aal2746

RESEARCH

Dynamics of the Fano resonance in real time

Kaldun et al., *p. 738*

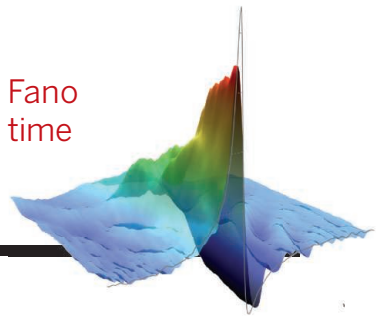

IN *SCIENCE* JOURNALS

Edited by **Stella Hurtley**

NEUROSCIENCE

Resolving a ticklish problem

What is the neural correlate of ticklishness? When Ishiyama and Brecht tickled rats, the animals produced noises and other joyful responses. During the tickling, the authors observed nerve cell activity in deep layers of the somatosensory cortex corresponding to the animals' trunks. Furthermore, microstimulation of this brain region evoked the same behavior. Just as in humans, mood could modulate this neuronal activity. Anxiety-inducing situations suppressed the cells' firing, and the animal could no longer be tickled. —PRS

Science, this issue p. 757

Rat brains respond to tickling.

WILDLIFE DISEASE

British squirrels infected with leprosy

With the exception of armadillos in the Americas, leprosy infections are considered almost exclusively restricted to humans. Avanzi *et al*. examined warty growths on the faces and extremities of red squirrels in the British Isles and found that two species of leprosy-causing organisms were to blame (see the Perspective by Stinear and Brosch). *Mycobacterium leprae* in the southern population of Brownsea Island squirrels originated from a medieval human strain. *M. lepromatosis* was found in red squirrels from elsewhere in the United Kingdom and Ireland. Human leprosy is proving hard to eradicate, despite available drugs. Perhaps other wildlife species are also reservoirs for this stubborn disease. —CA

Science, this issue p. 744; see also p. 702

INORGANIC CHEMISTRY

Coordinated scission of N–H or O–H bonds

Ammonia and water both have well-explored acid-base chemistry at room temperature, revolving around proton exchange. In contrast, radical chemistry involving H-atom exchange is comparatively rare in these molecules in the absence of a high-energy stimulus. Bezdek *et al.* now show that coordination of ammonia or water to a molybdenum complex substantially weakens the N–H or O–H bonds, so much so that heating to 60°C liberates hydrogen (see the Perspective by Hoover). Theoretical and electrochemical analyses reveal the underpinnings of the bond-weakening phenomenon. —JSY

Science, this issue p. 730; see also p. 707

NANOPHOTONICS

A cool route to nanospectroscopy

Confining light to a cavity is often used to enhance the interaction between the light and a particle stored within the cavity. Benz *et al.* worked with a self-assembled monolayer of biphenyl-4-thiol molecules sandwiched between a gold film and a gold nanoparticle. They used laser irradiation to move atoms in the nanoparticle and produced a "picocavity" that was stable at cryogenic temperatures. The authors were then able to obtain time-dependent Raman spectra from individual molecules. Such subwavelength cavities that can localize light to volumes well below 1 nm^3 will enable optical experiments on the atomic scale. —ISO

Science, this issue p. 726

ARCTIC SEA ICE

Why we are losing sea ice

Arctic sea ice is disappearing rapidly, leading to predictions of an ice-free summer in the near future. Simulations of the timing

CREDITS (FROM TOP): KALDUN *ET AL.*; SHIMPEI ISHIYAMA AND MICHAEL BRECHT

of summer sea-ice loss differ substantially, making it difficult to evaluate the pace of the loss. Notz and Stroeve observed a linear relationship between the monthly-mean September sea-ice area and cumulative CO_2 emissions. This allowed them to predict Arctic summer sea ice directly from the observational record. Interestingly, most models underestimate this loss. —HJS

Science, this issue p. 747

EVOLUTIONARY GENOMICS

Identifying genes under recent selection

Evolutionary analyses aim to identify recent genetic changes that are likely to have been subject to selection. Field *et al*. present a method to identify such changes, the singleton density score, which they applied to over 3000 human genomes. Over the past ~100 generations (2000 to 3000 years), Europeans are likely to have experienced selection for genetic variants, including those that affect skin and hair pigmentation, as well as height. —LMZ

Science, this issue p. 760

IMAGING

A look at early multiple sclerosis

In multiple sclerosis and similar diseases in animals, the brain becomes inflamed, which ultimately causes neurons to degenerate. Gerwien *et al*. found two protein-degrading enzymes that are absolutely required for this process: MMP-2 and MMP-9. MMP-9 resides in immune cells and is required for the entry of these cells into the brain as the disease begins. The authors developed tools to visualize MMP inhibitors at this initial stage of multiple sclerosis and its mouse equivalent, just as immune cells began their inflammatory infiltration of the brain. —KLK

Sci. Transl. Med. **8**, 364ra152 (2016).

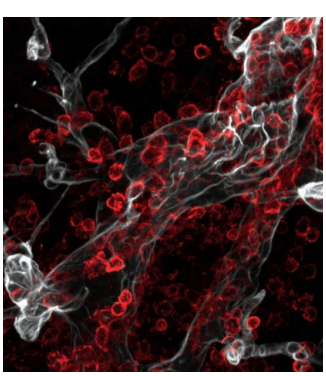

Inflammatory cells (red) infiltrating brain tissue

PHOTOS (FROM LEFT): GERWEIN *ET AL.*; FLIGHTLEVEL80/ISTOCKPHOTO.COM

RADIATION DAMAGE

AIMing to block tissue damage

Ionizing radiation kills actively dividing cells such as those in the gut and in the bone marrow. Hu *et al*. found a pathological role for the protein AIM2 in irradiation-induced tissue damage. AIM2 is best known for its role in sensing double-stranded DNA in the cytoplasm and alerting the body to infections. It seems that AIM2 also senses DNA damage caused by radiation and then triggers intestinal epithelial cells and bone marrow cells to die. Deficiency in AIM2 protected mice from irradiation-induced gastrointestinal syndrome and hematopoietic failure. —KLM

Science, this issue p. 765

CELL BIOLOGY

A new paradigm for IP_3 signaling

The second-messenger inositol trisphosphate (IP_3) stimulates calcium release from the endoplasmic reticulum (ER). Dickinson *et al*. triggered the focal release of IP_3 in animal cells and measured calcium "puffs"—intense, localized increases in calcium released from the ER (see the Focus by Leybaert). IP_3 diffused much more slowly within cells than had been originally measured in vitro. Thus, rather than functioning as a global cellular signal, IP_3 can produce local signals, increasing the complexity of information that can be encoded in responses to IP_3-generating stimuli. —NRG

Sci. Signal. **9**, ra108 and fs17 (2016).

IN OTHER JOURNALS

Edited by **Sacha Vignieri** *and* **Jesse Smith**

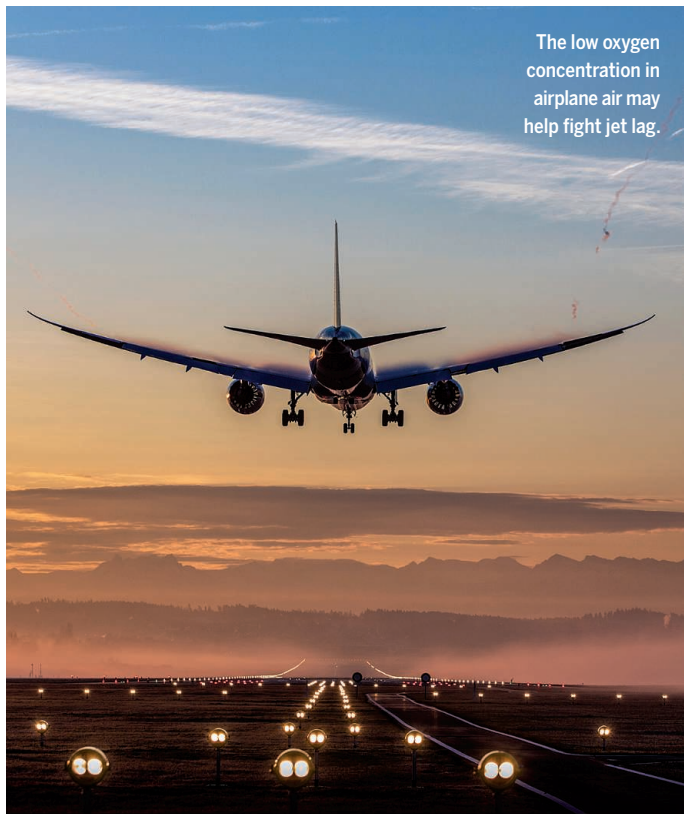

The low oxygen concentration in airplane air may help fight jet lag.

CIRCADIAN RHYTHMS

Airplane air

Can flying help alleviate jet lag? Studies of the biochemical mechanisms that synchronize biological clocks throughout the body show that the low-oxygen environment of airplanes may actually help you adjust to your new time zone. Adamovich *et al*. observed daily cycles in the concentration of oxygen in blood and tissues of mice kept on a normal light-dark cycle. These variations were sufficient to alter the abundance of the transcription factor HIF1α (hypoxia-inducible factor 1α). In cultured cells, changes in oxygen concentration could entrain the circadian clock only if HIF1α was present. When animals were subjected to a 6-hour change in the light cycle (like traveling eastward on a jet), animals kept in a low concentration of oxygen adapted more quickly. —LBR

Cell Metab. 10.1016/j.cmet.2016.09.014 (2016).

HOST DEFENSE

How macrophages build a wall

Granulomas are a defining feature of infection with *Mycobacterium tuberculosis*, the causative agent of tuberculosis. Macrophages are the primary component of these cell structures, which are thought to protect the host by walling off the pathogen. Cronan *et al*. studied granulomas in optically transparent zebrafish infected with *M. marinum* to directly visualize how they form. They observed that macrophages in

CONSERVATION GENOMICS

Essential immigrants

As more and more species near extinction, conservation efforts will need to understand the genetic structure and consequences of declining population size. Chen *et al.* document the negative effects of reduced population connectivity over multiple generations in the Florida scrub jay. Their 19-year data set demonstrates that, for the Florida scrub jay, immigration between small satellite populations into larger, more stable groups is an essential component for maintaining genetic diversity. The reduction in the number of individuals, and hence in the size of satellite populations and immigration, has resulted in increased levels of inbreeding and reduced fitness in this species, demonstrating the impact of habitat fragmentation. —LMZ

Curr. Biol. 10.1016/j.cub.2016.08.062 (2016).

Connectivity is essential for sustaining endangered Florida scrub jays.

granulomas undergo epithelial reprogramming, up-regulating many molecules and adhesion structures characteristic of epithelial cells. Disrupting this process by blocking E-cadherin, a protein that drives the epithelialization process, led to granulomas with a disorganized appearance. Unexpectedly, however, this reduced the fishes' bacterial burden, suggesting that granulomas may not always be host-protective. —KLM

Immunity **45**, 861 (2016).

NANOMATERIALS

A nano dagger to the heart

Nanomaterials consist of nanometer-scale molecules or particles, which can have unusual mechanical, electrical, or optical properties. Industrial-scale fabrication of such material requires an assessment of their potential toxicity. Zhu *et al*. use molecular modeling and intracellular imaging to show that long (high aspect ratio), stiff carbon nanotubes can damage lysosome vesicle membranes. Persistent contact with the tip of the tube results in loss of membrane lipids and lysosome membrane instability, potentially activating the cell death pathway. —GR

Proc. Natl. Acad. Sci. U.S.A. 10.1073/pnas.1605030113 (2016).

AQUATIC MICROBIOLOGY

Lake bacteria make methane from P

Freshwater lakes are a major contributor of methane to the atmosphere—more so than the world's oceans combined. Some anaerobic microorganisms produce methane in sediments or deep anoxic water, but methane can also be produced biologically in oxic surface water. In the upper layers of methane-supersaturated Lake Matano, Indonesia, Yao *et al*. find that bacterial methane production is linked to phosphorus availability. Heterotrophic bacteria break down methylphosphonate as a phosphorus source, releasing methane in the process. Methane production decreases in culture when phosphate is added. Models for methane emissions from lakes should therefore incorporate nutrient availability in oxic water columns as another potential factor to help improve global methane predictions. —NW

Appl. Environ. Microbiol. 10.1128/AEM.02399-16 (2016).

ADAPTIVE OPTICS

Becoming clearer step by step

When a camera or sensor is in an environment of strong illumination or high background noise, scattering from the object, or glare, can be so high that the object can be obscured. Daniel *et al*. used an adaptive optics technique to manipulate the wavefront of a coherent light source illuminating an object, in this case a toy mannequin, and showed that the direction of scattered light from the object can be controlled. As the wavefront of the illuminating light is iteratively manipulated through a spatial light modulator, the glare is reduced and the image becomes clearer. The technique is general and could be applied to different scenarios such as sensing, microscopy, and other demanding imaging tasks. —ISO

Optica **3**, 1104 (2016).

GEOPHYSICS

Metallic melt for the mantle

Ultralow velocity zones (ULVZs) are distinct and dense patches at the very base of Earth's rocky mantle. Liu *et al*. suggest that iron carbide may be a vital component of ULVZs on the basis of measurements of iron carbide melting temperatures. Iron carbides could form as iron and carbon exsolve from slabs subducting into the mantle. The high temperature near the base of the mantle could then lead to iron carbide melting and ponding in the ULVZ regions. If this hypothesis is correct, ULVZs are an unrecognized and important carbon reservoir within Earth. —BG

Proc. Natl. Acad. Sci. U.S.A. 10.1073/pnas.1519540113 (2016).

REVIEW SUMMARY

CLIMATE CHANGE

The broad footprint of climate change from genes to biomes to people

Brett R. Scheffers,* Luc De Meester, Tom C. L. Bridge, Ary A. Hoffmann, John M. Pandolfi, Richard T. Corlett, Stuart H. M. Butchart, Paul Pearce-Kelly, Kit M. Kovacs, David Dudgeon, Michela Pacifici, Carlo Rondinini, Wendy B. Foden, Tara G. Martin, Camilo Mora, David Bickford, James E. M. Watson

BACKGROUND: Climate change impacts have now been documented across every ecosystem on Earth, despite an average warming of only ~1°C so far. Here, we describe the full range and scale of climate change effects on global biodiversity that have been observed in natural systems. To do this, we identify a set of core ecological processes (32 in terrestrial and 31 each in marine and freshwater ecosystems) that underpin ecosystem functioning and support services to people. Of the 94 processes considered, 82% show evidence of impact from climate change in the peer-reviewed literature. Examples of observed impacts from meta-analyses and case studies go beyond well-established shifts in species ranges and changes to phenology and population dynamics to include disruptions that scale from the gene to the ecosystem.

ADVANCES: Species are undergoing evolutionary adaptation to temperature extremes, and climate change has substantial impacts on species physiology that include changes in tolerances to high temperatures, shifts in sex ratios in species with temperature-dependent sex determination, and increased metabolic costs of living in a warmer world. These physiological adjustments have observable impacts on morphology, with many species in both aquatic and terrestrial systems shrinking in body size because large surface-to-volume ratios are generally favored under warmer conditions. Other morphological changes include reductions in melanism to improve thermoregulation, and altered wing and bill length in birds. Broader-scale responses to climate change include changes in the phenology, abundance, and distribution of species. Temperate plants are budding and flowering earlier in spring and later in autumn. Comparable adjustments have been observed in marine and freshwater fish spawning events and in the timing of seasonal migrations of animals worldwide. Changes in the abundance and age structure of populations have also been observed, with widespread evidence of range expansion in warm-adapted species and range contraction in cold-adapted species. As a by-product of species redistributions, novel community interactions have emerged. Tropical and boreal species are increasingly incorporated into temperate and polar communities, respectively, and when possible, lowland species are increasingly assimilating into mountain communities. Multiplicative impacts from gene to community levels scale up to produce ecological regime shifts, in which one ecosystem state shifts to an alternative state.

OUTLOOK: The many observed impacts of climate change at different levels of biological organization point toward an increasingly unpredictable future for humans. Reduced genetic diversity in crops, inconsistent crop yields, decreased productivity in fisheries from reduced body size, and decreased fruit yields from fewer winter chill events threaten food security. Changes in the distribution of disease vectors alongside the emergence of novel pathogens and pests are a direct threat to human health as well as to crops, timber, and livestock resources. Humanity depends on intact, functioning ecosystems for a range of goods and services. Enhanced understanding of the observed impacts of climate change on core ecological processes is an essential first step to adapting to them and mitigating their influence on biodiversity and ecosystem service provision. ■

ON OUR WEBSITE

Read the full article at http://dx.doi.org/10.1126/science.aaf7671

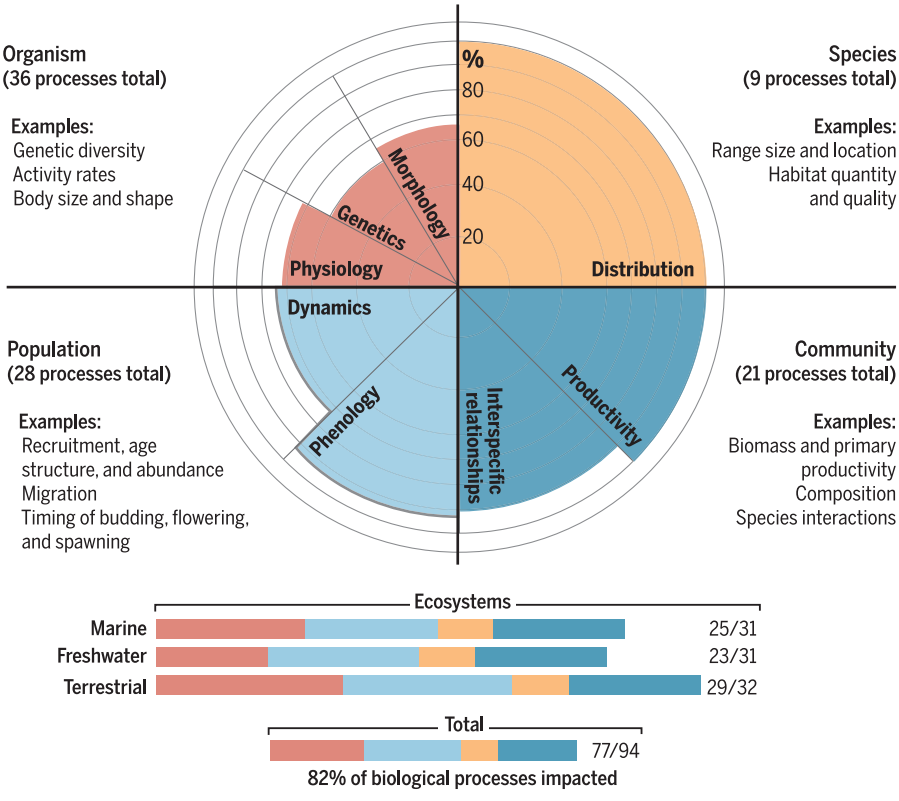

Climate change impacts on ecological processes in marine, freshwater, and terrestrial ecosystems. Impacts can be measured on multiple processes at different levels of biological organization within ecosystems. In total, 82% of 94 ecological processes show evidence of being affected by climate change. Within levels of organization, the percentage of processes impacted varies from 60% for genetics to 100% for species distribution.

The list of author affiliations is available in the full article online.
*Corresponding author. Email: brett.scheffers@ufl.edu
Cite this article as B. R. Scheffers *et al.*, *Science* **354**, aaf7671 (2016). DOI: 10.1126/science.aaf7671

REVIEW

CLIMATE CHANGE

The broad footprint of climate change from genes to biomes to people

Brett R. Scheffers,[1]* Luc De Meester,[2] Tom C. L. Bridge,[3,4] Ary A. Hoffmann,[5] John M. Pandolfi,[6] Richard T. Corlett,[7] Stuart H. M. Butchart,[8,9] Paul Pearce-Kelly,[10] Kit M. Kovacs,[11] David Dudgeon,[12] Michela Pacifici,[13] Carlo Rondinini,[13] Wendy B. Foden,[14] Tara G. Martin,[15] Camilo Mora,[16] David Bickford,[17]† James E. M. Watson[18,19]

Most ecological processes now show responses to anthropogenic climate change. In terrestrial, freshwater, and marine ecosystems, species are changing genetically, physiologically, morphologically, and phenologically and are shifting their distributions, which affects food webs and results in new interactions. Disruptions scale from the gene to the ecosystem and have documented consequences for people, including unpredictable fisheries and crop yields, loss of genetic diversity in wild crop varieties, and increasing impacts of pests and diseases. In addition to the more easily observed changes, such as shifts in flowering phenology, we argue that many hidden dynamics, such as genetic changes, are also taking place. Understanding shifts in ecological processes can guide human adaptation strategies. In addition to reducing greenhouse gases, climate action and policy must therefore focus equally on strategies that safeguard biodiversity and ecosystems.

Atmospheric concentrations of greenhouse gases from burning fossil fuels and deforestation are approaching levels that have not been detected in the past 20 million years (*1*). This has altered the chemical composition of the Earth's atmosphere, oceans, and fresh waters (*2*). As a result, temperatures in the upper ocean and on land are now ~1°C higher than in preindustrial times, and temperature, wind, and precipitation regimes have become more variable and extreme (*3*, *4*). These changes are having clear impacts on planetary biophysical processes, including desalinization and acidification of the world's oceans (*5*) and melting of permafrost, ice sheets, and glaciers (*6*, *7*). Lakes and rivers have increased in temperature, altering seasonal patterns of mixing and flows (*8*).

Changing climate regimes have been an important driver of natural selection in the past (*9*) and, as in the past, species are responding to the current human-induced climate event in various ways. Previous reviews have covered many of the more obvious changes in species ranges, phenologies, and population dynamics (*10*–*15*) but have usually focused on one ecological system at a time. Here, we discuss the full range and scale of climate change effects on biota, including some of the less obvious disruptions observed in natural systems. We present examples of case studies of observed impacts across terrestrial and aquatic biomes and find evidence that climate change is now affecting most biological and ecological processes on Earth—spanning genetics, organismal physiology and life-history, population distributions and dynamics, community structure, and ecosystem functioning (Fig. 1 and table S1). People depend on intact, functioning ecosystems for a range of goods and services, including those associated with climate adaptation (*16*). Understanding the observed impacts of current climate change on core ecological processes is therefore an essential first step in humans planning and adapting to changing ecosystem conditions.

Although inherently different, marine, freshwater, and terrestrial realms share a common hierarchy of levels of biological organization, ranging from genes to organisms, populations, species, communities, and ecosystems. Broadly adapting from Bellard *et al.* (*17*), we screened the literature (supplementary materials) to evaluate evidence that climate change is affecting ecological components across different levels of biological organization, each of which comprises a core set of ecological processes (Fig. 1, fig. S1, and table S1). We identify a set of core ecological processes on Earth (32 in terrestrial and 31 each in marine and freshwater), which together facilitate ecosystem functioning that supports services to people (*17*). These processes include changes in genetic diversity (genetics), metabolic rates (physiology), body size (morphology), timing of migration (phenology), recruitment (population dynamics), range size (distribution), loss of synchronization (interspecific relationships), and biomass (productivity) (*17*). Because our main goal is to assess what processes are affected by climate change, we define "impact" on each process as an observed change in that process linked to climate change. We do not differentiate between "positive" (adaptive, buffering, or mitigating) and "negative" (stress or damage) responses because responses may be positive at one level of biological organization (such as genetic adaptation to climate change) but negative at another (such as reduced genetic variation and capacity to deal with other stressors). We then consider the relevance of the affected ecological processes in human systems and illustrate observed impacts to ecosystem services such as food and resource security (fisheries, agriculture, forestry, and livestock production), human health, and hazard reduction.

Ecological impacts of climate change

Organisms

Genetics

There is now growing evidence that species are undergoing evolutionary adaptation to human-induced climate change. For example, between the 1960s and 2000s the water flea (*Daphnia magna*) evolved to cope with higher thermal extremes in the UK (*18*), and cornflower (*Centaurea cyanus*) life history traits have recently evolved in response to warmer springs across northern France (*19*). Other examples include the evolution of earlier migration timing in anadromous pink salmon (*Oncorhynchus gorbuscha*), with decreased frequency of incidence of a genetic marker that encodes for late migration (*20*). Time-series data that control for physiological acclimatization also show strong evidence for genetic responses to climate change. For example, Bradshaw and Holzapfel showed that genotypic values for the critical day length that induces diapause in the pitcher plant mosquito (*Wyeomyia smithii*) change with latitude, and that the latitudinal relationship has changed over the period from 1972 to 1996 (*21*). Onset of diapause now occurs later, which is consistent with a longer

[1]Department of Wildlife Ecology and Conservation, University of Florida, Gainesville, FL 32611-0430, USA. [2]Laboratory of Aquatic Ecology, Evolution and Conservation, KU Leuven, Ch. De Beriotstraat 32, 3000 Leuven, Belgium. [3]Australian Research Council Centre of Excellence for Coral Reef Studies, James Cook University, Townsville QLD 4811, Australia. [4]Queensland Museum, Townsville, Queensland 4810, Australia. [5]Bio21 Institute, School of Biosciences, University of Melbourne, Victoria 3010, Australia. [6]School of Biological Sciences and the Australian Research Council Centre of Excellence for Coral Reef Studies, The University of Queensland, Brisbane, Queensland 4072, Australia. [7]Center for Integrative Conservation, Xishuangbanna Tropical Botanical Gardens, Chinese Academy of Sciences, Yunnan 666303, China. [8]BirdLife International, David Attenborough Building, Pembroke Street, Cambridge CB2 3QZ, UK. [9]Department of Zoology, University of Cambridge, Downing Street, Cambridge CB2 3EJ, UK. [10]Zoological Society of London, Regent's Park, London NW1 4RY, UK. [11]Norwegian Polar Institute, FRAM Centre, 9296 Tromsø, Norway. [12]School of Biological Sciences, University of Hong Kong, Hong Kong SAR, China. [13]Global Mammal Assessment Program, Department of Biology and Biotechnologies, Sapienza Università di Roma, Viale dell'Università 32, I-00185 Rome, Italy. [14]Department of Botany and Zoology, University of Stellenbosch, P/Bag X1, Matieland, 7602 Stellenbosch, South Africa. [15]Department of Forest and Conservation Sciences, University of British Columbia, Vancouver, British Columbia, Canada. [16]Department of Geography, University of Hawaii, Honolulu, Hawaii, USA. [17]Department of Biological Sciences, National University of Singapore, 14 Science Drive 4, 117543, Singapore. [18]School of Geography, Planning and Environmental Management, The University of Queensland, Brisbane, Queensland 4072, Australia. [19]Global Conservation Program, Wildlife Conservation Society, 2300 Southern Boulevard, Bronx, NY 10460, USA.
***Corresponding author. Email: brett.scheffers@ufl.edu**
†Present address: Rimba, 4 Jalan 1/9D, 43650 Bandar Baru Bangi, Selangor, Malaysia.

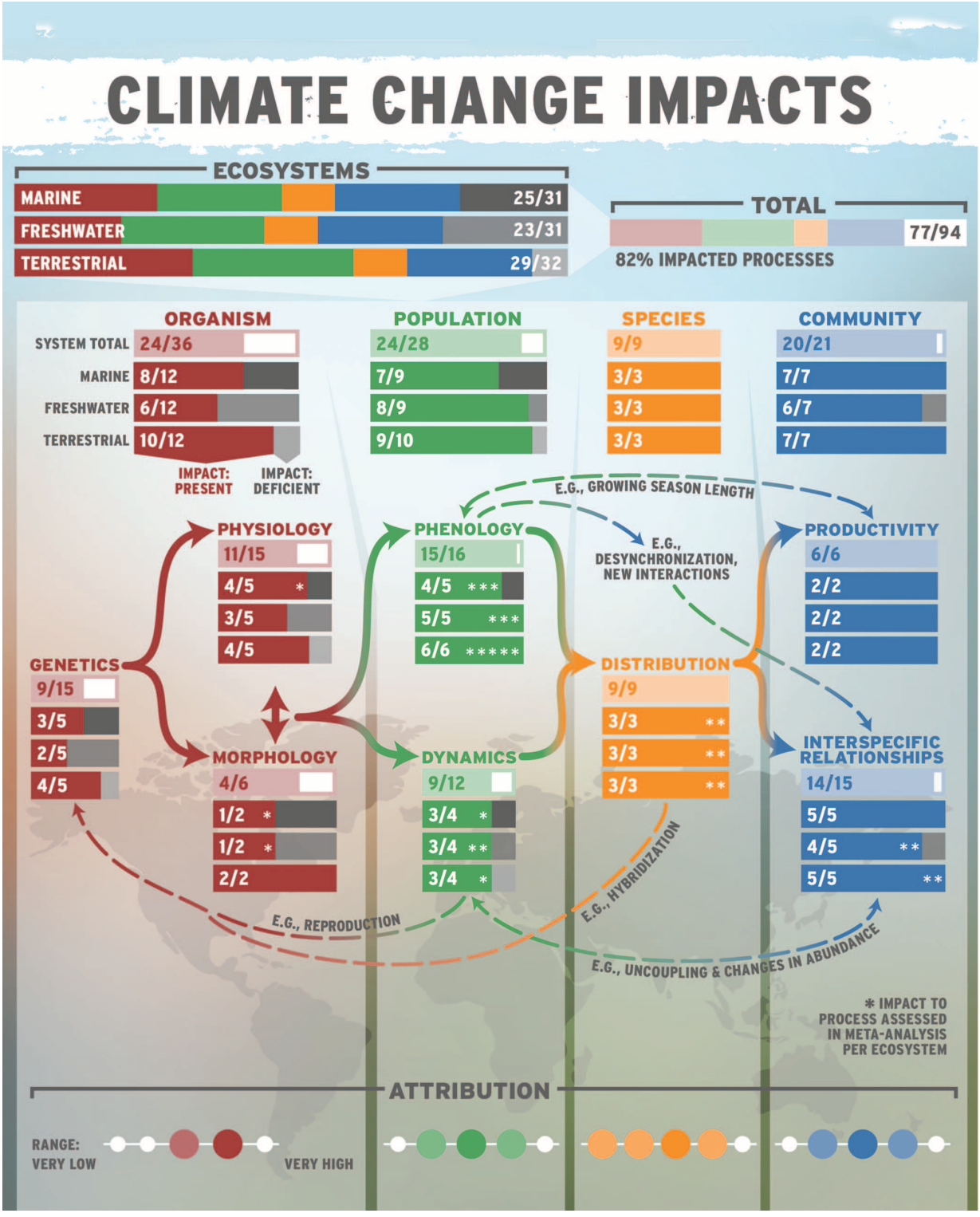

Fig. 1. Climate change impacts on Earth's marine, terrestrial, and freshwater systems. The presence of observed impacts on the different levels of biological organization and its inner components across the Earth's marine, terrestrial, and freshwater ecosystems. The denominator represents the total number of processes that we considered for each group, and the numerator is the number of these processes with evidence of impact (a complete list of processes is provided in fig. S1 and table S1). In total, 82% of all (n = 94) ecological processes that were considered have observed evidence of impact by climate change. Each process has at least one supporting case study. The asterisk indicates whether the affected process was assessed in a meta-analysis in addition to case studies. Thus, double-asterisk indicates that two processes were assessed in at least one meta-analysis. Confidence that the observed impact can be attributed to climate change was assigned for each level of organization and ranges from very low, low, medium, high, to very high; this assessment is based on tables 18-7, 18-8, and 18-11 in (*13*). The darkest circle indicates confidence level with the most literature support.

IMAGE CREDIT: STACEY JONES/MICHELE WOOD/IFAS

growing season under warmer conditions. Oceanic phytoplankton have adapted to a temperature change of +0.73°C associated with 15 years of climate warming in the Gulf of Cariaco, Venezuela, by adjusting their thermal niche by +0.45°C (*22*). Although such evidence from small organisms with short generation times is accumulating, we found little documented evidence of evolutionary change from species with longer generation times such as birds, mammals, and trees (*14*, *23*), although adaptation appears to be possible in some long-lived reef corals (*24*).

Changes in species ranges have altered or created new "hybridization zones" across the planet. For example, in North America, hybrid zones between black-capped (*Poecile atricapillus*) and Carolina chickadees (*P. carolinensis*) are shifting in response to warmer winter temperatures (*25*), and because the southern flying squirrel (*Glaucomys volans*) has expanded its range northward in eastern North America, it is now hybridizing with the northern flying squirrel (*G. sabrinus*) (*26*). In North American rivers and streams, hybridization between invasive rainbow trout (*Oncorhynchus mykiss*) and native cutthroat trout (*O. clarkia*) has increased in frequency as the former expand into warming waters (*27*). Such hybridization events have also been observed in some marine fishes, such as the coastal West Coast dusky cob (*Argyrosomus coronus*), and are expected to increase as species shift their ranges poleward in response to rapidly warming ocean conditions (*28*).

Physiology

Many species display temperature-driven trait plasticity in physiological processes such as thermal optima (*29*). Whereas some responses, such as acclimation to high temperatures, maximize fitness, others can reflect failure to cope with temperature stress and other climate-mediated changes. These responses can occur within a generation or between generations through maternal or epigenetic effects (*30*).

There is some observational evidence that warming has affected temperature-dependent sex determination (TSD) of species in marine and terrestrial systems. Snake pipefish (*Entelurus aequoreus*) in the northeastern Atlantic have altered their operational sex ratios and reproductive rates as a consequence of warmer sea surface temperatures (*31*). Most evidence for impacts on TSD in marine systems, however, is derived from experimental studies, which provide strong support for TSD changes in sea turtles and various fish species (*32*, *33*). In terrestrial and freshwater systems, TSD has been implicated in masculinization and feminization, respectively, of lizard and turtle populations (*34*, *35*).

In marine systems, physiological responses to both climate warming and changing ocean conditions are widespread (*36*, *37*). Matching field and laboratory data for the eelpout (*Zoarces viviparus*) show increased metabolic costs associated with warming in the North and Baltic Seas (*38*). In aquatic systems, warming increases oxygen demand but decreases oxygen content of the water, resulting in substantial metabolic costs (*39*). Although climate change per se does not cause acidification of the oceans, both arise directly from higher atmospheric carbon dioxide, and experimental evidence has raised concerns regarding negative effects of ocean acidification on calcification, growth, development, and survival of calcifying organisms (*12*). For example, acidification has led to extensive shell dissolution in populations of the pteropod *Limacina helicina* in northwest North America and in the Southern Ocean off Antarctica (*40*, *41*).

Morphology

Individuals in some species are becoming smaller with increasing warming because large surface-to-volume ratios are generally favored under warmer conditions (*42*)—a phenomenon that is linked to standard metabolic principles (*43*). In the Appalachian Mountains, six species of *Plethodon* woodland salamander have undergone, on average, an 8% reduction in body size over the past 50 years (*44*). Similarly, three species of passerine birds from the northeast United States show an average 4% decrease in wing length correlated with recent warming (*45*), and the long-distance migrant bird the red knot (*Calidris canutus*) is now producing smaller offspring with smaller bills, which reduces survival in juveniles because of altered foraging success on underground bivalves (*46*). In general, decreasing body size with warming is expected, but evidence from cold, high-altitude habitats suggests that increased primary productivity and longer growing seasons from warming have led to increased body size in some mammal species such as American marten (*Martes americana*) and yellow-bellied marmot (*Marmota flaviventris*) (*47*, *48*). In South Australia, leaf width in soapberry (*Dodonaea viscosa*) has decreased compared with the ancestral condition documented under cooler temperatures 127 years ago (*49*). Other climate change impacts on morphology include color changes in butterflies, dragonflies, and birds (*50*–*53*) and pronounced changes in skull shape in the alpine chipmunk (*Tamias alpinus*) (*54*).

Population

Phenology

For most species, migrations and life-history processes (such as budding and flowering in plants, hatching and fledging in birds, and hibernation in mammals) are closely tied to seasonal and interannual variation in climate, and there is now overwhelming evidence that both have been affected by climate change (*10*, *37*, *55*, *56*). Across marine, freshwater, and terrestrial ecosystems, spring phenologies have advanced by 2.3 to 5.1 days per decade (*10*, *57*). A combination of climate warming and higher atmospheric CO_2 concentrations has extended the growing period of many plant populations (*58*). In a large global analysis, which included 21 phenological metrics such as leaf-off and leaf-on dates and growing-season length, plant phenologies were found to have shifted by more than 2 standard deviations across 54% of Earth's land area during the past three decades (*59*).

In marine and freshwater systems, advances in the timing of annual phytoplankton blooms—the basis for many aquatic food webs—have occurred more rapidly than temporal shifts in terrestrial plants (*37*, *60*). Such changes in plankton phenology have been attributed to increases in water temperatures, reduction in the duration of ice cover, and the alteration of the seasonal duration of thermal stability or stratification of the water column.

Shifts in spawning times have been documented for 43 fish species in the northeast Pacific Ocean from 1951 to 2008, with earlier spawning associated with increased sea surface temperature and later spawning associated with delays in seasonal upwelling of nutrients toward the ocean surface (*61*). Similar impacts on breeding have been observed in terrestrial and marine bird species (*62*).

Changes in the timing of migration events have been extensively documented, including advances in spring arrival dates of long-distance migratory bird species in Europe, North America, and Australia (*63*–*65*). Similarly, long-term data on many amphibians and mammals have shown advancements in spring and delays in autumn migration (*66*–*68*) and altered peak calling periods of male amphibians (*67*–*69*). In the largest meta-analysis to date of phenological drivers and trends among species in the southern hemisphere, 82% of terrestrial data sets and 42% of marine data sets demonstrated an advance in phenology associated with rising temperature (*70*).

Abundance and population dynamics

Acute temperature stress can have severe negative effects on population dynamics such as abundance, recruitment, age structure, and sex ratios. Meta-analyses across thousands of species report that ~80% of communities across terrestrial, freshwater, and marine ecosystems exhibited a response in abundance that was in accordance with climate change predictions (*10*, *70*). In a meta-analysis of marine species, 52% of warm-adapted species increased in abundance, whereas 52% of cold-adapted species decreased (*71*). Temperature spikes may cause mass mortality of key ecosystem engineers in both temperate and tropical oceans. Excessive heat kills canopy-forming macroalgae in temperate marine systems (*72*) and causes bleaching and mass mortality of corals in the tropics (*73*). Reductions in sea ice extent have caused declines in abundances of ice-affiliated species in the Arctic [for example, ivory gulls (*Pagophila eburnea*), ringed seals (*Pusa hispida*), and polar bears (*Ursus maritimus*) (*74*)] whereas in some cases, such as on Beaufort Island in the southern Ross Sea, the loss of ice from receding glaciers resulted in increased abundances of Adélie penguins (*Pygoscelis adeliae*) (*75*). In the United States, the bull trout (*Salvelinus confluentus*) has lost >10% of its spawning grounds in central Idaho over the past 13 years because of increased water temperatures (*76*), while the brown trout (*Salmo*

trutta) has lost habitat in the Swiss Alps (*77*). In western Canada, reduced survival of adult migrating Fraser River sockeye salmon (*Oncorhynchus nerka*) has been observed with increased water temperatures (*78*), and in eastern Canadian lakes, golden-brown algae dramatically increased in abundance as water temperature increased 1.5°C during the latter part of the 20th century (*79*). Some of the best evidence for climate-change impacts on the abundance of terrestrial species comes from analyses of bird population trends derived from systematic monitoring schemes in Europe, with warm-adapted species having increased in abundance on average since the 1980s and cold-adapted species having declined (*80*).

Climate change can increase the abundance of temperature-sensitive disease vectors, with subsequent effects on disease outbreaks. In the African Serengeti, there is some evidence that a combination of extreme weather, high abundances of ticks carrying *Babesia*-piroplasm, and suppressed immunity to canine distemper virus led to widespread mortality of lions (*Panthera leo*) (*81*). In marine systems, field evidence shows that corals are increasingly susceptible to white band disease at higher temperatures, leading to declines in two of the most important reef-building acroporid (branching) corals in the western Atlantic (*82*).

Species

Distribution

One of the most rapid responses observed for marine, freshwater, and terrestrial species is a shift in their distributions to track optimal habitat conditions (*71*, *83*, *84*). Across land and aquatic ecosystems, species have expanded their leading (cold limit) edge by 19.7 km per decade, with marine species expanding by 72 km per decade compared with 6 km per decade in terrestrial species (*37*). The distributions of many marine taxa have shifted at higher velocities than those of terrestrial taxa (*37*) because areas with rapid changes in climate extend across broader regions of the ocean than on land, and connectivity in marine environments tends to be high (*85*). To illustrate this point, corals around Japan have shifted their range by up to 14 km per year over the past 80 years (*86*), and in waters off the southeast coast of Australia, intertidal invertebrate species have shifted their geographic distributions polewards at an average rate of 29 km per decade (*87*). Where connectivity allows for dispersal, some freshwater fishes are capable of shifting at rates comparable with those of marine and terrestrial taxa (*88*), but mean shifts by river fishes in some regions have been insufficient to compensate for measured temperature rises (*89*).

There has been a consistent overall trend for tropical, warm-adapted species to expand their ranges into environments previously dominated by temperate cold-tolerant species ("tropicalization") (*90*). A similar phenomenon has been documented in the Arctic, where boreal fish communities have responded to warming in the Barents Sea by shifting northward, resulting in a high turnover in Arctic fish communities ("borealization") (*91*). Similarly, on land, increased minimum temperatures have driven rapid changes in the range size (as well as distribution) of Swedish birds, with northern species retracting and southern species expanding northward (*92*).

In addition to latitudinal changes, many observed shifts in species distributions have occured across elevation gradients. In the mountains of New Guinea, birds have shifted their distributions upslope by 95 to 152 m from 1965 to 2013 (*93*). A similar upslope shift was observed in recent decades in mountainous stream-dwelling fish in France (*89*), North American plants (*94*), and Bornean insects (*95*). An analogous response has been the shift to deeper, colder waters among some marine fishes (*91*).

In some cases, species have shown no response or even downhill shifts in their distributions (*96*) or increased frequency of range disjunction rather than poleward or upward range shifts (*97*). Savage and Vellend (*98*) found upward range shifts in North American plant species and an overall trend toward biotic homogenization from 1970 to 2010, but their study also documents considerable time lags between warming and plant responses (*99*, *100*). Delayed community responses to increasing temperature may be in part due to the buffering effects of microhabitats (*101*, *102*) and possibly moisture, which is a critical, but less often studied, driver in the redistribution of species (*103*). For example, Crimmins *et al.* observed downhill movements for North American plants under climate change over an 80-year period, which they attribute to changes in water balance rather than temperature (*104*).

Community

Interspecific relationships

As a by-product of the redistribution of species in response to changing climate, existing interactions among species are being disrupted, and new interactions are emerging (*105*, *106*). These novel biotic interactions can exacerbate the impacts of abiotic climate change (*107*, *108*). Woody plants are invading arctic and alpine herb-dominated communities in response to rapid warming in recent decades, leading to secondary shifts in distribution of other plants and animals (*92*). In the Sierra Nevada Mountains of California, Tingley and Beissinger found high levels of avian community turnover during the past 100 years at the lowest and highest elevations (*109*), and in Greece, Sgardeli *et al.* found similar patterns of temperature-driven turnover in butterfly communities (*110*). There are surprisingly few studies of observed impacts of climate change on competitive interactions (*108*). In one example from Sweden, Wittwer *et al.* found that among four bird species occupying the same ecological guild, resident birds were able to adapt to warmer temperatures and outcompete the sole long-distance migrant, *Ficedula hypoleuca* (*111*).

New interactions among species can also lead to trophic disruptions such as overgrazing. In western Australia, for example, overgrazing of subtropical reefs by the poleward spread of tropical browsing fish has suppressed recovery of seaweeds after temperature-induced mortality (*112*). These types of trophic disruptions are escalating, with range shifts by tropical herbivorous fishes increasing herbivory rates in subtropical and temperate coastal ecosystems where seaweeds are the dominant habitat-forming taxa (*90*).

Phenological mismatches have been observed between butterflies and their annual host plants, with the plants dying before the insect larvae were ready to enter diapause (*113*). Similarly, an analysis of 27 years of predator-prey data from the UK showed asynchronous shifts between the tawny owl (*Strix aluco*) and its principle prey, the field vole (*Microtus agrestis*), which led to reduced owl fledging success (*114*). In Lake Washington, United States, spring diatom blooms advanced by over 20 days since 1962, resulting in predator-prey mismatches with their main grazer, the water flea (*Daphnia pulicaria*), and population declines in the latter (*60*). In Canadian Arctic lakes, asynchronous shifts in diatom blooms resulted in generalist water fleas being replaced by more specialist species (*115*). At higher trophic levels, warming has affected the fry and the juvenile life-history stages of lake char (*Salvelinus umbla*) via direct impacts on their zooplankton and vendace (*Coregonus alba*) food sources (*116*).

Productivity

Changes in productivity are one of the most critical impacts of climate change across aquatic and terrestrial ecosystems (*117*, *118*). In marine systems, climate-mediated changes in chlorophyll-a concentrations as a proxy of phytoplankton biomass have been highly variable (*119*). Depending on location, these include both dramatic increases and decreases in abundance as well as changes in phenology and distribution of phytoplankton over the past several decades. In a global study of phytoplankton since 1899, an ~1% decline in global median phytoplankton per year was strongly correlated with increases in sea surface temperature (*120*), whereas in the Antarctic Peninsula, phytoplankton increased by 66% in southern subregions and decreased by 12% in northern subregions over a 30-year period. These conflicting observations in the Antarctic are in part linked to changes in sea surface temperature but also changes in ice cover, cloudiness, and windiness, which effect water-column mixing (*121*).

In deep tropical freshwater lakes dominated by internal nutrient loading through regular mixing, warmer surface waters confer greater thermal stability, with reduced mixing and return of nutrients to the photic zone, substantially decreasing primary productivity (*122*), phytoplankton growth (*123*), and fish abundance (*122*). In contrast, eutrophication effects are exacerbated by higher temperatures in shallow lakes, resulting in increased productivity and phytoplankton and toxic cyanobacteria blooms (*124*).

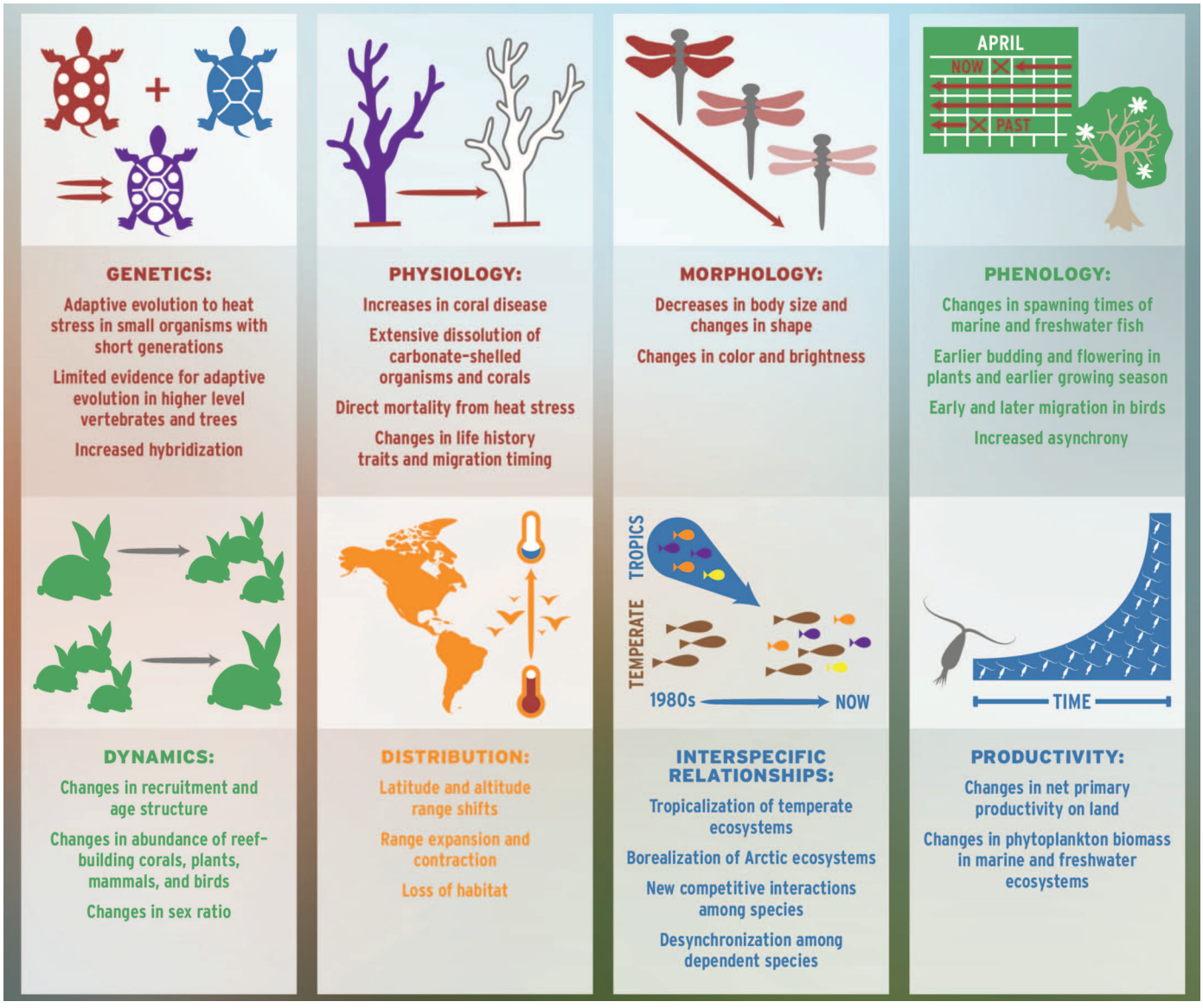

Fig. 2. Climate impacts on ecological processes. Examples of ecological components and processes affected by climate changes across marine, freshwater, and terrestrial ecosystems (fig. S1 and table S1).

IMAGE CREDIT: STACEY JONES/MICHELE WOOD/IFAS

Globally, terrestrial plant growth has increased with increasing temperatures and CO_2 levels. This may in part explain the on average 6% increase in net primary productivity (NPP) from 1982 to 1999 (*125*), although these changes in NPP may also be related to natural variation in El Niño–La Niña cycles (*126*). However, responses are highly variable, and some terrestrial systems are not experiencing increased productivity owing to either extreme temperatures or lack of water. Severe short-term droughts in climatically stable rainforest environments are unusual but in recent years have increased in frequency. These events have led to changes in forest canopy structure in Amazonia (*127*) and decreases in aboveground woody and leaf biomass in the Congo basin (*128*). Across large expanses of the Amazon, there has been an overall reduction in aboveground biomass owing to increased climate variability over the past three decades (*129*).

Impacts across ecosystems

All three biotic realms (terrestrial, freshwater, and marine) are being affected by climate change, and the evidence summarized here reveals that these impacts span the biological hierarchy from genes to communities. Of the 94 processes considered, we found that 82% have evidence of impact by climate change, and this has occurred with just 1°C of average warming globally (Fig. 1). Impacts range from genetic and physiological changes to responses in population abundance and distribution (Fig. 2).

The fact that evidence is missing for some processes is more likely to reflect data deficiencies than the absence of any response to climate change. We only considered field-based case studies that report changes in the processes through time. For many components, such as genetics (*23*) and physiology (*29*), there is strong evidence from experiments on a wide range of species that individuals and populations can and likely will respond to climate change. Thus, even though we found compelling evidence of widespread responses across the biological hierarchy, we still consider our discussion of impacted processes to be conservative. To illustrate this point, Box 1 shows the range of observed responses in the water flea *Daphnia*, which spans the entire hierarchy of biological organization.

Ecosystem state shifts

As ecological systems continue to accumulate stress through compromised ecological processes

Box 1. A complete hierarchy of climate change impact in one model system: the water flea *Daphnia*. Combining time-series data with experimental approaches can lend insights to the breadth of climate change impacts. For water fleas of the genus *Daphnia*, for instance, there is evidence for responses to temperature at all levels of biological organization. *Daphnia* are important grazers in lakes and ponds (*180*). They adapt to temperature increase through genetic changes in thermal tolerance (*18*), body size, and life history traits (*181*, *182*). In the laboratory, *Daphnia* exhibit phenotypic plasticity in physiology to changing temperatures [for example, hemoglobin quality and quantity (*183*) or metabolic activity (*184*)], behavior [such as swimming activity (*184*)], life history traits (*185*), and body size (*182*). *Daphnia* adjust their phenology (*186*) and abundance (*187*) in response to increases in temperature, which results in mismatches with phytoplankton dynamics (*60*). Warmer, drier weather over two decades can lead to expanded distributions and increased colonization capacity (*188*). Temperature influences interactions of *Daphnia* with predators (*189*) and parasites (*190*), and adaptation to increased temperature influences competitive strength (*185*). In the absence of fish, high abundances of *Daphnia* in +4°C heated mesocosms exert strong top-down control on phytoplankton (*191*).

either directly from climate change or interactively with other forced disturbances (discussion is provided in the supplementary materials), diminished resilience may lead to ecological regime shifts—in which one ecosystem state shifts to an alternative and potentially undesirable stable state. For example, some reefs are transitioning from coral- to algal-dominated states as a consequence of mass coral mortality (*130*), whereas kelp forests are turning into rocky barrens in temperate seas (*90*, *131*, *132*). In lakes, climate change has increased the risk of regime shifts from clear-water to turbid states and increased the occurrence of cyanobacteria blooms (*124*). If sufficient community-based processes are affected at regional scales, wholesale biome shifts can occur such as has been observed in Alaska, where tundra is transitioning to boreal conditions (*133*). These are clear signs of large-scale ecosystem change and disruption, in which disequilibrium rapidly pushes the system into a new state (*134*).

Using ecology to better understand climate change impacts on human well-being

Threats to production

The impacts of climate change on marine fisheries have major consequences for human societies because these currently provide ~17% of the global protein for people (*135*). There is, however, no current consensus on the costs and benefits of the ongoing global redistribution of fisheries because trends are highly variable. In the Arctic, commercially important fish, such as Atlantic cod (*Gadus morhua*) and walleye pollock (*Theragra chalcogramma*), have increased in biomass primarily because of increases in plankton production from reduced sea ice (*136*, *137*), whereas changes in fish biomass in the Southern Ocean are less clear (*138*). In Switzerland, which has experienced twice the average global temperature increase, trout catches have been halved over two decades because of rising temperatures in Alpine streams (*77*).

Changes in total marine productivity are not just attributed to abundance shifts but also morphological shifts. Indeed, some fish species appear to be shrinking, but attributing this solely to ocean warming is difficult because size-dependent responses can be triggered by commercial fishing as well as long-term climate change (*139*). However, long-term trend analyses show convincingly that eight commercial fish species in the North Sea underwent simultaneous reductions in body size over a 40-year period because of ocean warming, resulting in 23% lower yields (*140*). Reduced body size in fish is also being recorded in lakes and rivers throughout Europe and has been linked to increased temperature and climate-induced shifts in nutrient inputs (*141*, *142*).

Impacts on plant genetics and physiology are influencing human agricultural systems. For example, yields in rice, maize, and coffee have declined in response to the combined effects of rising temperatures and increasing precipitation variability over past decades (*143*–*145*). Genetics is being used to counteract decreasing yields in some key crops such as wheat [for which, globally, yields have declined by 6% since the early 1980s (*146*)] through crossing domesticated crops with wild relatives to maintain the evolutionary potential of varieties (*147*). Yet, some important wild strains are also showing signs of impact from climate change. Nevo *et al*. documented high levels of genetic changes in the progenitors of cultivated wheat and barley in Israel over the past 28 years (*148*). These wild cereals exhibited landscape-level changes in flowering time and a loss of genetic diversity in response to increasing temperatures.

Losing genetic resources in nature may undermine future development of novel crop varieties (*149*) and compromise key strategies that humans use to adapt to climate change. One such strategy is to use assisted gene flow, the managed movement of individuals or gametes between populations to mitigate local maladaptation in the short and long term (*150*). Where genetic introgression—the movement of genetic material from one species into the genome of another—can occur from unexploited natural populations to managed or exploited populations that are poorly adapted to warmer or drier conditions, adaptive changes may be facilitated (*147*), as in white spruce (*Picea glauca*), a tree commonly harvested for timber (*151*). Human-assisted evolution may also be a key strategy in maintaining reef-dependent fisheries by accelerating and enhancing the stress tolerance of corals (*152*).

Phenological changes due to milder winters are influencing crop and fruit production (*153*). Climate change has reduced winter chill events in temperate agricultural areas (*154*), which can desynchronize male and female flowers and trigger delayed pollination, delayed foliation, and reduced fruit yield and quality. To counter this, tree crop industries have developed adaptation measures such as low-chill cultivars with dormancy-breaking chemicals. For example, the "UFBest" peach requires four times fewer chill days than cultivars from more temperate climates (*155*). Advances in the timing of budding, flowering, and fruiting of plant species has induced earlier harvesting periods in some countries [such as Japan (*156*)].

Pollination is a key process linked to yields for a large number of crops. The short-lived, highly mobile insect species that provide pollination services to numerous crops have responded rapidly to changing climates by shifting their ranges throughout North America and Europe (*157*). Additionally, over the past 120 years, many plant-pollinator networks have been lost with overall decline in pollination services, which is attributed to a combination of habitat loss, pollution, and climate warming (*158*). Yet, observed changes in the phenology, abundance, and distribution of common pollinators have not been directly linked to declines in yields of animal-pollinated crops. This is likely due to limited data that directly link pollination services to crop yield over time and may, in part, reflect resilience provided by the diversity of insect species that pollinate many crops (*159*, *160*). More specialized pollination systems are expected to be more vulnerable to climate change. Humans have adapted to the declines in native pollinators by transporting domesticated pollinators to crop locations.

Pest and disease threats

Climate-induced ecosystem-level changes, such as forest die-offs, have an obvious impact on

PHOTO: JOACHIM MERGEAY

Table 1. Climate change consequences for humans. Affected ecological processes have direct consequences in food systems and human health.

	Organism	Population	Species	Community
	Genetics, physiology, morphology	**Phenology, dynamics**	**Distribution**	**Interspecific relationships, productivity**
Resource security	Rapid genetic adaptation to climate change in timber species	Increased herbivory on crops and timber by pests	Overall distribution shifts in marine and freshwater fisheries	Decline in plant-pollinator networks and pollination services
	Decreased crop yields in hot climates and increases in cool climates	Decreased genetic diversity and altered flowering time in wild cereals and novel crop varieties	Reduced range size or changes in pollinator abundance	Novel pests and invasive species
	Increased weed-crop competition and parasite-livestock interactions	Reduced fruit yields from fewer winter chill events		
	Decreased yield in fisheries from reduced body size	Reduced productivity in commercial fisheries		
Human health	Decline in reef calcifiers threatens coastal communities; loss of protection from storm surges and loss of food/protein sources	Increased costs and risk to subsistence communities from loss of sea ice and permafrost	Expanding and/or new distributions of disease vectors	Increased human-wildlife conflicts
	Rapid adaptation of disease vectors to new climatic conditions		Redistribution of arable land	Novel disease vectors

people, with a reduction in timber supplies and carbon sequestration, and changes in water quality and watershed volume (*161*–*163*). Several native insect species from North America, with no prior records of severe infestation, have recently emerged as severe pathogens of forest resources because of changes in population dynamics. These include the Aspen leaf miner (*Phyllocnistis populiella*), the leafblotch miner (*Micrurapteryx salicifoliella*), and the Janet's looper (*Nepytia janetae*), which have decimated millions of hectares of aspen, willows, and spruce-fir forests since the early 1990s (*164*). Known pests such as mountain and southern pine beetles (*Dendroctonus frontalis* and *D. ponderosae*, respectively) and spruce beetles (*D. rufipennis*) have recently expanded their distribution and infestation intensity on commercially important pine and spruce trees (*161*, *164*). These outbreaks may increase in the future because hundreds of plant pest and pathogen species have shifted their distributions 2 to 3.5 km year^{-1} poleward since the 1960s (*165*).

An emerging threat to human health under climate change is vector-borne disease (*166*). Vectors that have shifted their ranges and abundance can be found in marine, freshwater, and terrestrial systems. For example, in marine systems, unprecedented warming in the Baltic Sea led to emergence of *Vibrio* infections in Northern Europe (*167*, *168*), a geographic locality that had limited prior occurrence of this waterborne bacterial pathogen. Mosquitoes (e.g., *Aedes japonicus, A. aegypti, A. albopictus*) are extending their distribution into areas that are much warmer than their original habitats. As a result of ecological adaptation, mosquitos have become more competent vectors for spreading diseases such as chikungunya, dengue, and possibly the emerging Zika virus (*169*). Last, in terrestrial systems Levi *et al.* found that the nymph stage of the Lyme disease–carrying blacklegged tick (*Ixodes scapularis*) exhibited an overall advancement in nymph and larvae phenology since 1994, shifting the timing of greatest risk for pathogen transfer to humans to earlier in the year (*170*).

Losing intact ecosystems and their function

Changes in ecological processes might compromise the functionality of ecosystems. This is an important consideration because healthy systems (both terrestrial and marine) sequester substantial amounts of carbon (*171*), regulate local climate regimes (*172*), and reduce risks associated with climate-related hazards such as floods, sea-level rise, and cyclones (*173*). In island and coastal communities, coral reefs can reduce wave energy by an average of 97% (*174*), and coastal ecosystems such as mangroves and tidal marshes buffer storms (*175*), while on land intact native forests are important in reducing the frequency and severity of floods (*176*). In many cases, maintaining functioning systems offers more sustainable, cost-effective, and ecologically sound alternatives than conventional engineering solutions (*16*).

Science and action in a warmer world

The United Nations Framework Convention on Climate Change (UNFCCC) and the recent COP21 agreement in Paris presently offer the best opportunity for decisive action to reduce the current trajectory of climate change. This latter agreement set global warming targets of 1.5 to 2°C above preindustrial levels in order to avoid "dangerous climate change," yet the current 1°C average increase has already had broad and worrying impacts on natural systems, with accumulating consequences for people (Table 1). Minimizing the impacts of climate change on core ecological processes must now be a key policy priority for all nations, given the adoption of the UN Sustainable Development Goals aiming to increase human well-being. This will require continued funding of basic science focused on understanding how ecological processes are interacting with climate change, and of programs aimed at supporting ecosystem-based adaptations that enhance natural defences against climate hazards for people and nature and ensure ongoing provision of natural goods and services (*177*).

We must also recognize the role that intact natural ecosystems, particularly large areas, play in overcoming the challenges that climate change presents, not only as important repositories for carbon but also because of their ability to buffer and regulate local climate regimes and help human populations adapt to climate change (*16*, *173*). These systems are also critical for maintaining global biodiversity because the connectivity provided by large, contiguous areas spanning environmental gradients—such as altitude, depth, or salinity—will maximize the potential for gene flow and genetic adaptation while also allowing species to track shifting climate spatially (*178*).

The overriding priority of the UNFCCC is to set in motion a sustained global reduction in greenhouse gas emissions. This must be achieved alongside an improvement in our understanding of key ecological processes that form the foundation of biological and human systems, and in tandem with efforts to conserve the natural habitats in which such ecological processes operate.

It is now up to national governments to make good on the promises they made in Paris through regular tightening of emission targets, and also to recognize the importance of healthy ecosystems in times of unprecedented change (*179*). Time is running out for a globally synchronized response to climate change that integrates adequate protection of biodiversity and ecosystem services.

REFERENCES AND NOTES

1. D. J. Beerling, D. L. Royer, Convergent Cenozoic CO_2 history. *Nat. Geosci.* **4**, 418–420 (2011). doi: 10.1038/ngeo1186
2. P. Ciais *et al.*, in *Climate Change 2013: The Physical Science Basis. Contribution of Working Group I to the Fifth Assessment Report of the Intergovernmental Panel on Climate Change*, T. F. Stocker *et al.*, Eds. (Cambridge Univ. Press, 2014), pp. 465–570.
3. N. L. Bindoff *et al.*, in *Climate Change 2013: The Physical Science Basis. Contribution of Working Group I to the Fifth Assessment Report of the Intergovernmental Panel on Climate Change*, T. F. Stocker *et al.*, Eds. (Cambridge Univ. Press, 2013), pp. 867–952.
4. S. J. Smith, J. Edmonds, C. Hartin, A. Mundra, K. Calvin, Near-term acceleration in the rate of temperature change. *Nat. Clim. Chang.* **5**, 333–336 (2015). doi: 10.1038/nclimate2552
5. R. Curry, C. Mauritzen, Dilution of the northern North Atlantic Ocean in recent decades. *Science* **308**, 1772–1774 (2005). doi: 10.1126/science.1109477; pmid: 15961666
6. W. N. Meier *et al.*, Arctic sea ice in transformation: A review of recent observed changes and impacts on biology and human activity. *Rev. Geophys.* **52**, 185–217 (2014). doi: 10.1002/2013RG000431
7. B. Marzeion, J. G. Cogley, K. Richter, D. Parkes, Attribution of global glacier mass loss to anthropogenic and natural causes. *Science* **345**, 919–921 (2014). doi: 10.1126/science.1254702; pmid: 25123485
8. M. W. Swinton, L. W. Eichler, J. L. Farrell, C. W. Boylen, Evidence for water temperature increase in Lake George, NY: Impact on growing season duration and degree days. *Lake Reservior Manage.* **31**, 241–253 (2015). doi: 10.1080/10402381.2015.1067660
9. B. Sandel *et al.*, The influence of Late Quaternary climate-change velocity on species endemism. *Science* **334**, 660–664 (2011). doi: 10.1126/science.1210173; pmid: 21979937
10. C. Parmesan, G. Yohe, A globally coherent fingerprint of climate change impacts across natural systems. *Nature* **421**, 37–42 (2003). doi: 10.1038/nature01286; pmid: 12511946
11. C. Parmesan, Ecological and evolutionary responses to recent climate change. *Annu. Rev. Ecol. Evol. Syst.* **37**, 637–669 (2006). doi: 10.1146/annurev.ecolsys.37.091305.110100
12. K. J. Kroeker *et al.*, Impacts of ocean acidification on marine organisms: Quantifying sensitivities and interaction with warming. *Glob. Change Biol.* **19**, 1884–1896 (2013). doi: 10.1111/gcb.12179; pmid: 23505245
13. W. Cramer *et al.*, in *Climate Climate Change 2014: Impacts, Adaptation, and Vulnerability*, C. B. Field *et al.*, Eds. (Cambridge Univ. Press, 2014), pp. 979–1038.
14. J. Merilä, A. P. Hendry, Climate change, adaptation, and phenotypic plasticity: The problem and the evidence. *Evol. Appl.* **7**, 1–14 (2014). doi: 10.1111/eva.12137; pmid: 24454544
15. J.-P. Gattuso *et al.*, Contrasting futures for ocean and society from different anthropogenic CO_2 emissions scenarios. *Science* **349**, aac4722 (2015). pmid: 26138982
16. T. G. Martin, J. E. M. Watson, Intact ecosystems provide best defence against climate change. *Nat. Clim. Chang.* **6**, 122–124 (2016). doi: 10.1038/nclimate2918
17. C. Bellard, C. Bertelsmeier, P. Leadley, W. Thuiller, F. Courchamp, Impacts of climate change on the future of biodiversity. *Ecol. Lett.* **15**, 365–377 (2012). pmid: 22257223
18. N. Geerts *et al.*, Rapid evolution of thermal tolerance in the water flea *Daphnia*. *Nat. Clim. Chang.* **5**, 1–5 (2015).
19. M. Thomann, E. Imbert, R. C. Engstrand, P.-O. Cheptou, Contemporary evolution of plant reproductive strategies under global change is revealed by stored seeds. *J. Evol. Biol.* **28**, 766–778 (2015). doi: 10.1111/jeb.12603; pmid: 25682981
20. R. P. Kovach, A. J. Gharrett, D. A. Tallmon, Genetic change for earlier migration timing in a pink salmon population. *Proc. Biol. Sci.* **279**, 3870–3878 (2012). doi: 10.1098/rspb.2012.1158; pmid: 22787027
21. W. E. Bradshaw, C. M. Holzapfel, Genetic shift in photoperiodic response correlated with global warming. *Proc. Natl. Acad. Sci. U.S.A.* **98**, 14509–14511 (2001). doi: 10.1073/pnas.241391498; pmid: 11698659
22. A. J. Irwin, Z. V. Finkel, F. E. Müller-Karger, L. Troccoli Ghinaglia, Phytoplankton adapt to changing ocean environments. *Proc. Natl. Acad. Sci. U.S.A.* **112**, 5762–5766 (2015). doi: 10.1073/pnas.1414752112; pmid: 25902497
23. A. A. Hoffmann, C. M. Sgrò, Climate change and evolutionary adaptation. *Nature* **470**, 479–485 (2011). doi: 10.1038/nature09670; pmid: 21350480
24. S. R. Palumbi, D. J. Barshis, N. Traylor-Knowles, R. A. Bay, Mechanisms of reef coral resistance to future climate change. *Science* **344**, 895–898 (2014). pmid: 24762535
25. S. A. Taylor *et al.*, Climate-mediated movement of an avian hybrid zone. *Curr. Biol.* **24**, 671–676 (2014). doi: 10.1016/j.cub.2014.01.069; pmid: 24613306
26. C. J. Garroway *et al.*, Climate change induced hybridization in flying squirrels. *Glob. Change Biol.* **16**, 113–121 (2010). doi: 10.1111/j.1365-2486.2009.01948.x
27. C. C. Muhlfeld *et al.*, Invasive hybridization in a threatened species is accelerated by climate change. *Nat. Clim. Chang.* **4**, 620–624 (2014). doi: 10.1038/nclimate2252
28. W. M. Potts *et al.*, Ocean warming, a rapid distributional shift, and the hybridization of a coastal fish species. *Glob. Change Biol.* **20**, 2765–2777 (2014). doi: 10.1111/gcb.12612; pmid: 24753154
29. S. L. Chown *et al.*, Adapting to climate change: A perspective from evolutionary physiology. *Clim. Res.* **43**, 3–15 (2010). doi: 10.3354/cr00879
30. J. M. Donelson, P. L. Munday, Transgenerational plasticity mitigates the impact of global warming to offspring sex ratios. *Glob. Change Biol.* **21**, 2954–2962 (2015). doi: 10.1111/gcb.12912; pmid: 25820432
31. R. R. Kirby, D. G. Johns, J. A. Lindley, Fathers in hot water: Rising sea temperatures and a Northeastern Atlantic pipefish baby boom. *Biol. Lett.* **2**, 597–600 (2006). doi: 10.1098/rsbl.2006.0530; pmid: 17148298
32. L. A. Hawkes, A. C. Broderick, M. H. Godfrey, B. J. Godley, Investigating the potential impacts of climate change on a marine turtle population. *Glob. Change Biol.* **13**, 923–932 (2007). doi: 10.1111/j.1365-2486.2007.01320.x
33. N. Ospina-Álvarez, F. Piferrer, Temperature-dependent sex determination in fish revisited: Prevalence, a single sex ratio response pattern, and possible effects of climate change. *PLOS ONE* **3**, e2837 (2008). doi: 10.1371/journal.pone.0002837; pmid: 18665231
34. L. E. Schwanz, F. J. Janzen, Climate change and temperature-dependent sex determination: Can individual plasticity in nesting phenology prevent extreme sex ratios? *Physiol. Biochem. Zool.* **81**, 826–834 (2008). doi: 10.1086/590220; pmid: 18831689
35. R. S. Telemeco, M. J. Elphick, R. Shine, Nesting lizards (*Bassiana duperreyi*) compensate partly, but not completely, for climate change. *Ecology* **90**, 17–22 (2009). doi: 10.1890/08-1452.1; pmid: 19294908
36. P. Krishnan *et al.*, Elevated sea surface temperature during May 2010 induces mass bleaching of corals in the Andaman. *Curr. Sci.* **100**, 111–117 (2011).
37. E. S. Poloczanska *et al.*, Global imprint of climate change on marine life. *Nat. Clim. Chang.* **3**, 919–925 (2013).
38. H. O. Pörtner, R. Knust, Climate change affects marine fishes through the oxygen limitation of thermal tolerance. *Science* **315**, 95–97 (2007). doi: 10.1126/science.1135471; pmid: 17204649
39. C. Deutsch, A. Ferrel, B. Seibel, H.-O. Pörtner, R. B. Huey, Climate change tightens a metabolic constraint on marine habitats. *Science* **348**, 1132–1135 (2015). doi: 10.1126/science.aaa1605; pmid: 26045435
40. N. Bednaršek *et al.*, *Limacina helicina* shell dissolution as an indicator of declining habitat suitability owing to ocean acidification in the California Current Ecosystem. *Proc. R. Soc. B Biol. Sci.* **281**, 20140123 (2014).
41. N. Bednaršek *et al.*, Extensive dissolution of live pteropods in the Southern Ocean. *Nat. Geosci.* **5**, 881–885 (2012). doi: 10.1038/ngeo1635
42. J. Sheridan, D. Bickford, Shrinking body size as an ecological response to climate change. *Nat. Clim. Chang.* **1**, 401–406 (2011). doi: 10.1038/nclimate1259
43. J. H. Brown, J. F. Gillooly, A. P. Allen, V. M. Savage, G. B. West, Toward a metabolic theory of ecology. *Ecology* **85**, 1771–1789 (2004). doi: 10.1890/03-9000
44. N. M. Caruso, M. W. Sears, D. C. Adams, K. R. Lips, Widespread rapid reductions in body size of adult salamanders in response to climate change. *Glob. Change Biol.* **20**, 1751–1759 (2014). doi: 10.1111/gcb.12550; pmid: 24664864
45. D. E. McCoy, Connecticut birds and climate change: Bergmann's rule in the fourth dimension. *Northeast. Natural.* **19**, 323–334 (2012). doi: 10.1656/045.019.0213
46. J. A. van Gils *et al.*, Body shrinkage due to Arctic warming reduces red knot fitness in tropical wintering range. *Science* **352**, 819–821 (2016). doi: 10.1126/science.aad6351; pmid: 27174985
47. A. Ozgul *et al.*, Coupled dynamics of body mass and population growth in response to environmental change. *Nature* **466**, 482–485 (2010). doi: 10.1038/nature09210; pmid: 20651690
48. Y. Yom-Tov, S. Yom-Tov, G. Jarrell, Recent increase in body size of the American marten *Martes americana* in Alaska. *Biol. J. Linn. Soc. Lond.* **93**, 701–707 (2008). doi: 10.1111/j.1095-8312.2007.00950.x
49. G. R. Guerin, H. Wen, A. J. Lowe, Leaf morphology shift linked to climate change. *Biol. Lett.* **8**, 882–886 (2012). doi: 10.1098/rsbl.2012.0458; pmid: 22764114
50. A. Roulin, Melanin-based colour polymorphism responding to climate change. *Glob. Change Biol.* **20**, 3344–3350 (2014). doi: 10.1111/gcb.12594; pmid: 24700793
51. D. Zeuss, R. Brandl, M. Brändle, C. Rahbek, S. Brunzel, Global warming favours light-coloured insects in Europe. *Nat. Commun.* **5**, 3874 (2014). doi: 10.1038/ncomms4874; pmid: 24866819
52. J. G. Kingsolver, L. B. Buckley, Climate variability slows evolutionary responses of Colias butterflies to recent climate change. *Proc. Biol. Sci.* **282**, 20142470 (2015). doi: 10.1098/rspb.2014.2470; pmid: 25631995
53. P. Karell, K. Ahola, T. Karstinen, J. Valkama, J. E. Brommer, Climate change drives microevolution in a wild bird. *Nat. Commun.* **2**, 208 (2011). doi: 10.1038/ncomms1213; pmid: 21343926
54. R. E. Walsh *et al.*, Morphological and dietary responses of chipmunks to a century of climate change. *Glob. Chang. Biol.* (2016). doi: 10.1111/gcb.13216
55. M. E. Visser, C. Both, Shifts in phenology due to global climate change: the need for a yardstick. *Proc. R. Soc. B Biol. Sci.* **272**, 2561–2569 (2005).
56. C. Rézouki *et al.*, Socially mediated effects of climate change decrease survival of hibernating Alpine marmots. *J. Anim. Ecol.* **85**, 761–773 (2016). doi: 10.1111/1365-2656.12507; pmid: 26920650
57. T. L. Root *et al.*, Fingerprints of global warming on wild animals and plants. *Nature* **421**, 57–60 (2003). doi: 10.1038/nature01333; pmid: 12511952
58. M. Reyes-Fox *et al.*, Elevated CO_2 further lengthens growing season under warming conditions. *Nature* **510**, 259–262 (2014). doi: 10.1038/nature13207; pmid: 24759322
59. R. Buitenwerf, L. Rose, S. I. Higgins, Three decades of multi-dimensional change in global leaf phenology. *Nat. Clim. Chang.* **5**, 364–368 (2015). doi: 10.1038/nclimate2533
60. M. Winder, D. E. Schindler, Climate change uncouples trophic interactions in an aquatic ecosystem. *Ecology* **85**, 2100–2106 (2004). doi: 10.1890/04-0151
61. R. G. Asch, Climate change and decadal shifts in the phenology of larval fishes in the California Current ecosystem. *Proc. Natl. Acad. Sci. U.S.A.* **112**, E4065–E4074 (2015). doi: 10.1073/pnas.1421946112; pmid: 26159416
62. P. O. Dunn, A. P. Møller, Changes in breeding phenology and population size of birds. *J. Anim. Ecol.* **83**, 729–739 (2014). doi: 10.1111/1365-2656.12162; pmid: 24117440
63. P. Gienapp, R. Leimu, J. Merila, Responses to climate change in avian migration time–Microevolution versus phenotypic plasticity. *Clim. Res.* **35**, 25–35 (2007). doi: 10.3354/cr00712

64. A. H. Hurlbert, Z. Liang, Spatiotemporal variation in avian migration phenology: Citizen science reveals effects of climate change. *PLOS ONE* **7**, e31662 (2012). doi: 10.1371/journal.pone.0031662; pmid: 22384050
65. S. E. Travers *et al*., Climate change and shifting arrival date of migratory birds over a century in the northern Great Plains. *Wilson J. Ornithol.* **127**, 43–51 (2015). doi: 10.1676/14-033.1
66. C. Ramp, J. Delarue, P. J. Palsbøll, R. Sears, P. S. Hammond, Adapting to a warmer ocean—Seasonal shift of baleen whale movements over three decades. *PLOS ONE* **10**, e0121374 (2015). doi: 10.1371/journal.pone.0121374; pmid: 25785462
67. B. D. Todd, D. E. Scott, J. H. K. Pechmann, J. W. Gibbons, Climate change correlates with rapid delays and advancements in reproductive timing in an amphibian community. *Proc. R. Soc. B Biol. Sci.* **278**, 2191–2197 (2011).
68. A. A. Walpole, J. Bowman, D. C. Tozer, D. S. Badzinski, Community-level response to climate change: Shifts in anuran calling phenology. *Herpetol. Conserv. Biol.* **7**, 249–257 (2012).
69. A. B. Phillimore, J. D. Hadfield, O. R. Jones, R. J. Smithers, Differences in spawning date between populations of common frog reveal local adaptation. *Proc. Natl. Acad. Sci. U.S.A.* **107**, 8292–8297 (2010). doi: 10.1073/pnas.0913792107; pmid: 20404185
70. L. E. Chambers *et al*., Phenological changes in the southern hemisphere. *PLOS ONE* **8**, e75514 (2013). doi: 10.1371/journal.pone.0075514; pmid: 24098389
71. E. S. Poloczanska *et al*., Responses of marine organisms to climate change across oceans. *Front. Mar. Sci.* **3**, 1–21 (2016). doi: 10.3389/fmars.2016.00062
72. T. Wernberg *et al*., Seaweed communities in retreat from ocean warming. *Curr. Biol.* **21**, 1828–1832 (2011). doi: 10.1111/j.1365-2486.2012.02656.x
73. A. C. Baker, P. W. Glynn, B. Riegl, Climate change and coral reef bleaching: An ecological assessment of long-term impacts, recovery trends and future outlook. *Estuar. Coast. Shelf Sci.* **80**, 435–471 (2008). doi: 10.1016/j.ecss.2008.09.003
74. K. L. Laidre *et al*., Arctic marine mammal population status, sea ice habitat loss, and conservation recommendations for the 21st century. *Conserv. Biol.* **29**, 724–737 (2015). doi: 10.1111/cobi.12474; pmid: 25783745
75. M. A. LaRue *et al*., Climate change winners: Receding ice fields facilitate colony expansion and altered dynamics in an Adélie penguin metapopulation. *PLOS ONE* **8**, e60568 (2013). doi: 10.1371/journal.pone.0060568; pmid: 23573267
76. D. J. Isaak *et al*., Effects of climate change and wildfire on stream temperatures and salmonid thermal habitat in a mountain river network. *Ecol. Appl.* **20**, 1350–1371 (2010). doi: 10.1890/09-0822.1; pmid: 20666254
77. C. Cianfrani, H. F. Satizábal, C. Randin, A spatial modelling framework for assessing climate change impacts on freshwater ecosystems: Response of brown trout (*Salmo trutta* L.) biomass to warming water temperature. *Ecol. Modell.* **313**, 1–12 (2015). doi: 10.1016/j.ecolmodel.2015.06.023
78. E. G. Martins *et al*., Effects of river temperature and climate warming on stock-specific survival of adult migrating Fraser River sockeye salmon (*Oncorhynchus nerka*). *Glob. Change Biol.* **17**, 99–114 (2011). doi: 10.1111/j.1365-2486.2010.02241.x
79. B. Ginn, M. Rate, B. Cumming, J. Smol, Ecological distribution of scaled-chrysophyte assemblages from the sediments of 54 lakes in Nova Scotia and southern New Brunswick, Canada. *J. Paleolimnol.* **43**, 293–308 (2010). doi: 10.1007/s10933-009-9332-9
80. R. D. Gregory *et al*., An indicator of the impact of climatic change on European bird populations. *PLOS ONE* **4**, e4678 (2009). doi: 10.1371/journal.pone.0004678; pmid: 19259270
81. L. Munson *et al*., Climate extremes promote fatal co-infections during canine distemper epidemics in African lions. *PLOS ONE* **3**, e2545 (2008). doi: 10.1371/journal.pone.0002545; pmid: 18575601
82. C. J. Randall, R. van Woesik, Contemporary white-band disease in Caribbean corals driven by climate change. *Nat. Clim. Chang.* **5**, 375–379 (2015). doi: 10.1038/nclimate2530
83. C. Tayleur *et al*., Swedish birds are tracking temperature but not rainfall: Evidence from a decade of abundance changes. *Glob. Ecol. Biogeogr.* **24**, 859–872 (2015). doi: 10.1111/geb.12308
84. A. Lehikoinen, R. Virkkala, North by north-west: Climate change and directions of density shifts in birds. *Glob. Change Biol.* **22**, 1121–1129 (2016). doi: 10.1111/gcb.13150; pmid: 26691578
85. M. T. Burrows *et al*., The pace of shifting climate in marine and terrestrial ecosystems. *Science* **334**, 652–655 (2011). doi: 10.1126/science.1210288; pmid: 22053045
86. H. Yamano, K. Sugihara, K. Nomura, Rapid poleward range expansion of tropical reef corals in response to rising sea surface temperatures. *Geophys. Res. Lett.* **38**, 1–6 (2011). doi: 10.1029/2010GL046474
87. N. R. Pitt, E. S. Poloczanska, A. J. Hobday, Climate-driven range changes in Tasmanian intertidal fauna. *Mar. Freshw. Res.* **61**, 963–970 (2010). doi: 10.1071/MF09225
88. K. M. Alofs, D. Jackson, N. P. Lester, Ontario freshwater fishes demonstrate differing range-boundary shifts in a warming climate. *Divers. Distrib.* **20**, 123–136 (2014). doi: 10.1111/ddi.12130
89. L. Comte, G. Grenouillet, Do stream fish track climate change? Assessing distribution shifts in recent decades. *Ecography* **36**, 1236–1246 (2013). doi: 10.1111/j.1600-0587.2013.00282.x
90. A. Vergés *et al*., The tropicalization of temperate marine ecosystems: climate-mediated changes in herbivory and community phase shifts. *Proc. R. Soc. B Biol. Sci.* **281**, 20140846 (2014).
91. M. Fossheim *et al*., Recent warming leads to a rapid borealization of fish communities in the Arctic. *Nat. Clim. Chang.* **5**, 673–677 (2015). doi: 10.1038/nclimate2647
92. B. Elmhagen, J. Kindberg, P. Hellström, A. Angerbjörn, A boreal invasion in response to climate change? Range shifts and community effects in the borderland between forest and tundra. *Ambio* **44** (suppl. 1), S39–S50 (2015). doi: 10.1007/s13280-014-0606-8; pmid: 25576279
93. B. G. Freeman, A. M. Class Freeman, Rapid upslope shifts in New Guinean birds illustrate strong distributional responses of tropical montane species to global warming. *Proc. Natl. Acad. Sci. U.S.A.* **111**, 4490–4494 (2014). doi: 10.1073/pnas.1318190111; pmid: 24550460
94. A. Wolf, N. B. Zimmerman, W. R. L. Anderegg, P. E. Busby, J. Christensen, Altitudinal shifts of the native and introduced flora of California in the context of 20th-century warming. *Glob. Ecol. Biogeogr.* **25**, 418–429 (2016). doi: 10.1111/geb.12423
95. I.-C. Chen *et al*., Elevation increases in moth assemblages over 42 years on a tropical mountain. *Proc. Natl. Acad. Sci. U.S.A.* **106**, 1479–1483 (2009). doi: 10.1073/pnas.0809320106; pmid: 19164573
96. I.-C. Chen, J. K. Hill, R. Ohlemüller, D. B. Roy, C. D. Thomas, Rapid range shifts of species associated with high levels of climate warming. *Science* **333**, 1024–1026 (2011). doi: 10.1126/science.1206432; pmid: 21852500
97. E. Kuhn, J. Lenoir, C. Piedallu, J.-C. Gégout, Early signs of range disjunction of sub-mountainous plant species: an unexplored consequence of future and contemporary climate changes. *Glob. Chang. Biol.* **22**, 2094–2105 (2016).
98. J. Savage, M. Vellend, Elevational shifts, biotic homogenization and time lags in vegetation change during 40 years of climate warming. *Ecography* **38**, 546–555 (2015). doi: 10.1111/ecog.01131
99. G. Forero-Medina, J. Terborgh, S. J. Socolar, S. L. Pimm, Elevational ranges of birds on a tropical montane gradient lag behind warming temperatures. *PLOS ONE* **6**, e28535 (2011). doi: 10.1371/journal.pone.0028535; pmid: 22163309
100. F. A. La Sorte, W. Jetz, Tracking of climatic niche boundaries under recent climate change. *J. Anim. Ecol.* **81**, 914–925 (2012). doi: 10.1111/j.1365-2656.2012.01958.x; pmid: 22372840
101. P. De Frenne *et al*., Microclimate moderates plant responses to macroclimate warming. *Proc. Natl. Acad. Sci. U.S.A.* **110**, 18561–18565 (2013). doi: 10.1073/pnas.1311190110; pmid: 24167287
102. B. R. Scheffers, D. P. Edwards, A. Diesmos, S. E. Williams, T. A. Evans, Microhabitats reduce animal's exposure to climate extremes. *Glob. Change Biol.* **20**, 495–503 (2014). doi: 10.1111/gcb.12439; pmid: 24132984
103. C. M. McCain, R. K. Colwell, Assessing the threat to montane biodiversity from discordant shifts in temperature and precipitation in a changing climate. *Ecol. Lett.* **14**, 1236–1245 (2011). doi: 10.1111/j.1461-0248.2011.01695.x; pmid: 21981631
104. S. M. Crimmins, S. Z. Dobrowski, J. A. Greenberg, J. T. Abatzoglou, A. R. Mynsberge, Changes in climatic water balance drive downhill shifts in plant species' optimum elevations. *Science* **331**, 324–327 (2011). doi: 10.1126/science.1199040; pmid: 21252344
105. J. E. Jankowski, S. K. Robinson, D. J. Levey, Squeezed at the top: Interspecific aggression may constrain elevational ranges in tropical birds. *Ecology* **91**, 1877–1884 (2010). doi: 10.1890/09-2063.1; pmid: 20715605
106. J. G. Molinos *et al*., Climate velocity and the future global redistribution of marine biodiversity. *Nat. Clim. Chang.* 10.1038/nclimate2769 (2015). doi: 10.1038/nclimate2769
107. E. Cahill *et al*., How does climate change cause extinction? *Proc. R. Soc. B Biol. Sci.* (2012). doi: 10.1098/rspb.2012.1890
108. N. Ockendon *et al*., Mechanisms underpinning climatic impacts on natural populations: Altered species interactions are more important than direct effects. *Glob. Change Biol.* **20**, 2221–2229 (2014). doi: 10.1111/gcb.12559; pmid: 24677405
109. M. W. Tingley, S. R. Beissinger, Cryptic loss of montane avian richness and high community turnover over 100 years. *Ecology* **94**, 598–609 (2013). doi: 10.1890/12-0928.1; pmid: 23687886
110. V. Sgardeli, K. Zografou, J. M. Halley, Climate Change versus Ecological Drift: Assessing 13 years of turnover in a butterfly community. *Basic Appl. Ecol.* **17**, 283–290 (2016). doi: 10.1016/j.baae.2015.12.008
111. T. Wittwer, R. B. O'Hara, P. Caplat, T. Hickler, H. G. Smith, Long-term population dynamics of a migrant bird suggests interaction of climate change and competition with resident species. *Oikos* **124**, 1151–1159 (2015). doi: 10.1111/oik.01559
112. S. Bennett, T. Wernberg, E. S. Harvey, J. Santana-Garcon, B. J. Saunders, Tropical herbivores provide resilience to a climate-mediated phase shift on temperate reefs. *Ecol. Lett.* **18**, 714–723 (2015). doi: 10.1111/ele.12450; pmid: 25994785
113. C. Parmesan *et al*., Beyond climate change attribution in conservation and ecological research. *Ecol. Lett.* **16** (suppl. 1), 58–71 (2013). doi: 10.1111/ele.12098; pmid: 23679010
114. A. Millon *et al*., Dampening prey cycle overrides the impact of climate change on predator population dynamics: A long-term demographic study on tawny owls. *Glob. Change Biol.* **20**, 1770–1781 (2014). doi: 10.1111/gcb.12546; pmid: 24634279
115. J. R. Thienpont *et al*., Recent climate warming favours more specialized cladoceran taxa in western Canadian Arctic lakes. *J. Biogeogr.* **42**, 1553–1565 (2015). doi: 10.1111/jbi.12519
116. T. Jonsson, M. Setzer, A freshwater predator hit twice by the effects of warming across trophic levels. *Nat. Commun.* **6**, 5992 (2015). doi: 10.1038/ncomms6992; pmid: 25586020
117. M. Steinacher *et al*., Projected 21st century decrease in marine productivity: A multi-model analysis. *Biogeosciences* **7**, 979–1005 (2010). doi: 10.5194/bg-7-979-2010
118. F. Hofhansl, J. Kobler, S. Drage, E. Pölz, W. Wanek, Sensitivity of tropical lowland net primary production to climate anomalies. *EGU Gen. Assem. Conf. Abstr.* **16**, 10585 (2014).
119. G. C. Hays, A. J. Richardson, C. Robinson, Climate change and marine plankton. *Trends Ecol. Evol.* **20**, 337–344 (2005). doi: 10.1016/j.tree.2005.03.004; pmid: 16701390
120. D. G. Boyce, M. R. Lewis, B. Worm, Global phytoplankton decline over the past century. *Nature* **466**, 591–596 (2010). doi: 10.1038/nature09268; pmid: 20671703
121. M. Montes-Hugo *et al*., Recent changes in phytoplankton communities associated with rapid regional climate change along the western Antarctic Peninsula. *Science* **323**, 1470–1473 (2009). doi: 10.1126/science.1164533; pmid: 19286554
122. C. M. O'Reilly, S. R. Alin, P. D. Plisnier, A. S. Cohen, B. A. McKee, Climate change decreases aquatic ecosystem productivity of Lake Tanganyika, Africa. *Nature* **424**, 766–768 (2003). doi: 10.1038/nature01833; pmid: 12917682
123. H. Sarmento, A. M. Amado, J.-P. Descy, Climate change in tropical fresh waters (comment on the paper Plankton dynamics under different climatic conditions in space and time by de Senerpont Domis *et al.*, 2013). *Freshw. Biol.* **58**, 2208–2210 (2013). doi: 10.1111/fwb.12140
124. B. Moss *et al*., Allied attack: Climate change and eutrophication. *Inland Waters* **1**, 101–105 (2011). doi: 10.5268/IW-1.2.359
125. R. R. Nemani *et al*., Climate-driven increases in global terrestrial net primary production from 1982 to 1999. *Science* **300**, 1560–1563 (2003). doi: 10.1126/science.1082750; pmid: 12791990
126. A. Bastos, S. W. Running, C. Gouveia, R. M. Trigo, The global NPP dependence on ENSO: La Niña and the extraordinary year of 2011. *J. Geophys. Res. Biogeosci.* **118**, 1247–1255 (2013). doi: 10.1002/jgrg.20100
127. S. Saatchi *et al*., Persistent effects of a severe drought on Amazonian forest canopy. *Proc. Natl. Acad. Sci. U.S.A.*

110, 565–570 (2013). doi: 10.1073/pnas.1204651110; pmid: 23267086
128. L. Zhou *et al*., Widespread decline of Congo rainforest greenness in the past decade. *Nature* **509**, 86–90 (2014). doi: 10.1038/nature13265; pmid: 24759324
129. R. J. W. Brienen *et al*., Long-term decline of the Amazon carbon sink. *Nature* **519**, 344–348 (2015). doi: 10.1038/nature14283; pmid: 25788097
130. N. A. J. Graham, S. Jennings, M. A. MacNeil, D. Mouillot, S. K. Wilson, Predicting climate-driven regime shifts versus rebound potential in coral reefs. *Nature* **518**, 94–97 (2015). doi: 10.1038/nature14140; pmid: 25607371
131. S. D. Ling, C. R. Johnson, S. D. Frusher, K. R. Ridgway, Overfishing reduces resilience of kelp beds to climate-driven catastrophic phase shift. *Proc. Natl. Acad. Sci. U.S.A.* **106**, 22341–22345 (2009). doi: 10.1073/pnas.0907529106; pmid: 20018706
132. T. Wernberg *et al*., Climate-driven regime shift of a temperate marine ecosystem. *Science* **353**, 169–172 (2016). doi: 10.1126/science.aad8745; pmid: 27387951
133. P. S. A. Beck *et al*., Changes in forest productivity across Alaska consistent with biome shift. *Ecol. Lett.* **14**, 373–379 (2011). doi: 10.1111/j.1461-0248.2011.01598.x; pmid: 21332901
134. J. Gao, B. Barzel, A.-L. Barabási, Universal resilience patterns in complex networks. *Nature* **530**, 307–312 (2016). doi: 10.1038/nature16948; pmid: 26887493
135. FAO, *The State of World Fisheries and Aquaculture* (Rome, 2014).
136. P. Wassmann, C. M. Duarte, S. Agusti, M. K. Sejr, Footprints of climate change in the Arctic marine ecosystem. *Glob. Change Biol.* **17**, 1235–1249 (2011). doi: 10.1111/j.1365-2486.2010.02311.x
137. A. B. Hollowed, B. Planque, H. Loeng, Potential movement of fish and shellfish stocks from the sub-Arctic to the Arctic Ocean. *Fish. Oceanogr.* **22**, 355–370 (2013). doi: 10.1111/fog.12027
138. M. M. McBride *et al*., Krill, climate, and contrasting future scenarios for Arctic and Antarctic fisheries. *ICES J. Mar. Sci. J. du Cons.* **71**, 1932–1933 (2014). doi: 10.1093/icesjms/fsu002
139. M. J. Genner *et al*., Body size-dependent responses of a marine fish assemblage to climate change and fishing over a century-long scale. *Glob. Change Biol.* **16**, 517–527 (2010). doi: 10.1111/j.1365-2486.2009.02027.x
140. A. R. Baudron, C. L. Needle, A. D. Rijnsdorp, C. T. Marshall, Warming temperatures and smaller body sizes: Synchronous changes in growth of North Sea fishes. *Glob. Change Biol.* **20**, 1023–1031 (2014). doi: 10.1111/gcb.12514; pmid: 24375891
141. M. Daufresne, K. Lengfellner, U. Sommer, Global warming benefits the small in aquatic ecosystems. *Proc. Natl. Acad. Sci. U.S.A.* **106**, 12788–12793 (2009). doi: 10.1073/pnas.0902080106; pmid: 19620720
142. E. Jeppesen *et al*., Impacts of climate warming on the long-term dynamics of key fish species in 24 European lakes. *Hydrobiologia* **694**, 1–39 (2012). doi: 10.1007/s10750-012-1182-1
143. S. Peng *et al*., Rice yields decline with higher night temperature from global warming. *Proc. Natl. Acad. Sci. U.S.A.* **101**, 9971–9975 (2004). doi: 10.1073/pnas.0403720101; pmid: 15226500
144. J. R. Porter *et al*., in *Climate Change 2014: Impacts, Adaptation, and Vulnerability. Part A: Global and Sectoral Aspects. Contribution of Working Group II to the Fifth Assessment Report of the Intergovernmental Panel of Climate Change*, C. B. Field *et al*., Eds. (Cambridge Univ. Press, 2014), pp. 485–533.
145. C. W. Craparo, P. J. Van Asten, P. Läderach, L. T. P. Jassogne, S. W. Grab, Coffea arabica yields decline in Tanzania due to climate change: Global implications. *Agric. For. Meteorol.* **207**, 1–10 (2015). doi: 10.1016/j.agrformet.2015.03.005
146. D. B. Lobell, W. Schlenker, J. Costa-Roberts, Climate trends and global crop production since 1980. *Science* **333**, 616–620 (2011). doi: 10.1126/science.1204531; pmid: 21551030
147. J. A. Hamilton, J. M. Miller, Adaptive introgression as a resource for management and genetic conservation in a changing climate. *Conserv. Biol.* **30**, 33–41 (2016). doi: 10.1111/cobi.12574; pmid: 26096581
148. E. Nevo *et al*., Evolution of wild cereals during 28 years of global warming in Israel. *Proc. Natl. Acad. Sci. U.S.A.* **109**, 3412–3415 (2012). doi: 10.1073/pnas.1121411109; pmid: 22334646
149. P. Stratonovitch, M. A. Semenov, Heat tolerance around flowering in wheat identified as a key trait for increased yield potential in Europe under climate change. *J. Exp. Bot.* **66**, 3599–3609 (2015). doi: 10.1093/jxb/erv070; pmid: 25750425
150. S. N. Aitken, M. C. Whitlock, Assisted gene flow to facilitate local adaptation to climate change. *Annu. Rev. Ecol. Evol. Syst.* **44**, 367–388 (2013). doi: 10.1146/annurev-ecolsys-110512-135747
151. M. J. H. van Oppen, J. K. Oliver, H. M. Putnam, R. D. Gates, Building coral reef resilience through assisted evolution. *Proc. Natl. Acad. Sci. U.S.A.* **112**, 2307–2313 (2015). doi: 10.1073/pnas.1422301112; pmid: 25646461
152. B. Zheng, K. Chenu, S. C. Chapman, Velocity of temperature and flowering time in wheat—Assisting breeders to keep pace with climate change. *Glob. Change Biol.* **22**, 921–933 (2016). doi: 10.1111/gcb.13118; pmid: 26432666
153. E. Luedeling, J. Gebauer, A. Buerkert, Climate change effects on winter chill for tree crops with chilling requirements on the Arabian Peninsula. *Clim. Change* **96**, 219–237 (2009). doi: 10.1007/s10584-009-9581-7
154. J. X. Chaparro, W. B. Shermain, Peach tree named "UFBest" (2014); www.google.com/patents/USPP25129.
155. T. Sugiura, H. Sumida, S. Yokoyama, H. Ono, Overview of recent effects of global warming on agricultural production in Japan. *Jpn. Agric. Res. Q.* **46**, 7–13 (2012). doi: 10.6090/jarq.46.7
156. J. T. Kerr *et al*., Climate change impacts on bumblebees converge across continents. *Science* **349**, 177–180 (2015). pmid: 26160945
157. L. A. Burkle, J. C. Marlin, T. M. Knight, Plant-pollinator interactions over 120 years: Loss of species, co-occurrence, and function. *Science* **339**, 1611–1615 (2013). doi: 10.1126/science.1232728; pmid: 23449999
158. I. Bartomeus *et al*., Historical changes in northeastern US bee pollinators related to shared ecological traits. *Proc. Natl. Acad. Sci. U.S.A.* **110**, 4656–4660 (2013). doi: 10.1073/pnas.1218503110; pmid: 23487768
159. R. Rader, J. Reilly, I. Bartomeus, R. Winfree, Native bees buffer the negative impact of climate warming on honey bee pollination of watermelon crops. *Glob. Change Biol.* **19**, 3103–3110 (2013). doi: 10.1111/gcb.12264; pmid: 23704044
160. W. A. Kurz *et al*., Mountain pine beetle and forest carbon feedback to climate change. *Nature* **452**, 987–990 (2008). doi: 10.1038/nature06777; pmid: 18432244
161. W. R. L. Anderegg, J. M. Kane, L. D. L. Anderegg, Consequences of widespread tree mortality triggered by drought and temperature stress. *Nat. Clim. Chang.* **3**, 30–36 (2013). doi: 10.1038/nclimate1635
162. L. A. Bearup, R. M. Maxwell, D. W. Clow, J. E. Mccray, Hydrological effects of forest transpiration loss in bark beetle-impacted watersheds. *Nat. Clim. Chang.* **4**, 481–486 (2014). doi: 10.1038/nclimate2198
163. A. S. Weed, M. P. Ayres, J. A. Hicke, Consequences of climate change for biotic disturbances in North American forests. *Ecol. Monogr.* **83**, 441–470 (2013). doi: 10.1890/13-0160.1
164. D. P. Bebber, M. T. Ramotowski, S. J. Gurr, Crop pests and pathogens move polewards in a warming world. *Nat. Clim. Chang.* **3**, 985–988 (2013). doi: 10.1038/nclimate1990
165. S. Altizer, R. S. Ostfeld, P. T. J. Johnson, S. Kutz, C. D. Harvell, Climate change and infectious diseases: From evidence to a predictive framework. *Science* **341**, 514–519 (2013). pmid: 23908230
166. S. Paz, N. Bisharat, E. Paz, O. Kidar, D. Cohen, Climate change and the emergence of *Vibrio vulnificus* disease in Israel. *Environ. Res.* **103**, 390–396 (2007). doi: 10.1016/j.envres.2006.07.002; pmid: 16949069
167. C. Baker-Austin *et al*., Emerging Vibrio risk at high latitudes in response to ocean warming. *Nat. Clim. Chang.* **3**, 73–77 (2012). doi: 10.1038/nclimate1628
168. A. Egizi, N. H. Fefferman, D. M. Fonseca, Evidence that implicit assumptions of 'no evolution' of disease vectors in changing environments can be violated on a rapid timescale. *Philos. Trans. R. Soc. Lond. B Biol. Sci.* **370**, 20140136 (2015). doi: 10.1098/rstb.2014.0136; pmid: 25688024
169. T. Levi, F. Keesing, K. Oggenfuss, R. S. Ostfeld, Accelerated phenology of blacklegged ticks under climate warming. *Philos. Trans. R. Soc. London B Biol. Sci.* **370**, 20130556 (2015). pmid: 25688016
170. E. Mcleod *et al*., A blueprint for blue carbon: Toward an improved understanding of the role of vegetated coastal habitats in sequestering CO_2. *Front. Ecol. Environ* **9**, 552–560 (2011). doi: 10.1890/110004
171. R. A. Pielke Sr. *et al*., Land use/land cover changes and climate: Modeling analysis and observational evidence. *Wiley Interdiscip. Rev. Clim. Chang.* **2**, 828–850 (2011). doi: 10.1002/wcc.144
172. K. McKinnon, V. Hickey, Convenient solutions to an inconvenient truth: Ecosystem-based approaches to climate change. *Int. Bank Reconstr. Dev. World Bank*. **2** (2009).
173. F. Ferrario *et al*., The effectiveness of coral reefs for coastal hazard risk reduction and adaptation. *Nat. Commun.* **5**, 3794 (2014). doi: 10.1038/ncomms4794; pmid: 24825660
174. S. Temmerman *et al*., Ecosystem-based coastal defence in the face of global change. *Nature* **504**, 79–83 (2013). doi: 10.1038/nature12859; pmid: 24305151
175. C. J. A. Bradshaw, N. S. Sodhi, K. S. Peh, B. W. Brook, Global evidence that deforestation amplifies flood risk and severity in the developing world. *Glob. Change Biol.* **13**, 2379–2395 (2007). doi: 10.1111/j.1365-2486.2007.01446.x
176. S. L. Maxwell, O. Venter, K. R. Jones, J. E. M. Watson, Integrating human responses to climate change into conservation vulnerability assessments and adaptation planning. *Ann. N. Y. Acad. Sci.* **1355**, 98–116 (2015). doi: 10.1111/nyas.12952; pmid: 26555860
177. C. M. Sgrò, A. J. Lowe, A. A. Hoffmann, Building evolutionary resilience for conserving biodiversity under climate change. *Evol. Appl.* **4**, 326–337 (2011). doi: 10.1111/j.1752-4571.2010.00157.x; pmid: 25567976
178. D. G. Hole *et al*., Projected impacts of climate change on a continent-wide protected area network. *Ecol. Lett.* **12**, 420–431 (2009). doi: 10.1111/j.1461-0248.2009.01297.x; pmid: 19379136
179. B. E. Miner, L. De Meester, M. E. Pfrender, W. Lampert, N. G. Hairston Jr., Linking genes to communities and ecosystems: *Daphnia* as an ecogenomic model. *Proc. Biol. Sci.* **279**, 1873–1882 (2012). doi: 10.1098/rspb.2011.2404; pmid: 22298849
180. W. Van Doorslaer, R. Stoks, C. Duvivier, A. Bednarska, L. De Meester, Population dynamics determine genetic adaptation to temperature in *Daphnia*. *Evolution* **63**, 1867–1878 (2009). doi: 10.1111/j.1558-5646.2009.00679.x; pmid: 19473405
181. W. Van Doorslaer *et al*., Experimental thermal microevolution in community-embedded *Daphnia* populations. *Clim. Res.* **43**, 81–89 (2010). doi: 10.3354/cr00894
182. B. Zeis, D. Becker, P. Gerke, M. Koch, R. J. Paul, Hypoxia-inducible haemoglobins of *Daphnia pulex* and their role in the response to acute and chronic temperature increase. *Biochim. Biophys. Acta* **1834**, 1704–1710 (2013). doi: 10.1016/j.bbapap.2013.01.036; pmid: 23388388
183. R. J. Paul *et al*., Thermal acclimation in the microcrustacean *Daphnia*: A survey of behavioural, physiological and biochemical mechanisms. *J. Therm. Biol.* **29**, 655–662 (2004). doi: 10.1016/j.jtherbio.2004.08.035
184. W. van Doorslaer *et al*., Local adaptation to higher temperatures reduces immigration success of genotypes from a warmer region in the water flea *Daphnia*. *Glob. Change Biol.* **15**, 3046–3055 (2009). doi: 10.1111/j.1365-2486.2009.01980.x
185. D. Straile, R. Adrian, D. E. Schindler, Uniform temperature dependency in the phenology of a keystone herbivore in lakes of the Northern Hemisphere. *PLOS ONE* **7**, e45497 (2012). doi: 10.1371/journal.pone.0045497; pmid: 23071520
186. T. Blenckner *et al*., Large-scale climatic signatures in lakes across Europe: A meta-analysis. *Glob. Change Biol.* **13**, 1314–1326 (2007). doi: 10.1111/j.1365-2486.2007.01364.x
187. F. Altermatt, V. I. Pajunen, D. Ebert, Climate change affects colonization dynamics in a metacommunity of three *Daphnia* species. *Glob. Change Biol.* **14**, 1209–1220 (2008). doi: 10.1111/j.1365-2486.2008.01588.x
188. M. De Block, K. Pauwels, M. Van Den Broeck, L. De Meester, R. Stoks, Local genetic adaptation generates latitude-specific effects of warming on predator-prey interactions. *Glob. Change Biol.* **19**, 689–696 (2013). doi: 10.1111/gcb.12089; pmid: 23504827
189. S. R. Hall, A. J. Tessier, M. A. Duffy, M. Huebner, C. E. Cáceres, Warmer does not have to mean sicker: Temperature and predators can jointly drive timing of epidemics. *Ecology* **87**,

1684–1695 (2006). doi: 10.1890/0012-9658(2006)87[1684:WDNHTM]2.0.CO;2; pmid: 16922319

190. H. Feuchtmayr *et al.*, Differential effects of warming and nutrient loading on the timing and size of the spring zooplankton peak: An experimental approach with hypertrophic freshwater mesocosms. *J. Plankton Res.* **32**, 1715–1725 (2010). doi: 10.1093/plankt/fbq087

191. S. J. Franks, A. E. Weis, A change in climate causes rapid evolution of multiple life-history traits and their interactions in an annual plant. *J. Evol. Biol.* **21**, 1321–1334 (2008). doi: 10.1111/j.1420-9101.2008.01566.x; pmid: 18557796

ACKNOWLEDGMENTS

We thank the Intergovernmental Panel on Climate Change, Intergovernmental Platform on Biodiversity and Ecosystem Services, and the thousands of researchers that have studied biodiversity and ecosystem services and the impacts of climate change on Earth—many of whom we were not able to cite because of length restrictions of the journal. S. Greenspan, J. Greenspan, and E. Perry provided helpful discussion and feedback on this manuscript. S. Jones and M. Wood were instrumental in figure creation. L.D.M. acknowledges KU Leuven Research Fund PF/2010/07 and Future Earth core project BioGENESIS. We thank the International Union for Conservation of Nature Climate Change Specialist Group for collaborative discussions on climate change themes and impacts on conservation of species and ecosystems and three anonymous reviewers for constructive suggestions that improved our manuscript.

SUPPLEMENTARY MATERIALS

www.sciencemag.org/content/354/6313/aaf7671/suppl/DC1
Supplementary Text
Fig. S1
Table S1
References (*192*–*310*)

10.1126/science.aaf7671

RESEARCH ARTICLE SUMMARY

AMYLOIDOGENESIS

De novo design of a biologically active amyloid

Rodrigo Gallardo, Meine Ramakers, Frederik De Smet, Filip Claes, Ladan Khodaparast, Laleh Khodaparast, José R. Couceiro, Tobias Langenberg, Maxime Siemons, Sofie Nyström, Laurence J. Young, Romain F. Laine, Lydia Young, Enrico Radaelli, Iryna Benilova, Manoj Kumar, An Staes, Matyas Desager, Manu Beerens, Petra Vandervoort, Aernout Luttun, Kris Gevaert, Guy Bormans, Mieke Dewerchin, Johan Van Eldere, Peter Carmeliet, Greetje Vande Velde, Catherine Verfaillie, Clemens F. Kaminski, Bart De Strooper, Per Hammarström, K. Peter R. Nilsson, Louise Serpell, Joost Schymkowitz,* Frederic Rousseau*

INTRODUCTION: It has been shown that most proteins possess amyloidogenic segments. However, only about 30 human proteins are known to be involved in amyloid-associated pathologies, and it is still not clear what determines amyloid toxicity in these diseases. We investigated whether an endogenously expressed protein that contains sequences with known amyloidogenic segments, but is not known to aggregate either under normal or pathological conditions, can be induced to do so by seeding it with a peptide comprising the protein's own amyloidogenic fragment. We chose to target the protein vascular endothelial growth factor receptor 2 (VEGFR2) because it has well-characterized biological function and so could provide a model system with which to investigate the relationship between protein loss of function and amyloid toxicity in different cellular contexts.

RATIONALE: The capacity of the amyloid conformation of disease proteins to catalyze their own amyloid conversion demonstrates the sequence specificity of amyloid assembly. Because the core of amyloids consists of short amyloidogenic sequence fragments, we hypothesized that a short amyloidogenic protein sequence of VEGFR2, a protein normally not associated with protein aggregation, should be able to interact with and specifically induce the aggregation of VEGFR2, resulting in its functional knockdown. We used TANGO, an algorithm that predicts aggregation-prone sequences, to identify potential amyloidogenic fragments in VEGFR2. We synthesized these fragments as a tandem repeat in a peptide framework in which each unit is flanked by charged residues and coupled by a short peptide linker. The thinking behind this design was that the tandem repeats would promote the formation of diffusable soluble oligomeric aggregates, whereas the charged residues would kinetically stabilize these oligomers and reduce the rate of insoluble fibril formation.

RESULTS: By screening for loss of function, we identified one peptide, termed "vascin," that was highly potent at inhibiting VEGFR2. This sequence was derived from the translocation signaling sequence of VEGFR2. We found that vascin is an amyloidogenic peptide that readily forms small β-structured oligomers, ranging from dimers to nonamers, that slowly convert to amyloid fibrils. When added to cell culture medium, these oligomers are efficiently absorbed by the cell, where they interact with and promote the aggregation and partial degradation of nascent VEGFR2. Vascin aggregation does not induce the aggregation of known disease amyloids. Neither do vascin oligomers affect the function of the related EGF receptor or the surface translocation of other receptors. We found vascin only to be toxic to cells that are dependent on VEGFR2 function, suggesting that toxicity is due to loss of VEGFR2 function and not to vascin aggregation or vascin-induced VEGFR2 aggregation. Consistent with this, we found that vascin is active in vivo and could reduce tumor growth in a VEGFR2-sensitive subcutaneous B16 melanoma syngenic tumor model in mice but is not intrinsically toxic to other tissues.

CONCLUSION: We found that a short amyloidogenic protein fragment can induce the aggregation of a protein normally not associated with amyloidosis in a manner that recapitulates key biophysical and biochemical characteristics of natural amyloids. In addition, we found that amyloid toxicity is observed only in cells that both express VEGFR2 and are dependent on VEGFR2 activity for survival. Thus, rather than being generic, amyloid toxicity here appears to be both protein-specific and conditional on a requirement for VEGFR2 protein function. ■

ON OUR WEBSITE

Read the full article at http://dx.doi.org/10.1126/science.aah4949

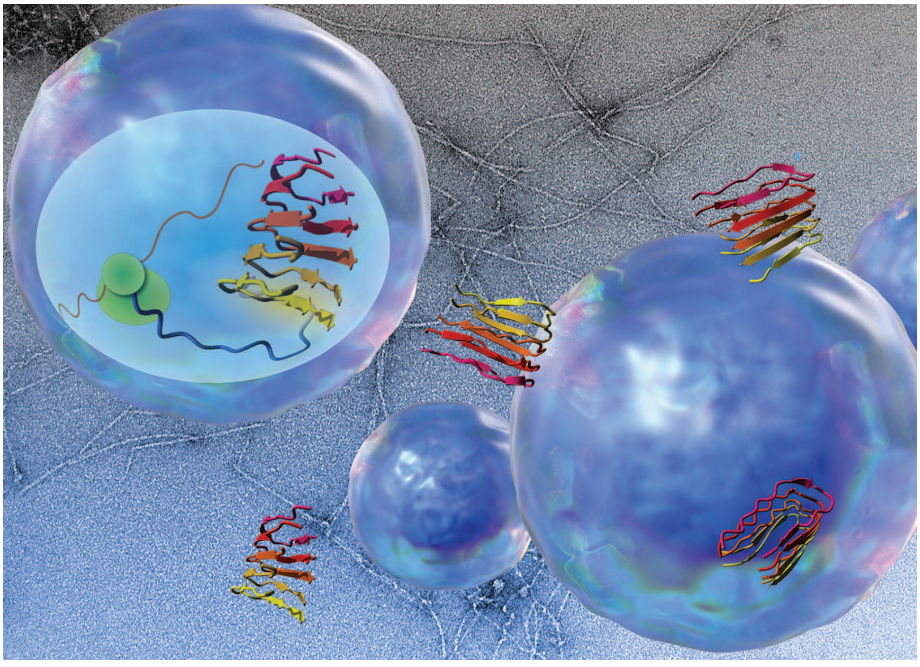

A synthetic amyloid peptide induces aggregation. We designed vascin, a synthetic amyloid peptide based on an amyloidogenic fragment of the signal peptide of VEGFR2. Vascin forms prefibrillar oligomers that penetrate mammalian cells and interacts with the nascent VEGFR2 protein, resulting in its aggregation and functional knockdown. [Composition includes parts of an image from iStock.com/luismmolina.]

The list of author affiliations is available in the full article online.
*Corresponding author. Email: frederic.rousseau@switch.vib-kuleuven.be (F.R.); joost.schymkowitz@switch.vib-kuleuven.be (J.S.)
Cite this article as R. Gallardo *et al.*, *Science* 354, aah4949 (2016). DOI: 10.1126/science.aah4949

RESEARCH ARTICLE

AMYLOIDOGENESIS

De novo design of a biologically active amyloid

Rodrigo Gallardo,[1,2] Meine Ramakers,[1,2] Frederik De Smet,[1,2] Filip Claes,[1,2] Ladan Khodaparast,[1,2,3] Laleh Khodaparast,[1,2,3] José R. Couceiro,[1,2] Tobias Langenberg,[1,2] Maxime Siemons,[1,2,4] Sofie Nyström,[5] Laurence J. Young,[6] Romain F. Laine,[6] Lydia Young,[7,8] Enrico Radaelli,[9,10] Iryna Benilova,[9,10] Manoj Kumar,[11] An Staes,[12,13] Matyas Desager,[1,2,4] Manu Beerens,[14] Petra Vandervoort,[14] Aernout Luttun,[14] Kris Gevaert,[12,13] Guy Bormans,[4] Mieke Dewerchin,[15,16] Johan Van Eldere,[3] Peter Carmeliet,[15,16] Greetje Vande Velde,[17] Catherine Verfaillie,[11] Clemens F. Kaminski,[6] Bart De Strooper,[9,10] Per Hammarström,[5] K. Peter R. Nilsson,[5] Louise Serpell,[18] Joost Schymkowitz,[1,2]* Frederic Rousseau[1,2]*

Most human proteins possess amyloidogenic segments, but only about 30 are associated with amyloid-associated pathologies, and it remains unclear what determines amyloid toxicity. We designed vascin, a synthetic amyloid peptide, based on an amyloidogenic fragment of vascular endothelial growth factor receptor 2 (VEGFR2), a protein that is not associated to amyloidosis. Vascin recapitulates key biophysical and biochemical characteristics of natural amyloids, penetrates cells, and seeds the aggregation of VEGFR2 through direct interaction. We found that amyloid toxicity is observed only in cells that both express VEGFR2 and are dependent on VEGFR2 activity for survival. Thus, amyloid toxicity here appears to be both protein-specific and conditional—determined by VEGFR2 loss of function in a biological context in which target protein function is essential.

Amyloid aggregation of proteins is driven by short amyloidogenic sequence segments within a protein chain (*1*, *2*) that have the potential to self-assemble into β-sheet ribbons to form the characteristic cross-β–structured spine of amyloid structures (*3*, *4*). It has been shown that most proteins do in fact possess such amyloidogenic sequence segments (*5*, *6*). Still, only about 30 human proteins are known to be involved in amyloid-associated diseases (*7*, *8*). Moreover, it is still not clear what determines amyloid toxicity in these diseases (*8*, *9*). We investigated whether an endogenously expressed protein that possesses amyloidogenic potential but aggregates under neither normal nor pathological conditions can be induced to do so by seeding with a peptide consisting of an amyloidogenic fragment of its own sequence. The use of amyloidogenic fragment peptides is motivated by the observation that aggregation of disease-associated amyloidogenic proteins can be seeded by such peptides in vitro (*10*, *11*) and that truncations of amyloid proteins have been associated with increased seeding potential in vivo (*12*, *13*). Moreover, it has been shown that amyloidogenic peptides and proteins are generally much more efficient at seeding aggregation of homotypic sequences (*14*–*16*), although examples of cross-seeding do exist (*17*–*19*). Seeding of protein aggregation in vitro appears to work universally and fits with the structural model of aggregation as the addition of new strands to a growing amyloid fibril (*8*). This imparts sequence specificity to the seeding process because the incorporation of nonhomologous sequences into the highly ordered in-register stacking of identical side chains in the fibril core is likely to be energetically disfavored (*13*, *20*, *21*). The seeding concept appears to hold true both in cell culture and in vivo, even for non–prion aggregation–associated peptides and proteins, which have since been called "prionoids" (*22*). As a target protein, we chose vascular endothelial growth factor receptor 2 (VEGFR2) because the function of this protein is well characterized. To ensure efficient seeding, we designed an amyloidogenic peptide termed "vascin," which consists of a tandem repeat of an amyloidogenic sequence segment in the VEGFR2 signal peptide.

We found that vascin is a bona fide amyloidogenic peptide that forms mature cross-β fibrils along with prefibrillar intermediates, including soluble oligomers and protofibrils. Moreover, we found that the peptide is able to enter cells and reach the cytoplasmic compartment and specifically induce the aggregation of endogenous VEGFR2, inhibiting its function in human umbilical vein endothelial cells (HUVECs) in vitro and reducing VEGFR2-dependent tumor progression in vivo.

It remains unclear what determines amyloid toxicity in amyloid diseases and whether cell death results from a consequence of direct amyloid toxicity (gain of function) or whether it is a consequence of loss of function (*23*, *24*). However, our detailed understanding of real amyloid disease models is often insufficient to address these questions directly. For many disease-associated amyloidogenic proteins—such as the β-amyloid (Aβ) peptide in Alzheimer's disease (*25*) and α-synuclein in Parkinson's disease (*26*)—we still have insufficient understanding both of their physiological role as well as the cellular interactions of the amyloid conformation in disease (*26*, *27*). We do, however, have a better understanding of the structural and biochemical characteristics that are common to most amyloid diseases. These features include the cross-β structural organization of the spine of the amyloid fibrils formed by short segments of the sequence; the population of prefibrillar intermediates, including soluble oligomers and protofibrils; and the capacity of amyloids to seed aggregation of the native conformation. Although our artificial amyloid model recapitulates these key structural and biochemical features of natural amyloids, it is also simple enough to investigate the relationship between protein loss of function and amyloid toxicity.

Our results show that vascin amyloids are not inherently toxic but that the emergence of amyloid toxicity is dependent on biological context. Vascin is not toxic to cells that do not express VEGFR2 or to cells expressing VEGFR2 but that are not dependent on VEGFR2 function. However, when introduced in VEGFR2-dependent cells, we found association of vascin amyloid toxicity and VEGFR2 loss of function. Therefore, our model system demonstrates that amyloidogenic protein fragments can induce aggregation of nonamyloidogenic proteins and that under these conditions, amyloid

[1]VIB Switch Laboratory, Leuven, Belgium. [2]Department for Cellular and Molecular Medicine, Katholieke Universiteit Leuven (KU Leuven), Belgium. [3]Laboratory of Clinical Bacteriology and Mycology, Department of Microbiology and Immunology, KU Leuven, Belgium. [4]Laboratory of Radiopharmacy, Department of Pharmaceutical and Pharmacological Sciences, KU Leuven, Belgium. [5]IFM Department of Chemistry, Linköping University, Linköping, Sweden. [6]Department of Chemical Engineering and Biotechnology, University of Cambridge, New Museums Site, Pembroke Street, Cambridge CB2 3RA, UK. [7]Astbury Centre for Structural Molecular Biology, University of Leeds, Leeds, UK. [8]School of Molecular and Cellular Biology, University of Leeds, Leeds, UK. [9]VIB Center for the Biology of Disease, 3000 Leuven, Belgium. [10]Center for Human Genetics and Leuven Institute for Neurodegenerative Diseases (LIND), KU Leuven, 3000 Leuven, Belgium. [11]Stem Cell Institute, KU Leuven, Leuven, Belgium. [12]VIB Medical Biotechnology Center, VIB, Ghent, Belgium. [13]Department of Biochemistry, Ghent University, Ghent, Belgium. [14]Department of Cardiovascular Sciences, Center for Molecular and Vascular Biology Research Unit, Endothelial Cell Biology Unit, KU Leuven, B-3000 Leuven, Belgium. [15]Laboratory of Angiogenesis and Vascular Metabolism, Department of Oncology, KU Leuven, B-3000 Leuven, Belgium. [16]Laboratory of Angiogenesis and Vascular Metabolism, Vesalius Research Center, VIB, Leuven B-3000, Belgium. [17]Biomedical MRI Unit/MoSAIC, Department of Imaging and Pathology, KU Leuven, Leuven, Belgium. [18]School of Life Sciences, University of Sussex, Falmer, East Sussex BN1 9QG, UK.
***Corresponding author. Email: frederic.rousseau@switch.vib-kuleuven.be (F.R.); joost.schymkowitz@switch.vib-kuleuven.be (J.S.)**

gain of function is a phenotypic effect resulting from cell-context–specific loss of function.

Results

Design of vascin, an amyloidogenic peptide derived from a VEGFR2 fragment

We analyzed the VEGFR2 proteins from mouse and human using the statistical thermodynamics algorithm TANGO (fig. S1A) (*28*). Because we envisaged testing the sequence ultimately in a mouse model, we opted for maximal compatibility with the mouse protein. Moreover, the two homologs share 84% sequence identity overall and 90% in the TANGO regions. To derive peptide sequences that are likely to form amyloid structure in isolation, but also have a high potential for forming soluble oligomers (*29*), we devised a strategy (*30*, *31*) that makes use of a sequence feature of functional amyloids and yeast prions, which often contain several aggregation-prone regions (APRs) (*32*) closely connected by disordered regions (*33*). Hence, we placed two APRs in a peptide, separated by a rigid proline-proline linker, mimicking these repeat patterns. In order to maintain colloidal stability and solubility of the sequence, we supercharged the peptides by flanking the APRs with either negatively charged aspartate or positively charged arginine residues. Given the length limitations imposed by the efficiency of solid-phase peptide synthesis, this design scheme imposes a length limitation on the APRs of seven amino acids. Hence, we selected 10 such high-scoring sequences (table S1) and generated the 38 peptide sequences listed in table S2, which explore both tandem repeats of the same APR as well as fusions of different APRs. Peptides were screened for their ability to inhibit VEGF signaling in human embryonic kidney (HEK) 293 cells transfected with mouse VEGFR2. To this end, cells were treated overnight with an apparent concentration of 20 μM peptide (assuming 100% synthesis efficiency), and extracellular signal–regulated kinase (ERK) phosphorylation was determined after stimulation for 5 min with 25 ng/mL VEGF (fig. S1B). At this concentration, we observed inhibition only with two peptides (B8 and B12). The effect was most pronounced with the peptide B8, which was based on a tandem repeat of the first high-scoring aggregation-prone region in the sequence that belongs to the signal peptide and has the sequence L_6AVALWF$_{12}$ (fig. S2A), resulting in the sequence DLAVALWFDPPDLAVALWFD [isoelectric point (pI) = 3.38, molecular weight (MW) = 2272.15 Da]. We termed this peptide vascin (fig. S2B), obtained additional material by means of solid-phase peptide synthesis followed by high-performance liquid chromatography purification (fig. S2C), and confirmed its identity with mass spectrometry (observed mass, 2272.4) (fig. S2D).

Vascin forms soluble β-structured oligomers that mature into amyloid fibrils

To determine the amyloidogenic nature of the peptide, vascin was dissolved to a final concentration of 300 μM in 1% (w/v) ammonium bicarbonate in ddH_2O. After 24 hours of incubation, transmission electron microscopy (TEM) revealed typical amyloid fibrils of ~10 nm in width consisting of protofilaments of 4 to 5 nm (Fig. 1, A to D, and fig. S3). Additionally, vascin fibrils bind amyloid sensor dyes, including thioflavin-T and the amyloid-specific oligothiophene h-HTAA (Fig. 1E) (*34*). X-ray diffraction of aligned bundles of vascin fibrils confirmed their cross-β nature, with characteristic diffractions at 4.7 and 10 Å (Fig. 1F). Together, these data confirm the amyloidogenic nature of vascin. In order to follow amyloid formation kinetics, we filtered 100 μM dissolved vascin 1% (w/v) ammonium bicarbonate in ddH_2O through a 0.2-μm regenerated cellulose filter and monitored particle size distribution using electrospray ionization–mass spectrometry linked to ion mobility spectrometry (ESI-IMS-MS) (Fig. 1G) (*35*) and dynamic light scattering (DLS) (Fig. 1H). At time zero, the MS resolved a mixture of monomers and multimers up to heptamers (Fig. 1G), whereas the particle sizes estimated through DLS ranged from 5 to 100 nm (assuming linear polymer particles). This indicates that the filtered vascin solution contains soluble oligomeric aggregates already at time zero. After 6 hours, particles reached sizes over 1 μm (Fig. 1H). The fact that no lag phase was observed in the evolution of the DLS autocorrelation function (fig. S4, A and B) further suggests that these soluble oligomers are able to directly proceed to amyloid fibril formation. In order to probe the secondary structure of these soluble aggregates, we monitored the same aggregation kinetics using Fourier transform infrared (FTIR) spectroscopy. The spectrum at time zero was dominated by maxima near 1630 and 1690 cm^{-1} (Fig. 1I), which is characteristic of β-sheet structure. Over the following 3 hours, the intensity of these peaks increased markedly, whereas the center of the peaks shifted gradually to 1622 and 1692 cm^{-1}, respectively (Fig. 1, I and J). These peaks were quite narrow, and regions outside the peaks showed very little absorption, suggesting that most of the peptide sequence is involved in β-structured hydrogen bonding. FTIR kinetics therefore indicate that vascin largely adopts a β-structured conformation upon solubilization in 1% ammonium bicarbonate and that these species mature into amyloid fibrils over time. Last, we measured binding to 8-anilino-1-naphthalenesulphonic acid (ANS) during vascin amyloid formation (fig. S4C), revealing high binding of this dye at time zero. The latter is a typical feature of interaction-prone cytotoxic prefibrillar oligomers that present a high degree of solvent-exposed hydrophobic surface (*36*). The binding of ANS increased over time, suggesting that hydrophobic surfaces stay exposed upon fibril formation. We also verified the amyloidotypic double peak fluorescence spectrum of vascin with the luminescent conjugated oligothiophene hHTAA in contrast to the scrambled peptide (fig. S4D). Given that the above observations were made at 300 μM peptide, in which the signal-to-noise ratio for biophysical characterization is optimal, we also verified that vascin readily formed amyloid fibrils at the lower concentration of 30 μM (fig. S5). Compared with vascin, a scrambled version of the peptide (supplementary text, note S1) formed small soluble aggregates with hydrodynamic radii smaller than 100 nm, as estimated by means of DLS (fig. S6 A and B), that exhibited a nonfibrillar morphology via TEM (fig. S6C) and displayed marginal affinity for the amyloid sensor dyes, with no specific emission spectrum for amyloid fibers (Fig. 1E and fig. S4D). Similar observations were made with a vascin variant in which proline mutations were introduced to break the β-sheet propensity of the APRs in vascin (supplementary text, note S2, and fig. S7). In contrast, a version of vascin based on the human sequence (h. vascin, DLAVALWLDPPDLAVALWLD), containing a single mutation of phenylalanine to leucine at position 7 of the APR, displayed similar amyloid formation as that of the original mouse sequence (fig. S8).

The biophysical characterization above confirms that vascin is an amyloidogenic peptide that readily forms β-structured soluble oligomeric aggregates that mature into cross-β–structured amyloid fibrils in a broad concentration range.

Vascin inactivates VEGFR2 in HUVECs by specifically inducing its aggregation

Because vascin is an amyloidogenic peptide derived from a VEGFR2 fragment, we investigated whether it displays biological activity toward VEGFR2 in cultured cells. First, we monitored cellular uptake of vascin using carboxyfluorescein-labeled vascin (CF-vascin) in HUVECs. We observed cellular uptake during the first hour of incubation as small vesicles or inclusions that contained diffuse homogeneous peptide (Fig. 2A). Moreover, these inclusions were positive for the amyloid sensor dye pFTAA (Fig. 2, B and C), showing that the peptide remains in an amyloid-like conformation inside the cells. Co-staining for the endoplasmic reticulum (ER) protein calnexin revealed that the peptides are on the cytoplasmic side of the ER (Fig. 2D), where they partially overlap with staining for ribosomes (Fig. 2E). Proximity ligation (Duo-Link) by using antibodies against VEGFR2 and the carboxyfluorescein label on vascin (Fig. 2F), quantified by use of image analysis from high-content microscopy, demonstrated direct interaction between vascin and VEGFR2 (Fig. 2G). This result was further confirmed with two-color direct stochastic optical reconstruction microscopy (*d*STORM) super-resolution imaging (*37*) by using 0.5 μM of Alexa647-labeled vascin and Alexa568-labeled immunodetection of VEGFR2 (Fig. 2, H and I).

Coimmunoprecipitation of VEGFR2 from lysates of vascin-treated HUVECs was performed with polyethylene glycol (PEG)–biotin–labeled peptide, again demonstrating direct interaction between vascin and VEGFR2 (Fig. 3A). To investigate the consequences of the interaction between vascin and VEGFR2 on the aggregation status of the receptor, we determined the difference in distribution of VEGFR2 between soluble and insoluble fractions of lysates from HUVECs treated with 20 μM vascin. Upon vascin treatment, we could observe a clear redistribution of full-length and partially degraded VEGFR2 toward the insoluble

fraction, whereas this was not the case upon treatment with scrambled vascin (Fig. 3B). In addition, the induced insoluble VEGFR2 displays partial resistance to the ionic detergent SDS, a hallmark of amyloid-like aggregation (Fig. 3C). To confirm that vascin-mediated aggregation of VEGFR2 in HUVECs leads to its loss of function, we determined the dose-response curve of vascin on VEGFR2 autophosphorylation and ERK phosphorylation [mesoscale discovery enzyme-linked immunosorbent assay (MSD ELISA)] after stimulating HUVECs for 5 min with 1.3 nM VEGF. HUVECs displayed a clear dose-responsive inhibition by vascin with a median inhibitory concentration (IC_{50}) of 6.8 ± 0.5 μM for receptor autophosphorylation and 8.3 ± 0.4 μM for ERK phosphorylation (Fig. 3, D and E). The human version of vascin showed similar inhibition, which was not observed when using the scrambled or proline controls (Fig. 3F). Using fluorescence-activated cell sorting (FACS), we observed a concomitant reduction in the surface expression of VEGFR2 in HUVECs, but not of the unrelated cell-surface protein CD29 (Fig. 3G and fig. S9), confirming loss of VEGFR2 function in HUVECs. Together, these data show that vascin is internalized by HUVECs and reaches the cytoplasmic compartment, where it directly binds to VEGFR2 and localizes with ribosomes, resulting in the functional inactivation through aggregation of VEGFR2. This effect seemed to be specific, as

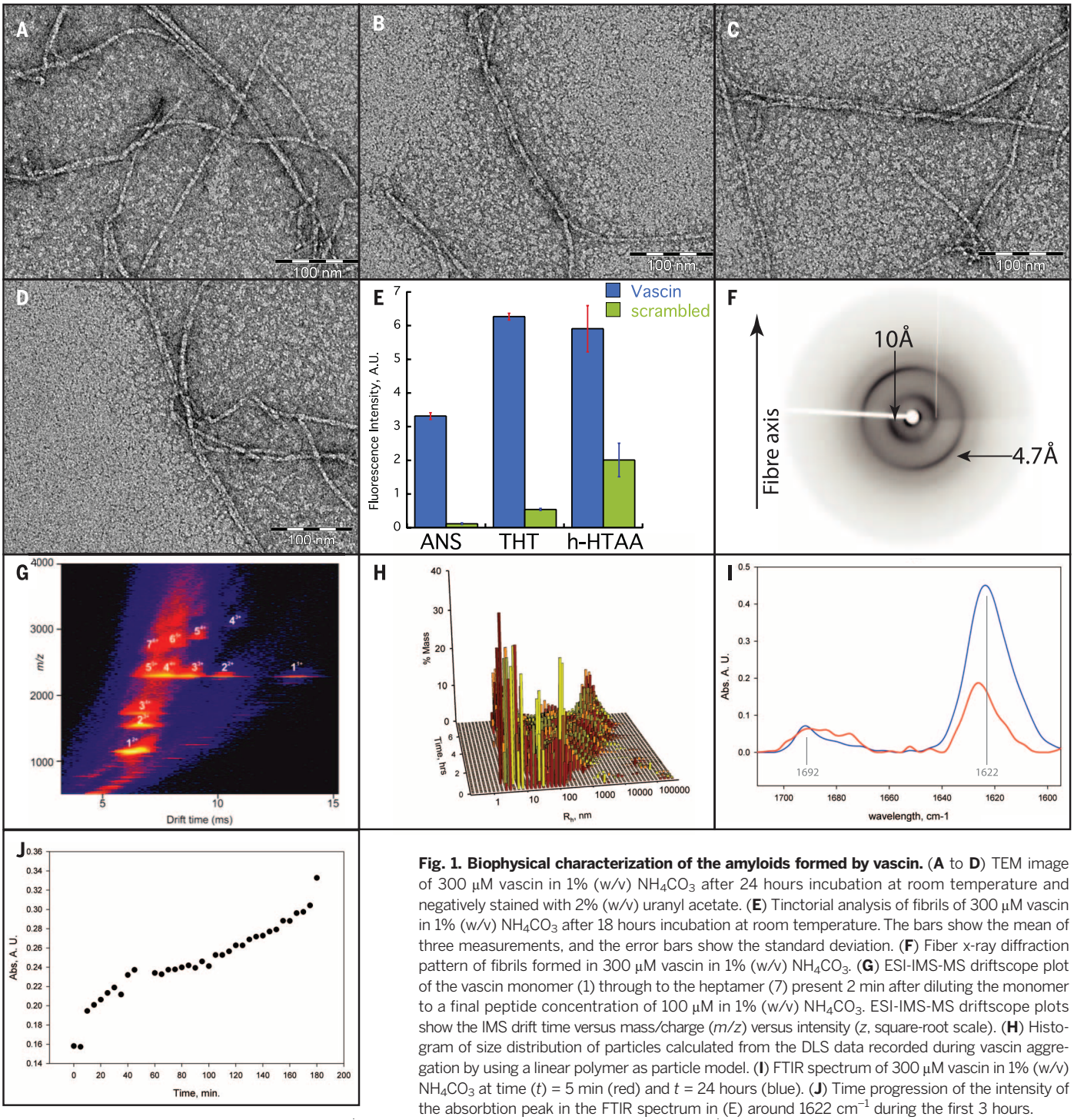

Fig. 1. Biophysical characterization of the amyloids formed by vascin. (**A** to **D**) TEM image of 300 μM vascin in 1% (w/v) NH_4CO_3 after 24 hours incubation at room temperature and negatively stained with 2% (w/v) uranyl acetate. (**E**) Tinctorial analysis of fibrils of 300 μM vascin in 1% (w/v) NH_4CO_3 after 18 hours incubation at room temperature. The bars show the mean of three measurements, and the error bars show the standard deviation. (**F**) Fiber x-ray diffraction pattern of fibrils formed in 300 μM vascin in 1% (w/v) NH_4CO_3. (**G**) ESI-IMS-MS driftscope plot of the vascin monomer (1) through to the heptamer (7) present 2 min after diluting the monomer to a final peptide concentration of 100 μM in 1% (w/v) NH_4CO_3. ESI-IMS-MS driftscope plots show the IMS drift time versus mass/charge (*m/z*) versus intensity (*z*, square-root scale). (**H**) Histogram of size distribution of particles calculated from the DLS data recorded during vascin aggregation by using a linear polymer as particle model. (**I**) FTIR spectrum of 300 μM vascin in 1% (w/v) NH_4CO_3 at time (*t*) = 5 min (red) and *t* = 24 hours (blue). (**J**) Time progression of the intensity of the absorbtion peak in the FTIR spectrum in (E) around 1622 cm^{-1} during the first 3 hours.

indicated by the CD29 result. Moreover, we observed no effect of vascin on EGF signaling in HeLa cells, which do not endogenously express VEGFR2 but the functionally homologous EGFR. Treatment of this cell line with 20 μM vascin showed no inhibition of ERK phosphorylation when stimulated with EGF (Fig. 3H), showing that the inhibitory effect of vascin on ERK phosphorylation is specific for VEGFR2 stimulation. To test whether known amyloidogenic proteins were affected by vascin, we investigated the effect of adding vascin to solutions of the Alzheimer β-peptide 1-42 (Aβ) (Fig. 3I) or the human prion protein (PrP) (Fig. 3J) and monitored aggregation through ThT fluorescence emission. The mean lag time for unseeded aggregation of Aβ1-40 was 350 min, whereas addition of preformed Aβ fibrils decreased the lag time to 130 min. Addition of vascin fibril variants did not lead to significant decrease of fibrillation lag times other than for scrambled vascin, where the significance level in a paired t test was $P > 0.03$. The mean lag time for spontaneous conversion of HuPrP23-231 was 1100 min. The conversion rate upon addition of preformed HuPrP90-231 fibrils was shortened to 135 min, whereas addition of preformed vascin fibril variants did not lead to significant alteration of lag time. These data demonstrate that no vascin cross-seeding occurs for these proteins.

Vascin reduces VEGFR2-dependent tumor growth in mice

To establish the effect of vascin in vivo, we turned to a functional angiogenesis model that is sensitive to inhibition of VEGFR2 in vivo and used a subcutaneous B16 melanoma syngenic tumor model in C57BL/6 inbred mice. Tumor growth of this line is strongly reduced by VEGFR2-specific inhibition approaches, such as the tyrosine kinase inhibitor protein tyrosine kinase (PTK) 787/ZK 222584 (*38*), providing a sensitive phenotypic

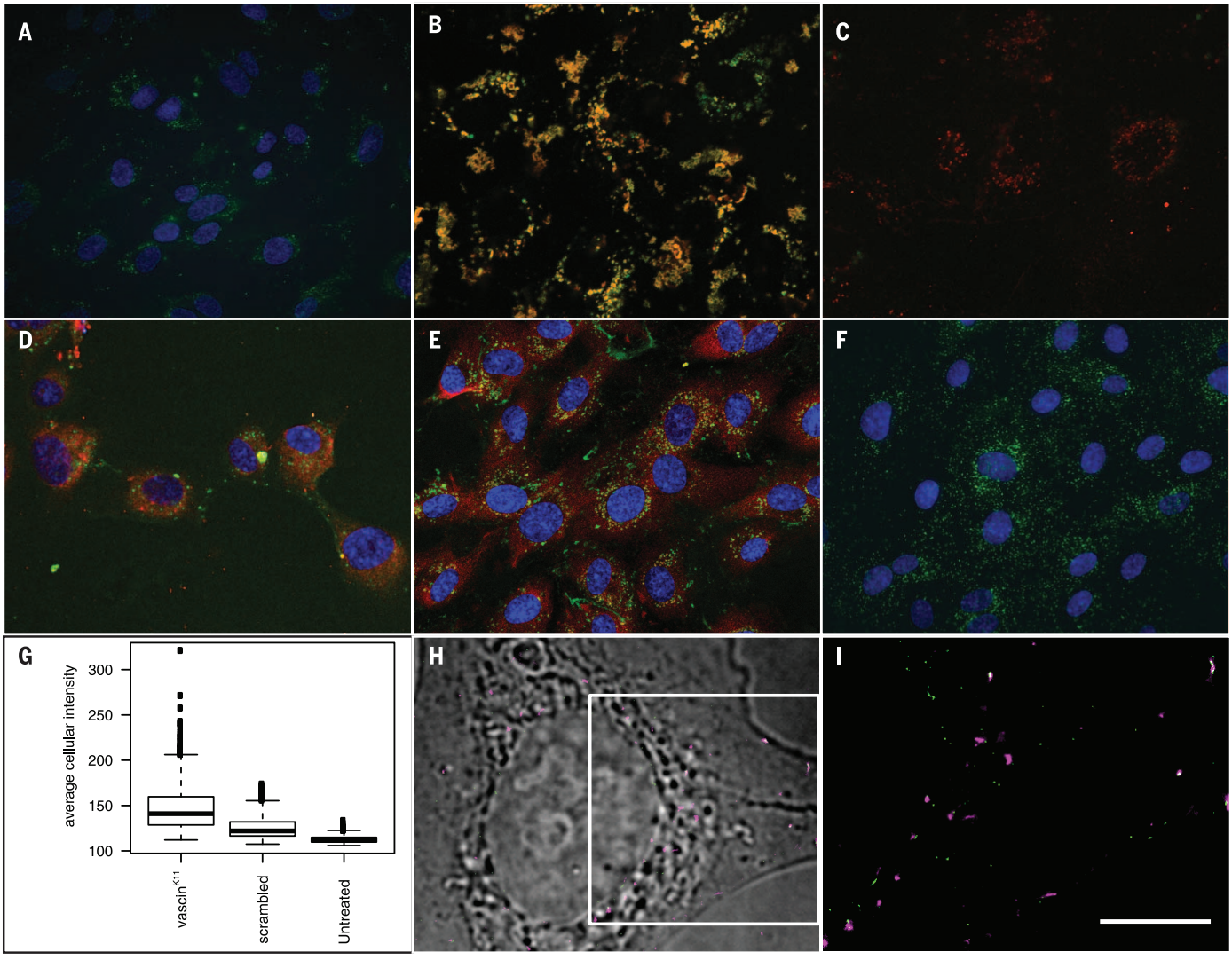

Fig. 2. Vascin directly interacts with VEGFR2 in cells. (**A**) Cellular distribution of CF-vascin^{K11} (green) at 1 μM in HUVECs. (**B**) Overlay between the fluorescence of Alexa647-labeled vascin^{K11} (20 μM, red) and the amyloid-specific dye pFTAA (15 μM, green). Overlap is shown as yellow coloring. (**C**) Equivalent image as (B) for the proline mutant of vascin. (**D**) HUVECs treated for 4 hours with CF-vascin^{K11} (2.5 μM, green) and co-immunostained for the ER-specific marker calnexin (red). (**E**) HUVECs treated for 4 hours with CF-vascin^{K11} (5.0 μM, green) and co-immunostained for the ribosomal protein S6 (red). (**F**) Proximity ligation (Duo-Link) between CF-vascin^{K11} at 5.0 μM and VEGFR2 performed in HUVECs treated for 4 hours with peptide. For (A), (D), (E), and (F), the nuclei are stained with 4′,6-diamidino-2-phenylindole in blue. (**G**) Quantification of the Duo-Link signal by high-content microscopy of HUVECs treated with vascin as depicted in (E). For each condition, ~700 cells were analyzed, and the average fluorescence intensity per cell is shown. The box shows the interquartile range of the 25 to 75 percentile. The line in the middle of the box indicates the median, and the lines extending from the box indicate the 99% limits of the distribution. Outliers are shown as squares. (**H**) dSTORM image of HUVECs treated for 4 hours with 0.5 μM Alexa647-labeled vascin^{K11} (purple) and co-immunostained for VEGFR2 (green). Scale bar, 1 μm. (**I**) Magnification of image in (G). White pixels indicate the interaction of vascin and VEGFR2. Scale bar, 1 μm.

readout for the anticipated effect of vascin. To assess whether vascin administration would be tolerated by C57BL/6 mice, we first performed a dose-escalation study by means of daily intravenous tail vein injection in two 6-week-old, inbred C57BL/6 mice, starting from 1 to 10 mg/kg PEG-biotin vascin, which corresponded to the highest stock concentration of the peptide that we could reach with the available material. No adverse effects to

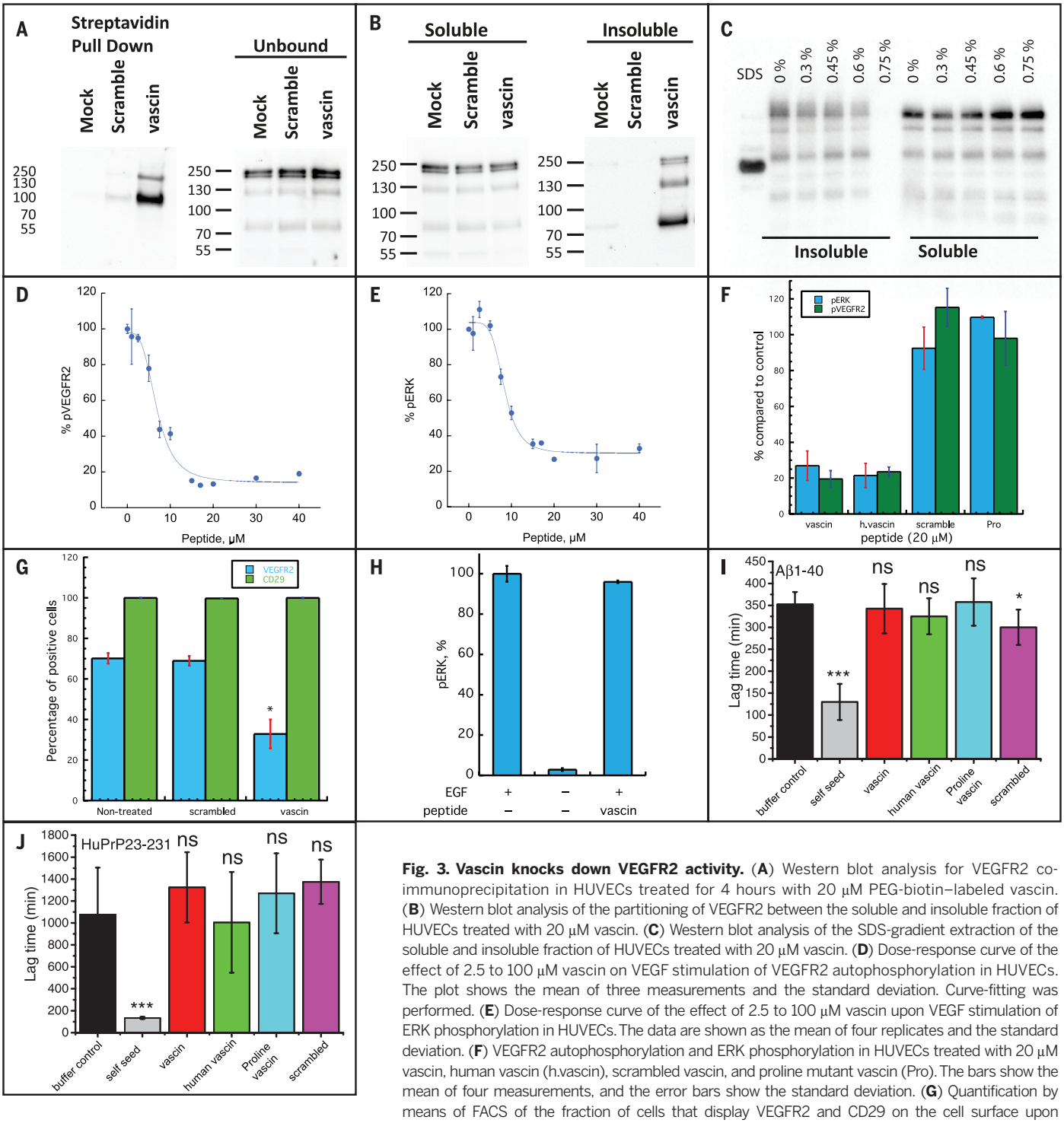

Fig. 3. Vascin knocks down VEGFR2 activity. (**A**) Western blot analysis for VEGFR2 co-immunoprecipitation in HUVECs treated for 4 hours with 20 µM PEG-biotin–labeled vascin. (**B**) Western blot analysis of the partitioning of VEGFR2 between the soluble and insoluble fraction of HUVECs treated with 20 µM vascin. (**C**) Western blot analysis of the SDS-gradient extraction of the soluble and insoluble fraction of HUVECs treated with 20 µM vascin. (**D**) Dose-response curve of the effect of 2.5 to 100 µM vascin on VEGF stimulation of VEGFR2 autophosphorylation in HUVECs. The plot shows the mean of three measurements and the standard deviation. Curve-fitting was performed. (**E**) Dose-response curve of the effect of 2.5 to 100 µM vascin upon VEGF stimulation of ERK phosphorylation in HUVECs. The data are shown as the mean of four replicates and the standard deviation. (**F**) VEGFR2 autophosphorylation and ERK phosphorylation in HUVECs treated with 20 µM vascin, human vascin (h.vascin), scrambled vascin, and proline mutant vascin (Pro). The bars show the mean of four measurements, and the error bars show the standard deviation. (**G**) Quantification by means of FACS of the fraction of cells that display VEGFR2 and CD29 on the cell surface upon treatment with vascin or scrambled vascin at 20 µM. Per condition, 10,000 cells were analyzed. The bars show the mean of three measurements, and the error bars show the standard deviation. *$P < 0.05$ calculated by Student's t test compared with the nontreated condition. (**H**) Quantification of ERK phosphorylation level as determined by means of MSD assay upon EGF stimulation of HeLa cells treated with 20 µM vascin. The data are shown as the mean of four replicates and the standard deviation. (**I**) Lag phase of the aggregation kinetics of the Alzheimer β-peptide 1-40 (Aβ1-40) observed with Thioflavin T fluorescence in the presence of 1% molar fraction of homotypic seeds (self seed), or the equivalent amount of seeds of vascin, human vascin, scrambled vascin, or the proline mutant vascin. (**J**) Equivalent experiment to (I) for the human prion protein (HuPrP23-231). All aggregation kinetics experiments were run in six replicates, and the bars show the mean value, with error bars showing the standard deviation. The statistically significant differences were identified using the Student's t test.

the basic physiological and behavioral parameters of the animals were apparent across this concentration range, including body weight, food and water consumption, home cage activity, and locomotion. To test the effect of vascin on tumor growth, B16 cells were injected subcutaneously in the right dorsal flank of 8-week-old C57BL/6 mice. Starting from 3 days after tumor injection and until day 17, mice were treated daily by means of intravenous injection of 10 mg/kg PEG-biotin vascin (n = 10 mice) or scrambled vascin as the negative control (n = 10 mice). Another negative control group received intravenous injection of the vehicle (50 mM Tris HCl pH 7.5, n = 10 mice), and the positive control group (n = 5 mice) received the kinase inhibitor PTK787 orally (75mg/kg). Tumor growth was similar in animals treated with scrambled vascin or vehicle and markedly reduced in animals that received the PTK inhibitor. In the vascin-treated group, tumor growth was significantly inhibited compared with that in the negative controls over the entire experiment [analysis of variance (ANOVA) with Tukey post-hoc] and up to day 14 to a similar extent as the PTK-treated group (Fig. 4A).

In order to exclude overall toxicity effects of vascin on the general physiology of the mouse, we executed a short-term toxicology study in which we treated groups of five mice daily with intravenous injections of vascin (10 mg/kg, group A), scrambled (10 mg/kg, group B), or vehicle (50 mM Tris pH 7.5) for 14 days (the same duration as that of the tumor growth experiment). Gross examination at necropsy did not reveal any macroscopic changes (fig. S10A). Concerning organ weights (fig. S10B), hematology (fig. S10C), and clinical chemistry (fig. S10D), no statistically significant differences were observed among groups. Also, no significant variations were observed among the experimental groups in terms of lesion spectrum, frequency, and severity. In addition, we examined brain sections from all the animals for amyloid deposition and associated astrogliosis. Thioflavin-S–positive deposits in the brain parenchyma were not detected (fig. S11, A, B, and C), and co-staining with GFAP (glial fibrillary acidic protein) did not show any morphological evidence of astrogliosis, in sharp contrast to the positive control (fig. S11D), for which we used a transgenic Alzheimer's disease mouse model that has marked amyloid deposition throughout the cortex and hippocampus (*39*).

In order to demonstrate the arrival and presence of vascin at the tumor site, two groups of tumor-bearing mice were injected intravenously with 10 mg/kg CF-vascin or vehicle (50 mM Tris HCl pH 7.5, negative control) and imaged with whole-body fluorescence imaging. Because the melanin expression by the tumors strongly absorbs light, which hampers the in vivo detection of

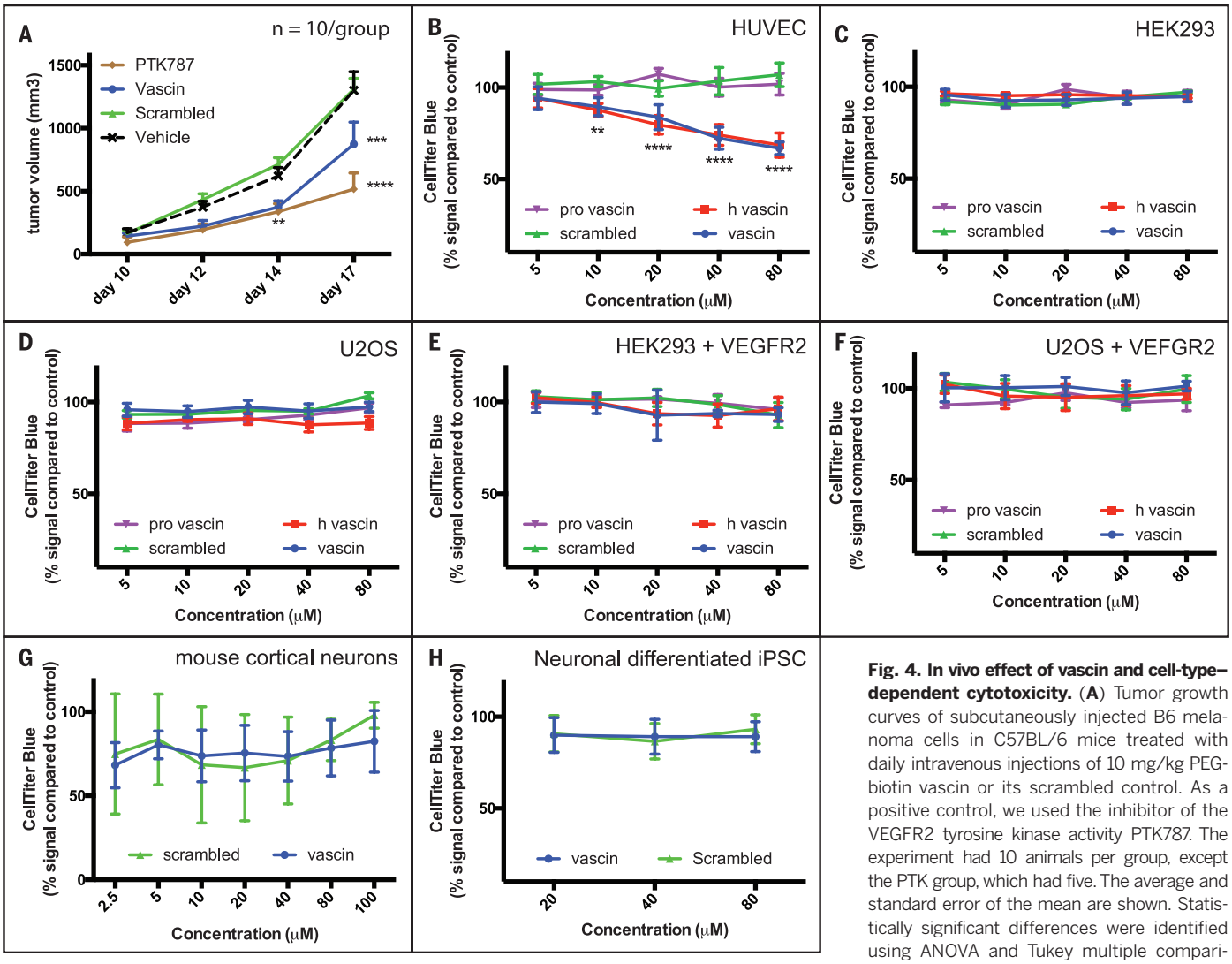

Fig. 4. In vivo effect of vascin and cell-type–dependent cytotoxicity. (**A**) Tumor growth curves of subcutaneously injected B6 melanoma cells in C57BL/6 mice treated with daily intravenous injections of 10 mg/kg PEG-biotin vascin or its scrambled control. As a positive control, we used the inhibitor of the VEGFR2 tyrosine kinase activity PTK787. The experiment had 10 animals per group, except the PTK group, which had five. The average and standard error of the mean are shown. Statistically significant differences were identified using ANOVA and Tukey multiple comparison testing. (**B** to **H**) Dose-dependent toxicity of vascin or its scrambled control tested from 2.5 to 100 μM by the CellTiter-Blue assay on (B) HUVECs, (C) HEK293 cells, (D) U2OS cells, (E) HEK293 cells transiently overexpressing VEGFR2, (F) U2OS cells transiently overexpressing VEGFR2, (G) cortical primary neuron cells from mouse, and (H) cortical neuronal progeny obtained from human iPSCs after a neuronal differentiation protocol. All toxicity data are shown as the mean of five measurements with standard deviations, except the iPSC data, which were 48 replicates. Statistically significant differences were identified by using ANOVA and Tukey multiple comparison testing.

fluorescence, tumors were isolated 30 min after injection and imaged ex vivo. The resulting fluorescence images showed strong green fluorescence emission for tumors isolated from CF-vascin–injected mice, whereas no fluorescence could be detected from tumors isolated from vehicle-injected control mice (fig. S12A), supporting the presence of vascin-CF at the tumor site according to macroscopic CF-fluorescence measurements. To further verify the presence of CF-vascin inside the tumor tissue with microscopic resolution, we additionally examined the presence of CF-vascin with fibered confocal fluorescence microscopy (FCFM) on tumor samples from the same mice. Inserting the fiber-optical probe inside the tumor tissue sample of vehicle-injected control mice did not show any fluorescence signal, whereas the tumor samples of CF-vascin–injected mice were clearly positive for green fluorescence (fig. S12B). To quantify vascin in B16 tumors, the specific light absorption by melanomas was calibrated through the addition of different known quantities of CF-vascin to series of tumor tissue dilutions and compared with a standard curve of fluorescence intensity for a dilution series of pure CF-vascin. Both were found to be linear in a large concentration range and for two different fluorescence imaging modalities, cross-validating the results (fig. S13, A and B). The tumor-specific fluorescence attenuation was then used to estimate the concentration of CF-vascin in tumors isolated from CF-vascin–treated mice, which was established to be 26.4 ± 10.5 μM, a concentration that is well above the IC_{50}.

Taken together, these data are consistent with a direct inhibitory activity of vascin on VEGFR2 function in vivo in the same manner that was observed in cells.

Amyloid toxicity is conditional to VEGFR2 dependence of cells

We determined loss of VEGFR2 function and vascin amyloid toxicity in several cell lines. CellTiter-Blue cytotoxicity assays (Fig. 4B) revealed that in HUVECs, loss of function of the receptor (IC_{50} of 6.8 ± 0.5 μM for receptor autophosphorylation and 8.3 ± 0.4 μM for ERK phosphorylation) goes hand in hand with cytotoxicity. On the other hand, in HEK293 or U2OS cells neither 2.5 to 100 μM of vascin nor its scrambled counterpart were found to be toxic (Fig. 4, C and D). Upon transfection of VEGFR2 in HEK293, we observed that after VEGF stimulation, ERK phosphorylation was inhibited upon treatment with 20 μM vascin (fig. S14A), which induced the aggregation of the VEGFR2, as evidenced on the fractionation assay (fig. S14B). However, no noticeable toxicity of vascin to HEK293 cells expressing VEGFR2 was observed in the range of 2.5 to 100 μM (Fig. 4E). This demonstrates that vascin is not toxic to HEK293 cells in the absence of VEGFR2 but also that aggregation of transiently expressed VEGFR2 in these lines does not affect cell viability. Similar observations were made with U2OS cells expressing VEGFR2 (Fig. 4F). Thus, vascin does not display generic amyloid toxicity, and the aggregation of VEGFR2 by vascin is in itself also not toxic. Last, because neurons are particularly sensitive to aggregate toxicity, we assessed the toxicity of vascin to primary cortical neurons, which do not express VEGFR2. Although with these neurons we observed significant toxicity upon peptide treatment (Fig. 4G), CellTiter-Blue reaction levels were similar for the vascin and its scrambled non-amyloid variant, suggesting that the toxicity was not amyloid-specific but rather reflects the high sensitivity of these cultures, which also resulted in a large variability in the assay. To verify this further, we turned to human induced pluripotent stem cells (iPSCs) differentiated to a cortical neuronal phenotype, which was verified by using quantitative reverse transcription polymerase chain reaction and immunostaining for markers specific for this cell type (fig. S15). In these cultures, we observed a lack of amyloid-specific toxicity, although there is 10% toxicity associated with administration of vascin or the scrambled control (Fig. 4H).

Together, these data suggest that amyloid toxicity is not dependent on cell type or even on target protein aggregation, but that amyloid toxicity is mainly determined from the biological context in which the target protein is inactivated by aggregation. Because HUVEC survival is dependent on VEFGR2 function, its molecular loss of function by aggregation translates to gain of toxic phenotype.

Discussion

About 30 amyloidogenic proteins are known to contribute to human disease. These diseases include neurodegenerative diseases such as Alzheimer's or Parkinson's disease but also organ-specific and systemic amyloidosis such as diabetes mellitus type 2 or light chain amyloidosis (*7*). Although the pathophysiological profiles of these diseases are disparate—involving the aggregation of different proteins, affecting distinctive cell types or tissues, and having very different progression rates—they also share common structural, biochemical, and biological features, suggesting that amyloids might also have similar modes of interaction with cellular components (*8*). Although amyloids of different proteins have been shown to interact with lipids (*40*), proteins (*41*), and nucleic acids (*42*), it is currently unclear which of these interactions are relevant for disease. Although some amyloid interactions are rather unspecific—for example, with biological lipids (*43*)—other amyloid interactions are highly specific (*20*). The most prominent of these is the self-interaction of amyloidogenic sequences during amyloid fibril formation, which includes both amyloid nucleation and fiber elongation (*44*, *45*). Proteome-wide studies using amyloid prediction algorithms suggest that most proteins possess amyloidogenic sequence segments within their structure, even though they do not form amyloid under normal conditions (*5*, *6*). Given the sequence specificity of amyloid seeding, this suggests that amyloid aggregation should be specifically inducible in non–amyloid-associated proteins by exposing them to amyloidogenic peptides derived from their own sequence.

Here, we demonstrate that aggregation of endogenously expressed VEGFR2 can be induced under physiological conditions by exposing it to vascin, a peptide consisting of a tandem repeat of an amyloidogenic sequence in its signal peptide. We found that vascin possesses all attributes of natural amyloids, including cross-β structure, the population of amyloid precursor aggregates, and the ability to reach the cytoplasmic compartment of cells, confirming that the signal peptide of VEGFR2 possesses a genuine amyloidogenic sequence. In addition, we found that vascin is able to induce VEGFR2 aggregation through direct interaction with VEGFR2. Because vascin is targeting the VEGFR2-signaling peptide, seeding of VEGFR2 aggregation is likely to be cotranslational, as suggested by ribosomal colocalization of vascin in the cytoplasm and the occurrence of partial VEGFR2 degradation along with its aggregation. This results in VEGFR2 inactivation in vitro but also in vivo, where it inhibits VEGFR2-dependent tumor growth upon intravascular administration. Both the aggregation as well as the inhibition of VEGFR2 appear to be specific. Scrambled vascin or the proline mutant do not interact with VEGFR2, nor does it provoke VEGFR2 aggregation or inhibition. In addition, whereas vascin suppresses cell-surface presentation of VEGFR2, it does not affect trafficking of other receptors such as CD29 or EGFR. Last, vascin-induced VEGFR2 aggregation is not inherently toxic because it does not affect the viability of VEGFR2-overexpressing HEK293 cells. Together, these findings show that VEGFR2, a protein not associated with amyloid disease, can be specifically induced to aggregate in the presence of specific amyloid seeds that are derived from its own sequence.

There may be multiple reasons why large-scale amyloidosis is not observed under natural conditions despite the likely prevalence of potentially amyloidogenic sequences in many proteins. First, most amyloidogenic sequences are buried in globular protein domains, which is probably the main protective factor against amyloidosis (*46*). Moreover, most misfolded proteins will be actively degraded in the cell before they have the opportunity to aggregate (*47*). Second, even in unfolded or intrinsically disordered proteins, most amyloidogenic sequences are generally still sufficiently protected from aggregation by structural mechanisms such as gatekeeping (the inhibition of aggregation by charged residues adjacent to the amyloidogenic segment) (*48*) and entropic bristles (unstructured protein segments that entropically prevent the association of amyloidogenic sequences) (*49*). Last, interaction with molecular chaperones will also contribute to the inhibition of aggregation (*50*). The reason why vascin can overcome these potential protective mechanisms is not yet clear but might reside in its design; vascin comprises a tandem repeat of an amyloidogenic sequence, which exacerbates the aggregation propensity of this sequence and leads to the formation of soluble and stable oligomeric aggregates, and these are likely to provide efficient sites for seeding. Incidentally, yeast prions often consist of peptide sequence repeats (*32*), and the stability of soluble oligomers consisting of tandem peptide repeats recently allowed their structure solvation by means of x-ray crystallography (*29*).

The toxic gain of function observed in many amyloid-associated diseases remains poorly explained. This is mainly due to the impossibility of relating loss-of-function effects to the aggregation process of a given protein. For many amyloid proteins, especially in neurodegeneration, the functional role of the affected protein is often complex and not entirely understood (*25*, *26*), which makes it difficult to unequivocally identify loss-of-function effects. In addition, the interactions of amyloid with cellular components in disease are also not clarified, so that again gain of toxic function is not directly tractable at the molecular level. The availability of our artificial amyloid model provides an opportunity to study the relationship between amyloid toxicity and specific protein loss of function. While recapitulating essential amyloid features, our model also allows monitoring the effect of amyloidosis on a functionally well-characterized protein. Moreover, the use of a VEGFR2 fragment allows the assessment of amyloid toxicity independent of VEGFR2 function.

Our results demonstrate that using this setup, vascin does not display generic toxic properties but rather the contrary. Vascin gain of function is specific (it is dependent on the presence of VEGFR2) but also conditional (VEGFR2 needs to be expressed in the cell, but the cell also needs to be dependent on VEGFR2 for its survival and proliferation). In VEGFR2-dependent HUVECs, vascin toxicity and VEGFR2 loss of function correlate in a dose-responsive manner, whereas this is not the case in VEGFR2-expressing HEK293 cells. Therefore, together these results illustrate how amyloid toxicity can result from a conjunction of protein-specific and cell-dependent protein loss of function. Whether lack of generalized toxicity is coupled to the availability of specific "aggregation epitopes" during or after translation remains to be further explored. It is possible that only selected APRs, occurring in the right structural context, would be sensitive to co-aggregation. However, the results in other model systems, such as plants (*31*) and bacteria (*30*), suggest that this is not the most likely scenario, but that the selectivity comes from the seqeunce specificity of the amyloid interaction (*20*, *51*). Further studies are needed to clarify this point.

Materials and methods

Bioinformatics

We used the TANGO algorithm for all APR identifications in this manuscript. We used a cutoff on the TANGO score of 5 per residue since this gives a Mathews Correlation Coefficient between prediction and experiment of 0.92 (*28*). The settings of TANGO were Temperature = 298 K, pH = 7.5, Ionic Strength = 0.10 M.

Peptides

Peptides were synthesized in-house using an Intavis Multipep RSi synthesis robot. Raw peptides were stored as dry ether precipitates at −20°C prior to use. Purified peptides were lyophilized and closed under nitrogen atmosphere and stored at −20°C prior to use. Stock solutions of each peptide were prepared fresh in 1% w/v ammonium bicarbonate in MiliQ water, filtered through 0.22 μm regenerated cellulose filter (Whatman, USA) and used immediately. The concentration of the peptides stocks was determined by absorbance at 280 nm using the calculated molar extinction coefficient ε = 11380 $M^{-1}cm^{-1}$.

Cell lines and media

HUVEC cells (Lonza) were grown in EGM2 complete medium (Lonza) in flasks pre-coated with 0.1% gelatin. The cells were never allowed to grow confluent and were only used for experiments between passage p3 and p9. U2-Os and HEK293 cells were maintained in DMEM medium, supplemented with 10% FBS, 1 mM sodium pyruvate, non-essential amino acids and antibiotics (penicillin/streptomycin). Lipofectamine 2000 (Life Technologies) was used to transiently transfect HEK293 and U2OS cells with an expression vector for VEGFR2 (pCDNA3) generating the cell lines $HEK293^{VEGFR2}$ and $U2OS^{VEGFR2}$. All peptide treatments were done in DMEM/F12 medium without additives. Toxicity of the peptide treatments was evaluated using the CellTiter-Blue Cell Viability Assay according to the instructions of the manufacturer (Promega, USA).

Quantification of growth factor signaling

HUVEC, HEK293, U2OS, $HEK293^{VEGFR2}$ and $U2OS^{VEGFR2}$ cells were treated with peptide overnight. The next day cells were stimulated with 25 ng/ml recombinant mouse-VEGF (493-MV, R&D Systems) or recombinant human-EGF (236-EG, R&D Systems) for exactly 5 min at 37°C. Cells were washed twice with ice cold PBS and lysed in RIPA lysis buffer (ThermoFisher Scientific) supplement with Complete protease inhibitor (Roche) and PhosSTOP phosphatase inhibitor (Roche). Quantification of VEGFR2 autophosphorylation and ERK phosphorylation was performed by electrochemiluminescence ELISA using the following kits according to the manufacturer's recommended protocol: Phospho-VEGFR-2(Tyr1054) (K151DJD, Meso Scale Discovery) and Phospho(Thr202/Tyr204; Thr185/Tyr187)/Total ERK1/2 (K15107D, Meso Scale Discovery).

X-ray fiber diffraction

X-ray fiber diffraction samples were made by allowing a droplet of the stock fibril solution to dry between two wax tipped capillary tubes. X-ray diffraction data was collected using a Rigaku rotating anode (CuKa) with Saturn CCD detector with exposure times of 30–60 s and specimen to detector distance of 50 or 100 mm. Reflections were measured using CLEARER (*52*).

In vivo experiments

All animal procedures were approved by the local animal ethical committee. Female C57BL/6 mice, 8 weeks of age, were purchased from Janvier (France). The B16.F10 melanoma cell line was obtained from the American Type Culture Collection (ATCC) and maintained in Dulbecco's Modified Eagle's Medium (DMEM) supplemented with 10% fetal bovine serum. B16 cells (5×10^5 cells/mouse) were implanted subcutaneously in the right dorsal flank of C57BL/6 mice. Starting from 3 days after tumor implantation, mice were randomized in three groups and treated daily by intravenous delivery of vascin or scrambled vascin (10mg/kg), or by oral delivery of PTK787 (75mg/kg). Tumors growth was monitored by caliper measurement every 2–3 days starting from 10 days after tumor injection. The experiment had 10 animals per group at onset, except the PTK group, which had five.

Transmission Electron Microscopy (TEM)

For each sample 7 μL aliquots of peptide solution were adsorbed for 1 min to formvar film coated copper grids of 400-mesh (Agar Scientific Ltd., England) that were first glow discharged to improve adsorption. After sample adsorption grids were washed by contact with 5 drops of ultrapure water and stained by contact with one drop of uranyl acetate (2% w/v in MiliQ water) for 45 s. The grids were examined using a JEM-2100 transmission electron microscope (Jeol, Japan) at 80 keV.

Biophysical characterization

Dynamic light scattering (DLS) measurements were made at room temperature with a DynaPro DLS plate reader instrument (Wyatt, Santa Barbara, CA, USA) equipped with a 830-nm laser source. Samples (100 μL 300 μM peptide stock) were placed into a flat-bottom 96-well microclear plate (Greiner, Germany). The autocorrelation of scattered light intensity at a 90° angle was recorded for 10 s and averaged over 40 recordings to obtain a single data point. The Wyatt Dynamics software was used to calculate the hydrodynamic radius by assuming linear polymer particles. Attenuated Total Reflection Fourier Transform Infrared Spectroscopy (ATR FTIR) was performed using a Bruker Tensor 27 infrared spectrophotometer (Bruker, Germany) equipped with a Bio-ATR II accessory (Harrick Scientific Products, USA). Spectra were recorded in the range of 900–3500 cm^{-1} at a spectral resolution of 2 cm^{-1} by accumulating 256 data acquisitions. The spectrophotometer was continuously purged with dried air. Spectra were corrected for atmospheric water vapor interference, baseline-subtracted, and vector normalized in the amide II area (1500 to 1600 cm-1) as implemented in OPUS software (Bruker). Tinctorial analysis was performed by incubating vascin or its scrambled version at the concentration indicated on each figure with 20 μM ThT, 20 μM ANS or 0.3 μM h-HTAA and fluorescence emission was recorded in a PolarStar Optima plate reader (BMG labtech, Germany) equipped with 360 nm and 490 nm excitation filters and 460 nm and 520 nm emission filters. All filters had 10 nm band-pass. Emission fluorescence spectra of h-HTAA bound to vascin or scrambled vascin were recorded in a FlexStation 3 (Molecular Devices, USA) at the same concentration of peptide and fluorophore listed above, with excitation at 480 nm and emission recorded between 490 nm and 620 nm using 10 nm band-pass.

Statistics

Statistical analysis was performed using Prism, Origin or R. Unpaired student's *t* test and ANOVA

were used to determine significant differences between samples unless otherwise indicated. Significance levels: * for $P < 0.05$, ** for $P < 0.01$, *** for $P < 0.001$.

REFERENCES AND NOTES

1. K. Dudgeon, K. Famm, D. Christ, Sequence determinants of protein aggregation in human VH domains. *Protein Eng. Des. Sel.* **22**, 217–220 (2009). doi: 10.1093/protein/gzn059; pmid: 18957405
2. S. Ventura *et al*., Short amino acid stretches can mediate amyloid formation in globular proteins: The Src homology 3 (SH3) case. *Proc. Natl. Acad. Sci. U.S.A.* **101**, 7258–7263 (2004). doi: 10.1073/pnas.0308249101; pmid: 15123800
3. O. S. Makin, L. C. Serpell, Structures for amyloid fibrils. *FEBS J.* **272**, 5950–5961 (2005). doi: 10.1111/j.1742-4658.2005.05025.x; pmid: 16302960
4. D. Eisenberg *et al*., Amyloid and prion structures. *FASEB J.* **23**, 423 (2009).
5. F. Rousseau, L. Serrano, J. W. H. Schymkowitz, How evolutionary pressure against protein aggregation shaped chaperone specificity. *J. Mol. Biol.* **355**, 1037–1047 (2006). doi: 10.1016/j.jmb.2005.11.035; pmid: 16359707
6. L. Goldschmidt, P. K. Teng, R. Riek, D. Eisenberg, Identifying the amylome, proteins capable of forming amyloid-like fibrils. *Proc. Natl. Acad. Sci. U.S.A.* **107**, 3487–3492 (2010). doi: 10.1073/pnas.0915166107; pmid: 20133726
7. F. Chiti, C. M. Dobson, Protein misfolding, functional amyloid, and human disease. *Annu. Rev. Biochem.* **75**, 333–366 (2006). doi: 10.1146/annurev.biochem.75.101304.123901; pmid: 16756495
8. D. Eisenberg, M. Jucker, The amyloid state of proteins in human diseases. *Cell* **148**, 1188–1203 (2012). doi: 10.1016/j.cell.2012.02.022; pmid: 22424229
9. K. E. Marshall, R. Marchante, W. F. Xue, L. C. Serpell, The relationship between amyloid structure and cytotoxicity. *Prion* **8**, 192–196 (2014). doi: 10.4161/pri.28860; pmid: 24819071
10. M. R. Krebs *et al*., Formation and seeding of amyloid fibrils from wild-type hen lysozyme and a peptide fragment from the beta-domain. *J. Mol. Biol.* **300**, 541–549 (2000). doi: 10.1006/jmbi.2000.3862; pmid: 10884350
11. J. T. Jarrett, E. P. Berger, P. T. Lansbury Jr., The carboxy terminus of the beta amyloid protein is critical for the seeding of amyloid formation: Implications for the pathogenesis of Alzheimer's disease. *Biochemistry* **32**, 4693–4697 (1993). doi: 10.1021/bi00069a001; pmid: 8490014
12. W. Li *et al*., Aggregation promoting C-terminal truncation of alpha-synuclein is a normal cellular process and is enhanced by the familial Parkinson's disease-linked mutations. *Proc. Natl. Acad. Sci. U.S.A.* **102**, 2162–2167 (2005). doi: 10.1073/pnas.0406976102; pmid: 15684072
13. Y. Wang, S. Garg, E. M. Mandelkow, E. Mandelkow, Proteolytic processing of tau. *Biochem. Soc. Trans.* **38**, 955–961 (2010). doi: 10.1042/BST0380955; pmid: 20658984
14. S. Nyström, P. Hammarström, Generic amyloidogenicity of mammalian prion proteins from species susceptible and resistant to prions. *Sci Rep* **5**, 10101 (2015). doi: 10.1038/srep10101; pmid: 25960067
15. R. S. Rajan, M. E. Illing, N. F. Bence, R. R. Kopito, Specificity in intracellular protein aggregation and inclusion body formation. *Proc. Natl. Acad. Sci. U.S.A.* **98**, 13060–13065 (2001). doi: 10.1073/pnas.181479798; pmid: 11687604
16. M. R. Krebs, L. A. Morozova-Roche, K. Daniel, C. V. Robinson, C. M. Dobson, Observation of sequence specificity in the seeding of protein amyloid fibrils. *Protein Sci.* **13**, 1933–1938 (2004). doi: 10.1110/ps.04707004; pmid: 15215533
17. J. Xu *et al*., Gain of function of mutant p53 by coaggregation with multiple tumor suppressors. *Nat. Chem. Biol.* **7**, 285–295 (2011). doi: 10.1038/nchembio.546; pmid: 21445056
18. K. Ono, R. Takahashi, T. Ikeda, M. Yamada, Cross-seeding effects of amyloid β-protein and α-synuclein. *J. Neurochem.* **122**, 883–890 (2012). doi: 10.1111/j.1471-4159.2012.07847.x; pmid: 22734715
19. M. E. Oskarsson *et al*., In vivo seeding and cross-seeding of localized amyloidosis: A molecular link between type 2 diabetes and Alzheimer disease. *Am. J. Pathol.* **185**, 834–846 (2015). doi: 10.1016/j.ajpath.2014.11.016; pmid: 25700985
20. A. Ganesan *et al*., Selectivity of aggregation-determining interactions. *J. Mol. Biol.* **427**, 236–247 (2015). doi: 10.1016/j.jmb.2014.09.027; pmid: 25451783
21. W. Surmacz-Chwedoruk, V. Babenko, W. Dzwolak, Master and slave relationship between two types of self-propagating insulin amyloid fibrils. *J. Phys. Chem. B* **118**, 13582–13589 (2014). doi: 10.1021/jp510980b; pmid: 25373010
22. K. H. Ashe, A. Aguzzi, Prions, prionoids and pathogenic proteins in Alzheimer disease. *Prion* **7**, 55–59 (2013). doi: 10.4161/pri.23061; pmid: 23208281
23. K. F. Winklhofer, J. Tatzelt, C. Haass, The two faces of protein misfolding: Gain- and loss-of-function in neurodegenerative diseases. *EMBO J.* **27**, 336–349 (2008). doi: 10.1038/sj.emboj.7601930; pmid: 18216876
24. M. Jucker, L. C. Walker, Self-propagation of pathogenic protein aggregates in neurodegenerative diseases. *Nature* **501**, 45–51 (2013). doi: 10.1038/nature12481; pmid: 24005412
25. H. A. Pearson, C. Peers, Physiological roles for amyloid beta peptides. *J. Physiol.* **575**, 5–10 (2006). doi: 10.1113/jphysiol.2006.111203; pmid: 16809372
26. J. T. Bendor, T. P. Logan, R. H. Edwards, The function of α-synuclein. *Neuron* **79**, 1044–1066 (2013). doi: 10.1016/j.neuron.2013.09.004; pmid: 24050397
27. I. Benilova, E. Karran, B. De Strooper, The toxic Aβ oligomer and Alzheimer's disease: An emperor in need of clothes. *Nat. Neurosci.* **15**, 349–357 (2012). doi: 10.1038/nn.3028; pmid: 22286176
28. A. M. Fernandez-Escamilla, F. Rousseau, J. Schymkowitz, L. Serrano, Prediction of sequence-dependent and mutational effects on the aggregation of peptides and proteins. *Nat. Biotechnol.* **22**, 1302–1306 (2004). doi: 10.1038/nbt1012; pmid: 15361882
29. A. Laganowsky *et al*., Atomic view of a toxic amyloid small oligomer. *Science* **335**, 1228–1231 (2012). doi: 10.1126/science.1213151; pmid: 22403391
30. N. G. Bednarska *et al*., Protein aggregation as an antibiotic design strategy. *Mol. Microbiol.* **99**, 849–865 (2016). doi: 10.1111/mmi.13269; pmid: 26559925
31. C. Betti *et al*., Sequence-specific protein aggregation generates defined protein knockdowns in plants. *Plant Physiol.* **171**, 773–787 (2016). pmid: 27208282
32. E. D. Ross, A. Minton, R. B. Wickner, Prion domains: Sequences, structures and interactions. *Nat. Cell Biol.* **7**, 1039–1044 (2005). doi: 10.1038/ncb1105-1039; pmid: 16385730
33. R. Sabate, F. Rousseau, J. Schymkowitz, S. Ventura, What makes a protein sequence a prion? *PLOS Comput. Biol.* **11**, e1004013 (2015). doi: 10.1371/journal.pcbi.1004013; pmid: 25569335
34. T. Klingstedt *et al*., Synthesis of a library of oligothiophenes and their utilization as fluorescent ligands for spectral assignment of protein aggregates. *Org. Biomol. Chem.* **9**, 8356–8370 (2011). doi: 10.1039/c1ob05637a; pmid: 22051883
35. L. M. Young *et al*., Screening and classifying small-molecule inhibitors of amyloid formation using ion mobility spectrometry-mass spectrometry. *Nat. Chem.* **7**, 73–81 (2015). doi: 10.1038/nchem.2129; pmid: 25515893
36. S. Campioni *et al*., A causative link between the structure of aberrant protein oligomers and their toxicity. *Nat. Chem. Biol.* **6**, 140–147 (2010). doi: 10.1038/nchembio.283; pmid: 20081829
37. D. Pinotsi *et al*., Direct observation of heterogeneous amyloid fibril growth kinetics via two-color super-resolution microscopy. *Nano Lett.* **14**, 339–345 (2014). doi: 10.1021/nl4041093; pmid: 24303845
38. J. M. Wood *et al*., PTK787/ZK 222584, a novel and potent inhibitor of vascular endothelial growth factor receptor tyrosine kinases, impairs vascular endothelial growth factor-induced responses and tumor growth after oral administration. *Cancer Res.* **60**, 2178–2189 (2000). pmid: 10786682
39. R. Radde *et al*., Aβ42-driven cerebral amyloidosis in transgenic mice reveals early and robust pathology. *EMBO Rep.* **7**, 940–946 (2006). doi: 10.1038/sj.embor.7400784; pmid: 16906128
40. H. A. Lashuel, D. Hartley, B. M. Petre, T. Walz, P. T. Lansbury Jr., Neurodegenerative disease: Amyloid pores from pathogenic mutations. *Nature* **418**, 291 (2002). doi: 10.1038/418291a; pmid: 12124613
41. H. Olzscha *et al*., Amyloid-like aggregates sequester numerous metastable proteins with essential cellular functions. *Cell* **144**, 67–78 (2011). doi: 10.1016/j.cell.2010.11.050; pmid: 21215370
42. D. Cirillo *et al*., Neurodegenerative diseases: Quantitative predictions of protein-RNA interactions. *RNA* **19**, 129–140 (2013). doi: 10.1261/rna.034777.112; pmid: 23264567
43. G. P. Gorbenko, P. K. Kinnunen, The role of lipid-protein interactions in amyloid-type protein fibril formation. *Chem. Phys. Lipids* **141**, 72–82 (2006). doi: 10.1016/j.chemphyslip.2006.02.006; pmid: 16569401
44. R. Wetzel, Kinetics and thermodynamics of amyloid fibril assembly. *Acc. Chem. Res.* **39**, 671–679 (2006). doi: 10.1021/ar050069h; pmid: 16981684
45. S. I. Cohen *et al*., Proliferation of amyloid-β42 aggregates occurs through a secondary nucleation mechanism. *Proc. Natl. Acad. Sci. U.S.A.* **110**, 9758–9763 (2013). doi: 10.1073/pnas.1218402110; pmid: 23703910
46. F. Chiti, C. M. Dobson, Amyloid formation by globular proteins under native conditions. *Nat. Chem. Biol.* **5**, 15–22 (2009). doi: 10.1038/nchembio.131; pmid: 19088715
47. G. De Baets *et al*., An evolutionary trade-off between protein turnover rate and protein aggregation favors a higher aggregation propensity in fast degrading proteins. *PLOS Comput. Biol.* **7**, e1002090 (2011). pmid: 21731483
48. G. De Baets, J. Van Durme, F. Rousseau, J. Schymkowitz, A genome-wide sequence-structure analysis suggests aggregation gatekeepers constitute an evolutionary constrained functional class. *J. Mol. Biol.* **426**, 2405–2412 (2014). doi: 10.1016/j.jmb.2014.04.007; pmid: 24735868
49. A. A. Santner *et al*., Sweeping away protein aggregation with entropic bristles: Intrinsically disordered protein fusions enhance soluble expression. *Biochemistry* **51**, 7250–7262 (2012). doi: 10.1021/bi300653m; pmid: 22924672
50. R. I. Morimoto, The heat shock response: Systems biology of proteotoxic stress in aging and disease. *Cold Spring Harb. Symp. Quant. Biol.* **76**, 91–99 (2011). doi: 10.1101/sqb.2012.76.010637; pmid: 22371371
51. J. R. Couceiro *et al*., Sequence-dependent internalization of aggregating peptides. *J. Biol. Chem.* **290**, 242–258 (2015). doi: 10.1074/jbc.M114.586636; pmid: 25391649
52. S. Zibaee, O. S. Makin, M. Goedert, L. C. Serpell, A simple algorithm locates beta-strands in the amyloid fibril core of alpha-synuclein, Aβ, and τ using the amino acid sequence alone. *Protein Sci.* **16**, 906–918 (2007).

ACKNOWLEDGMENTS

This work was supported by the European Research Council (ERC) under the European Union's Horizon 2020 Framework Programme, ERC grant agreement 647458 (MANGO) to J.S. The Switch Laboratory was supported by grants from VIB, Industrial Research Funds of KU Leuven (IOF), the Funds for Scientific Research Flanders (FWO), the Flanders Institute for Science and Technology (IWT), and the Federal Office for Scientific Affairs of Belgium (Belspo), IUAP P7/16. G.V.V., F.D.S., and F.C. were supported by postdoctoral fellowships of FWO. G.V.V. was also supported by KU Leuven competitive funding (PF/10/014). L.Y. is funded by a Wellcome Trust Institutional Strategic Support Fund (ISSF) (grant 015615/Z/14/Z). The Synapt high-definition mass spectroscopy mass spectrometer was purchased with funds from the Biotechnology and Biological Sciences Research Council through its Research Equipment Initiative scheme (BB/E012558/1). The Linköping University laboratories were supported by The Göran Gustafsson Foundation, The Swedish Research Council, and The Swedish Alzheimer Foundation. P.C. was supported by FWO, Methusalem funding by the Flemish government, and an AXA Research grant. M.K. is supported by a Marie Skłodowska-Curie Individual Fellowship under the European Union's Horizon 2020 Framework Programme (grant H2020-MSCA-IF-2014-ST). C.V. was supported by the KU Leuven Stem Cell Programme. F.R. and J.S. are inventors on patent applications WO2007/071789 and WO2012/123419 submitted by VIB vzw, Belgium, that covers the use of targeted protein aggregation for therapeutic or biotechnological applications. The authors declare no other financial interests in this work. B.D.S. also held an appointment with the Institute of Neurology. University College of London, UK, and is a paid consultant for Janssen Pharmaceuticals NV, Belgium, and Remynd NV, Belgium. Human embryonic stem H9 cells are available from the University of Wisconsin under a materials transfer agreement.

SUPPLEMENTARY MATERIALS

www.sciencemag.org/content/354/6313/aah4949/suppl/DC1
Materials and Methods
Supplementary Text
Figs. S1 to S15
Tables S1 to S3
References (*53*–*67*)

6 July 2016; accepted 23 September 2016
10.1126/science.aah4949

RESEARCH ARTICLE

INFLUENZA EPIDEMIOLOGY

Potent protection against H5N1 and H7N9 influenza via childhood hemagglutinin imprinting

Katelyn M. Gostic,[1] Monique Ambrose,[1] Michael Worobey,[2]* James O. Lloyd-Smith[1,3]*

Two zoonotic influenza A viruses (IAV) of global concern, H5N1 and H7N9, exhibit unexplained differences in age distribution of human cases. Using data from all known human cases of these viruses, we show that an individual's first IAV infection confers lifelong protection against severe disease from novel hemagglutinin (HA) subtypes in the same phylogenetic group. Statistical modeling shows that protective HA imprinting is the crucial explanatory factor, and it provides 75% protection against severe infection and 80% protection against death for both H5N1 and H7N9. Our results enable us to predict age distributions of severe disease for future pandemics and demonstrate that a novel strain's pandemic potential increases yearly when a group-mismatched HA subtype dominates seasonal influenza circulation. These findings open new frontiers for rational pandemic risk assessment.

The spillover of novel influenza A viruses (IAV) is a persistent threat to global health. H5N1 and H7N9 are particularly concerning avian-origin IAVs, each having caused hundreds of severe or fatal human cases (*1*). Despite commonalities in their reservoir hosts and epidemiology, these viruses show puzzling differences in age distribution of observed human cases (*1*, *2*). Existing explanations—including possible protection against H5N1 among older birth-year cohorts exposed to the neuraminidase of H1N1 as children (*3*, *4*) or age biases in exposure to infected poultry (*5*–*7*)—cannot fully explain these opposing patterns of severe disease and mortality. Another idea is that severity of H5N1 and H7N9 differs by age and so leads to case ascertainment biases (*1*), but no explanatory mechanism has been proposed.

The key antigenic determinants for IAV susceptibility are the virus's two surface glycoproteins, hemagglutinin (HA) and neuraminidase (NA), where different numbered subtypes canonically indicate no cross-immunity. However, recent experiments have revealed that broadly protective immune responses can provide cross-immunity between different HA subtypes, particularly subtypes in the same phylogenetic group (*8*–*14*). HA group 1 contains human seasonal subtypes H1, H2, and avian H5, whereas group 2 contains seasonal H3 and avian H7 (Fig. 1A and fig. S1). Combining these insights into heterosubtypic immunity with the concept of "original antigenic sin" (*15*) or "antigenic seniority" (*16*), we hypothesized that individuals imprint on the HA group of their first IAV exposure and thereby experience a reduced risk of severe disease from novel IAVs within that same phylogenetic group. This hypothesis predicts that the 1968 pandemic, which marked the transition from an era of group 1 HA circulation (1918–1968) to a group 2–dominated one (1968 to the present) (Fig. 1B), caused a major shift in population susceptibility that would explain why H5N1 cases are generally detected in younger people than are H7N9 cases (*2*, *17*–*19*). Our analysis of human cases of H5N1 and H7N9 revealed strong evidence that childhood HA imprinting indeed provides profound, lifelong protection against severe infection and death from these viruses. These findings allowed us to develop new approaches for IAV pandemic risk assessment, preparedness, and response but also raise possible challenges for future vaccination strategies.

Reconstructing IAV exposure history by birth year

To investigate whether an individual's initial childhood exposure to IAV influences later susceptibility to H5 and H7 viruses, we estimated the fraction of each birth-year cohort from 1918 to 2015 with first exposure to H1, H2, or H3—or the fraction still naïve—for each country in our study (China, Egypt, Cambodia, Indonesia, Thailand, and Vietnam). We estimated the annual probability of IAV infection in children using published age-seroprevalence data (*20*, *21*) and then rescaled this baseline attack rate to account for year-to-year variability in IAV circulation intensity (supplementary text).

One resulting country-specific reconstruction of HA history is depicted in Fig. 1C. Although H3N2 has dominated since 1968, a non-negligible fraction of many birth-year cohorts from the 1970s onward was exposed first to H1N1 viruses, with notable peaks near the reemergence of H1N1 in 1977 and the 2009 pandemic.

H5N1 and H7N9 cases track HA imprinting patterns

Next, we compiled data on all known human cases of H5N1 and H7N9 with reported patient age (Fig. 2, A and B). These data encompass mostly clinically severe and fatal cases; total incidence remains unknown. Thus, our analysis focused on the determinants of severe cases. The possible existence of many undetected mild cases, as hypothesized for H7N9 (*1*), is consistent with HA imprinting because broadly protective immune responses are expected to provide partial protection (*8*, *14*), i.e., to reduce severity without preventing infection altogether (*4*, *12*, *22*–*25*).

The preponderance of observed H7N9 cases among older cohorts and of H5N1 cases among younger cohorts is clear (Fig. 2, A and B). These patterns reflect birth year, not age: H5N1 cases occurred during 19 years from 1997 to 2015, yet cases from all years exhibit similar dependence on birth year. Analysis of 361 H5N1 cases in Egypt, the one country with many cases across the past decade, shows no trend in case birth years through time, whereas case age increased steadily (P = 0.0003, Spearman's correlation) (fig. S2). So, on average, the same birth cohorts remained at high risk of severe infection, even as members grew 10 years older.

The case data normalized to demographic age distributions in affected countries are depicted in Fig. 2, C and D. (If all birth cohorts had equal risk of severe infection, case incidence would be proportional to age distribution.) Bars above the midline thus represent birth years showing excess risk; bars below indicate a shortfall. This normalization highlights two points: (i) Excess incidence and mortality data for H5N1 and H7N9 are near-mirror images of each other. (ii) The group 1–to–group 2 HA transition in 1968 is the key inflection point, with those born before the emergence of H3N2 showing protection against severe cases of H5N1 but not H7N9 and those born after 1968 showing the opposite pattern. For H7N9, severe case incidence also spikes in birth years around 1977 and 2009, when resurgent H1N1 circulation would have caused considerable mismatched imprinting. One-sided binomial exact tests showed that excess H5N1 incidence had a lower probability of occurring in cohorts born before 1968 ($P < 1e^{-10}$), whereas excess H7N9 incidence was more probable in these same cohorts ($P < 1e^{-9}$). The same pattern held for excess mortality (supplementary text). These patterns suggest that the immune system imprints on conserved HA epitopes from the first-ever exposure to IAV, which results in heterosubtypic (but within-group) protection against severe infection.

Even more striking is the tight correspondence of observed H5N1 and H7N9 incidence and mortality with a priori predictions based on HA imprinting patterns and demographic age distributions (Fig. 2). We emphasize that the black lines in Fig. 2 are not fitted to the case data but

[1]Department of Ecology and Evolutionary Biology, University of California, Los Angeles, Los Angeles, CA 90095, USA. [2]Department of Ecology and Evolutionary Biology, University of Arizona, Tucson, AZ 85721, USA. [3]Fogarty International Center, National Institutes of Health, Bethesda, MD 20892, USA.
*Corresponding author. Email: worobey@email.arizona.edu (M.W.); jlloydsmith@ucla.edu (J.O.L.-S.)

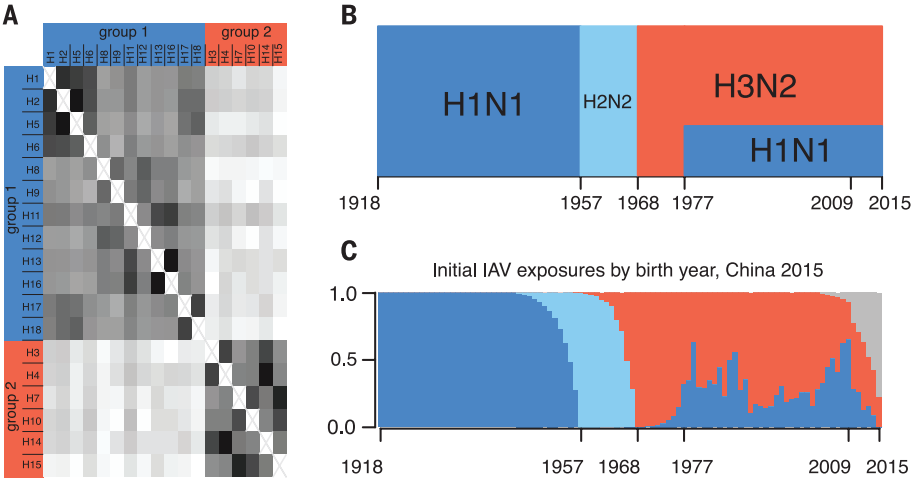

Fig. 1. HA groups and reconstruction of 20th-century HA imprinting. (**A**) HA groups 1 and 2, and pairwise amino acid similarities in the HA stem region. Darker-colored cells indicate higher similarity (see fig. S1). Each within-group subtype pair is more similar (83.2 to 97.8%) than any between-group pair (75.9 to 81.7%). (**B**) History of seasonal IAV circulation. (**C**) Estimated fraction of each birth cohort in China with initial exposure to each subtype. Estimated patterns in other countries (not shown) are identical up to 1977 and very similar thereafter. Pandemic years are marked on the horizontal axis. Blue represents group 1 HA viruses, red represents group 2, and gray represents naïve children who have not yet experienced an IAV infection.

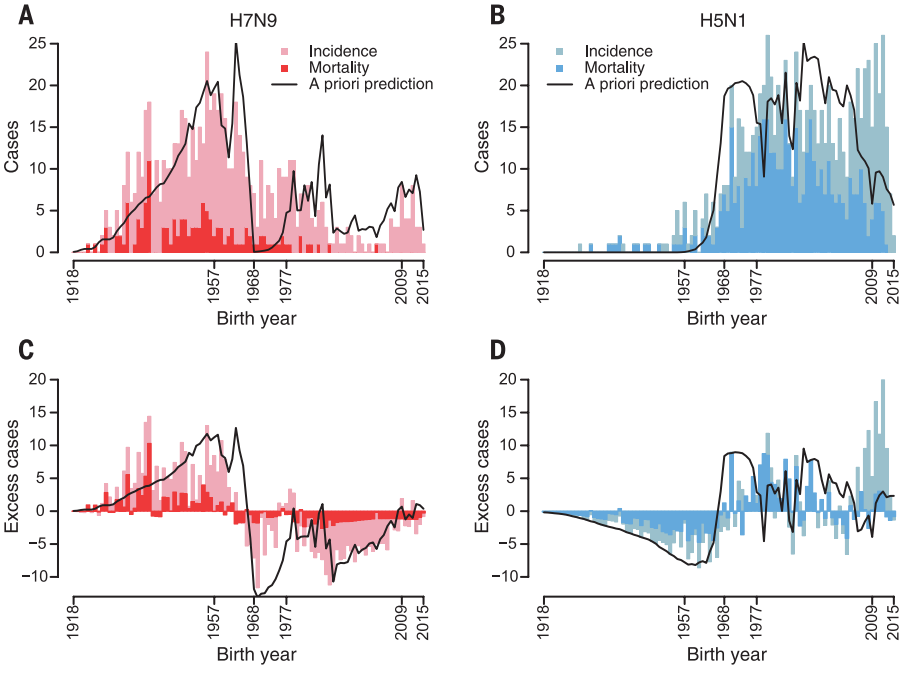

Fig. 2. H7N9 and H5N1 observed cases and deaths by birth year. Black lines show a priori predictions based on demographic age distribution and reconstructed patterns of HA imprinting. (**A**) 680 H7N9 cases from China, 2013–2015, and (**B**) 835 H5N1 cases from Cambodia, China, Egypt, Indonesia, Thailand, and Vietnam, 1997–2015. (**C** and **D**) Case data normalized to demographic age distribution from appropriate countries and case observation years.

are independent predictions [e.g., (Fig. 1C)]. Differences between the predictions and data are remarkably small—some noise arises from generalization across time and countries (e.g., attack rates for the reconstruction came from German data, but focal populations are largely Asian) and from small case numbers. Incorporating additional epidemiological factors and estimating the protective efficacy of imprinting further improved correspondence between predictions and data (fig. S3). In contrast, NA imprinting patterns (which fully capture patterns of childhood exposure to N1) are a poor fit to H5N1 and H7N9 data from 1957–1968 cohorts (fig. S4), and NA-mediated protection is not supported by statistical modeling.

HA imprinting explains age distributions

To formally assess the HA imprinting hypothesis alongside previous explanations (*1*, *3*–*7*) for observed H5N1 and H7N9 age distributions, we developed a set of multinomial models. These models related the probability that a case occurred in a given birth cohort to country- and year-specific demography; to risk factors including age-based risk of exposure to poultry, age-based risk of severe disease or case ascertainment; and to reconstructed patterns of first exposure (and, hence, potential immunological imprinting) to HA or NA subtypes (table S1). Model comparison showed that HA imprinting was the dominant explanatory factor for observed incidence and mortality patterns for both H5N1 and H7N9 (Table 1). It was the only tested factor included in all plausible models for both viruses (i.e., all models with Akaike weights greater than $4e^{-5}$).

The best models also included age-based risk of severe disease, echoing patterns known from seasonal influenza epidemiology. Age-based poultry exposure risk [estimated based on contact data from China (*6*, *7*)] was included for H7N9 but not H5N1, which may reflect that age-specific poultry exposures vary across the multiple countries affected by H5N1 or that humans interact differently with ill (H5N1-infected) versus asymptomatic (H7N9-infected) poultry. In models including HA imprinting, NA imprinting never showed any significant effect (table S2). Remarkably, despite differences between the viruses and age cohorts involved, the estimated protective effects of HA imprinting were nearly identical for H7N9 and H5N1. In all models, protective HA imprinting reduced the risk of severe infection with H5N1 or H7N9 by ~75% and the risk of death by ~80% (Table 1, figs. S5 to S7, and table S2).

Antigenic seniority across influenza subtypes

Most individuals born before the emergence of H3N2 in 1968 and exposed first to group 1 HA antigens (Fig. 1) have also been exposed to H3N2 after 1968—probably multiple times. Yet these seasonal group 2 exposures later in life evidently fail to override group 1 HA imprinting from childhood (Fig. 2). The birth year–specific protection seen for human H5N1 and H7N9 thus clearly indicates that clinically relevant antigenic seniority—preferential recall of immunological reactivities to antigens encountered earlier in life upon later exposure to cross-reactive antigens (*16*)—can act across HA subtypes of the same HA group, not only within subtypes as often assumed.

Although the precise mechanism underlying antigenic seniority in this context remains to be determined, antibodies directed against conserved HA epitopes provide a plausible explanation for protection at the level of HA groups. For example, research following the 2009 H1N1 pandemic drew attention to the fact that primary exposure to a

novel IAV can preferentially boost broadly protective antibodies that bind conserved HA head or stem epitopes shared by different HA subtypes (*8*–*14*), even though immune memory against more variable epitopes on the novel HA head may be absent. This absence may in fact enable robust expression of otherwise-subdominant, broadly protective responses to conserved epitopes such as those on the HA stem (*8*). In particular, primary exposure to H5N1 or H7N9 can activate HA stem–specific reactivities induced by previous infection by H1 or H3, respectively (*12*, *13*, *26*). Indeed, others have suggested that heterosubtypic antibodies might attenuate disease from other IAV strains and may be imprinted to some degree by childhood exposure, although their serological assays provided no ability to detect or predict actual patterns of protection relevant to H5N1 and H7N9 in human populations (*27*).

Given the immunodominant nature of HA head reactivities (*13*, *14*, *26*, *28*), conserved HA head epitopes shared within, but not between, HA groups (*29*) may play a role in these patterns of protection. Cross-reactive HA-specific $CD4^+$ or $CD8^+$ T cell responses should also be investigated, because they, too, are likely to be disproportionately shared within HA groups (given the sequence similarities within each clade) and might be especially capable of facilitating the sort of long-term immunity indicated by the data.

Nevertheless, current data, including the high degree of sequence conservation of stem domains within each HA group (Fig. 1A and fig. S1), seem most consistent with a stem-directed mechanism for the antigenic seniority acting at the HA-group level (*13*). Divergence in HA stem amino acid sequences within each phylogenetic group is comparable to divergence in HA head sequences within a single HA subtype [i.e., the scale at which antigenic seniority is already known to act (*16*)] (fig. S1), but stem divergences between the two HA groups are markedly higher. Notably, H3 and H7 are as divergent as any pair of group 2 HAs; because H3 childhood exposure provides protection against H7, it may thus protect as well or better against the other group 2 HAs (H4, H10, H14, and H15) but perhaps not at all against more divergent group 1 HAs (fig. S1C). Similarly, the joint consideration of protein sequence conservation patterns (Fig. 1A and fig. S1) along with immunological and epidemiological data suggests that H1 or H2 childhood exposure may protect generally against zoonotic group 1 HAs but not group 2 HAs.

The putative generality in HA imprinting protection patterns for novel HA subtypes other than H5N1 or H7N9 is tentatively supported by the preponderance of HA group–mismatched childhood exposures among the small number of clinically significant human cases detected to date. By pooling data from 28 human cases of H5N6, H6N1, H7N7, H9N2, H10N7, and H10N8, we found that age patterns are consistent with HA imprinting (P = 0.019; see supplementary text), but case numbers are insufficient to investigate particular subtypes. Immunological experiments [e.g., using chimeric HA proteins (*12*)] are needed to systematically map HA cross-protection patterns across all HA subtypes, both within and between HA groups.

Table 1. Estimated protection against severe infection from HA imprinting. D, demography; E, exposure to poultry; A, high-risk age groups; H, HA imprinting; N, NA imprinting (see supplementary methods and table S1).

Factors in model	HA imprinting protection (95% CI)	ΔAIC	Akaike weight
H5N1			
DAH	0.75 (0.65–0.82)	0.00	0.9994
DEAH	0.83 (0.76–0.88)	15.35	4.65E-4
DEANH	0.83 (0.73–0.88)	17.32	1.74E-4
DH	0.80 (0.71–0.85)	69.18	9.50E-16
DEH	0.87 (0.80–0.90)	103.31	3.69E-23
DENH	0.86 (0.78–0.90)	105.29	1.37E-23
H7N9			
DEAH	0.76 (0.67–0.82)	0.00	1.00
DAH	0.81 (0.74–0.87)	42.87	4.09E-10
DEH	0.84 (0.78–0.88)	61.59	4.23E-14
DENH	0.83 (0.75–0.88)	62.26	3.02E-14
DH	0.88 (0.84–0.92)	138.40	8.83E-31

Rational projections of future pandemic risk

For any new pandemic IAV strain capable of efficient human-to-human transmission, HA imprinting patterns would combine with age-based mixing patterns (*30*–*32*) to determine the epidemiological impacts of the first pandemic wave. We created projections for a putative pandemic-capable strain of subtype H5 or H7—such as a gain-of-function strain or a natural variant with mutations increasing human-to-human transmissibility. The data on observed H7N9 and H5N1 cases enabled us to quantify how matched HA imprinting reduces the probability of developing a severe infection, but not how matched imprinting affects an individual's probability of acquiring a milder infection or the infectivity of such mild infections. People who become infected despite prior immunity likely transmit influenza at reduced rates owing to diminished viral titers and viral shedding, as observed in humans and in animal models (*4*, *12*, *22*–*25*). We thus assumed, conservatively, that imprinting does not change the probability of acquiring infection upon exposure but can reduce severity and infectivity in individuals with protective HA imprinting.

The projected age-structured attack rate of severe cases for hypothetical pandemics of H5 or H7 IAV occurring in 2015 in the United Kingdom is illustrated in Fig. 3A. The projected risk profiles for severe infection are shaped strongly by HA imprinting, including the prediction that individuals above 50 years of age (i.e., born well before 1968 and first exposed to a group 1 HA) would experience much lower morbidity than younger age groups in an H5 pandemic. Similar projections for China and Vietnam reveal the influence of demographic differences between countries (fig. S8). The qualitative patterns in projected age impacts are robust to a wide range of assumptions about how seasonal influenza vaccination might affect imprinting (Fig. 3A) and to the assumed infectivity of mild cases arising in individuals with protective HA imprinting (fig. S8A).

Projections for pandemics occurring a decade from now highlight predictable shifts in severe disease risk patterns as the imprinted population ages, with the key pivot point around birth years near 1968 shifted to older ages (fig. S8). Impacts in the youngest age groups would depend on patterns of IAV circulation in the coming decade. All pandemic projections that account for HA imprinting exhibit markedly lower severe attack rates than projections assuming no imprinting protection (Fig. 3A and fig. S8). Total attack rates (including mild and subclinical cases) would be

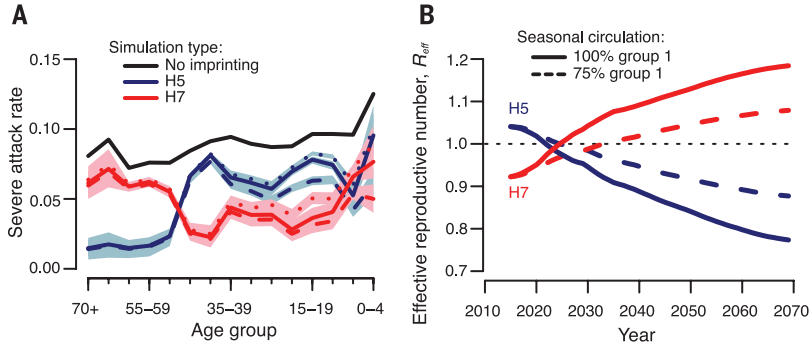

Fig. 3. Projected effects of HA imprinting on future pandemics. (**A**) Attack rate of severe cases, by age group, for hypothetical H5 (blue) and H7 (red) IAV pandemics in 2015 [R_0 = 2.5, relative infectiousness of imprinting-protected individuals (α) = 0.5], if one assumes UK demography and age-structured mixing (see supplementary text). Lines show the average of 100 simulated outcomes, and shaded regions show the central 95%. Three vaccination scenarios were explored: vaccination of IAV-naïve children could cause dual imprinting to both HA groups (dashed lines), prevent imprinting to both groups (dotted lines), or have no effect on imprinting (solid lines). (**B**) Projected change in R_{eff}, for hypothetical H5 (blue) or H7 (red) IAV with R_0 = 1.2 and α = 0.5, if group 1 IAVs make up 100% or 75% of seasonal circulation after 2015.

higher and more evenly distributed across age groups than the severe attack rates shown here.

Over any prolonged period when IAV circulation is dominated by one HA group, imprinting generates growing herd immunity against zoonotic IAV strains from that group. Conversely, zoonotic strains from the mismatched HA group benefit from the rising proportion of humans without protection. So long as mild cases arising in people with group-matched imprinting contribute any less to transmission than unprotected cases, or if some fraction of infection events is prevented by imprinting-derived immunity, imprinting will alter the transmissibility of zoonotic IAV strains in the human population. This is summarized by the effective reproductive number, R_{eff}, which quantifies transmission in a partially immune population (Fig. 3B). Crucially, a zoonotic strain that is initially subcritical (i.e., with $R_{eff} < 1$ and therefore unable to spread sustainably) could—solely because of susceptibility changes in the human population—emerge as supercritical and hence as a pandemic threat, if the mismatched HA group dominates IAV circulation for a sufficient period (Fig. 3B).

Our work implies that we have never seen a true "virgin soil" influenza pandemic and that all prior estimates of R_0 for pandemic IAVs are systematic underestimates because they do not account for protection induced by HA imprinting. Conversely, we see that imprinting raises the threshold R_0 necessary for a novel subtype to invade. Note that the cocirculation of group 1 and 2 HAs since 1977 has balanced herd immunity in a way that increases the inherent transmissibility needed for a novel subtype from either HA group to invade. As a generality, R_{eff} for zoonotic influenza strains will change through time depending on seasonal influenza patterns and demographic background, and the magnitude of change will depend on the infectivity of imprinting-protected cases (fig. S9).

Discussion

Our findings show that major patterns in zoonotic IAV epidemiology, previously attributed to patient age, are in fact driven by birth year. IAV strains circulating during an individual's childhood confer long-term protection against novel HA subtypes from the same phylogenetic group. Hence, antigenic seniority extends across IAV subtypes, introducing previously unrecognized generational structure to influenza epidemiology. These immune imprinting effects have implications for public health and highlight that influenza virulence represents a joint phenotype between virus and host—even for strains not yet adapted to the human population.

These findings support the hypothesis that the unusually high mortality in young adults during the 1918 H1N1 (group 1) pandemic may have arisen primarily from mismatched H3 (group 2) imprinting in the cohort born between ~1880 and 1900 (*19*). This same cohort was strongly affected during the (group 1) 1957 pandemic (*33*), yet they suffered no excess mortality when they were even older, during the (group 2) 1968 pandemic (*34*). The possibility that mismatched HA imprinting currently contributes to the greater health impacts of seasonal H3N2 (relative to H1N1) in today's older age classes is worth investigating. And a diagnostic assay to determine whether an individual was imprinted on a group 1 or group 2 HA may be useful for individualized clinical care and vaccine design strategies, both for pandemic and seasonal IAVs.

Our findings raise questions about whether seasonal influenza vaccination might boost broadly protective anti-HA responses (*27*) or alter imprinting from natural infection in IAV-naïve children. By exposing IAV-naïve children simultaneously to group 1 (H1N1) and group 2 (H3N2) antigens, vaccination might confer dual imprinting to both HA groups or prevent strong imprinting against either HA group—or it could have no effect beyond delaying the age of imprinting via the first natural infection. Our sensitivity analyses demonstrated that, given the low IAV vaccination coverage in H5N1- and H7N9-affected countries, none of these effects would change our study's conclusions (fig. S7). However, to properly inform early childhood vaccine policy, future research must determine which, if any, of these effects occur.

HA group imprinting also might complicate "universal" vaccination approaches targeting conserved HA epitopes. Our findings indicate potent, long-lasting cross-protection between subtypes, putatively based on such responses. However, universal vaccination may have to outperform natural infection in its ability to induce broad immunity in the face of previous imprinting. The persistence of group 1 imprinting in older adults, despite decades of natural exposure to H3N2 after 1968 (Fig. 2), as well as the relative weakness of group 2 anti-HA stem reactivities in these older cohorts (*11*), suggests that HA exposures later in life do not readily alter broadly protective responses in individuals already imprinted to a particular HA group. To be effective, would bivalent (group 1 and group 2 HA stem) universal vaccines need to be delivered to infants before natural IAV infection? Or might universal vaccines even impair natural, long-term protection of the sort we have detected against H5N1 and H7N9 if received before an individual's first natural IAV infection?

Our findings are consistent with the known potential for repeated infection by seasonal IAV subtypes. Group-matched imprinting, like other broadly protective IAV immune responses, is expected to protect against severe disease but not necessarily against infection (*8*, *12*, *14*). This parallels the reduced severity observed for repeat infections with seasonal strains (*22*, *23*, *25*). Furthermore, reexposure to a seasonal subtype typically elicits memory responses against the immunodominant HA head, which mask subdominant broadly protective responses involved in group-level imprinting (*26*).

For any country with suitable contact and demographic data, the methods shown here can provide rolling estimates of which age groups would be at highest risk for severe disease should particular novel HA subtypes emerge. Such projections could guide cohort- or region-specific prevention, preparation, or control. Quantitative projections of changes in R_{eff}—and hence pandemic risk—will require further research into the protection arising from matched imprinting: Is some fraction of cases prevented entirely, and by what factor is infectivity reduced in mild cases arising in protected individuals?

Our findings show that emergence risk cannot be considered in isolation, even for "novel" pathogens that have not circulated in humans before. These pathogens are commonly assumed to have a blank slate of immunologically naïve humans to infect, but cross-protection from related pathogens can generate substantial population immunity. When this community of related pathogens undergoes major shifts, as during influenza pandemics, the landscape of population immunity changes accordingly. Thus, emergence of novel pathogens can be governed by bottom-up control, with population immunity acting in an important and predictable manner to modulate the widely recognized effects of virological and ecological risk factors. This perspective opens new frontiers for quantitative and mechanistic analysis of emergence risk.

REFERENCES AND NOTES

1. Y. Qin *et al.*, *Clin. Infect. Dis.* **61**, 563–571 (2015).
2. B. J. Cowling *et al.*, *Lancet* **382**, 129–137 (2013).
3. A. J. Kucharski, W. J. Edmunds, *Epidemiol. Infect.* **143**, 1119–1124 (2015).
4. M. R. Sandbulte *et al.*, *PLOS Med.* **4**, e59 (2007).
5. C. Rivers, K. Lum, B. Lewis, S. Eubank, *PLOS Curr.* **5**, (2013).
6. B. J. Cowling *et al.*, *Euro Surveill.* **18**, 20475 (2013).
7. L. Wang *et al.*, *Emerg. Infect. Dis.* **20**, 1296–1305 (2014).
8. J. Wrammert *et al.*, *J. Exp. Med.* **208**, 181–193 (2011).
9. N. Pica *et al.*, *Proc. Natl. Acad. Sci. U.S.A.* **109**, 2573–2578 (2012).
10. G.-M. Li *et al.*, *Proc. Natl. Acad. Sci. U.S.A.* **109**, 9047–9052 (2012).
11. M. S. Miller *et al.*, *Sci. Transl. Med.* **5**, 198ra107 (2013).
12. F. Krammer *et al.*, *J. Virol.* **88**, 2340–2343 (2014).
13. A. H. Ellebedy *et al.*, *Proc. Natl. Acad. Sci. U.S.A.* **111**, 13133–13138 (2014).
14. P. Palese, T. T. Wang, *MBio* **2**, e00150-11 (2011).
15. T. Francis, *Proc. Am. Philos. Soc.* **104**, 572–578 (1960).
16. J. Lessler *et al.*, *PLOS Pathog.* **8**, e1002802 (2012).
17. M. Smallman-Raynor, A. D. Cliff, *Emerg. Infect. Dis.* **13**, 510–512 (2007).
18. M. Terajima, M. D. T. Co, F. A. Ennis, *Lancet Infect. Dis.* **14**, 101 (2014).
19. M. Worobey, G.-Z. Han, A. Rambaut, *Proc. Natl. Acad. Sci. U.S.A.* **111**, 8107–8112 (2014).
20. A. Sauerbrei, R. Schmidt-Ott, H. Hoyer, P. Wutzler, *Med. Microbiol. Immunol. (Berl.)* **198**, 93–101 (2009).
21. A. Sauerbrei *et al.*, *Euro Surveill.* **19**, 20687 (2014).
22. K. L. Laurie *et al.*, *J. Infect. Dis.* **202**, 1011–1020 (2010).
23. J. L. Schulman, E. D. Kilbourne, *J. Bacteriol.* **89**, 170–174 (1965).
24. K. V. Houser, M. B. Pearce, J. M. Katz, T. M. Tumpey, *J. Virol.* **87**, 13480–13489 (2013).
25. T. M. Wilkinson *et al.*, *Nat. Med.* **18**, 274–280 (2012).
26. S. F. Andrews *et al.*, *Sci. Transl. Med.* **7**, 316ra192 (2015).
27. I. Kohler *et al.*, *Clin. Infect. Dis.* **59**, 1386–1393 (2014).
28. J. Sui *et al.*, *Nat. Struct. Mol. Biol.* **16**, 265–273 (2009).

29. C. J. Henry Dunand *et al.*, *J. Clin. Invest.* **125**, 1255–1268 (2015).
30. J. Mossong *et al.*, *PLOS Med.* **5**, e74 (2008).
31. J. M. Read *et al.*, *Proc. Biol. Sci.* **281**, 20140268 (2014).
32. P. Horby *et al.*, *PLOS ONE* **6**, e16965 (2011).
33. C. C. Dauer, R. E. Serfling, *Am. Rev. Respir. Dis.* **83**, 15–28 (1961).
34. L. Simonsen, T. A. Reichert, M. A. Miller, *Int. Congr. Ser.* **1263**, 791–794 (2004).

ACKNOWLEDGMENTS

We thank the Lloyd-Smith lab and the Worobey lab for helpful comments, C. Viboud for providing insight into historic influenza data, T. Mega and S. Wu for assistance compiling data, B. Cowling for sharing poultry exposure data, and P. Horby for sharing Vietnam contact data. K.M.G. is supported by the National Institute of General Medical Sciences of the National Institutes of Health (T32GM008185). M.A. is supported by the National Science Foundation Graduate Research Fellowship (DGE-1144087). M.W. is supported by the David and Lucile Packard Foundation. J.O.L-S. is supported by the National Science Foundation (EF-0928690); the Research and Policy for Infectious Disease Dynamics (RAPIDD) program of the Science and Technology Directorate, Department of Homeland Security; and Fogarty International Center, National Institutes of Health. The content is solely the responsibility of the authors and does not necessarily represent the official views of the National Institutes of Health. The authors declare no competing financial interests. Case data and code for model fitting are available as supplementary data files. Requests for materials should be addressed to M.W. or J.O.L.-S.

SUPPLEMENTARY MATERIALS

www.sciencemag.org/content/354/6313/722/suppl/DC1
Materials and Methods
Supplementary Text
Figs. S1 to S12
Tables S1 to S4
Database S1
References (*35*–*75*)

14 May 2016; accepted 3 October 2016
10.1126/science.aag1322

REPORTS

NANOPHOTONICS

Single-molecule optomechanics in "picocavities"

Felix Benz,[1] Mikolaj K. Schmidt,[2] Alexander Dreismann,[1] Rohit Chikkaraddy,[1] Yao Zhang,[2] Angela Demetriadou,[2,3] Cloudy Carnegie,[1] Hamid Ohadi,[1] Bart de Nijs,[1] Ruben Esteban,[2] Javier Aizpurua,[2]* Jeremy J. Baumberg[1]*

Trapping light with noble metal nanostructures overcomes the diffraction limit and can confine light to volumes typically on the order of 30 cubic nanometers. We found that individual atomic features inside the gap of a plasmonic nanoassembly can localize light to volumes well below 1 cubic nanometer ("picocavities"), enabling optical experiments on the atomic scale. These atomic features are dynamically formed and disassembled by laser irradiation. Although unstable at room temperature, picocavities can be stabilized at cryogenic temperatures, allowing single atomic cavities to be probed for many minutes. Unlike traditional optomechanical resonators, such extreme optical confinement yields a factor of 10^6 enhancement of optomechanical coupling between the picocavity field and vibrations of individual molecular bonds. This work sets the basis for developing nanoscale nonlinear quantum optics on the single-molecule level.

Coinage metal nanostructures support localized surface plasmons, which confine optical fields to much smaller than their wavelength (*1*). This extreme enhancement enables vibrational spectroscopy within small volumes, even down to single molecules (*2*, *3*). For many years, lateral resolution was believed to be ~10 nm (*4*); however, recent experiments have resolved the atomic structure of single molecules using tip-enhanced Raman spectroscopy (TERS) (*3*) and have demonstrated direct sequencing of RNA strands (*5*). Atomistic simulations also suggest that plasmonic confinement to atomic scales is possible (*6*).

Here, we show that light-activated mobilization of surface atoms in a plasmonic hotspot triggers the formation of additional "picocavities" bounded by a single gold atom. Because of strong optical field gradients that switch the Raman selection rules, the ultrasmall localization of light in these cavities alters the number and variety of vibrational modes of trapped molecules observed. The resulting cascaded ultrastrong plasmonic confinement pumps specific molecular bonds, thereby creating nonthermal vibrational populations and constituting an optomechanical resonator. Remarkably, cryogenic control of the plasmonic nanometric cavity allows for systematic and stable monitoring of picocavity formation and disassembly. We thus demonstrate the possibility of resolving the dynamics of individual bonds within molecules. The existence, monitoring, and selective control of these picocavities will be important not only in photochemistry and photophysics but also as a platform for optomechanics, coherent control, and quantum information devices.

To produce stable, robust picocavities, we bypass complex scanning tip spectroscopies, instead using straightforward self-assembly to create "nanoparticle-on-mirror" (NPoM) geometries (Fig. 1A). Individual gold nanoparticles are spaced above a planar gold substrate by a nanometer-thick self-assembled monolayer (SAM) of biphenyl-4-thiol (Fig. 1B). Both the scattering and surface-enhanced Raman spectroscopy (SERS) signals from individual constructs are highly reproducible. All measurements are recorded at cryogenic temperatures, using a modified dark-field microscope and laser pumping at 633 nm (*7*). Low-temperature time-series SERS spectra from a typical gold nanoparticle (Fig. 1C) show vibrational modes that can be divided into two sets: A first set of vibrational modes is ever-present with constant intensity ("persistent lines") while a second "blinking" set of lines appears (arrows), disappears, and changes intensity over time.

Comparing the observed spectra with density functional theory (DFT) simulations confirms that both types of lines originate from the biphenyl-4-thiol SAM. However, in the blinking set, the relative intensities are altered, and normally Raman-inactive lines [infrared (IR) absorption lines] are mixed into the SERS spectrum. Each realization of this fluctuating state displays different lines for each enhancement, indicating selective excitation of specific vibrations (see fig. S13 for additional spectra). By contrast, SERS intensities in the persistent set are unaffected by the appearance of blinking lines. As shown below, this suggests that the blinking lines originate from a very small volume inside the plasmonic gap, containing only a single molecule. Such tight localization yields extremely high field gradients, accounting for the observation of Raman-inactive IR modes (*8*). Additional evidence implies that these small hotspots are actually sub-nm^3 volumes that we term "picocavities," each consisting of only one gold atom. Full electromagnetic simulations (Fig. 1, D and E) show that picocavities locally boost the near-field intensity, leaving the rest of the plasmonic hotspot unaffected. The high field intensity within the extremely small (<1 nm^3) local hotspot (Fig. 1, D and E) markedly enhances the SERS intensity of nearby molecules. We find that picocavities are spontaneously formed and destroyed under laser illumination but can be stabilized.

Picocavities are atomic-scale subnanometer structures forming an extreme class of optical localization that pushes electromagnetic coupling to the limit. To exploit and monitor their optical activity and to experimentally estimate the picocavity localization volume V_{loc}, we explore how they modify the Raman scattering when exciting a molecular vibration. This process is greatly amplified by the extreme confinement of the incident light in the plasmonic gap. As a result, the population n of excited vibrational states (at frequencies

[1]NanoPhotonics Centre, Cavendish Laboratory, Department of Physics, University of Cambridge, Cambridge CB3 0HE, UK. [2]Materials Physics Center CSIC-UPV/EHU and Donostia International Physics Center, 20018 Donostia–San Sebastián, Spain. [3]Blackett Laboratory, London SW7 2AZ, UK.
*Corresponding author. Email: jjb12@cam.ac.uk (J.J.B.); aizpurua@ehu.es (J.A.)

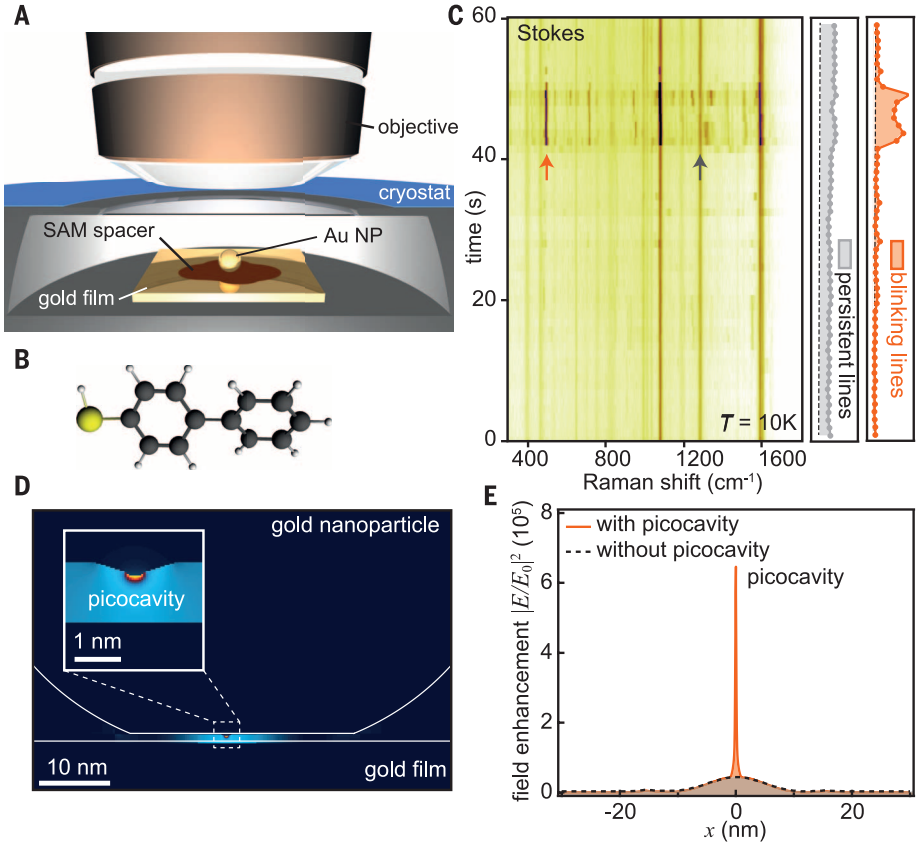

Fig. 1. Raman spectra from molecules in picocavities and near-field light distribution. (**A**) Schematic cooled nanoparticle-on-mirror (NPoM) geometry. (**B**) Biphenyl-4-thiol molecule in monolayer. (**C**) SERS time series from a single 90-nm NPoM with 60 μW/μm^2 pump (arrows correspond to persistent and blinking lines; see right). (**D** and **E**) Simulations of a faceted gold nanoparticle with and without atomic protrusion at x = 0 nm. (D) Near-field map. Inset is an enlarged view of the picocavity showing subnanometer localization of optical field. (E) Near-field intensity across the gap.

ω_m) is boosted above that provided by thermal excitations from the environment at temperature T,

$$n_{th} = \left[\exp\left(\frac{\hbar\omega_m}{k_B T}\right) - 1\right]^{-1} \quad (1)$$

by an additional contribution due to the optomechanical coupling of the plasmonic cavity with the molecular vibration (*9*), where $\hbar$ is the Planck constant divided by 2π and k_B is the Boltzmann constant. We first model the interaction of quantized plasmons with phonons in the classical limit of weak coupling strength g between the vibrations and cavity plasmons [with $g << (\omega_m, \kappa)$ for cavity decay rate κ] through the optomechanical Hamiltonian described in (*7*, *9*, *10*). This gives

$$n = \frac{\Gamma_{opt} n_{rad} + \Gamma_m n_{th}}{\Gamma_{opt} + \Gamma_m} \quad (2)$$

where $\Gamma_{opt}(V_{loc}) \propto g^2 I$ is the volume-dependent optomechanical amplification rate, which in turn depends on optomechanical coupling strength $g(V_{loc})$ and laser power I, and Γ_m is the phonon decay rate (*7*, *9*). At T = 10 K ($k_B T$ = 0.9 meV), population n_{th} can be neglected because vibrational energies ($\hbar\omega_m$ = 124 meV for 1000 cm^{-1}) greatly exceed thermal energies. Depending on the detuning of the laser from the cavity, Γ_{opt} can either be positive (damping the vibration) or negative (amplifying the vibration). For sufficiently high intensities or sufficiently strong coupling, amplification (Γ_{opt}) overcomes phonon decay (Γ_m), creating a nonthermal phonon population (dominating when $\Gamma_{opt} n_{rad} >> \Gamma_m n_{th}$). Experimentally measuring this vibrational state population at increasing laser power allows evaluation of the Raman localization volume V_{loc} (*7*).

In the regime of vibrational pumping, n can be quantified by simultaneously recording both the Stokes and anti-Stokes parts of the SERS spectrum and evaluating their ratio for each mode (*11*, *12*). The plasmon contribution to the population (arising from the quantum backaction mechanism) follows

$$n_{rad} = \left[4\omega_m(\omega_c - \omega_\ell)\mathcal{L}_-\right]^{-1} \quad (3)$$

where

$$\mathcal{L}_\pm = \left[(\omega_c - \omega_\ell \pm \omega_m)^2 + \left(\frac{\kappa}{2}\right)^2\right]^{-1} \quad (4)$$

is a Lorentzian profile of the field enhancement supported by the cavity resonance at frequency ω_c, illuminated by the laser with frequency ω_ℓ. The ratio of anti-Stokes to Stokes scattering is then

$$\frac{S(\omega_{aS})}{S(\omega_S)} \approx \left(\frac{\omega_\ell + \omega_m}{\omega_\ell - \omega_m}\right)^4 \frac{\mathcal{L}_-}{\mathcal{L}_+} \frac{n}{1+n} \quad (5)$$

Although the above analytic formalism is correct for coupling $g << \kappa$, corrections are needed from the full numerical solution of the underlying optomechanical Hamiltonian [see implementation in (*7*)] to properly extract estimates of the localization volume.

Low-temperature SERS shows that prominent anti-Stokes SERS lines blue-shifted from the laser (Fig. 2A) appear always and only when the additional fluctuating Stokes lines are present. Time-series SERS spectra (Fig. 2B) show that none of the persistent Stokes lines are seen in the anti-Stokes spectra (dashed lines), reflecting the low excited-state population at 10 K for most molecules within the NPoM gap but outside the picocavity. Taking the measured anti-Stokes/Stokes ratio, we use Eq. 5 in the thermal limit (setting $n = n_{th}$) to extract for each vibrational mode an effective temperature (marked in Fig. 2A), far exceeding the sample temperature (up to 2000 K for certain lines). These effective temperatures are different for each line and increase with increasing vibrational energy, thus providing clear proof that the vibrational populations are nonthermal and that the pumping contribution to the population cannot be ignored. Plasmons do not directly heat the molecules, as shown by the absence of characteristic anti-Stokes background signals, previously shown to track the temperature of metallic nanostructures (*13*); the gold remains cold throughout, as expected for these sub–100-μW optical powers.

In such time-series SERS scans, whenever the picocavity regime appears, spectral wandering of the vibrational energies of 0.1 to 1 cm^{-1} s^{-1} is seen (Fig. 2B), which is a typical signature of single-molecule SERS (*14*, *15*). This provides additional confirmation that the blinking lines come from a very small subregion of the NPoM gap containing individual molecules. Further proof comes from observation of IR-active lines, which arise from the strong field gradients around the picocavity that alter the SERS selection rules (*3*, *8*) and necessarily require field localization of <0.5 nm, consistent with picocavities in the nanogap. Theoretically, this effect can be reproduced by recalculating the SERS spectrum from the full Raman tensor (obtained by DFT) assuming only local illumination. Using a field localization of 0.4 nm, extracted from the picocavity field confinement lateral width (Fig. 1D), the observed experimental spectra (Fig. 2, C and D, bottom) can be modeled only when repositioning the picocavity relative to the molecule (Fig. 2, C and D, top; insets depict geometries used for each). To reproduce our experimental spectra, confinement on the order of a

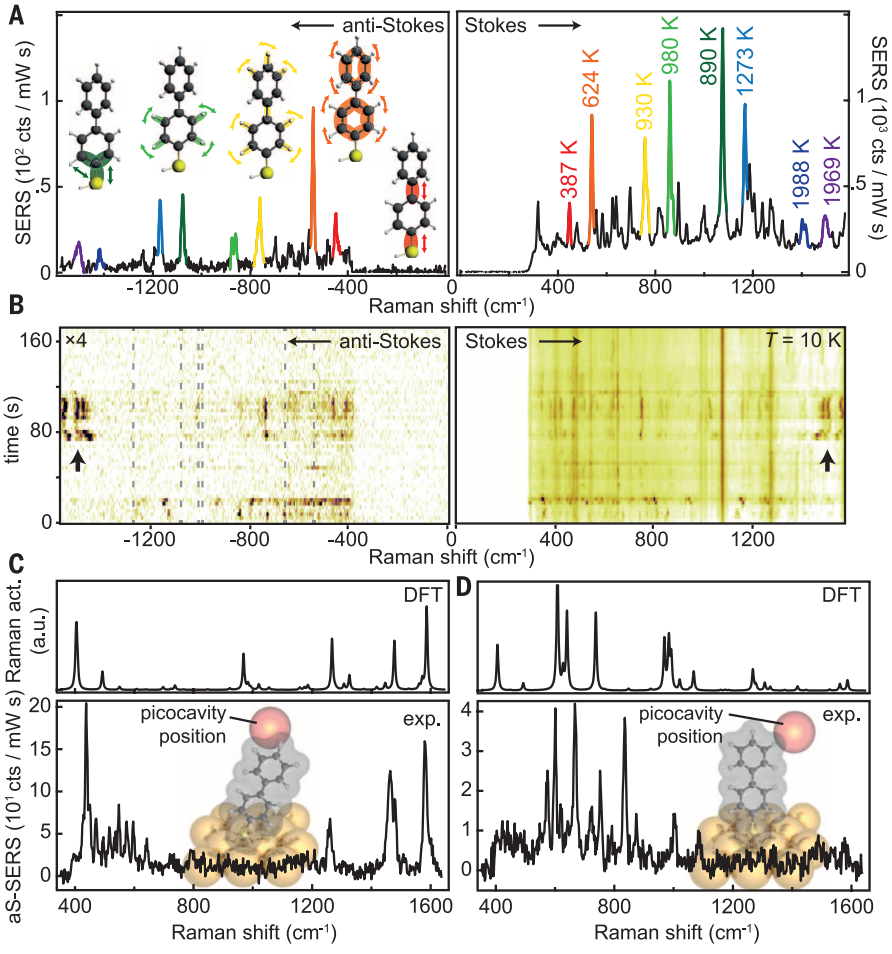

Fig. 2. Raman spectra reveal changes of SERS selection rules. (**A**) Anti-Stokes/Stokes spectra at a time when additional picocavity-induced lines are present. Colors correspond to same lines on Stokes and anti-Stokes sides, with vibrational eigenmodes and effective temperatures shown. (**B**) Time-series anti-Stokes and Stokes SERS. Dashed lines (aS) mark expected aS line positions corresponding to ever-present (persistent) S lines from the many molecules in the larger nanocavity. (**C** and **D**) Comparison of two experimental spectra (bottom) with DFT simulated spectra (top) under the assumption of atomic-scale field confinement (inset shows geometries; red sphere denotes field localization for simulations).

single gold atom is required (*7*), giving direct proof for the atomic confinement of the optical field. In this regime, individual bonds within molecules can be accessed.

Using our Raman formalism to extract V_{loc} requires confirmation that vibrational pumping dominates, for which a linear power dependence of the anti-Stokes/Stokes ratio is expected (*9*, *11*, *12*), as seen from Eq. 5 for small n. Previous investigations have encountered difficulty in stabilizing nanostructures while measuring such power dependences. We avoided this problem by modifying our experiments to identify in real time whenever blinking lines appear and then immediately cycling the laser power (Fig. 3A shows typical data). We thus repeatedly recorded anti-Stokes/Stokes ratios for different 633-nm laser powers. Extracting power series for several different lines (Fig. 3, B and C), recorded on different nanoparticles at different times, always gave a quadratic power dependence of the anti-Stokes signal and a linear power dependence for the anti-Stokes/Stokes ratio (and hence the phonon population), supporting the presence of vibrational pumping. However, the slope of these linear fits changed from mode to mode and also differed for different realizations on different nanoparticles. This suggests that the slope is a measure of picocavity geometry, which controls the different optomechanical coupling strengths of the molecular vibrations, because $g \propto 1/V_{loc}$.

From more than 50 picocavities, we observed coupling strengths $\hbar g$ = 5 to 40 meV (Fig. 3D), reaching $g/\kappa \sim 0.2$. From Eq. 2, such high coupling strengths [compared to <1 μeV for conventional optomechanical systems (*9*, *16*–*19*)] correspond to extremely small Raman localization volumes of <1 nm^3 (*7*). This extremely tight localization agrees with electromagnetic simulations using atomic-scale features in the gap region, also giving lateral localizations of ~0.23 nm [full width at half maximum (FWHM) of intensity; Fig. 1E], as well as with previous theory

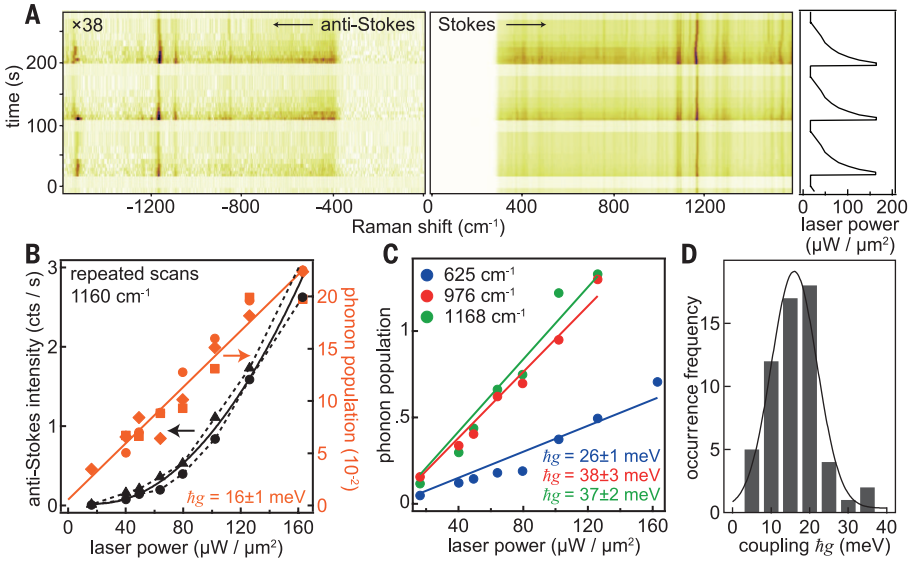

Fig. 3. Vibrational pumping of molecular vibrations in picocavities. (**A**) SERS time scan for varying laser power (shown on right). (**B**) Extracted laser power dependence of anti-Stokes intensity and phonon population for different measurements on the same picocavity. (**C**) Power dependence of phonon population for different vibrational modes in the same picocavity. (**D**) Distribution of observed optomechanical coupling strengths g.

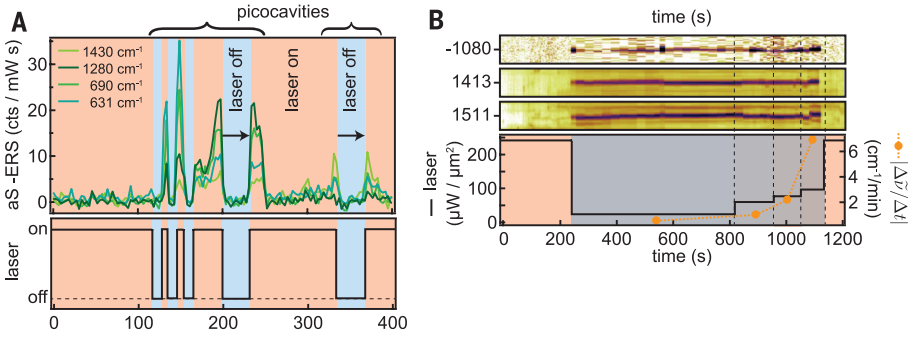

Fig. 4. Picocavity stability in the dark. (**A**) Anti-Stokes intensities as the laser (bottom) is switched on and off demonstrate the picocavity stability, which persists (arrows) without the laser. (**B**) Picocavities are also stable at low laser powers. Anti-Stokes intensities are observed as laser power is dropped by a factor of 10 when picocavity formation is detected. After waiting 10 min, the power is increased stepwise. SERS intensities are normalized by laser power. The lower graph shows the simultaneously measured rate of spectral wandering (orange) versus laser power.

predicting atomic-scale confinement of optical fields (*6*, *20*). This optical confinement explains atomic resolution in tip-based experiments (*3*, *5*) and approaches the quantum limit derived previously (*4*), $V \sim Rd_{QR}^2$, but with the radius of curvature R now set by the size of single atoms $R \sim 0.15$ nm and tunneling length scale $d_{QR} \sim 0.4$ nm, giving $V_{\min} \sim 10^{-2}$ nm^3. We highlight the strongly inhomogeneous distribution of the picocavity field within the plasmonic gap, resulting in a complex relationship between the Raman localization volume and standard quantum optical definitions of mode volume (*7*).

To account for both formation and disassembly of picocavities at cryogenic temperatures requires atomic surface reconstructions facilitated by irradiation. To demonstrate the dependence on laser power, we immediately switched off the laser once the formation of a picocavity was detected. After a delay time, varied between 3 and 30 s, the laser was switched on again (Fig. 4A), allowing us to examine whether the atomic configuration relaxes in the dark. In all cases, we found that the SERS spectra reappear with exactly the same strength as before the laser is switched off (see also fig. S14). This further proves that the additional strong Stokes and anti-Stokes SERS lines originate from a robust formation of these picocavities and cannot be attributed to heating of the molecules; for a process involving heating, one instead expects the system to cool back down once the laser is switched off.

Even when the laser power was reduced instead of being switched off, the lifetime of these picocavities was greatly extended (Fig. 4B), thus allowing continuous monitoring. A picocavity was easily stabilized for more than 10 min by reducing the laser power by a factor of 10 after cavity formation was observed. After 10 min at the lower laser power, the power was increased stepwise, and disassembly was observed at a laser power density of 100 μW/μm^2. Both formation and disassembly of the picocavity were abrupt (<1 s), whereas fluctuations of the vibrational energies were found to increase as the laser power increased. Hence, the fluctuation of the molecular vibrational energies is possibly driven by Au atom movement (see Fig. 4B and fig. S12).

Laser illumination not only destabilizes the picocavity atomic configurations but also is crucial in their formation. To demonstrate this, we recorded several time-series SERS scans for different laser powers and extracted the occurrence frequency of picocavity formation. We found a clear Arrhenius-type behavior with critical laser power density $P_c = 256 \pm 15$ μW/μm^2, corresponding to an energy of 0.7 eV (*7*). This energy is comparable to previously reported activation energies for gold adatom surface diffusion of 0.9 eV (*21*). Repeating the experiments using silver instead of gold, we observed a higher critical power density of $P_c = 388 \pm 48$ μW/μm^2 but otherwise similar behavior. We cannot yet identify whether this critical P_c corresponds to a characteristic thermal hopping barrier or to optical forces arising from the extreme field gradients around single-atom protrusions. However, we note that formation of a picocavity can be facilitated by the stability of gold-thiol "staples": Two thiols cooperatively pull a gold atom into an elevated position, forming a bridgelike arrangement [see (*22*) and references therein].

Our findings are also in line with observations that SERS blinking has both a thermal-activated and a light-activated component (*23*). Picocavities only appear in near-field–sensitive measurements such as SERS, whereas no changes are seen in far-field scattering that depend only on the properties of the larger hosting nanocavity. Our findings suggest that picocavities are omnipresent in SERS and TERS measurements on nanoscale plasmonic hotspots (such as colloidal aggregates, dimers, and NPoMs) and are responsible for single-molecule and atomic resolution that has been obtained. The extreme optical confinement yields selective amplification of molecular vibrations of only a few bonds within the single molecule isolated by each picocavity, presumably depending on the exact mutual configuration of Au atom protrusion and bound thiol orientation. Optical field strengths of 0.3 V/nm here may be further exploited.

Picocavities are stable at cryogenic temperatures but at room temperature are in constant dynamical creation and destruction. They form as a result of photon-assisted surface reconstruction of gold. Stabilizing these picocavities while probing them takes plasmonic-molecule coupling to the extreme and opens widespread possibilities for studying and exploiting light-molecule coupling—for instance, in molecular interactions, chemical reactions, superradiant emission, electron transfers, and single-molecule electrochemistry—and advances the fundamental access of light to the building blocks of matter.

REFERENCES AND NOTES

1. W. L. Barnes, A. Dereux, T. W. Ebbesen, *Nature* **424**, 824–830 (2003).
2. K. Kneipp *et al.*, *Phys. Rev. Lett.* **78**, 1667–1670 (1997).
3. R. Zhang *et al.*, *Nature* **498**, 82–86 (2013).
4. K. J. Savage *et al.*, *Nature* **491**, 574–577 (2012).
5. E. Bailo, V. Deckert, *Angew. Chem. Int. Ed.* **47**, 1658–1661 (2008).
6. M. Barbry *et al.*, *Nano Lett.* **15**, 3410–3419 (2015).
7. See supplementary materials on *Science* Online.
8. M. Moskovits, D. P. DiLella, K. J. Maynard, *Langmuir* **4**, 67–76 (1988).
9. M. K. Schmidt, R. Esteban, A. González-Tudela, G. Giedke, J. Aizpurua, *ACS Nano* **10**, 6291–6298 (2016).
10. P. Roelli, C. Galland, N. Piro, T. J. Kippenberg, *Nat. Nanotechnol.* **11**, 164–169 (2016).
11. R. C. Maher, C. M. Galloway, E. C. Le Ru, L. F. Cohen, P. G. Etchegoin, *Chem. Soc. Rev.* **37**, 965–979 (2008).
12. D. R. Ward, D. A. Corley, J. M. Tour, D. Natelson, *Nat. Nanotechnol.* **6**, 33–38 (2011).
13. J. T. Hugall, J. J. Baumberg, *Nano Lett.* **15**, 2600–2604 (2015).
14. S. Nie, S. R. Emory, *Science* **275**, 1102–1106 (1997).
15. C. C. Neacsu, J. Dreyer, N. Behr, M. B. Raschke, *Phys. Rev. B* **73**, 193406 (2006).
16. R. Esteban, T. V. Teperik, J. J. Greffet, *Phys. Rev. Lett.* **104**, 026802 (2010).
17. X. Zeng *et al.*, *Opt. Express* **22**, 14517–14523 (2014).
18. M. Liu, T.-W. Lee, S. K. Gray, P. Guyot-Sionnest, M. Pelton, *Phys. Rev. Lett.* **102**, 107401 (2009).
19. X.-W. Chen, M. Agio, V. Sandoghdar, *Phys. Rev. Lett.* **108**, 233001 (2012).
20. X. Chen, J. E. Moore, M. Zekarias, L. Jensen, *Nat. Commun.* **6**, 8921 (2015).
21. T.-S. Lin, Y.-W. Chung, *Surf. Sci.* **207**, 539–546 (1989).
22. T. Bürgi, *Nanoscale* **7**, 15553–15567 (2015).
23. S. R. Emory, R. A. Jensen, T. Wenda, M. Han, S. Nie, *Faraday Discuss.* **132**, 249–259 (2006).

ACKNOWLEDGMENTS

Supported by Project FIS2013-41184-P from MINECO (Ministerio de Economía y Competitividad) and IT756-13 from the Basque government consolidated groups (M.K.S., Y.Z., A. Demetriadou, R.E., and J.A.); the Winton Programme for the Physics of Sustainability (F.B.); the Dr. Manmohan Singh scholarship from St. John's College (R.C.); the UK National Physical Laboratory (C.C.); the Fellows Gipuzkoa Program of the Gipuzkoako Foru Aldundia via FEDER funds of the European Union "Una manera de hacer Europa" (R.E.); UK Engineering and Physical Sciences Research Council grants EP/G060649/1 and EP/L027151/1; and European Research Council grant LINASS 320503. Source data can be found at DOI: 10.17863/CAM.1675.

SUPPLEMENTARY MATERIALS

www.sciencemag.org/content/354/6313/726/suppl/DC1
Materials and Methods
Figs. S1 to S16
References (*24*–*35*)

11 July 2016; accepted 30 September 2016
10.1126/science.aah5243

INORGANIC CHEMISTRY

Coordination-induced weakening of ammonia, water, and hydrazine X–H bonds in a molybdenum complex

Máté J. Bezdek, Sheng Guo, Paul J. Chirik*

Although scores of transition metal complexes incorporating ammonia or water ligands have been characterized over the past century, little is known about how coordination influences the strength of the nitrogen-hydrogen and oxygen-hydrogen bonds. Here we report the synthesis of a molybdenum ammonia complex supported by terpyridine and phosphine ligands that lowers the nitrogen-hydrogen bond dissociation free energy from 99.5 (gas phase) to an experimentally measured value of 45.8 kilocalories per mole (agreeing closely with a value of 45.1 kilocalories per mole calculated by density functional theory). This bond weakening enables spontaneous dihydrogen evolution upon gentle heating, as well as the hydrogenation of styrene. Analogous molybdenum complexes promote dihydrogen evolution from coordinated water and hydrazine. Electrochemical and theoretical studies elucidate the contributions of metal redox potential and ammonia acidity to this effect.

Ammonia and water are ubiquitous small molecules with strong bonds between hydrogen and the central atom (*1*). For over a century, transition metal–ammine (NH_3) and –aquo (H_2O) compounds have defined bonding paradigms in chemistry (*2*), found application in cancer therapy (*3*), and promoted important fundamental chemical reactions such as electron transfer that rely on the inertness of the N–H or O–H bonds in the supporting ligands (Fig. 1) (*4*).

Common strategies for activation of ammonia and water include oxidative addition to a transition metal center (*5*–*7*), deprotonation by transition metal hydrides (*8*), reaction with bimetallic compounds (*9*), cooperative chemistry between a transition metal and a supporting ligand (*10*–*12*), and element-hydrogen (X–H) bond cleavage through reaction with main group compounds (*13*–*16*). Using these strategies, however, activation of the strong X–H bond is not coupled to H–H bond formation (*17*).

An alternative and less commonly explored strategy is homolytic cleavage of the X–H bond. Because of the high gas-phase bond dissociation free energies (BDFEs; 99.5 and 111.0 kcal/mol for NH_3 and H_2O, respectively) (*1*), interaction with a transition metal or other appropriate reagent is necessary to induce bond weakening. As shown in Fig. 1, most classical transition metal compounds with ammine (aquo) ligands have N–H (O–H) bond strengths that are only slightly perturbed from the gas-phase value. Because experimental data are lacking, we used density functional theory (DFT) to compute N–H BDFEs.

Coordination-induced bond weakening, whereby interaction of a ligand results in a considerable lowering of the X–H BDFE, has recently been identified or implicated in rare instances (*18*–*23*) and has been applied by Knowles's group (*24*) and others (*25*–*27*) in reactions of organic molecules involving N–H and O–H bonds, respectively. Cuerva's group (*26*, *27*) and ours (*28*) have demonstrated the effectiveness of bis(cyclopentadienyl) titanium(III) complexes in weakening the O–H bonds of water and the N–H bonds of ammonia. However, this strategy has not yet been shown to be capable of weakening the N–H or O–H bond sufficiently to provide the thermodynamic driving force for H_2 evolution ($BDFE_{X-H}$ < gas-phase free energy of H-atom formation = 48.6 kcal/mol; Fig. 1) (*1*). In $(\eta^5\text{-}C_5Me_4SiMe_3)_2TiCl(NH_3)$, for example, the N–H BDFE was calculated to be 61 kcal/mol, too high to spontaneously form H_2 (*28*). Here we describe a terpyridine bis(phosphine) molybdenum complex that, by virtue of its coordination environment and redox properties, enables H_2 evolution from coordinated ammonia, water, and hydrazine. This effect is termed "nonclassical" coordination.

Chloride abstraction from (^{Ph}Tpy)(PPh_2Me)$_2$Mo(Cl) (**1-Cl**; ^{Ph}Tpy, 4′-Ph-2,2′,6′,2″-terpyridine; Ph, phenyl) (*29*) with $NaBArF^{24}$ {ArF^{24}, $[C_6H_3\text{-}3,5\text{-}(CF_3)_2]_4$} in benzene solution at ambient temperature in the presence of 1 equivalent of ammonia resulted in isolation of a yellow-green crystalline solid identified as [(^{Ph}Tpy)(PPh_2Me)$_2$Mo(NH_3)] ($BArF^{24}$) [**(1-NH$_3$)$^+$**] in 77% yield (Fig. 2A). The formally Mo(I) ammonia complex has a spin S = 1/2 ground state [effective magnetic moment (μ_{eff}) = 1.7 Bohr magneton (μ_B), 23°C by magnetic susceptibility balance] and exhibits an isotropic electron paramagnetic resonance (EPR) signal (isotropic g value = 1.988) in fluid benzene solution (23°C) with hyperfine coupling to two 100%-abundant I = 1/2 phosphorus nuclei {isotropic hyperfine coupling constant [A_{iso}(^{31}P)] = 33 MHz}, as well as to the two naturally occurring spin-active molybdenum nuclei, ^{95}Mo and ^{97}Mo [A_{iso}($^{95/97}$Mo) = 80 MHz; I = 5/2; 15.92% ^{95}Mo and 9.55% ^{97}Mo]. The solid-state structure was

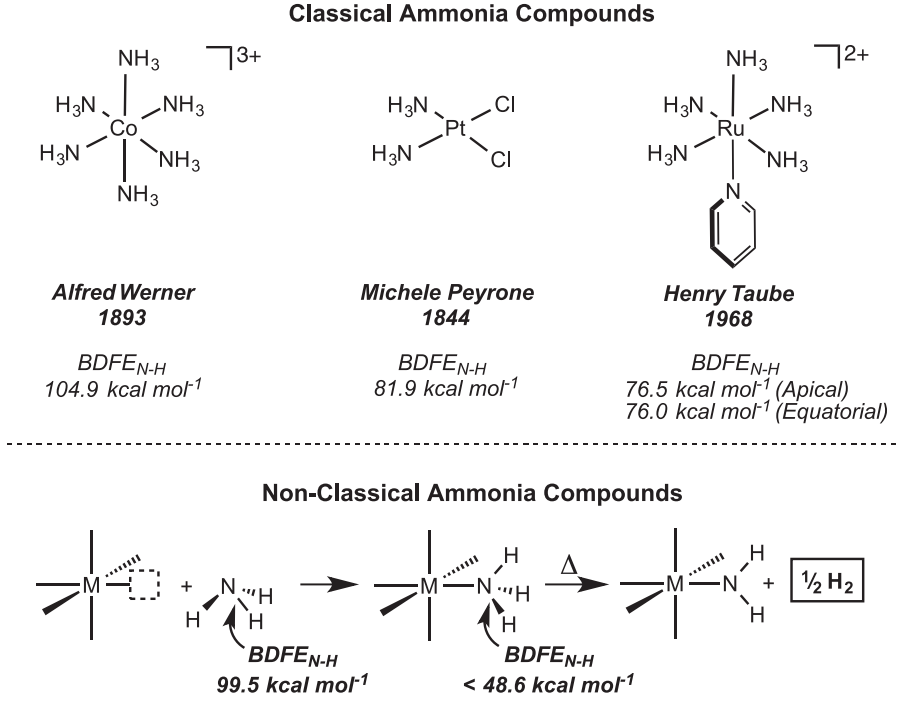

Fig. 1. Comparison of classical coordination compounds of ammonia and nonclassical compounds that enable bond weakening by coordination, which in turn enables hydrogen evolution. Classical compounds are from (*2*–*4*), with N–H BDFEs computed using DFT. Nonclassical coordination is defined as a ligand containing X–H bonds that are thermodynamically unstable to H_2 loss. M, metal.

Department of Chemistry, Princeton University, Princeton, NJ 08544, USA.
*Corresponding author. Email: pchirik@princeton.edu

determined by x-ray diffraction and confirms formation of an octahedral molybdenum complex with the ammonia ligand trans to the central pyridine of the terpyridine chelate with a Mo–NH_3 bond distance of 2.236(3) Å. The solid-state infrared spectrum (KBr) of **(1-NH_3)$^+$** exhibits three isotopically sensitive low-energy vibrations at 2919, 2899, and 2847 cm^{-1}, consistent with a coordinated ammine ligand. These vibrations are likely perturbed by hydrogen bonding, given that the solid-state structure of **(1-NH_3)$^+$** revealed a close [2.395(3) Å] H-F interaction between the ammine hydrogens and the CF_3 group of the $(BArF^{24})^-$ counterion (Fig. 2B).

Experiments were conducted to establish an upper bound for the N–H bond strength in **(1-NH_3)$^+$**. Addition of 1 equivalent of 2,4,6-tri-*tert*-butylphenoxyl radical ($^tBu_3C_6H_2O$•) resulted in rapid H-atom abstraction from the ammonia ligand to quantitatively yield the olive-green diamagnetic molybdenum(II) amide complex, [(^{Ph}Tpy)(PPh_2Me)$_2$Mo(NH_2)](BArF^{24}) [**(1-NH_2)$^+$**], setting the BDFE of the N–H bond as <77 kcal/mol (*30*) (Fig. 2A). The ^{1}H nuclear magnetic resonance (NMR) spectrum of **(1-NH_2)$^+$** in benzene-d_6 shows the number of resonances expected for a C_{2v} symmetric compound with a diagnostic downfield triplet centered at 10.02 parts per million (ppm) (*J*-coupling constant $^3J_{P-H}$ = 16.7 Hz) assigned to the terminal amide hydrogens. The ^{15}N NMR spectrum of **(1-$^{15}NH_2$)$^+$** (prepared from $^{15}NH_3$) in benzene-d_6 features a triplet centered at 235.5 ppm ($^1J_{N-H}$ = 68.5 Hz), as well as a doublet in the ^{31}P NMR spectrum at 15.58 ppm ($^2J_{P-N}$ = 4.1 Hz). The infrared spectrum (KBr) of **(1-NH_2)$^+$** contains two peaks assignable to a -NH_2 fragment at 3354 and 3287 cm^{-1} that shift to 2512 and 2426 cm^{-1}, respectively, in the deuterated isotopolog, **(1-ND_2)$^+$**. The solid-state structure was determined by x-ray diffraction, establishing an octahedral molybdenum complex in analogy with **(1-NH_3)$^+$**. The Mo–NH_2 bond distance of 1.994(3) Å is considerably contracted compared with the Mo–NH_3 distance of 2.236(3) Å in **(1-NH_3)$^+$**, consistent with formation of an anionic ligand.

To more accurately define the N–H bond strength in **(1-NH_3)$^+$**, the ammonia complex was treated with [(η^5-C_5Me_5)Cr(CO_3)]$_2$ (Fig. 2A). Immediate and quantitative formation of **(1-NH_2)$^+$** and (η^5-C_5Me_5)Cr(CO_3)(H) established an N–H bond strength of <62 kcal/mol (*31*). DFT calculations for **(1-NH_3)$^+$** gave a computed N–H bond strength of 45.1 kcal/mol, consistent with H-atom abstraction experiments.

The very low N–H bond strength of coordinated ammonia in **(1-NH_3)$^+$** suggested that spontaneous H_2 formation should be possible. Gently heating a benzene-d_6 solution of **(1-NH_3)$^+$** to 60°C for 6 hours resulted in clean and quantitative formation of **(1-NH_2)$^+$** with concomitant H_2 evolution, as confirmed by Toepler pump experiments (92% yield of H_2; Fig. 3A). Carrying out the reaction in the presence of 1.5 equivalents of styrene (per Mo) furnished ethylbenzene in 25% yield, providing additional evidence for coordination-induced bond weakening and the application of ammonia as a hydrogen storage medium for

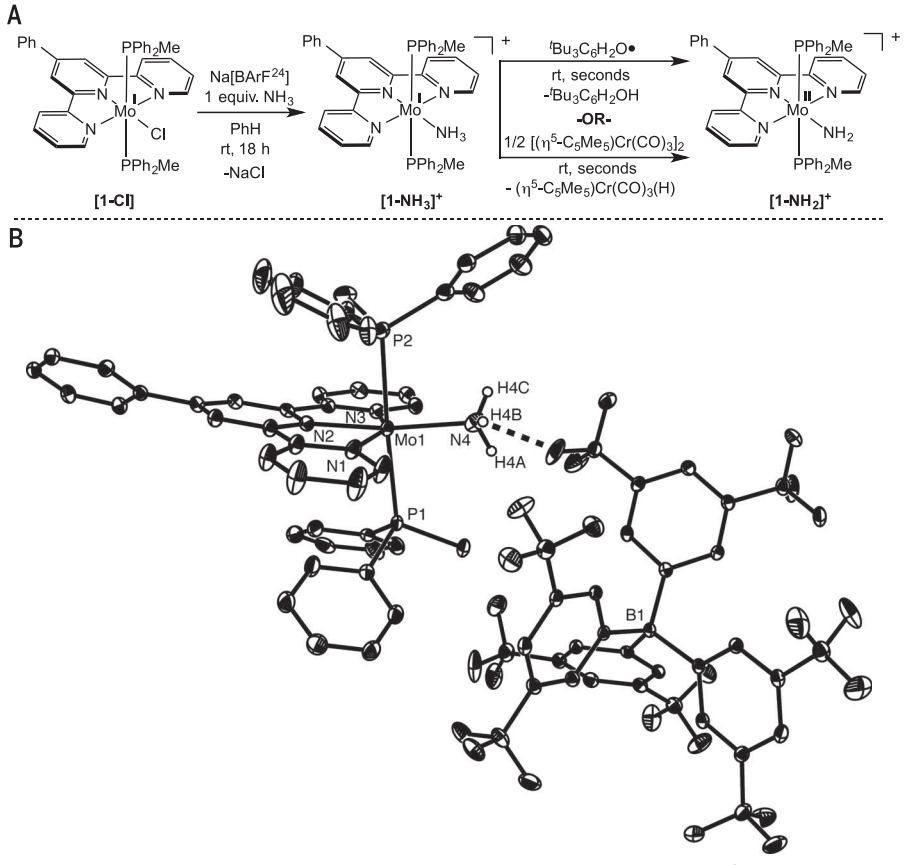

Fig. 2. N–H bond weakening in Mo-coordinated ammonia. (**A**) Synthesis of **(1-NH_3)$^+$** and hydrogen-atom abstraction by using substituted phenoxyl radical and chromium reagents. (**B**) Solid-state structure of **(1-NH_3)$^+$** illustrated using 30% probability ellipsoids. Hydrogen atoms, except those connected to N4, have been omitted for clarity. rt, room temperature; h, hours; equiv., equivalent.

the reduction of organic molecules. Dihydrogen evolution accompanied ethylbenzene formation and is likely the source of the relatively low yield. A maximum yield of 50% is possible based on reaction stoichiometry (2:1 molybdenum: styrene). The reduction of the olefin likely occurs through successive H-atom transfer steps, given that experiments in the presence of excess phosphine produced no inhibition. Performing the same procedure with **(1-ND_3)$^+$** yielded 1′,2′-d_2-ethylbenzene, 1′-d_1-ethylbenzene, 2′-d_1-ethylbenzene, and ethylbenzene in a 1:1:1:1 ratio, as detected by quantitative ^{13}C-NMR spectroscopy (fig. S1), with a combined yield of 25%. Overall, a 1:1 ratio of deuterium incorporation into the methylene and methyl positions of styrene was observed by ^{2}H NMR spectroscopy. These results are consistent with reversible H-atom transfer between **(1-ND_3)$^+$** and styrene and provide direct chemical evidence for the DFT-computed N–H BDFE of 45.1 kcal/mol, given that the C-H bond strength adjacent to a benzylic radical is known to be 45 kcal/mol (*32*, *33*).

Studies were also conducted to explore the pathway of H_2 evolution from **(1-NH_3)$^+$**. A crossover experiment was performed whereby a 1:1 mixture of **(1-NH_3)$^+$** and **(1-ND_3)$^+$** was heated to 60°C for 6 hours and the evolved gas was collected and analyzed. Both H_2 and D_2 were detected by ^{1}H and ^{2}H NMR spectroscopy, respectively, together with a nonstatistical amount of HD gas (H_2:HD was 5:1 by ^{1}H NMR integration). In addition, a statistical mixture of the isotopologs **(1-NH_2)$^+$**, **(1-NHD)$^+$**, and **(1-ND_2)$^+$** was detected at the completion of the reaction by ^{31}P NMR spectroscopy (fig. S2). The origin of the HD gas and the statistical mixture of molybdenum amides was investigated by a series of mixing experiments. Exchange among the products was evaluated by monitoring a 1:1 mixture of **(1-NH_2)$^+$** and **(1-ND_2)$^+$** in benzene-d_6 by ^{31}P NMR spectroscopy. A statistical distribution of the isotopologs **(1-NH_2)$^+$**, **(1-NHD)$^+$**, and **(1-ND_2)$^+$** was observed immediately after mixing at 23°C, demonstrating H-D exchange between products proceeding faster than hydrogen evolution. Isotopic exchange between the molybdenum ammine compound and the molybdenum amide product was also evaluated. Analysis of the ^{31}P NMR spectrum of a benzene-d_6 solution of a 1:1 mixture of **(1-ND_3)$^+$** and **(1-NH_2)$^+$** revealed immediate isotopic exchange into the molybdenum amide, demonstrating exchange between reactants and products. It is likely to be this pathway that accounts for the nonstatistical amount of HD gas observed, because dihydrogen evolution is slower

than the exchange between reactants and products. Because the starting ammine complexes are paramagnetic, N-H and N-D exchange between **(1-NH$_3$)$^+$** and **(1-ND$_3$)$^+$** were not directly measured. On the basis of these results, a pathway involving bimetallic H_2 evolution is disfavored; intermolecular chemistry with a large N-H or N-D kinetic isotope effect, however, cannot be rigorously eliminated.

The spontaneous liberation of H_2 from coordinated ammonia prompted investigation of other small molecules to determine the generality of hydrogen evolution from coordination-induced bond weakening. DFT calculations for the putative molybdenum aquo [**(1-OH$_2$)$^+$**] and hydrazine {**[1-(κ^2-N$_2$H$_4$)]$^+$**} complexes established exceedingly weak O–H and N–H bonds of 33.7 and 34.6 kcal/mol, respectively. Accordingly, treatment of a benzene solution containing **1-Cl** with 1 equivalent of NaBAr^{F24} in the presence of hydrazine or water furnished the diamagnetic yellow-brown solids [(^{Ph}Tpy)(PPh$_2$Me)$_2$Mo(κ^2-NHNH$_2$)](BAr^{F24}) {**[1-(κ^2-NHNH$_2$)]$^+$**} and [(^{Ph}Tpy)(PPh$_2$Me)$_2$Mo(OH)](BAr^{F24}) [**(1-OH)$^+$**] in 68 and 61% yields, respectively. In each case, H_2 gas evolution was confirmed by Toepler pump experiments (73 and 58% yield of H_2, respectively; Fig. 3, B and C). Although the benzene-d_6 ^{1}H, ^{13}C, and ^{31}P NMR spectra of **(1-OH)$^+$** are consistent with a C_{2v} symmetric compound, the side-on bound hydrazido ligand in **[1-(κ^2-NHNH$_2$)]$^+$** lowers the overall symmetry of the molecule to C_s. The syntheses of the deuterated isotopologs **[1-(κ^2-NDND$_2$)]$^+$** and **(1-OD)$^+$** were carried out using N_2D_4 and D_2O, respectively, and enabled assignment of the N–H/D and O–H/D peaks in the solid-state (KBr) infrared spectra. The N–H peaks of **[1-(κ^2-NHNH$_2$)]$^+$** appear at 3315, 3240, and 3186 cm^{-1} {2547, 2503, and 2434 cm^{-1} in **[1-(κ^2-NDND$_2$)]$^+$**}; the sharp OH peak of **(1-OH)$^+$** appears at 3558 cm^{-1} [2627 cm^{-1} in **(1-OD)$^+$**]. These results support the assignment of the hydrazido and hydroxo ligands in **[1-(κ^2-NHNH$_2$)]$^+$** and **(1-OH)$^+$**, respectively. The intermediacies of the putative hydrazine and water complexes **[1-(κ^2-N$_2$H$_4$)]$^+$** and **(1-OH$_2$)$^+$** were probed by performing the syntheses of **[1-(κ^2-NHNH$_2$)]$^+$** and **(1-OH)$^+$** in the presence of 1 equivalent of ^{t}Bu$_3$C$_6$H$_2$O•. ^{1}H NMR spectra revealed immediate and quantitative formation of **[1-(κ^2-NHNH$_2$)]$^+$** and **(1-OH)$^+$**, along with the stoichiometric generation of ^{t}Bu$_3$C$_6$H$_2$OH. No H_2 was evolved in these reactions, implying the intermediacy of metal-bound hydrazine and aquo complexes preceding H_2 evolution in the absence of a radical abstracting reagent.

The solid-state structures of **[1-(κ^2-NHNH$_2$)]$^+$** and **(1-OH)$^+$** were determined by x-ray diffraction (figs. S14 and S15). With **(1-OH)$^+$**, an octahedral coordination geometry around molybdenum was observed with trans phosphine ligands, similar to **(1-NH$_3$)$^+$** and **(1-NH$_2$)$^+$**. The coordination environment of seven-coordinate **[1-(κ^2-NHNH$_2$)]$^+$** is best described as pentagonal bipyramidal, where the tridentate terpyridine chelate and the bidentate hydrazido ligand occupy the vertices of an equatorial pentagon, with apical phosphine ligands completing the coordination sphere of molybdenum.

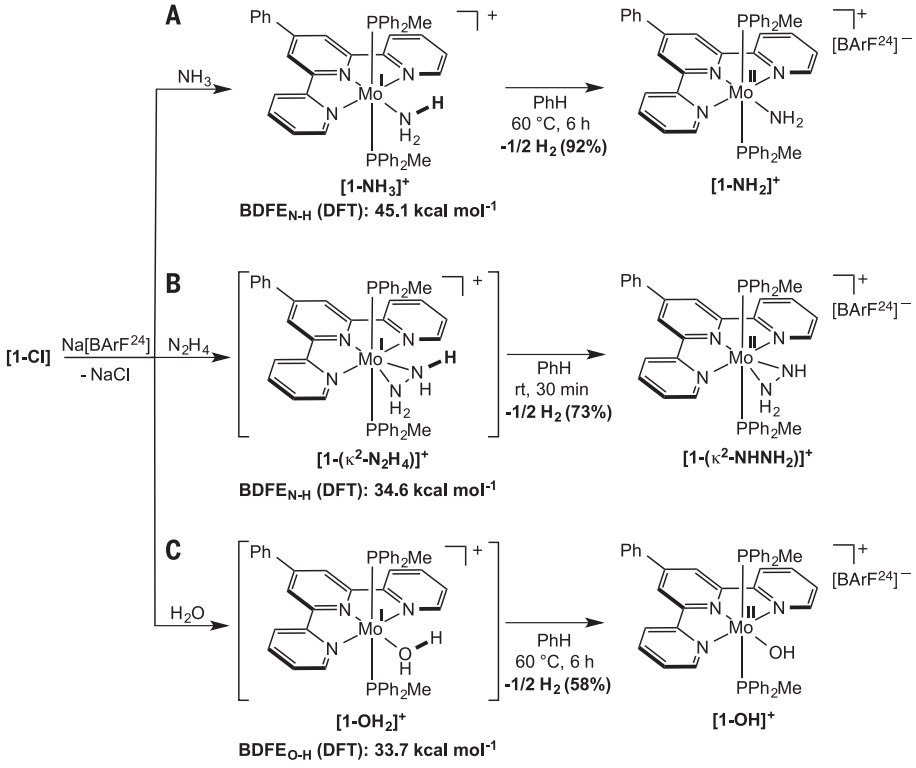

Fig. 3. Spontaneous hydrogen evolution from molybdenum complexes. (**A**) Mo-ammonia complex, (**B**) Mo-hydrazine complex, and (**C**) Mo-aquo complex.

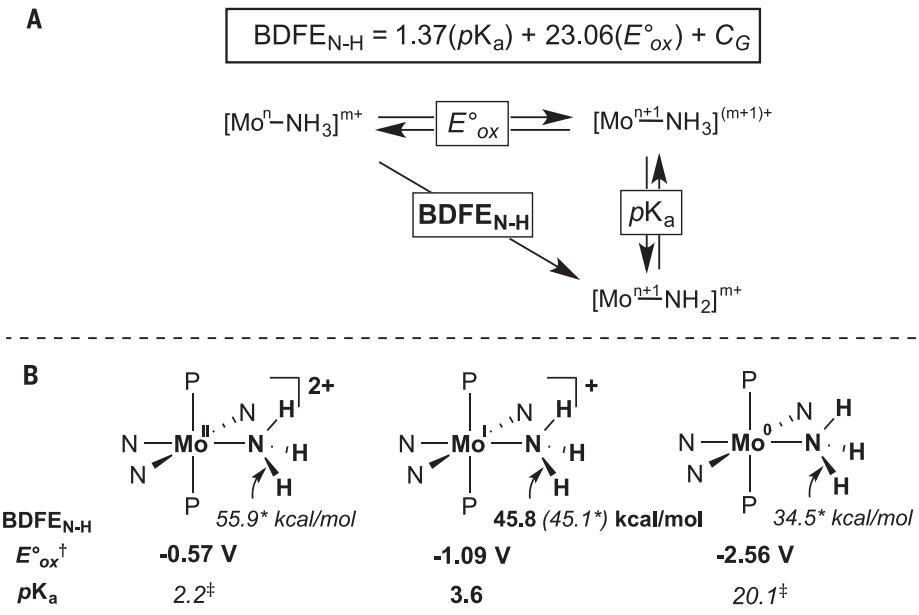

Fig. 4. Contributions of oxidation potential and pK_a to the bond-weakening process. (**A**) Thermochemical expression for N–H BDFEs. C_G, solvent-specific $H^+/H•$ standard reduction potential. (**B**) Oxidation potentials and pK_a measurements for a series of molybdenum complexes of varying oxidation states. Bolded values are experimentally measured, whereas italicized values are DFT-computed. *Values obtained from gas-phase DFT calculations. †Oxidation potentials reported relative to Fc/Fc^+ in THF solution with 0.1 M [^{n}Bu$_4$N][PF$_6$] as the electrolyte. ‡Calculated value in THF solution from the Bordwell equation for the reaction $[Mo^{n+1}\text{-}NH_3]^{(m+1)+} \rightarrow [Mo^{n+1}\text{-}NH_2]^{m+}$, assuming the corresponding DFT-calculated N–H BDFE value, the experimentally determined $E°_{ox}$ value, and a C_G constant of 66 kcal/mol in THF solvent (*40*). The superscripts *m* and *n* are the integer overall charge of the complex and the integer oxidation state of the metal center, respectively.

The solid-state structure of **[1-(κ²-NHNH₂)]⁺** revealed a rare example of a side-on bound κ²-hydrazido fragment, consistent with the C_s molecular symmetry observed by ^{1}H and ^{13}C NMR spectroscopy.

Having demonstrated the generality of the method, we sought to further elucidate the properties of the Mo complex underlying the bond-weakening phenomenon. The Bordwell equation (*34*, *35*) expresses the BDFE of a given N–H bond in terms of the oxidation potential of the metal complex and acidity of the N–H bond upon oxidation (Fig. 4A). As such, the electrochemical behavior of **(1-NH₃)⁺** was examined, and the one-electron oxidized compound **(1-NH₃)²⁺** was synthesized with the goal of experimentally determining the pK_a (where K_a is the acid dissociation constant), thereby obtaining an experimental value for the N–H BDFE in **(1-NH₃)⁺** (Fig. 4A).

The cyclic voltammogram in tetrahydrofuran (THF) solvent (fig. S16) of the formally Mo(I) complex **(1-NH₃)⁺** exhibits two reversible anodic waves, one at –1.09 V (relative to ferrocene/ferrocenium), which is assigned to one-electron oxidation to the dicationic complex [(^{Ph}Tpy)(PPh_2Me)$_2$Mo(NH_3)][$BArF^{24}$]$_2$ [**(1-NH₃)²⁺**]. The second wave, centered at –0.57 V, is assigned as the second oxidation event to furnish the two-electron oxidized compound **(1-NH₃)³⁺**. The cyclic voltammogram also exhibits a quasi-reversible cathodic wave at –2.56 V, likely corresponding to the reduction to **(1-NH₃)⁰**.

With experimental oxidation potentials in hand for **(1-NH₃)²⁺**, **(1-NH₃)⁺**, and **(1-NH₃)⁰**, the isolation of the one-electron oxidized product **(1-NH₃)²⁺** was targeted to determine the N–H pK_a and hence measure BDFE for **(1-NH₃)⁺**. Addition of [H(OEt_2)$_2$]($BArF^{24}$) (Et, ethyl) to **(1-NH₂)⁺** yielded the NMR- and EPR-silent S = 1 product (μ_{eff} = 2.7 μB, 23°C by magnetic susceptibility balance) **(1-NH₃)²⁺** in 78% yield. The N–H pK_a of **(1-NH₃)²⁺** was determined by measurement of the equilibrium concentration ratio with its conjugate base **(1-NH₂)⁺** in the presence of 2-methoxy pyridine (pK_a = 2.6 in THF) (*36*). Using this method, the average of three equilibration experiments established the pK_a of **(1-NH₃)²⁺** as 3.6 in THF solution (table S1 and fig. S17). This value, coupled with the experimentally determined oxidation potential (E^o_{ox}) of **(1-NH₃)⁺** (–1.09 V), allowed for the determination of an experimental N–H BDFE of 45.8 kcal/mol for **(1-NH₃)⁺** in THF solution by using the Bordwell equation. This value is in excellent agreement with the DFT-computed gas-phase value of 45.1 kcal/mol. Both the acidity, likely arising from the overall cationic charge on the complex, and the reducing nature of the metal, a result of the formal Mo(I) oxidation state, contribute to the observed N–H bond weakening in **(1-NH₃)⁺**.

To elucidate the individual contributions of metal reduction potential and N–H pK_a on the phenomenon of bond weakening, computational (DFT) studies were carried out to determine the N–H BDFEs in the series of complexes **(1-NH₃)²⁺**, **(1-NH₃)⁺**, and **(1-NH₃)⁰**. The successive one-electron reduction from **(1-NH₃)²⁺** to **(1-NH₃)⁺** to **(1-NH₃)⁰** results in a concomitant lowering of the N–H BDFE (Fig. 4B). Using the DFT-computed N–H BDFEs and experimentally determined oxidation potentials, application of the Bordwell equation allows evaluation of the pK_a values for the members of the redox series for which an experimental determination is not possible. The pK_a values shown in Fig. 4B correspond to the oxidized form of the compound presented, as shown in the square scheme in Fig. 4A.

Although calculated differences of ~11 kcal/mol in the N–H BDFE accompany each one-electron redox step, the dominant term in the Bordwell equation varies depending on the charge of the molybdenum complex. The most reduced member of the series, **(1-NH₃)⁰**, has the least acidic pK_a contribution to the strength of its N–H bond (pK_a = 20.1) and demonstrates that the large negative potential (E^o_{ox} = –2.56) is the dominant component of the bond-weakening phenomenon. Attempts to synthesize this compound by chemical reduction of **(1-NH₃)⁺** have been unsuccessful, yielding a complex mixture of products upon treatment with potassium graphite. Although the origin of the decomposition is not definitive, isolation of a compound with a N–H BDFE of 34.5 kcal/mol would likely be challenging.

The corresponding molybdenum cation, **(1-NH₃)⁺**, has a pK_a contribution to the N–H bond strength that is 17 units lower than the value calculated for **(1-NH₃)⁰**, consistent with known trends in metal-aquo complexes, where increased charge density and electropositivity increase O–H acidity (*37*). Further decrease in the pK_a term of the N–H bond strength of **(1-NH₃)²⁺** is minimal; only a slight decrease in pK_a to 2.2 was observed. The leveling in acidity suggests that although both **(1-NH₃)²⁺** and **(1-NH₃)⁺** have weak N–H bonds, the spontaneous H_2 evolution in the latter is largely driven by the reduction potential of the formally Mo(I) complex.

Elucidation and delineation of the origin of coordination-induced bond weakening provide design principles for applications ranging from catalysis to bioinorganic chemistry to alternative energy. In cases where the function of ligands containing N–H and O–H is to stabilize metal complexes, often with various oxidation states throughout a catalytic cycle, combinations of oxidation potentials and pK_a values that promote this effect should be suppressed. Alternatively, in applications such as small-molecule activation or the use of NH_3 as a hydrogen storage medium (*38*, *39*), these properties can be rationally tuned to favor weakening of X–H bonds. The kinetic stabilization of **(1-NH₃)⁺**, a molecule with an unusually weak N–H bond, should inspire synthetic efforts to prepare additional examples of such coordination compounds.

REFERENCES AND NOTES

1. J. J. Warren, T. A. Tronic, J. M. Mayer, *Chem. Rev.* **110**, 6961–7001 (2010).
2. A. Werner, *Anorg. Chem.* **3**, 267–330 (1893).
3. M. Peyrone, *Ann. Chem. Pharm.* **51**, 1–29 (1844).
4. P. Ford, D. F. Rudd, R. Gaunder, H. Taube, *J. Am. Chem. Soc.* **90**, 1187–1194 (1968).
5. A. L. Casalnuovo, J. C. Calabrese, D. Milstein, *Inorg. Chem.* **26**, 971–973 (1987).
6. J. Zhao, A. S. Goldman, J. F. Hartwig, *Science* **307**, 1080–1082 (2005).
7. O. V. Ozerov, *Chem. Soc. Rev.* **38**, 83–88 (2009).
8. G. L. Hillhouse, J. E. Bercaw, *J. Am. Chem. Soc.* **106**, 5472–5478 (1984).
9. C. M. Fafard, D. Adhikari, B. M. Foxman, D. J. Mindiola, O. V. Ozerov, *J. Am. Chem. Soc.* **129**, 10318–10319 (2007).
10. E. Khaskin, M. A. Iron, L. J. W. Shimon, J. Zhang, D. Milstein, *J. Am. Chem. Soc.* **132**, 8542–8543 (2010).
11. D. V. Gutsulyak, W. E. Piers, J. Borau-Garcia, M. Parvez, *J. Am. Chem. Soc.* **135**, 11776–11779 (2013).
12. Y. H. Chang, Y. Nakajima, H. Tanaka, K. Yoshizawa, F. Ozawa, *J. Am. Chem. Soc.* **135**, 11791–11794 (2013).
13. G. D. Frey, V. Lavallo, B. Donnadieu, W. W. Schoeller, G. Bertrand, *Science* **316**, 439–441 (2007).
14. Y. Peng, B. D. Ellis, X. Wang, P. P. Power, *J. Am. Chem. Soc.* **130**, 12268–12269 (2008).
15. S. M. McCarthy *et al.*, *J. Am. Chem. Soc.* **136**, 4640–4650 (2014).
16. T. P. Robinson, D. M. De Rosa, S. Aldridge, J. M. Goicoechea, *Angew. Chem. Int. Ed.* **54**, 13758–13763 (2015).
17. E. B. Hulley, J. B. Bonanno, P. T. Wolczanski, T. R. Cundari, E. B. Lobkovsky, *Inorg. Chem.* **49**, 8524–8544 (2010).
18. R. T. Jonas, T. D. P. Stack, *J. Am. Chem. Soc.* **119**, 8566–8567 (1997).
19. J. P. Roth, J. M. Mayer, *Inorg. Chem.* **38**, 2760–2761 (1999).
20. H. Fang *et al.*, *Chem. Sci.* **5**, 916–921 (2014).
21. S. P. Semproni, C. Milsmann, P. J. Chirik, *J. Am. Chem. Soc.* **136**, 9211–9224 (2014).
22. D. P. Estes, D. C. Grills, J. R. Norton, *J. Am. Chem. Soc.* **136**, 17362–17365 (2014).
23. J. M. Hoover, B. L. Ryland, S. S. Stahl, *J. Am. Chem. Soc.* **135**, 2357–2367 (2013).
24. K. T. Tarantino, D. C. Miller, T. A. Callon, R. R. Knowles, *J. Am. Chem. Soc.* **137**, 6440–6443 (2015).
25. D. A. Spiegel, K. B. Wiberg, L. N. Schacherer, M. R. Medeiros, J. L. Wood, *J. Am. Chem. Soc.* **127**, 12513–12515 (2005).
26. J. M. Cuerva *et al.*, *Angew. Chem. Int. Ed.* **45**, 5522–5526 (2006).
27. M. Paradas *et al.*, *J. Am. Chem. Soc.* **132**, 12748–12756 (2010).
28. I. Pappas, P. J. Chirik, *J. Am. Chem. Soc.* **137**, 3498–3501 (2015).
29. M. J. Bezdek, S. Guo, P. J. Chirik, *Inorg. Chem.* **55**, 3117–3127 (2016).
30. E. A. Mader *et al.*, *J. Am. Chem. Soc.* **131**, 4335–4345 (2009).
31. G. Kiss, K. Zhang, S. L. Mukerjee, C. D. Hoff, G. C. Roper, *J. Am. Chem. Soc.* **112**, 5657–5658 (1990).
32. X.-M. Zhang, *J. Org. Chem.* **63**, 1872–1877 (1998).
33. L. Tang *et al.*, *J. Am. Chem. Soc.* **125**, 10093–10102 (2003).
34. F. G. Bordwell, M. J. Bausch, *J. Am. Chem. Soc.* **108**, 1979–1985 (1986).
35. M. Tilset, in *Electron Transfer in Chemistry* (Wiley-VCH, 2001), pp. 677–713.
36. T. Rodima *et al.*, *J. Org. Chem.* **67**, 1873–1881 (2002).
37. C. F. Baes Jr., R. E. Mesmer, *The Hydrolysis of Cations* (Wiley Interscience, 1976).
38. N. V. Rees, R. G. Compton, *Energy Environ. Sci.* **4**, 1255–1260 (2011).
39. A. Klerke, C. H. Christensen, J. K. Nørskov, T. Vegge, *J. Mater. Chem.* **18**, 2304–2310 (2008).
40. E. P. Cappellani *et al.*, *J. Am. Chem. Soc.* **116**, 3375–3388 (1994).

ACKNOWLEDGMENTS

Financial support was provided by the U.S. Department of Energy, Office of Science, Basic Energy Science (grant DE-SC0006498). M.J.B. thanks the Natural Sciences and Engineering Research Council of Canada for a predoctoral fellowship (PGS-D). Crystallographic parameters are available free of charge from the Cambridge Crystallographic Data Centre for the structures of **(1-NH₂)⁺** (CCDC 1477445), **(1-OH)⁺** (CCDC 1477446), **[1-(κ²-NHNH₂)]⁺** (CCDC 1477447), and **(1-NH₃)⁺** (CCDC 1477448). Additional data supporting the conclusions are in the supplementary materials. The authors thank R. Knowles (Princeton University) for insightful discussions.

SUPPLEMENTARY MATERIALS

www.sciencemag.org/content/354/6313/730/suppl/DC1
Materials and Methods
Figs. S1 to S17
Table S1
Crystallographic Data
References (*41*–*46*)

1 May 2016; resubmitted 17 July 2016
Accepted 13 September 2016
10.1126/science.aag0246

CHEMICAL PHYSICS

Attosecond dynamics through a Fano resonance: Monitoring the birth of a photoelectron

V. Gruson,[1]* L. Barreau,[1]* Á. Jiménez-Galan,[2] F. Risoud,[3] J. Caillat,[3] A. Maquet,[3] B. Carré,[1] F. Lepetit,[1] J.-F. Hergott,[1] T. Ruchon,[1] L. Argenti,[2]† R. Taïeb,[3] F. Martín,[2,4,5]‡ P. Salières[1]‡

The dynamics of quantum systems are encoded in the amplitude and phase of wave packets. However, the rapidity of electron dynamics on the attosecond scale has precluded the complete characterization of electron wave packets in the time domain. Using spectrally resolved electron interferometry, we were able to measure the amplitude and phase of a photoelectron wave packet created through a Fano autoionizing resonance in helium. In our setup, replicas obtained by two-photon transitions interfere with reference wave packets that are formed through smooth continua, allowing the full temporal reconstruction, purely from experimental data, of the resonant wave packet released in the continuum. In turn, this resolves the buildup of the autoionizing resonance on an attosecond time scale. Our results, in excellent agreement with ab initio time-dependent calculations, raise prospects for detailed investigations of ultrafast photoemission dynamics governed by electron correlation, as well as coherent control over structured electron wave packets.

Tracking electronic dynamics on the attosecond time scale and angstrom length scale is a key to understanding and controlling the quantum mechanical underpinnings of physical and chemical transformations (*1*). One of the most fundamental electronic processes in this context is photoionization, the dynamics of which are fully encoded in the released electron wave packet (EWP) and the final ionic state. The development of broadband coherent sources of attosecond pulses has opened the possibility of investigating these processes with attosecond resolution. On such a short time scale, few techniques (*2*–*5*) are able to provide access to both spectral amplitude and phase. The spectral derivative of the phase, the group delay, is a practical quantity for describing general wave packet properties reflecting the ionization dynamics. Recently, photoemission delays have been measured in a variety of systems: noble gas atoms (*6*–*8*), molecules (*9*), and solids (*10*). In the gas phase, these attosecond delays give insight into the scattering of the electron in the ionic potential; in the solid state, they provide information on the transport dynamics toward the surface. However, the physical relevance of group delays is restricted to fairly unstructured wave packets.

The necessity to go beyond simple delays arises for more complex ionization dynamics when the broadband excitation encompasses continuum structures associated with, for example, autoionizing states, shape resonances, and Cooper minima (*11*–*13*). These structures induce strong spectral variations of the amplitude and phase of the EWP corresponding to different time scales, ranging from the attosecond to the femtosecond domains. In general, the long-term evolution of the EWP amplitude [e.g., the lifetime of Fano autoionizing resonances (*14*)] can be characterized directly in the time domain (*15*), or in the spectral domain with the use of conventional spectroscopic techniques (*16*). However, the EWP phase is required for reconstruction of the full ionization dynamics. In particular, the short-term response associated with broadband excitation remains unexplored (*17*). It is mainly determined by the spectral phase variation over the resonance bandwidth, which has so far not been measured. An additional difficulty is that the characterization techniques often involve strong infrared probe fields that (i) strongly perturb the resonant structures (*18*–*20*) so that the field-free intrinsic dynamics cannot be accessed, and (ii) require elaborate theoretical input for decoding the electron spectrograms (*21*).

Here, we extend attosecond photoionization spectroscopy to the full reconstruction of the time-dependent EWPs produced by coherent broadband excitation through resonant structures. To this end, we have developed a perturbative interferometric scheme enabling the direct measurement of the spectral amplitude and phase of the unperturbed resonant EWP. Interferences between the latter and a reference nonresonant EWP are achieved through two-photon replicas obtained by photoionizing the target with an extreme ultraviolet (XUV) harmonic comb combined with the mid-infrared (MIR) fundamental field. This spectrally resolved technique is easy to implement and offers straightforward access to the EWP characteristics without complex analysis or theoretical input. We apply it to the investigation of the test case of the doubly excited 2s2p autoionizing resonance of helium, for which ab initio time-dependent calculations can be performed (*22*, *23*), thereby providing a benchmark for our experimental study.

Autoionization occurs when a system is excited in structured spectral regions where resonant states are embedded into a continuum. The system can then either directly ionize or transiently remain in the resonant bound state before ionizing. Coupling between the resonant state and continuum states of the same energy through configuration interaction leads to the well-known Fano spectral line shapes (*14*). Of particular interest is the autoionization decay from doubly excited states (*16*) that is a direct consequence of the electron-electron repulsion. Using our spectrally resolved technique, we directly access the complete ionization dynamics (including interferences at birth time) and monitor the resonance buildup on a subfemtosecond time scale—an endeavor of attosecond science (*17*, *24*).

The concept of the method is shown in Fig. 1A. We photoionize helium with a comb of mutually coherent odd harmonics derived from an optical parametric amplifier (OPA) MIR source. The harmonic of order 63 (H_{63}) is driven into the 2s2p resonance, at 60.15 eV from the ground state, by tuning the OPA central wavelength λ_{OPA} to 1295 nm. Because the harmonic width (400 meV) is much larger than the resonance width (Γ = 37 meV), a broad resonant EWP with complex spectral amplitude $A_R(E)$ is produced. Simultaneously, nonresonant EWPs are created by the neighboring harmonics H_{61} and H_{65} in smooth regions of the continuum; each of these can serve as a reference, denoted $A_{NR}(E)$, to probe the resonant EWP.

To induce interference, we use two-photon transitions to create replicas that spectrally overlap with each other. A weak fraction of the fundamental MIR pulse, of angular frequency $\omega_0 = 2\pi c/\lambda_{OPA}$, is superimposed on the harmonic comb with a delay τ. Its intensity (~2×10^{11} W/cm^2) is sufficiently high to induce perturbative two-photon XUV-MIR transitions but is low enough to avoid transitions involving more than one MIR photon [e.g., depletion of the doubly excited state by multiphoton ionization (*15*), or distortion of the resonance line shape (*19*)]. Most important, the MIR spectral width (26 meV) is smaller than both the harmonic and resonance widths, ensuring that each EWP produced in the two-photon process is a faithful, spectrally shifted, replica of the unperturbed EWP produced in

[1]LIDYL, CEA, CNRS, Université Paris-Saclay, CEA Saclay, 91191 Gif-Sur-Yvette, France. [2]Departamento de Química, Módulo 13, Universidad Autónoma de Madrid, 28049 Madrid, Spain. [3]Sorbonne Université, UPMC Université Paris 6, UMR 7614, Laboratoire de Chimie Physique-Matière et Rayonnement, 75231 Paris Cedex 05, France, and CNRS, UMR 7614, LCPMR, Paris, France. [4]Instituto Madrileño de Estudios Avanzados en Nanociencia (IMDEA-Nanociencia), Cantoblanco, 28049 Madrid, Spain. [5]Condensed Matter Physics Center (IFIMAC), Universidad Autónoma de Madrid, 28049 Madrid, Spain.
*These authors contributed equally to this work. †Present address: Department of Physics and CREOL, University of Central Florida, Orlando, FL 32816, USA. ‡Corresponding author. Email: fernando.martin@uam.es (F.M.); pascal.salieres@cea.fr (P.S.)

the XUV one-photon process. Because of the frequency relation between the odd-harmonic XUV comb and the fundamental MIR laser, the resonant EWP upshifted by absorption of a MIR photon, $A_{R+1}(\tau, E + \hbar\omega_0) \propto A_R(E) \exp(i\omega_0\tau)$, and the reference EWP downshifted by stimulated emission of a MIR photon, $A_{NR-1}(\tau, E + \hbar\omega_0) \propto A_{NR}(E + 2\hbar\omega_0) \exp(-i\omega_0\tau)$, coherently add up in the single sideband (SB_{64}) that lies between the lines associated with H_{63} and H_{65}. Similarly, the resonant EWP downshifted by emission of a MIR photon interferes in sideband SB_{62} with the EWP upshifted by absorption of a MIR photon from H_{61}. We designate E the photoelectron energy in the resonant EWP, and $\overline{E} = E \pm \hbar\omega_0$ the photoelectron energy of the resonant EWP replicas in SB_{64} and SB_{62}, respectively.

The spectrum of these sidebands is thus modulated by the interference between the resonant and nonresonant replicas, depending on the XUV-MIR delay τ (*25*). For SB_{64}, the spectrum is given by

$$\begin{aligned} S_{64}(\tau,\overline{E}) &= |A_{R+1}(\tau,\overline{E}) + A_{NR-1}(\tau,\overline{E})|^2 \\ &= |A_{R+1}(\overline{E})|^2 + |A_{NR-1}(\overline{E})|^2 + \\ &\quad 2|A_{R+1}(\overline{E})||A_{NR-1}(\overline{E})| \\ &\quad \times \cos[2\omega_0\tau + \Delta\varphi_{64}(\overline{E}) + \Delta\eta_{scat}(\overline{E})] \end{aligned} \quad (1)$$

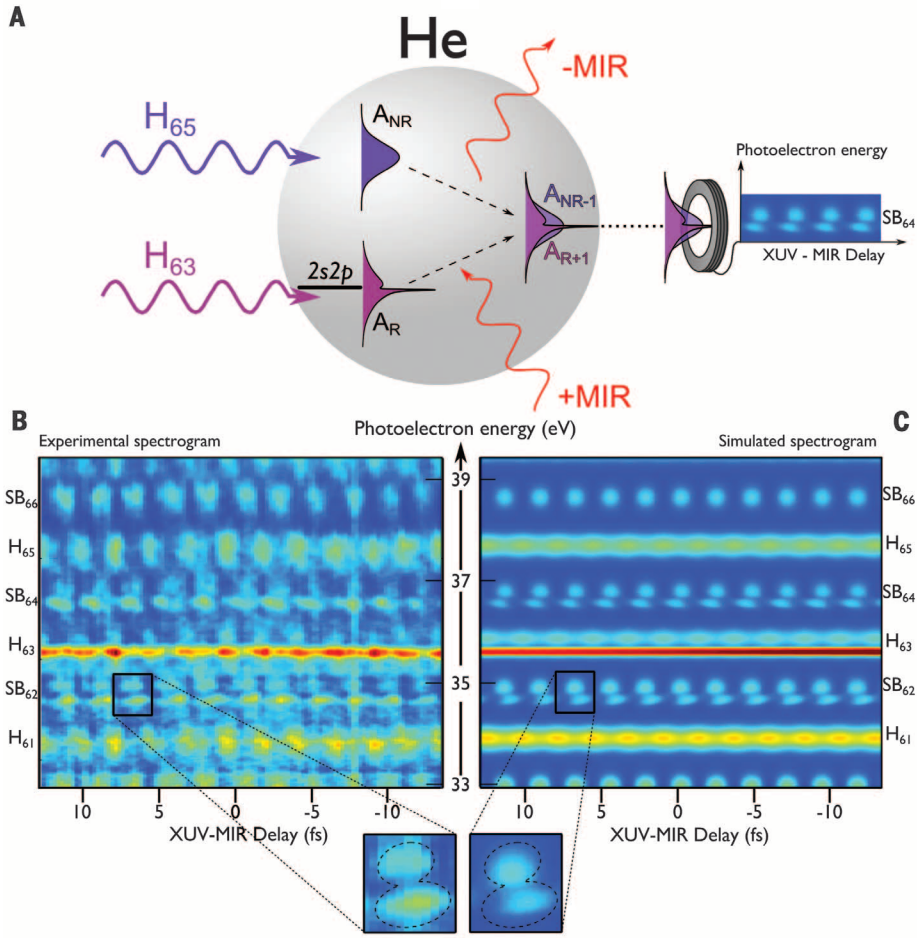

Fig. 1. Principle and resulting spectrogram of spectrally resolved attosecond electron interferometry for the complete characterization of resonant EWPs. (**A**) Principle of the electron interferometry technique. Resonant A_R and reference nonresonant A_{NR} EWPs are produced by successive coherent harmonics. Replicas of these EWPs are created at the same final energy by two-photon transitions induced by a weak fundamental MIR field, where the atom absorbs a MIR photon, leading to the A_{R+1} EWP, or emits a MIR photon, leading to the A_{NR-1} EWP. The spectrally resolved interferences are measured in a time-of-flight electron spectrometer as a function of the XUV-MIR delay τ, controlled with interferometric accuracy; these interferences provide access to the spectral phase of the resonant A_R EWP. (**B** and **C**) Experimental spectrogram (B) and theoretical spectrogram (C) in the 33- to 39-eV region for a 1295-nm OPA wavelength (*25*). H_{63} overlaps the 2s2p resonance of helium located 60.15 eV above the ground state (E_R = 35.55 eV). Single-photon ionization by the odd harmonic orders results in main lines spaced by twice the MIR photon energy, $2\hbar\omega_0$ = 1.92 eV. Between these lines appear sidebands corresponding to two-photon ionization. The oscillations of the two sidebands on both sides of the resonant H_{63} (i.e., SB_{62} and SB_{64}) encode the spectral phase of the resonant EWP. A close-up of one SB_{62} beating shows the structured shape of this resonant EWP and the dephasing of the oscillations of the different spectral components.

where the two contributions to the replicas' relative phase are (i) $2\omega_0\tau$, the phase introduced by the absorption or simulated emission of the MIR photon, and (ii) the relative phase between the initial one-photon EWPs. The latter is split into $\Delta\varphi_{64}(\overline{E}) = \varphi_{65}(\overline{E} + \hbar\omega_0) - \varphi_{63}(\overline{E} - \hbar\omega_0)$, the phase difference between the two ionizing harmonics, and $\Delta\eta_{scat}(\overline{E}) = \eta_{scat}(\overline{E} + \hbar\omega_0) - \eta_{scat}(\overline{E} - \hbar\omega_0)$, the difference between the nonresonant and resonant scattering phases of the two intermediate states. In our conditions, the variations over the sideband width of both $\Delta\varphi_{64}(\overline{E})$ and $\eta_{scat}(\overline{E} + \hbar\omega_0)$ are negligible in comparison with that of the resonant scattering phase $\eta_{scat}(\overline{E} - \hbar\omega_0)$ (*25*). The latter contains information about the scattering of the photoelectron by the remaining core, including strongly correlated scattering by the other electron close to the resonance. This phase is the measurable quantity addressed by our study.

Using a high-resolution (~1.9%) magnetic-bottle spectrometer with a length of 2 m, we have access to the photoelectron spectrogram—electron yield as a function of energy E and delay τ—spectrally resolved within the harmonics and sideband widths (Fig. 1B). As a result of its large bandwidth, H_{63} produces a photoelectron spectrum exhibiting a double structure with a Fano-type resonant peak and a smoother peak. This shape is replicated on each of the closest resonant sidebands (SB_{62} and SB_{64}). Strikingly, the components of the double structure oscillate with different phases when τ is varied, in both SB_{62} and SB_{64}.

These phase variations are further evidenced by a spectrally resolved analysis: For each sampled energy within the sideband width, we perform a Fourier transform of $S_{63\pm1}(\tau, E + \hbar\omega_0)$ with respect to τ to extract the amplitude and phase of the component oscillating at $2\omega_0$ (see Eq. 1 and Fig. 2). The SB_{62} phase shows a strong increase of ~1 rad within the resonant peak, followed by a sudden drop at the amplitude minimum ($\overline{E}$ ~ 34.75 eV), and a rather flat behavior under the smooth peak. The SB_{64} phase has a very similar shape and magnitude but with an opposite sign due to opposite configuration of the resonant and reference EWPs in the interferometer. This correspondence confirms the direct imprint of the intermediate resonance on the neighboring sidebands.

The $2\omega_0$ component of the resonant sidebands thus provides a good measure of the $|A_R(E)| \exp[i\eta_{scat}(E)]$ EWP that would result from one-photon Fourier-limited excitation. This allows a detailed study of the temporal characteristics of resonant photoemission, in particular of the electron flux into the continuum, through the direct reconstruction of this EWP in the time domain:

$$\tilde{A}_R(t) = \frac{1}{2\pi}\int_{-\infty}^{+\infty} |A_R(E)| \exp[i\eta_{scat}(E)] \exp\left(\frac{-iEt}{\hbar}\right) dE \quad (2)$$

The temporal profile obtained from SB_{64} is shown in Fig. 3A. It presents a strong peak at the

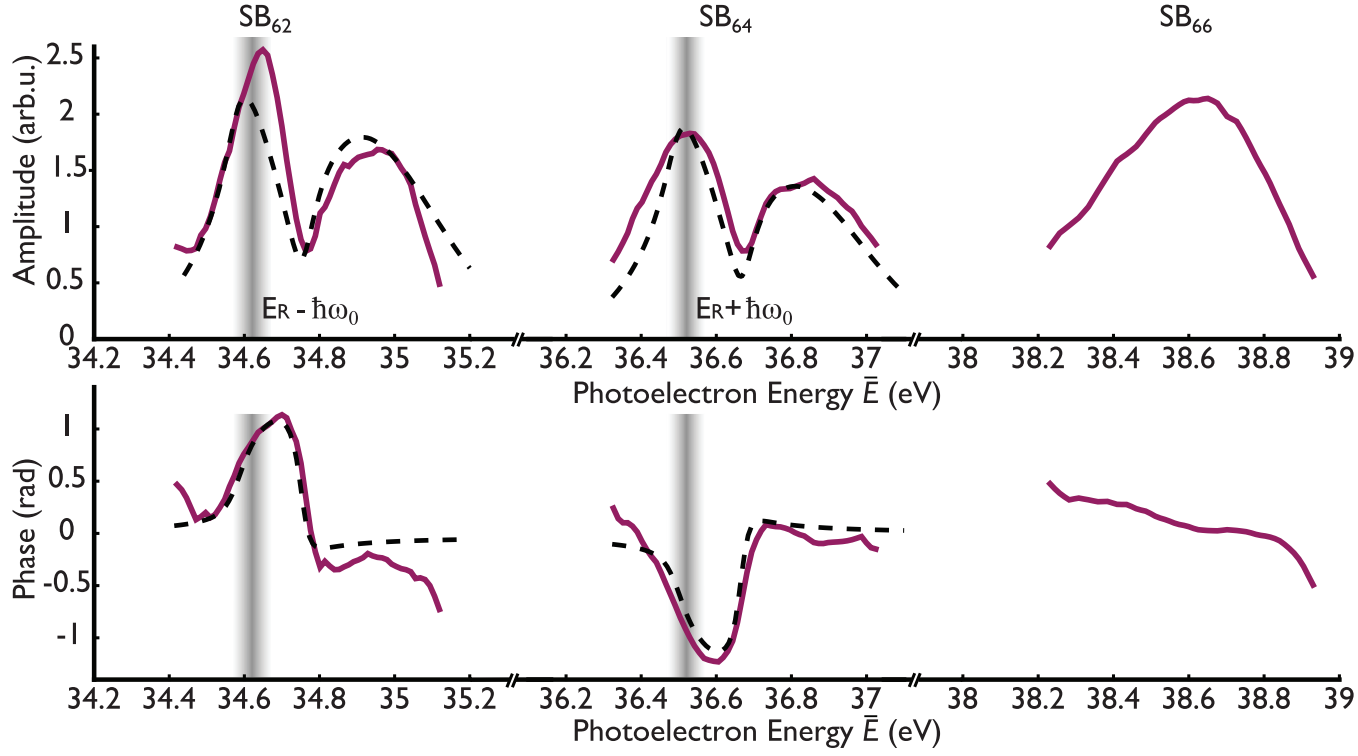

Fig. 2. Resonant EWP in the spectral domain. Upper and lower panels respectively show spectral amplitude and phase of the $2\omega_0$ component of SB_{62} (left), SB_{64} (center), and SB_{66} (right) from the spectrograms in Fig. 1, B and C. The phase origin is set to 0 by removing the linear variation due to the ionizing harmonic radiation (attochirp) (*30*). The experimental data (purple curves) show very good agreement with the simulations (dashed black lines). The resonance position shifted by one MIR photon is indicated in gray. The measured spectral amplitudes and phases of the resonant SB_{62} and SB_{64} are easily related to the amplitude $|A_R(E)|$ and phase $\eta_{scat}(E)$ of the resonant one-photon EWP (see Eq. 1). The main limitation comes from the current spectrometer resolution (in our conditions, a relative resolution of ~1.9% resulting in a width of ~190 meV at 10 eV) that broadens the resonant peak and its phase variations. The nonresonant SB_{66} exhibits a Gaussian amplitude (which mostly reflects the ionizing XUV spectral profile) and a smooth close-to-linear phase. This provides a temporal reference for the ionization dynamics.

origin—given by the maximum of the Fourier transform of the nonresonant SB_{66} (*25*)—followed by a deep minimum around 4 fs and then a revival with a decay within ~10 fs. The presence of a fast phase jump (~2 rad within ~2 fs) at the position of the minimum indicates that it results from a destructive interference between two wave packet components, the origin of which is detailed below.

To benchmark the measured data, we theoretically investigated the multicolor XUV + MIR ionization of He in the vicinity of the 2s2p resonance. Fully correlated ab initio time-dependent calculations (*22*) were used to validate an analytical model of the two-photon transitions accounting for the actual pulses' bandwidths (*23*). The simulated photoelectron spectrogram, taking into account the spectrometer resolution, remarkably reproduces the structured shape of the resonant sidebands as well as the dephasing between their two components (Fig. 1C). The analysis of the $2\omega_0$ oscillations of SB_{62} and SB_{64} gives spectral phase variations in excellent agreement with the experimental data (Fig. 2). The temporal profile $\tilde{A}_R(t)$ obtained by Fourier transform (Fig. 3) is also well reproduced, with a smaller revival but a similar decay time of ~10 fs. This reduced effective lifetime is a direct consequence of the finite spectrometer resolution. When the latter is assumed infinite, the time profile has the same behavior at short times but a longer decay, corresponding to the 17-fs lifetime of the resonance. Analytical calculations show that in our conditions, the reconstructed EWP does mirror the one-photon resonant EWP (*25*). These findings confirm that, except for a faster decay of the long-term tail due to our current electron spectrometer resolution, the essential physics of the early time frame of EWP creation is directly accessed from purely experimental data.

To further highlight the insight provided by this experimental technique, we undertook an in-depth analysis of the measured EWP characteristics in terms of Fano's formalism for autoionization (*14*). Resonant ionization can be described as the interference between two distinct paths: (i) the direct transition to the continuum, and (ii) the resonant transition through the doubly excited state that eventually decays in the continuum through configuration interaction within the resonance lifetime (Fig. 3B). The normalized total transition amplitude can then be written as the coherent sum of two contributions, a constant background term and a Breit-Wigner amplitude for the resonance:

$$R(E) = \frac{\varepsilon + q}{\varepsilon + i} = 1 + \frac{q - i}{\varepsilon + i} \qquad (3)$$

where $\varepsilon = 2(E - E_R)/\Gamma$ is the reduced energy detuning from the resonance at energy E_R, in units of its half width $\Gamma/2$. The Fano parameter q [−2.77 for the He(2s2p) resonance (*16*)] measures the relative weight of the two paths. Their interference leads to the well-known asymmetric Fano line shape $|R(E)|^2$ and to the resonant scattering phase: $\eta_{scat}(E) = \arg R(E) = \text{atan}(\varepsilon) + \pi/2 - \pi\Theta(\varepsilon + q)$, where Θ is the Heaviside function. This phase is experimentally accessed here (Fig. 2).

The spectral amplitude of an EWP created by Gaussian harmonic excitation $H(E)$ is given by $R(E)H(E)$. Its temporal counterpart is $\tilde{A}_R(t) = [\tilde{R} * \tilde{H}](t)$, where $\tilde{R}(t)$ and $\tilde{H}(t)$ are Fourier transforms of the spectral amplitudes, in particular

$$\tilde{R}(t) = \delta(t) - i\frac{\Gamma}{2\hbar}(q - i)\exp\left[-\left(\frac{iE_R}{\hbar} + \frac{\Gamma}{2\hbar}\right)t\right]\Theta(t) \qquad (4)$$

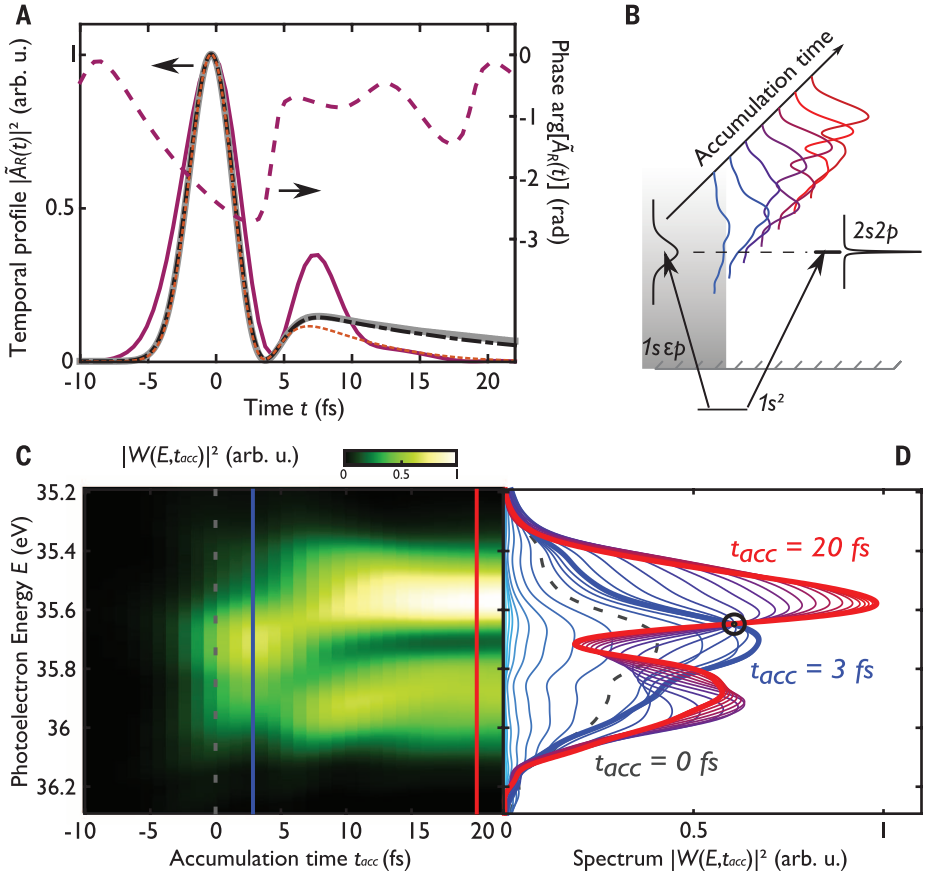

Fig. 3. Resonant EWP in the time domain and time-resolved reconstruction of the resonance buildup. (**A**) Temporal profile of the resonant EWP obtained by Fourier transform of the SB_{64} data (i) from the experimental spectrogram (solid purple curve) and corresponding temporal phase (dashed purple curve), and (ii) from the simulated spectrogram, taking into account (dotted orange curve), or not (dot-dashed black curve), the finite spectrometer resolution. The latter fully coincides with the one-photon resonant EWP profile from a direct analytical calculation (solid gray curve) (*25*), thereby demonstrating the validity of our interferometric technique. (**B**) Illustration of the formation dynamics of the resonant spectrum resulting from interference between the two paths in the Fano autoionization model. (**C**) Reconstruction of the time-resolved buildup of the resonant spectrum using the time-energy analysis introduced in Eq. 5. The photoelectron spectrum is plotted as a function of the upper temporal limit (accumulation time t_{acc}) used for the inverse Fourier transform. The dashed gray curve, solid blue curve, and solid red curve indicate accumulation times of 0, 3, and 20 fs, respectively. (**D**) Lineouts of (C) every 1 fs. This figure evidences first the growth of the direct path until a maximum is reached at ~3 fs (blue curves), and then the increasing spectral interference with the resonant path that finally results in the Fano line shape (red curves). At 35.6 eV, an isosbestic-like point is crossed by all curves from 3 fs onward (black circle), evidencing a position in the final line shape where only the direct path contributes.

(*24*). The temporal profile $\tilde{A}_R(t)$ thus decomposes into a Gaussian nonresonant term and a resonant contribution, like our experimental data (Fig. 3A). The destructive temporal interference between the two terms leads to the amplitude minimum and phase jump identified around t = 4 fs.

To illustrate how the interference between the two paths governs the formation of the resonance line shape, Wickenhauser *et al.* (*17*) introduced a time-frequency analysis based on the limited inverse Fourier transform:

$$W(E,t_{acc}) = \int_{-\infty}^{t_{acc}} \tilde{A}_R(t) \exp\left(\frac{iEt}{\hbar}\right) dt \qquad (5)$$

which shows how the spectrum builds up until accumulation time t_{acc}. The result of this transform applied to the experimental EWP in Fig. 3A is shown in Fig. 3, C and D. The chronology of the resonance formation can be nicely interpreted within Fano's formalism. In a first stage until ~3 fs, a close-to-Gaussian spectrum reflecting the ionizing harmonic spectral shape emerges: The direct path to the continuum dominates. Then the resonant path starts contributing as the populated doubly excited state decays in the continuum: Interferences coherently build up until ~20 fs, consistent with the temporal profile in Fig. 3A, to eventually converge toward the asymmetric measured spectrum. The resonance growth can thus be decomposed in two nearly consecutive steps governed by fairly different time scales.

The buildup of the resonant profile reveals the presence of a notable point around E = 35.6 eV where, as soon as the direct ionization is completed, the spectrum barely changes with t_{acc} any longer. This can be explained by splitting the $|R(E)|^2$ spectrum from Eq. 3 into three terms:

$$|R(E)|^2 = 1 + \frac{q^2+1}{\varepsilon^2+1} + 2\frac{q\varepsilon - 1}{\varepsilon^2+1} \qquad (6)$$

(*26*). At this isosbestic-like point—that is, for $\varepsilon = [(1/q) - q]/2$—the bound (second term) and coupling (third term) contributions ultimately cancel each other, leaving only the direct continuum contribution (first term). This point thus gives a useful landmark in the resonant line shape (e.g., for cross section calibration or reference purposes).

Spectrally resolved electron interferometry thus provides insight into the ultrafast strongly correlated multielectron dynamics underlying autoionization decay. Given the generality and wide applicability of the Fano formalism [see, e.g., (*26*)], we anticipate that our approach, combined with progress in attosecond pulse production and particle detection (e.g., access to photoelectron angular distributions), will open prospects for studies of complex photoemission dynamics close to resonances and, more generally, structured EWP dynamics in a variety of systems, from molecules (*27*–*29*) and nanostructures (*26*) to surfaces (*10*). Furthermore, the well-defined amplitude and phase distortions induced by the resonance offer a means for shaping the broadband EWP, bringing opportunities for coherent control in the attosecond regime.

REFERENCES AND NOTES

1. F. Krausz, M. Ivanov, *Rev. Mod. Phys.* **81**, 163–234 (2009).
2. M. Hentschel *et al.*, *Nature* **414**, 509–513 (2001).
3. P. M. Paul *et al.*, *Science* **292**, 1689–1692 (2001).
4. Y. Mairesse, F. Quéré, *Phys. Rev. A* **71**, 011401(R) (2005).
5. M. Chini, S. Gilbertson, S. D. Khan, Z. Chang, *Opt. Express* **18**, 13006–13016 (2010).
6. M. Schultze *et al.*, *Science* **328**, 1658–1662 (2010).
7. K. Klünder *et al.*, *Phys. Rev. Lett.* **106**, 143002 (2011).
8. R. Pazourek, S. Nagele, J. Burgdörfer, *Rev. Mod. Phys.* **87**, 765–802 (2015).
9. S. Haessler *et al.*, *Phys. Rev. A* **80**, 011404 (2009).
10. A. L. Cavalieri *et al.*, *Nature* **449**, 1029–1032 (2007).
11. S. B. Schoun *et al.*, *Phys. Rev. Lett.* **112**, 153001 (2014).
12. M. Sabbar *et al.*, *Phys. Rev. Lett.* **115**, 133001 (2015).
13. M. Kotur *et al.*, *Nat. Commun.* **7**, 10566 (2016).
14. U. Fano, *Phys. Rev.* **124**, 1866–1878 (1961).
15. S. Gilbertson *et al.*, *Phys. Rev. Lett.* **105**, 263003 (2010).
16. M. Domke, K. Schulz, G. Remmers, G. Kaindl, D. Wintgen, *Phys. Rev. A* **53**, 1424–1438 (1996).
17. M. Wickenhauser, J. Burgdörfer, F. Krausz, M. Drescher, *Phys. Rev. Lett.* **94**, 023002 (2005).
18. Z.-H. Loh, C. H. Greene, S. R. Leone, *Chem. Phys.* **350**, 7–13 (2008).
19. C. Ott *et al.*, *Science* **340**, 716–720 (2013).
20. C. Ott *et al.*, *Nature* **516**, 374–378 (2014).

21. S. R. Leone *et al.*, *Nat. Photonics* **8**, 162–166 (2014).
22. Á. Jiménez-Galán, L. Argenti, F. Martín, *Phys. Rev. Lett.* **113**, 263001 (2014).
23. A. Jiménez-Galán, F. Martín, L. Argenti, *Phys. Rev. A* **93**, 023429 (2016).
24. Z. X. Zhao, C. D. Lin, *Phys. Rev. A* **71**, 060702 (2005).
25. See supplementary materials on *Science* Online.
26. A. E. Miroshnichenko, S. Flach, Y. S. Kivshar, *Rev. Mod. Phys.* **82**, 2257–2298 (2010).
27. A. S. Sandhu *et al.*, *Science* **322**, 1081–1085 (2008).
28. J. Caillat *et al.*, *Phys. Rev. Lett.* **106**, 093002 (2011).
29. P. Hockett, E. Frumker, D. M. Villeneuve, P. B. Corkum, *J. Phys. B* **49**, 095602 (2016).
30. Y. Mairesse *et al.*, *Science* **302**, 1540–1543 (2003).

ACKNOWLEDGMENTS

We thank S. Weber for crucial contributions to the PLFA attosecond beamline; D. Cubaynes, M. Meyer, F. Penent, and J. Palaudoux for setup and testing of the electron spectrometer; and O. Smirnova for fruitful discussions. Supported by European Union grant H2020-MSCA-ITN-MEDEA-641789, Agence Nationale de la Recherche grants ANR-15-CE30-0001-01-CIMBAAD and ANR11-EQPX0005-ATTOLAB, European Research Council advanced grant XCHEM 290853, European COST Action grant XLIC CM1204, and MINECO Project grant FIS2013-42002-R. We acknowledge allocation of computer time from CCC-UAM and Mare Nostrum BSC.

SUPPLEMENTARY MATERIALS

www.sciencemag.org/content/354/6313/734/suppl/DC1
Supplementary Text
Figs. S1 to S7
Movie S1
References (*31*–*43*)

8 July 2016; accepted 5 October 2016
10.1126/science.aah5188

CHEMICAL PHYSICS

Observing the ultrafast buildup of a Fano resonance in the time domain

A. Kaldun,[1]*† A. Blättermann,[1]† V. Stooß,[1] S. Donsa,[2] H. Wei,[3] R. Pazourek,[2] S. Nagele,[2] C. Ott,[1] C. D. Lin,[3] J. Burgdörfer,[2] T. Pfeifer[1,4]‡

Although the time-dependent buildup of asymmetric Fano line shapes in absorption spectra has been of great theoretical interest in the past decade, experimental verification of the predictions has been elusive. Here, we report the experimental observation of the emergence of a Fano resonance in the prototype system of helium by interrupting the autoionization process of a correlated two-electron excited state with a strong laser field. The tunable temporal gate between excitation and termination of the resonance allows us to follow the formation of a Fano line shape in time. The agreement with ab initio calculations validates our experimental time-gating technique for addressing an even broader range of topics, such as the emergence of electron correlation, the onset of electron-internuclear coupling, and quasi-particle formation.

Fano resonances generally occur in the course of excitation of discrete quantum states embedded in and coupled to a continuum (*1*, *2*). As such, they play a fundamental role in nuclear, atomic, molecular, and condensed-matter physics as well as photonics (*3*–*12*). In the prominent example of helium, the discrete doubly excited states are located within different sets of continua, where the prominent 2s2p state is coupled only to the continuum of singly ionized ground-state Helium He^+ (1s). Coulomb interaction among the two electrons leads to autoionization, thus coupling the discrete state and the 1s continuum and giving rise to the famous asymmetric Fano line profiles. Following the early scientific work on attosecond dynamics in laser-driven helium (*13*, *14*), several recent theoretical calculations have predicted the time-dependent formation of Fano resonances (*15*–*20*). However, up to now no such experiment has been performed.

Here, we report a measurement of the time-dependent formation of a Fano resonance in the prototype system of helium. We observed the transient buildup of the 2s2p doubly excited state via extreme ultraviolet (XUV) absorption spectroscopy using high-harmonic radiation. Monitoring the formation of the Fano line was achieved by rapidly terminating the coherent dipole response of the atom via saturated strong-field ionization (SFI) by use of an intense near-infrared (NIR) laser pulse. The key idea is that the NIR pulse acts as a temporal gate of the Fano resonance decay. By varying the time delay between the XUV and the NIR pulse with subfemtosecond precision, we tracked the evolution of the Fano line shape in real time (Fig. 1). To that end, we used laser intensities beyond the Fano-phase control regime discussed in previous work (*7*) to fully deplete the doubly excited state by means of SFI at variable time delays instead of just shifting its phase at a constant (near zero) time delay.

Although recent theoretical work has concentrated on the photoelectron spectrum for accessing the autoionization process, we made use of the fact that state-of-the-art optical spectrometers (*7*, *21*) attain at least an order of magnitude better energy resolution as compared with that of electron spectrometers (*22*), thus allowing for the observation of subtle changes in the spectral profile.

Upon excitation, the XUV pulse triggers the dynamic buildup of the Fano resonance by inducing an oscillating dipole moment, which in turn gives rise to the optical dipole response of the transition. Signatures in the transmitted XUV spectrum are related to the imaginary part of the frequency-domain dipole response (*7*). The time-delayed strong-field NIR pulse is then used to ionize the system, depleting the autoionizing level and ending the buildup process of the spectral line. The experimental results in Fig. 2 show the time-dependent formation of the 2s2p Fano absorption line. For the unperturbed case—in the absence of the NIR pulse as depicted in Fig. 2 (gray line)—we measured the original Fano line shape. The intensity of the 7-fs full width at half maximum (FWHM) NIR pulse was set high enough (~10^{13} W/cm^2) so that the doubly excited states were completely ionized. The dipole oscillation, and with that the resonant optical response of the atom, was thus terminated within the NIR pulse duration. Because this interruption due to SFI is considerably shorter than the lifetime of the state, we can sample the time-dependent formation of the line shape (*20*). For positive time delays τ, the terminating NIR pulse arrives after the XUV excitation pulse. When τ is small as compared with the state's lifetime of ~17 fs, the short duration in which radiation is emitted by the XUV-triggered dipole oscillation is insufficient to form a well-defined Fano line, as can be seen in Fig. 2 for τ less than 10 fs. At $\tau \approx 6$ fs, the effect of the NIR is strongest, and the spectral line is smeared out completely. When the autoionizing state is immediately depopulated after its excitation, the spectral response is mainly determined by the excitation process driven by the attosecond XUV pulse and, because of the fast termination by the NIR pulse, spans several electron volts. This result agrees with several theoretical studies (*15*, *16*) that show that the energy distribution of the electrons ejected within one third of the state lifetime (corresponding to 6 fs in the case of the 2s2p state in helium) after the initial excitation is governed by the frequency range of the excitation pulse. Now, by increasing the time delay τ between excitation and ionization, the doubly excited state has time to decay, and the interference with the direct contributions builds up; the oscillating dipole is granted more and more time to emit the optical response. This gives rise to a narrower

[1]Max-Planck-Institut für Kernphysik, Saupfercheckweg 1, 69117 Heidelberg, Germany. [2]Institute for Theoretical Physics, Vienna University of Technology, Wiedner Hauptstraße 8, 1040 Vienna, Austria. [3]Department of Physics, Kansas State University, 230 Cardwell Hall, Manhattan, KS 66506, USA. [4]Center for Quantum Dynamics, Universität Heidelberg, 69120 Heidelberg, Germany, EU.
*Present address: Stanford PULSE Institute, SLAC National Accelerator Laboratory, 2575 Sand Hill Road, Menlo Park, CA 94025, USA. †These authors contributed equally to this work.
‡Corresponding author. Email: thomas.pfeifer@mpi-hd.mpg.de

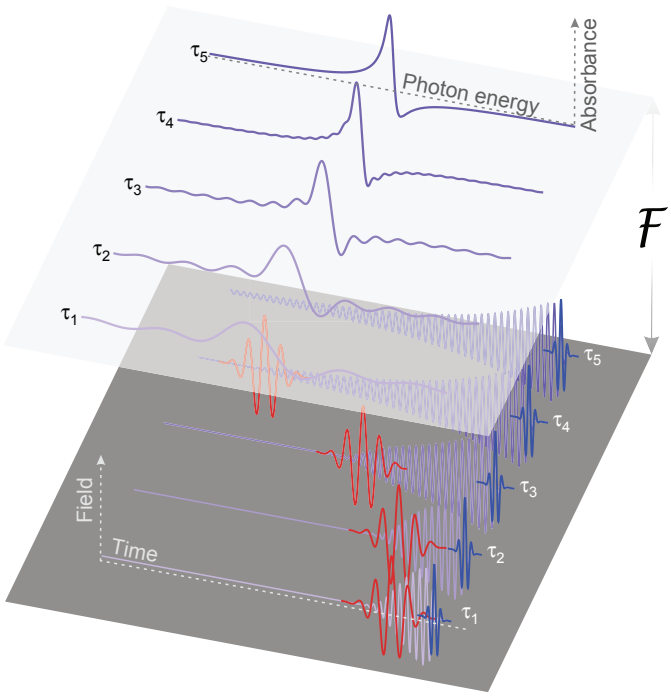

Fig. 1. Time-dependent formation of a Fano profile. The top (spectral domain) and the bottom (time domain) planes schematically show the connection between the measured absorption line shape and the temporal evolution of the dipole response (purple) for five time delays τ_1 to τ_5. After excitation of the autoionizing state by the XUV pulse (blue), the dipole decays exponentially, until the decay is terminated through complete ionization of the excited state in an intense few-cycle NIR field (red). By experimentally controlling the time delay between excitation (start) and ionization (stop), the buildup of the asymmetric Fano resonance is resolved in time.

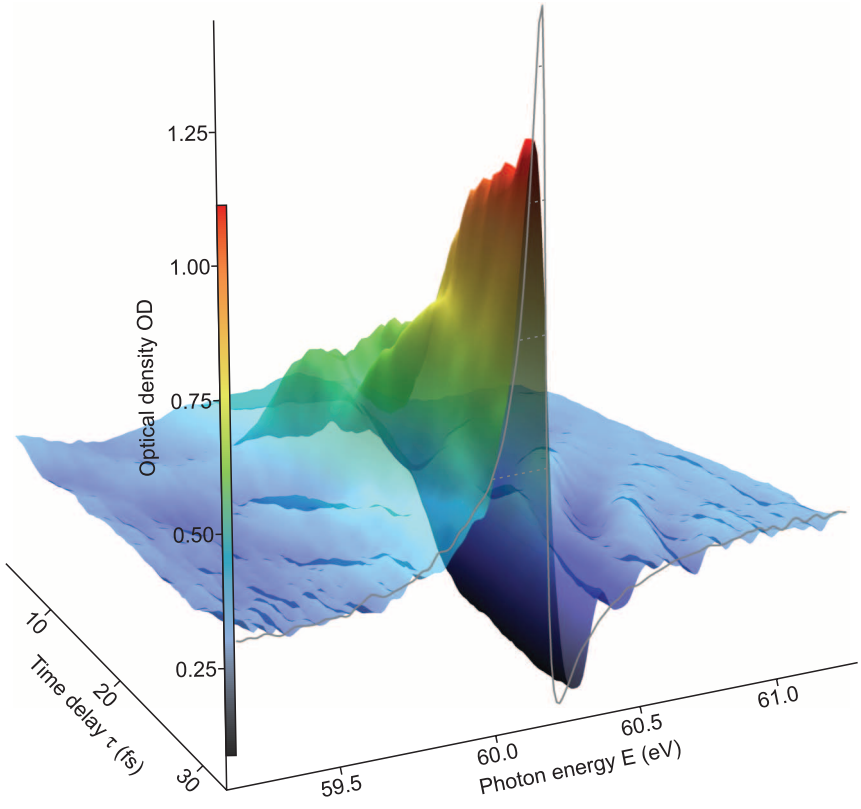

Fig. 2. Experimental observation of the Fano line formation in doubly excited helium. Transient absorption spectrum in terms of the optical density (OD) of the helium target (vertical axis) as a function of the XUV photon energy E and time delay $\tau \geq 0$ between XUV excitation and subsequent NIR ionization of the 2s2p state. For better readability, the OD values are color-coded. The reference spectrum (gray line; dashed bars indicate the OD values from 0.5 to 1.25) shows the unperturbed 2s2p line, which corresponds to the limit for $\tau \to \infty$. The experimental data were averaged over one optical cycle in order to suppress the fast oscillation of the 2s2p state absorbance due to two-photon coupling to the sp_{23+} state (*28*, *29*) and to increase the signal-to-noise ratio.

spectral line, with the details of the autoionization process encoded in it. After approximately one lifetime, at $\tau \approx 15$ fs, the Fano spectral signature is already more pronounced and continuously narrows down as the time delay is increased. For time delays substantially longer than the lifetime, the original Fano absorption profile is recovered. At the end of the delay range presented in Fig. 2, the measured line shape already closely resembles the Fano line. However, this comparison is affected by the finite experimental resolution (50 meV FWHM), which has a noticeable effect on the narrow unperturbed line. According to analytic theory (*16*, *18*, *20*), it takes roughly 100 fs for the 2s2p Fano line to develop an amplitude of 95%, and 140 fs to develop an amplitude of 99%, regarding the peak amplitude in the limit $\tau \to \infty$. Our experiment captures the most substantial changes in the line shape; further extending the time delay is not possible with our current setup.

In order to analyze our experimental observations, we solved the full two-electron Schrödinger equation of the helium atom numerically from first principles (supplementary text) (*23*). First, we verified the temporal gating mechanism by studying the residual population of the 2s2p state after SFI as a function of the time delay (Fig. 3). Although for large negative time delays the population remains unaffected, already at $\tau \approx -5$ fs less than 10% of the population remains bound because of SFI in the rising flank of the NIR pulse (peak intensity of 20 TW/cm^2). Near-complete depletion to well below 1% is first reached around $\tau \approx 4$ to 5 fs, which is in good agreement with the experimental observation. With a fall time (10 to 90% depletion) of <4 fs, the efficiency of the gate closure by the NIR pulse on time scales short as compared with the lifetime is confirmed. Moreover, as can be expected for a strong-field ionization process, the depletion of the excited state depends exponentially on the applied field strength (Fig. 3, inset).

We next compared both experiment and ab initio calculation to the analytic description of an isolated Fano resonance that is excited and depleted impulsively. The existing analytical predictions describe the photoelectron spectrum in different scenarios: either the time-dependent buildup of the continuum component of the Fano resonance (*16*, *18*, *24*), or the final distribution of photoelectrons after a sudden removal of the bound population (*20*). The four resulting photoelectron spectra are identical in the case of an isolated Fano resonance and an infinitely short gate. In order to be directly comparable with our experiment, we derived (supplementary text) an analytic expression of the transient absorption spectrum based on the description by Chu and Lin (*18*)

$$\sigma(\epsilon,\tau) \propto \mathrm{Re}\left\{1+\frac{(q-i)^2}{1-i\epsilon}\left[1-e^{-\frac{\Gamma}{2}(1-i\epsilon)\tau}\right]\right\} \quad (1)$$

Here, q and Γ are the Fano q-parameter and the resonance width, respectively, and ϵ is the

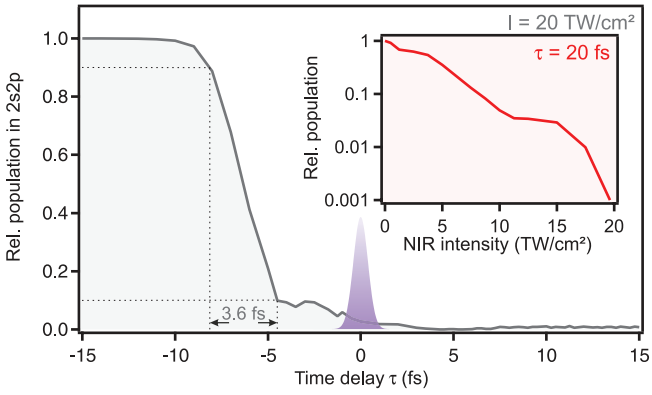

Fig. 3. Calculated occupation of the 2s2p state after SFI. For each time delay τ between the XUV and the strong NIR pulse (20 TW/cm^2), the occupation is obtained through projection onto the field-free quasi-bound state at a fixed time of 40.5 fs after the excitation by the XUV pulse. (Inset) The occupation of the 2s2p level for a fixed time delay τ = 20 fs and varying NIR peak intensity. The purple pulse indicates the arrival of the XUV pulse with respect to which the NIR is delayed by τ.

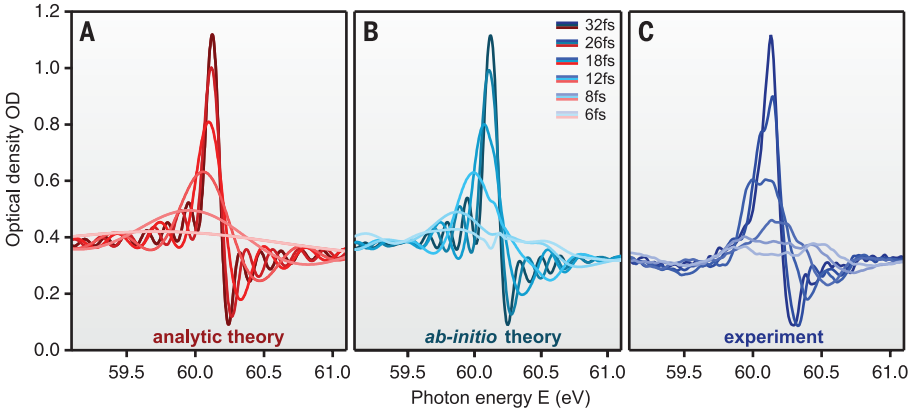

Fig. 4. Comparison between analytic theory, ab initio calculation, and experimental results for the helium 2s2p Fano line formation. (**A**) Absorption spectra calculated for a series of time delays between XUV and NIR according to the analytic expression of Eq. 1. (**B**) Numerically simulated absorption spectra for a 7-fs FWHM NIR pulse, with peak intensity of 20 TW/cm^2. (**C**) Experimentally recorded spectra. The theoretical spectral amplitudes in (A) and (B) are scaled to match the experimental peak and valley at 32 fs. Because of the finite duration of the NIR pulse in (B) and (C), the effective beginning of the line formation is not at τ = 0. Thus, the analytic spectra are shifted by 4.5 fs in time-delay in order to ensure comparability among the three data sets.

scaled photon energy [$\epsilon = 2(E - E_R)/\Gamma$, where E_R is the resonance energy]. The buildup of the Fano resonance is shown in Fig. 4 as predicted by the analytic theory (Fig. 4A) [parameters of the 2s2p line are taken from (*25*)], compared with the numerical simulation (Fig. 4B), and with the experimental data (Fig. 4C). Conceptually, the main difference is that in Fig. 4A, the depletion is treated instantaneously so that the dynamics of the quantum system are unperturbed up to the ionization event, whereas a finite-duration NIR laser pulse is applied in Fig. 4B, to model the experimental scenario (Fig. 4C). Moreover, the experimental spectra are additionally affected by a deviation of the laser pulse shape from a clean Gaussian pulse used in Fig. 4B. Still, the experimental spectra clearly resolve the buildup of the Fano resonance, validating the time-gating technique we used. The three spectra agree well with respect to their shapes and peak-to-baseline ratios, especially at later stages of the buildup (Fig. 4, darker colors), when the effect of the strong probe on the recovered line shape is small. Because the exact laser pulse profile in the experiment deviates from a Gaussian pulse used in the simulations, we cannot expect perfect quantitative agreement. Directly at the beginning of the buildup (Fig. 4, lighter colors), all spectra share a smeared-out appearance, reflecting the time-energy Fourier uncertainty relation. The ab initio calculation and the experiment agree particularly well also at these early times because they both exhibit broad wings with a similar structure, whereas the analytic spectrum is virtually flat. The discrepancy compared with the analytic theory shows that in the region of temporal overlap, the strong NIR field has a noticeable effect on the measured line shape, which is not included in the analytic model. For instance, when the NIR is present during the XUV excitation step, the 2s2p state itself is modified by the strong field (for example, by strong coupling to other states) so that the simplified sequential picture of populating (XUV) and depleting (NIR) the 2s2p state does not apply. Nevertheless, because experiment and ab initio theory agree well across the whole delay range, the physical mechanism of the time-resolved buildup of the Fano resonance is captured by the measurement. An experimental approach to reduce the pulse overlap issue would be to use NIR laser pulses with shorter duration, which could be brought closer in time to the XUV pulse without affecting the excitation.

In the future, the general method of terminating the coherent dipole response by means of laser-driven saturated ionization could be used to temporally resolve the buildup of a wide range of processes that can be tracked via their absorption spectrum. In particular for the case of overlapping resonances (*20*, *26*, *27*), this time-gating approach might be used to access the complementary time-domain information on states that are difficult to separate spectrally. Further processes of interest include the emergence of electron-electron or electron-internuclear correlations in more complex systems such as molecules, liquids, or solids and the birth of quasi-particle spectral signatures in crystals—or even more generally, the correlation dynamics in open quantum systems.

REFERENCES AND NOTES

1. H. Beutler, *Z. Phys.* **93**, 177–196 (1935).
2. U. Fano, *Nuovo Cim.* **12**, 154–161 (1935).
3. S. E. A. Orrigo *et al.*, *Phys. Lett. B* **633**, 469–473 (2006).
4. A. E. Miroshnichenko, S. Flach, Y. S. Kivshar, *Rev. Mod. Phys.* **82**, 2257–2298 (2010).
5. B. Luk'yanchuk *et al.*, *Nat. Mater.* **9**, 707–715 (2010).
6. R. Röhlsberger, H.-C. Wille, K. Schlage, B. Sahoo, *Nature* **482**, 199–203 (2012).
7. C. Ott *et al.*, *Science* **340**, 716–720 (2013).
8. P. Fan, Z. Yu, S. Fan, M. L. Brongersma, *Nat. Mater.* **13**, 471–475 (2014).
9. K. P. Heeg *et al.*, *Phys. Rev. Lett.* **114**, 207401 (2015).
10. M. Reduzzi *et al.*, *J. Phys. At. Mol. Opt. Phys.* **49**, 065102 (2016).
11. M. Kotur *et al.*, *Nat. Commun.* **7**, 10566 (2016).
12. J. Herrmann *et al.*, *Phys. Rev. A* **88**, 043843 (2013).
13. C. A. Nicolaides, T. Mercouris, Y. Komninos, *J. Phys. At. Mol. Opt. Phys.* **35**, L271 (2002).
14. Th. Mercouris, Y. Komninos, C. A. Nicolaides, *Phys. Rev. A* **69**, 032502 (2004).
15. M. Wickenhauser, J. Burgdörfer, F. Krausz, M. Drescher, *Phys. Rev. Lett.* **94**, 023002 (2005).
16. Th. Mercouris, Y. Komninos, C. A. Nicolaides, *Phys. Rev. A* **75**, 013407 (2007).
17. C. A. Nicolaides, T. Mercouris, Y. Komninos, *Phys. Rev. A* **80**, 055402 (2009).
18. W.-C. Chu, C. D. Lin, *Phys. Rev. A* **82**, 053415 (2010).
19. L. Argenti, E. Lindroth, *Phys. Rev. Lett.* **105**, 053002 (2010).
20. L. Argenti *et al.*, *Phys. Rev. A* **87**, 053405 (2013).
21. X. Wang, M. Chini, Y. Cheng, Y. Wu, Z. Chang, *Appl. Opt.* **52**, 323–329 (2013).
22. J. H. D. Eland, R. Feifel, *Chem. Phys.* **327**, 85–90 (2006).
23. J. Feist *et al.*, *Phys. Rev. A* **77**, 043420 (2008).
24. M. Wickenhauser, thesis, Vienna University of Technology, p. 53 (2006)
25. K. Schulz *et al.*, *Phys. Rev. Lett.* **77**, 3086–3089 (1996).

26. K. Meyer *et al.*, *Proc. Natl. Acad. Sci. U.S.A.* **112**, 15613–15618 (2015).
27. M. Wickenhauser, J. Burgdörfer, F. Krausz, M. Drescher, *J. Mod. Opt.* **53**, 247–257 (2006).
28. A. Kaldun *et al.*, *Phys. Rev. Lett.* **112**, 103001 (2014).
29. A. Blättermann, C. Ott, A. Kaldun, T. Ding, T. Pfeifer, *J. Phys. At. Mol. Opt. Phys.* **47**, 124008 (2014).

ACKNOWLEDGMENTS

We thank J. Feist for his work in the development of the time-dependent Schrödinger equation helium code used for the ab initio simulations. A.K., A.B., V.S., C.O., and T.P. acknowledge funding by the Deutsche Forschungsgemeinschaft (DFG) (PF 790/1-1) and the European Research Council (ERC) (X-MuSiC-616783). S.D., R.P., S.N., and J.B. are supported by the Fonds zur Förderung der wissenschaftlichen Forschung (FWF) Austria (SFB-049 NextLite, and P21141-N16) and the Wiener Wissenschafts-, Forschungs- und Technologiefonds project MA14-002. S.D. thanks the International Max Planck Research School of Advanced Photon Science (IMPRS-APS) for financial support. Ab initio calculations were performed by using the Vienna Scientific Cluster (VSC). C.D.L. and H.W. are supported by Chemical Sciences, Geosciences and Biosciences Division, Office of Basic Energy Sciences, Office of Science, U.S. Department of Energy under grant DE-FG02-86ER13491.

SUPPLEMENTARY MATERIALS

www.sciencemag.org/content/354/6313/738/suppl/DC1
Materials and Methods
Supplementary Text
References (*30*–*36*)

2 August 2016; accepted 30 September 2016
10.1126/science.aah6972

CATALYSIS

A bioinspired iron catalyst for nitrate and perchlorate reduction

Courtney L. Ford,* Yun Ji Park,* Ellen M. Matson, Zachary Gordon, Alison R. Fout†

Nitrate and perchlorate have considerable use in technology, synthetic materials, and agriculture; as a result, they have become pervasive water pollutants. Industrial strategies to chemically reduce these oxyanions often require the use of harsh conditions, but microorganisms can efficiently reduce them enzymatically. We developed an iron catalyst inspired by the active sites of nitrate reductase and (per)chlorate reductase enzymes. The catalyst features a secondary coordination sphere that aids in oxyanion deoxygenation. Upon reduction of the oxyanions, an iron(III)-oxo is formed, which in the presence of protons and electrons regenerates the catalyst and releases water.

The most efficient reduction of nitrogen- and chlorine-containing oxyanions is achieved by the microbial metalloenzymes (per)chlorate reductase and nitrate reductase during anaerobic respiration (*1*, *2*). The active sites of the two metalloenzymes are similar and allow each enzyme to reduce both nitrogen- and chlorine-containing oxyanions (Fig. 1) (*1*, *2*). Both reductases also feature extensive hydrogen-bonding networks, which facilitate the movement of protons and water about the active site and stabilize reactive intermediates (*1*–*3*). Disruption of this network in nitrate reductase via mutagenesis results in the complete loss of activity because of the low stability of high-valent Mo=O intermediates (*3*, *4*). Furthermore, positively charged residues near the active site in (per)chlorate reductase aid in the binding of perchlorate to the Mo-center (*3*). The noncovalent interactions found within the metalloenzymes play an important role in facilitating reactivity (*1*–*11*). Incorporating these interactions into transition-metal complexes may aid in oxyanion reactivity because most transition-metal systems are not capable of these reductions (*12*–*17*).

The challenge in reducing these oxyanions lies not only in their unfavorable reduction potentials but also in their low binding affinity to transition-metal centers (*12*). These inorganic oxyanions have long been touted for their weak complexation, poor nucleophilicity, and consequently their kinetic inertness toward oxidation and reduction (*12*). Therefore, harsh reaction conditions (such as low pH, high temperature, photolysis, and/or long reaction times) are required to facilitate oxyanion reduction in homogenous systems (*12*–*17*).

Inspired by the active sites of nitrate and (per)chlorate reductase, we developed a nonheme platform that incorporates the following features: (i) an earth-abundant redox-active metal center (iron) and (ii) a secondary coordination sphere that facilitates deoxygenation of substrates and high-valent iron-oxo intermediates. Previously, we reported the synthesis and characterization of a family of late, first-row transition-metal complexes [N(afa^{Cy})$_3$MOTf]OTf (M = Mn, Fe, and Co), featuring the dative (azafulvene-amine) coordination mode of the ligand and the presence of the amino-derived secondary coordination sphere (*18*–*22*). The ability of the ligand to undergo tautomerization may be a key feature during multi-electron reactions because it can facilitate proton and electron transfer between the substrate and the metal center. Furthermore, the secondary coordination sphere orients substrates binding to the metal center, as demonstrated in our nitrite reduction studies, in which a single hydrogen bond stabilized a key metal-nitrito intermediate (*21*, *22*).

The addition of tetrabutylammonium nitrite ([NBu$_4$][NO$_2$]) to 2 equivalents (eq) of [N(afa^{Cy})$_3$FeOTf]OTf (Fe^{II}-OTf; OTf, trifluoromethanesulfonate) afforded the iron(III)-oxo complex [N(afa^{Cy})$_3$FeO]OTf (Fe^{III}-O) and NO(g), which was trapped by Fe^{II}-OTf to furnish the iron(II)-nitrosyl species [N(afa^{Cy})$_3$FeNO]OTf$_2$ (Fe^{II}-NO) (*21*). Given the facile one-electron reduction of nitrite by Fe^{II}-OTf, we sought to explore the reduction of

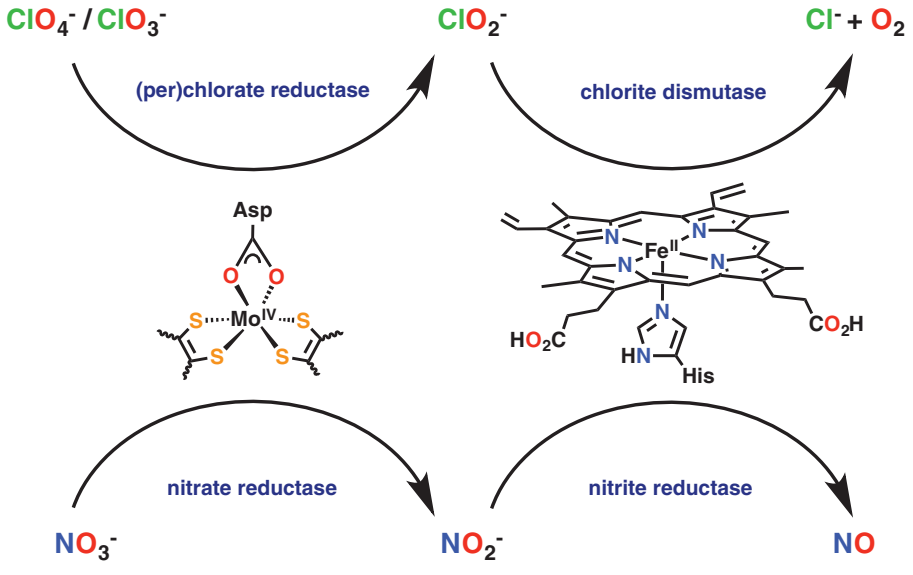

Fig. 1. Biological oxyanion reduction. The active sites of the enzymes responsible for the reduction of chlorine- and nitrogen-containing oxyanions are depicted.

School of Chemical Sciences, University of Illinois at Urbana-Champaign, 600 South Mathews Avenue, Urbana, IL 61801, USA.
*These authors contributed equally to this work. †Corresponding author. Email: fout@illinois.edu

nitrate. Hypothesizing that if the Fe^{II}-OTf could perform the two-electron reduction of nitrate to generate nitrite, the reduction of nitrite would then proceed as before to release NO(g), akin to the described reactivities of nitrate reductase and nitrite reductase, respectively. Fe^{III}-O and Fe^{II}-NO formed when tetrabutylammonium nitrate, $[NBu_4][NO_3]$, was added to 3 eq of Fe^{II}-OTf in the presence of triethylamine (NEt_3) (fig. S3) (*23*). Two thirds of the isolated product consisted of Fe^{III}-O, and one third was Fe^{II}-NO (67 and 28% isolated yield, respectively, based on the initial mass of Fe^{II}-OTf).

After the successful reduction of nitrate, we investigated the more challenging reduction of perchlorate (Fig. 2). Because of the low binding affinity of perchlorate to transition metals, our initial perchlorate reduction studies used iron(II)-perchlorate generated in situ via salt metathesis of $FeCl_2$ and 2 eq of $AgClO_4$. Ligand, $H_3N(pi^{Cy})_3$, was then added, resulting in an immediate color change from colorless to red-brown. Crystals suitable for x-ray diffraction (Fig. 2A) revealed an iron(III)-oxo with an outer-sphere perchlorate anion, $[N(afa^{Cy})_3FeO]ClO_4$, $[Fe^{III}O]$-ClO_4. The bond lengths of $[Fe^{III}$-$O]ClO_4$ were similar to those previously reported for Fe^{III}-O, with an Fe–O distance of 1.8055(11) Å, compared with 1.8079(9) Å for Fe^{III}-O (*21*). Furthermore, all three amino moieties are engaged in hydrogen-bonding to the oxygen atom.

In order to probe perchlorate binding to the metal center, the redox-inactive zinc perchlorate complex $[N(afa^{Cy})_3ZnClO_4]ClO_4$ (Zn-ClO_4) was obtained from the addition of the ligand to Zn$(ClO_4)_2$. Solid-state structural characterization of the complex revealed a perchlorate anion bound to zinc with no hydrogen-bonding interactions from the amino moieties of the ligand (Fig. 2B). Instead, one arm engages in hydrogen-bonding to the outer-sphere perchlorate anion. Zn-ClO_4 was robust and showed no perchlorate deoxygenation. These experiments confirmed that the secondary coordination sphere is not used in perchlorate coordination but rather facilitates the reduction of ClO_4^- through stabilization of the resulting metal-oxo center.

The labile ClO_4^- ligand was also transiently installed on iron from the reaction of tetrabutylammonium perchlorate ($[NBu_4][ClO_4]$) to 5 eq of Fe^{II}-OTf in the presence of NEt_3. The ^1H nuclear magnetic resonance (NMR) spectrum of the reaction revealed the formation of two products, one of which was identified as Fe^{III}-O. We propose that the reaction proceeds via sequential oxygen atom transfer events from perchlorate to afford Fe^{III}-O and the iron(II)-chloride compound $[N(afa^{Cy})_3FeCl]OTf$ (Fe^{II}-Cl) in a 4:1 ratio. Independent synthesis of Fe^{II}-Cl confirmed this formulation. Crystallographic refinement revealed a trigonal bipyramidal geometry about the iron(II) center, with an axial chloride ligand and an outer-sphere triflate anion (Fig. 2C). Because of the low hydrogen-bonding affinity of chloride, the ligand does not hydrogen-bond to chloride and instead hydrogen-bonds to the outersphere triflate.

We propose that the reduction of perchlorate proceeds stepwise via sequential deoxygenations from perchlorate to chlorate, chlorite, and hypochlorite (Fig. 2D). To test this hypothesis, we investigated the reactivity of Fe^{II}-OTf toward the other chlorine oxyanions. In each case, we obtained mixtures of Fe^{III}-O and Fe^{II}-Cl. In order to quantify the ratios of Fe^{III}-O and Fe^{II}-Cl produced from the reduction of each chlorine oxyanion, we used the reaction Fe^{III}-O with 1,2-diphenylhydrazine (DPH) (vide infra) to yield azobenzene. Because Fe^{II}-Cl did not react with DPH, the addition of DPH (in equimolar amounts based on Fe^{II}-OTf) to the chlorine oxyanion reduction mixture would yield a mixture of azobenzene and unreacted DPH whose ratio would match that of the oxygen and chlorine present in the starting oxyanion, assuming complete reduction. This method successfully demonstrated the ratios of oxygen and chlorine present in perchlorate, chlorate, and hypochlorite; the ratios of azobenzene to DPH quantified with ^1H NMR spectroscopy were 4.36:1, 2.54:1, and 0.67:1, respectively (fig. S8).

We also investigated the reduction of Fe^{III}-O to test the possibility of whether Fe^{II}-OTf could be regenerated with concomitant release of water; two protons and one electron were required for this transformation. For this purpose, DPH (a $2H^+/2e^-$ source) (*24*) and Fc*OTf (as a sacrificial oxidant; Fc*OTf is decamethylferrocenium triflate) were added to Fe^{III}-O, regenerating Fe^{II}-OTf (fig. S11) (*23*) in 74% isolated yield,

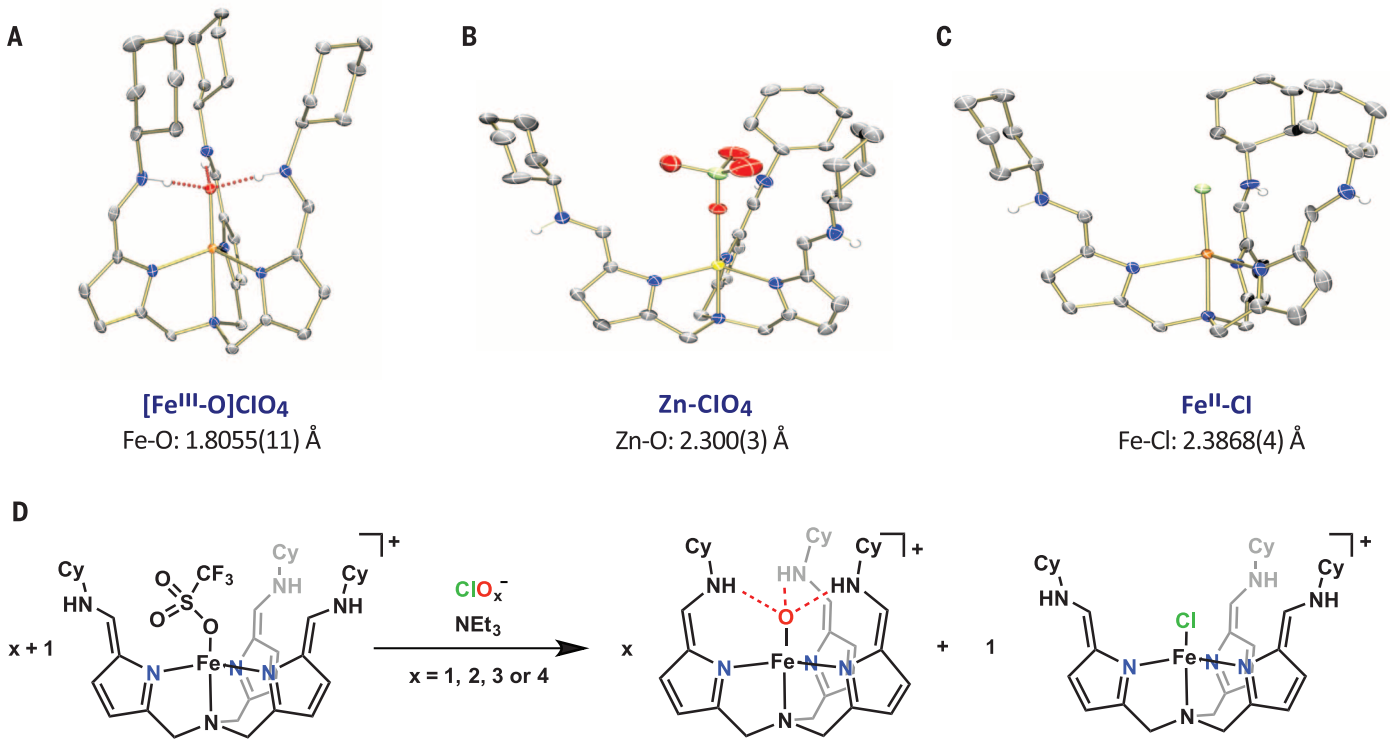

Fig. 2. Solid-state molecular structures and stoichiometric chlorine oxyanion reduction. Crystal structure of (**A**) $[Fe^{III}$-$O]ClO_4$, (**B**) Zn^{II}- ClO_4, and (**C**) Fe^{II}-Cl. Thermal ellipsoids are at the 50% probability level; solvent molecules and selected H-atoms have been omitted for clarity. (**D**) Stoichiometric chlorine oxyanion reduction.

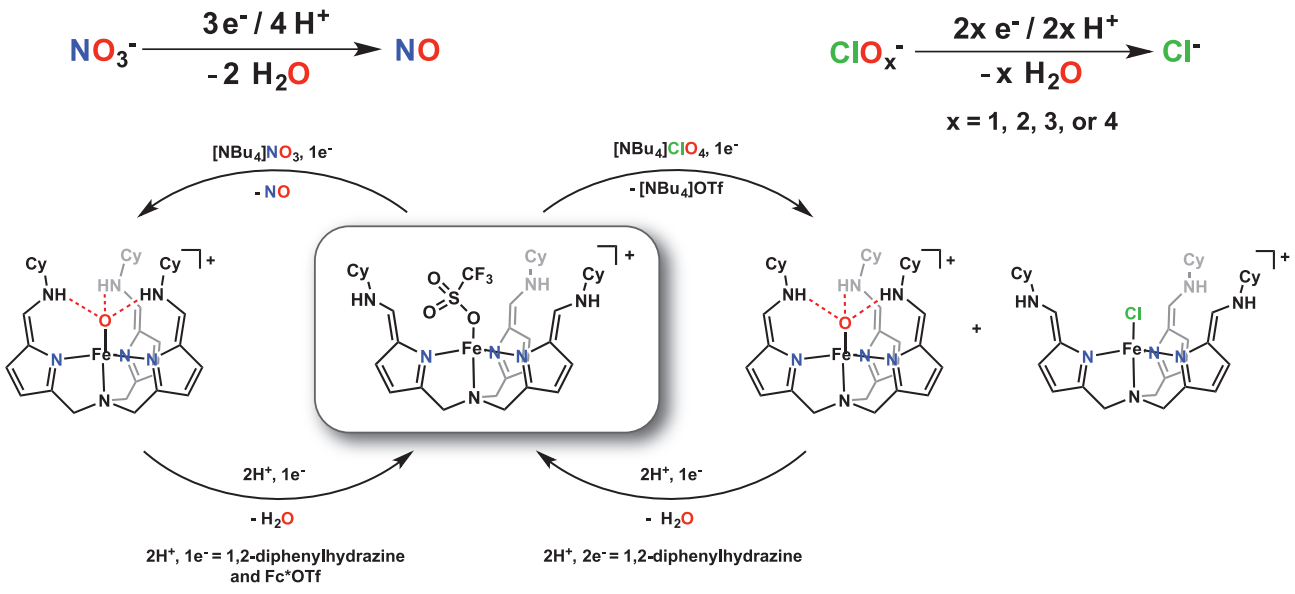

Fig. 3. Catalytic nitrate and perchlorate reduction.

concomitant with the formation of 0.89 eq of water, as assayed with Karl Fischer titration. Similarly, when Fe^{III}-O was generated in situ from 0.5 eq of $NaNO_3$ and reduced under identical conditions, 0.83 eq of water was formed.

Having shown that Fe^{III}-O is cleanly regenerated with DPH/Fc*OTf, we examined the possibility that the oxyanion deoxygenation could be catalytic, beginning with nitrate. Using (TPP)Co (TPP, 5,10,15,20-tetraphenylporphyrin) to trap and subsequently quantify the NO(g) produced during the reaction, we tested the reactivity of 3 eq of $NaNO_3$ [relative to (TPP)Co], 6 eq of DPH, and 3 eq of Fc*OTf as a control reaction for nitrate reduction. Quantifying by means of ^{1}H NMR spectroscopy the amount of (TPP)CoNO formed revealed that NO(g) was produced under these conditions; 0.18 eq of (TPP)CoNO was detected after 27 hours, and 0.24 eq of (TPP)CoNO was detected after 42 hours [0.5 eq of (TPP)CoNO corresponds to TON of 1]. When Fe^{II}-OTf was added to the reaction mixture, over seven times the amount of NO(g) was trapped by (TPP)Co as compared with the control reaction; 1.46 eq of (TPP)CoNO was detected after 27 hours, and 1.74 eq of (TPP)CoNO was detected after 42 hours, resulting in a turnover number (TON) of 3.5 (Fig. 3).

We hypothesize that the catalytic reduction of perchlorate would proceed similarly; however, because of the explosion hazards associated with perchlorate reagents, we limited the scale of the catalytic reaction to no more than 10 mg of $[NBu_4][ClO_4]$. Fe^{II}-OTf was mixed with $[NBu_4][ClO_4]$ and 4 eq of DPH and stirred overnight. Analysis of the crude reaction mixture by means of ^{1}H NMR spectroscopy revealed that 3.4 eq of the DPH was converted to azobenzene, providing an indirect measurement of the amount of perchlorate that was fully reduced. In the subsequent work-up, Fe^{II}-Cl was crystallized in 75% yield. This yield of Fe^{II}-Cl corresponds to a TON of 3 (Fig. 3). Although we were unable to determine whether the reaction proceeds by sequential two-electron reductions, from perchlorate to chlorate to chlorite to hypochlorite, the reaction proceeds through four steps because four oxygen atoms must be transferred from perchlorate to generate chloride. Moreover, the stoichiometric reaction of each chlorine oxyanion with Fe^{II}-OTf yielded the same two products, Fe^{III}-O and Fe^{II}-Cl, in the expected ratios.

The uses of nitrogen- and chlorine-containing oxyanions are both extensive and varied, with notable applications in fertilizers, bleaching agents, propellants, and explosives (*5*–*8*). Because of their high solubility and mobility in water, they have become pervasive contaminants in many sources of drinking water (*5*–*8*). Remediation of polluted water by reduction of these oxyanions to benign products would thus have tremendous impact. The described catalytic deoxygenation of perchlorate and nitrate features mild reaction conditions. Our bioinspired iron catalyst is a first step toward a potentially more sustainable reduction strategy. Future improvements focusing on improved turnover numbers and a detailed mechanistic understanding will provide insights into catalyst design for future remediation efforts.

REFERENCES AND NOTES

1. H. Zheng, G. Wisedchaisri, T. Gonen, *Nature* **497**, 647–651 (2013).
2. M. D. Youngblut *et al.*, *J. Biol. Chem.* **291**, 9190–9202 (2016).
3. S. Ghafari, M. Hasan, M. K. Aroua, *Bioresour. Technol.* **99**, 3965–3974 (2008).
4. M. J. Oosterkamp, F. Mehboob, G. Schraa, C. M. Plugge, A. J. M. Stams, *Biochem. Soc. Trans.* **39**, 230–235 (2011).
5. E. T. Urbansky, M. R. Schock, *J. Environ. Manage.* **56**, 79–95 (1999).
6. R. Srinivasan, G. A. Sorial, *Separ. Purif. Tech.* **69**, 7–21 (2009).
7. L. Ye, H. You, J. You, J. Yao, H. Su, *Desalination* **298**, 1–12 (2012).
8. N. Bardiya, J.-H. Bae, *Microbiol. Res.* **166**, 237–254 (2011).
9. A. Magalon *et al.*, *Biochemistry* **37**, 7363–7370 (1998).
10. M. G. Bertero *et al.*, *Nat. Struct. Biol.* **10**, 681–687 (2003).
11. T. Giblin, W. T. Frankenberger Jr., *Microbiol. Res.* **156**, 311–315 (2001).
12. M. M. Abu-Omar, *Comm. Inorg. Chem.* **24**, 15–37 (2003).
13. M. M. Abu-Omar, L. D. McPherson, J. Arias, V. M. Béreau, *Angew. Chem.* **39**, 4310–4313 (2000).
14. J. Liu *et al.*, *Environ. Sci. Technol.* **50**, 5874–5881 (2016).
15. J. Liu *et al.*, *ACS Catal.* **5**, 511–522 (2015).
16. K. S. Suslick, R. A. Watson, *Inorg. Chem.* **30**, 912–919 (1991).
17. K. S. Suslick, F. V. Acholla, B. R. Cook, *J. Am. Chem. Soc.* **109**, 2818–2819 (1987).
18. E. M. Matson, J. A. Bertke, A. R. Fout, *Inorg. Chem.* **53**, 4450–4458 (2014).
19. E. M. Matson, Y. J. Park, J. A. Bertke, A. R. Fout, *Dalton Trans.* **44**, 10377–10384 (2015).
20. E. M. Matson, Z. Gordon, B. Lin, M. J. Nilges, A. R. Fout, *Dalton Trans.* **43**, 16992–16995 (2014).
21. E. M. Matson, Y. J. Park, A. R. Fout, *J. Am. Chem. Soc.* **136**, 17398–17401 (2014).
22. Y. J. Park, E. M. Matson, M. J. Nilges, A. R. Fout, *Chem. Commun. (Camb.)* **51**, 5310–5313 (2015).
23. Materials and methods are available as supplementary materials on *Science* Online.
24. R. L. Shook *et al.*, *J. Am. Chem. Soc.* **133**, 5810–5817 (2011).

ACKNOWLEDGMENTS

This work was supported by the U.S. Department of Energy, Office of Science, Office of Basic Energy Sciences, Chemical Sciences, Geosciences, and Biosciences Division under award DE-SC-0016026 and the University of Illinois at Urbana-Champaign. Y.P. was supported by the American Association for the Advancement of Science Milligan Mason Award for Women in the Chemical Sciences, awarded to A.R.F. We thank T. Betley, T. Rauchfuss, and K. Suslick for helpful discussions and S. Denmark and Y. Lu for use of their instruments. The crystallographic data CCDC-1510909-1510911 can be obtained free of charge from the Cambridge Crystallographic Data Centre (www.ccdc.cam.ac.uk/data_request/cif). Data are available in the supplementary materials.

SUPPLEMENTARY MATERIALS

www.sciencemag.org/content/354/6313/741/suppl/DC1
Materials and Methods
Figs. S1 to S14
Tables S1 to S8
References (*25*–*28*)

7 September 2016; accepted 11 October 2016
10.1126/science.aah6886

WILDLIFE DISEASE

Red squirrels in the British Isles are infected with leprosy bacilli

Charlotte Avanzi,[1]* Jorge del-Pozo,[2]* Andrej Benjak,[1]* Karen Stevenson,[3] Victor R. Simpson,[4] Philippe Busso,[1] Joyce McLuckie,[3] Chloé Loiseau,[1]† Colin Lawton,[5] Janne Schoening,[6] Darren J. Shaw,[2] Jérémie Piton,[1] Lucio Vera-Cabrera,[7] Jesùs S. Velarde-Felix,[7] Fergal McDermott,[6] Stephen V. Gordon,[6,8,9,10] Stewart T. Cole,[1]‡ Anna L. Meredith[2]‡

Leprosy, caused by infection with *Mycobacterium leprae* or the recently discovered *Mycobacterium lepromatosis*, was once endemic in humans in the British Isles. Red squirrels in Great Britain (*Sciurus vulgaris*) have increasingly been observed with leprosy-like lesions on the head and limbs. Using genomics, histopathology, and serology, we found *M. lepromatosis* in squirrels from England, Ireland, and Scotland, and *M. leprae* in squirrels from Brownsea Island, England. Infection was detected in overtly diseased and seemingly healthy animals. Phylogenetic comparisons of British and Irish *M. lepromatosis* with two Mexican strains from humans show that they diverged from a common ancestor around 27,000 years ago, whereas the *M. leprae* strain is closest to one that circulated in Medieval England. Red squirrels are thus a reservoir for leprosy in the British Isles.

Often considered a disease of the past, leprosy remains a public health problem in certain low- and middle-income countries, with ~220,000 new cases reported annually (*1*). Leprosy was rife in Europe in the Middle Ages but disappeared during the 15th and 16th centuries, probably because of social segregation, other infectious diseases such as plague, or changes in host immunity (*2*–*5*). Today, all British clinical cases occur in individuals with a history of residence in a leprosy-endemic country (*6*). The disease manifests in different forms, ranging from multibacillary (or lepromatous) to paucibacillary (or tuberculoid), depending on the immunogenetics of the host (*4*). In all forms, skin lesions are accompanied by peripheral nerve damage, which causes sensory loss and may lead to deformities.

It had generally been accepted that leprosy resulted solely from interhuman transmission of *Mycobacterium leprae*. But in recent years, compelling evidence emerged from the southern United States for zoonotic cases after exposure to infected nine-banded armadillos (*Dasypus novemcinctus*) (*7*–*9*). Furthermore, *M. leprae* was considered to be the sole causative agent of leprosy until 2008, when a new species, *Mycobacterium lepromatosis*, was identified in patients with diffuse lepromatous leprosy (DLL) (*10*). Such cases were primarily associated with Mexico and the Caribbean region (*11*). Comparison of the genome sequences of *M. lepromatosis* and *M. leprae* revealed that despite separating millions of years ago, the two genomes are remarkably similar in their size, organization, and (pseudo)gene content, but show only 88% sequence identity (*11*).

The Eurasian red squirrel *Sciurus vulgaris* is a widespread Palearctic species found from Ireland in the west to Kamchatka in the east (*12*, *13*). However, in the United Kingdom, the *S. vulgaris* population of ~140,000 is severely threatened by habitat loss, squirrel poxvirus infection, and competition with >2.5 million gray squirrels, *Sciurus carolinensis*, introduced from North America (*14*, *15*). Because of their endangered status, red squirrels are now protected (*16*). Recent detection of mycobacterial infection in red squirrels was reported in Scotland, with lesions and histopathology characteristic of DLL and evidence for *M. lepromatosis* being the etiological agent (*17*). Similarly affected squirrels were observed on the Isle of Wight and Brownsea Island in southern England (*18*), and observations of squirrel leprosy in Scotland are increasing (Fig. 1). Here, we investigated the leprosy outbreak using 70 red squirrel cadavers from Great Britain, with or without disease signs; 40 cadavers from Ireland, where no sightings of squirrels with leprosy signs have been reported; and four Scottish gray squirrel cadavers.

A differential polymerase chain reaction (PCR) screen was implemented to detect *M. leprae* and *M. lepromatosis* DNA (*11*). We analyzed a total of 172 tissue samples from 13 animals with leprosy features and 101 without leprosy features (tables S1 and S2) (*19*). Six Scottish squirrels (two without clinical signs) (*17*), two from Ireland (no clinical signs), and one from the Isle of Wight, England (*18*) contained *M. lepromatosis* in several tissue samples from different anatomical sites, whereas all 25 red squirrels (17 without clinical signs) tested from Brownsea Island were infected with *M. leprae* (Fig. 1 and table S3). No cases of co-infection were observed (table S3). From the combined results, we concluded that 21% [21/101; 95% confidence interval (CI), 13 to 30%] of the squirrels without clinical signs and all 13 of the animals with clinical signs harbored leprosy bacilli.

Serological tests were performed on nine diseased and 14 healthy red squirrels from Scotland and England, as well as the four gray squirrels. The grays were all seronegative, whereas 13 of 23 blood samples from red squirrels contained antibodies for the leprosy-specific antigen PGL-1 (phenolic glycolipid–1) (*20*) (table S4). Serology is useful to confirm the disease and to predict infection in live animals but cannot be used for species identification, as both *M. leprae* and *M. lepromatosis* produce this cell wall antigen (*11*).

Diseased Scottish squirrels infected with *M. lepromatosis* displayed a range of macroscopic lesions, including alopecia and extensive swelling of the snout, lips, eyelids, ear pinnae, and limb extremities (Fig. 1, Fig. 2A, fig. S1, and tables S2 and S5) (*19*). Histopathological examination of four such squirrels (Fig. 2B) revealed granulomatous dermatitis, sheets of epithelioid macrophages, and large numbers of acid-fast bacilli (AFB). There was neural involvement with the presence of AFB in nerve endings; neuritis was patchy and more frequently perineural (Fig. 2C). Inflammation was not focused exclusively around nerves and was mostly dermal. There were no signs of vasculitis, but AFB were present intravascularly (Fig. 2C). Similar lesions were observed in eight squirrels from Brownsea Island infected with *M. leprae*, although these animals also harbored numerous AFB in the spleen (Fig. 2C). Overall, the macroscopic signs and histopathology were characteristic of lepromatous leprosy (Fig. 2, A and B, and figs. S2 and S3). From post mortem inspection of diseased squirrels, it was not possible to distinguish between infection with *M. lepromatosis* or *M. leprae*, as is the case in human leprosy (*11*, *21*, *22*).

To obtain deeper insight into the strains responsible and to perform phylogenetic analyses, we used a variety of DNA enrichment techniques (table S6) prior to Illumina sequencing, which was necessary because neither *M. leprae* nor *M. lepromatosis* can be cultured (*19*). Sufficient sequence coverage of *M. lepromatosis* genomes from seven squirrels was obtained (table S7). In parallel, we sequenced an additional genome of *M. lepromatosis*, Pl-02, from a PGL-1–seropositive patient from Sinaloa, Mexico (tables S1 and S4). The resultant sequence reads were mapped against the reference *M. lepromatosis* genome

[1]Global Health Institute, Ecole Polytechnique Fédérale de Lausanne, 1015 Lausanne, Switzerland. [2]Royal (Dick) School of Veterinary Studies and Roslin Institute, University of Edinburgh, Easter Bush Campus, Roslin, Scotland, UK. [3]Moredun Research Institute, Pentlands Science Park, Bush Loan, Edinburgh, Scotland, UK. [4]Wildlife Veterinary Investigation Centre, Chacewater, Cornwall, UK. [5]School of Natural Sciences, Ryan Institute, National University of Ireland, Galway, Ireland. [6]UCD School of Veterinary Medicine, University College Dublin, Belfield, Dublin, Ireland. [7]Laboratorio Interdisciplinario de Investigación Dermatológica, Servicio de Dermatología, Hospital Universitario, Monterrey, N.L., Mexico. [8]UCD School of Medicine, University College Dublin, Belfield, Dublin, Ireland. [9]UCD School of Biomolecular and Biomedical Science, University College Dublin, Belfield, Dublin, Ireland. [10]UCD Conway Institute of Biomolecular and Biomedical Research, University College Dublin, Belfield, Dublin, Ireland. *These authors contributed equally to this work. †Present address: Department of Medical Parasitology and Infection Biology, Swiss Tropical and Public Health Institute, 4002 Basel, Switzerland. ‡Corresponding author: Email: stewart.cole@epfl.ch (S.T.C.); anna.meredith@ed.ac.uk (A.L.M.)

sequence from a patient from Monterrey, Mexico (*11*) to identify polymorphisms. Consistent with previous *M. leprae* genome comparisons (*9*, *11*, *23*), there was an exceptionally high level of sequence conservation between *M. lepromatosis* strains (99.99% identity) despite their different geographic origins. The two Mexican patient isolates differed by only seven single-nucleotide polymorphisms (SNPs), whereas the number of SNPs in the six British and Irish strains ranged from 1 to 17 on pairwise comparisons (table S8). Overall, there are roughly 400 SNPs that distinguish *M. lepromatosis* strains from Mexico and the British Isles (table S8). Clustering of Mexican and British *M. lepromatosis* strains into two distinct lineages was supported by maximum-parsimony (fig. S4) and neighbor-joining (fig. S5) phylogenetic reconstructions. On the basis of the *M. leprae* mutation rate (*19*) and using the Bayesian inference software BEAST (*24*), we estimated that the British Isles and Mexican strains diverged from their most recent common ancestor around 27,000 years ago, whereas the Irish and British strains diverged as recently as 200 years ago (Fig. 3A). The latter estimate is consistent with the date of the first campaign to reintroduce the red squirrel into Ireland from England between 1820 and 1856, following its extinction in the 17th century (*12*, *25*). This suggests that these animals may already have been infected with *M. lepromatosis* when they were reintroduced.

Finding *M. leprae* in red squirrels in England was unexpected, because leprosy was eradicated from the British Isles several centuries ago, thus demonstrating that a pathogen can persist in the environment long after its clearance from the human reservoir. Furthermore, this is only the second report of *M. leprae* in nonprimate species. From Bayesian and maximum-parsimony analysis (Fig. 3B and fig. S4A), we note that the two closest relatives to the strain of *M. leprae* found on Brownsea Island were both from medieval Europe. Intriguingly, one of these (SK2) originated from the skeletal remains of a leprosy victim buried about 730 years ago in Winchester, a city situated a mere 70 km from Brownsea Island (Fig. 1). Like SK2, the Brownsea Island strain of *M. leprae* belongs to sequence type 3I, which forms a distinct *M. leprae* branch (Fig. 3B) (*3*) and is now endemic in wild armadillos in the southern United States (*9*). Thus, *M. leprae* with this particular sequence type is capable of infecting at least three different hosts: humans, red squirrels, and armadillos.

Because there were no obvious genomic polymorphisms restricted to the *M. leprae* 3I type that might account for this broad host range (tables S9 and S10), we explored the possibility that these three species might share a major susceptibility gene and focused on *TLR1*. This candidate gene, encoding the surface-exposed Toll-like receptor 1 (TLR1) displayed on various epithelial and immune cells, is known to be associated with susceptibility to leprosy (Fig. 4A). A dysfunctional *TLR1* allele encoding an $Ile^{602} \rightarrow Ser$ variant with an altered transmembrane domain is prevalent in Caucasians and is associated with a decreased risk for leprosy (*5*, *26*). By contrast, the *TLR1* $Asn^{248} \rightarrow Ser$ variant is associated with an increased risk of leprosy in humans. This mutation is located in the ninth repeat of the extracellular leucine-rich repeat (LRR) region of TLR1 (*27*). Furthermore, in nine-banded armadillos, an $Arg^{627} \rightarrow Gly$ change in TLR1 [close to the Toll-interleukin receptor (TIR) domain; Fig. 4A] seemingly confers resistance to leprosy (*28*). Using PCR, the coding exon of *TLR1* was amplified and sequenced from 58 red squirrels (with or without lesions) and three gray squirrels (tables S11, S12, and S14) (*19*). Upon comparison of the sequences and TLR1 alignments (table S13), no polymorphisms were observed at the same sites associated with leprosy in humans and armadillos. However, in some red squirrels, two distinct polymorphic sites exist: a single SNP leading to a $Ser^{494} \rightarrow Asn$ mutation in the 19th repeat of the LRR region, and a cluster of linked mutations that produce $Ser^{657} \rightarrow Asn$ (S657N), $Leu^{660} \rightarrow Val$ (L660V), and $Asn^{662} \rightarrow Cys$ (N662C) variants in helix 1 of the TIR domain (Fig. 4B). These mutations were found less frequently in squirrels infected with leprosy bacilli than in healthy animals, which suggests that they may confer protection (for S494N, odds ratio = 5.77; 95% CI, 1.42 to 23.41;

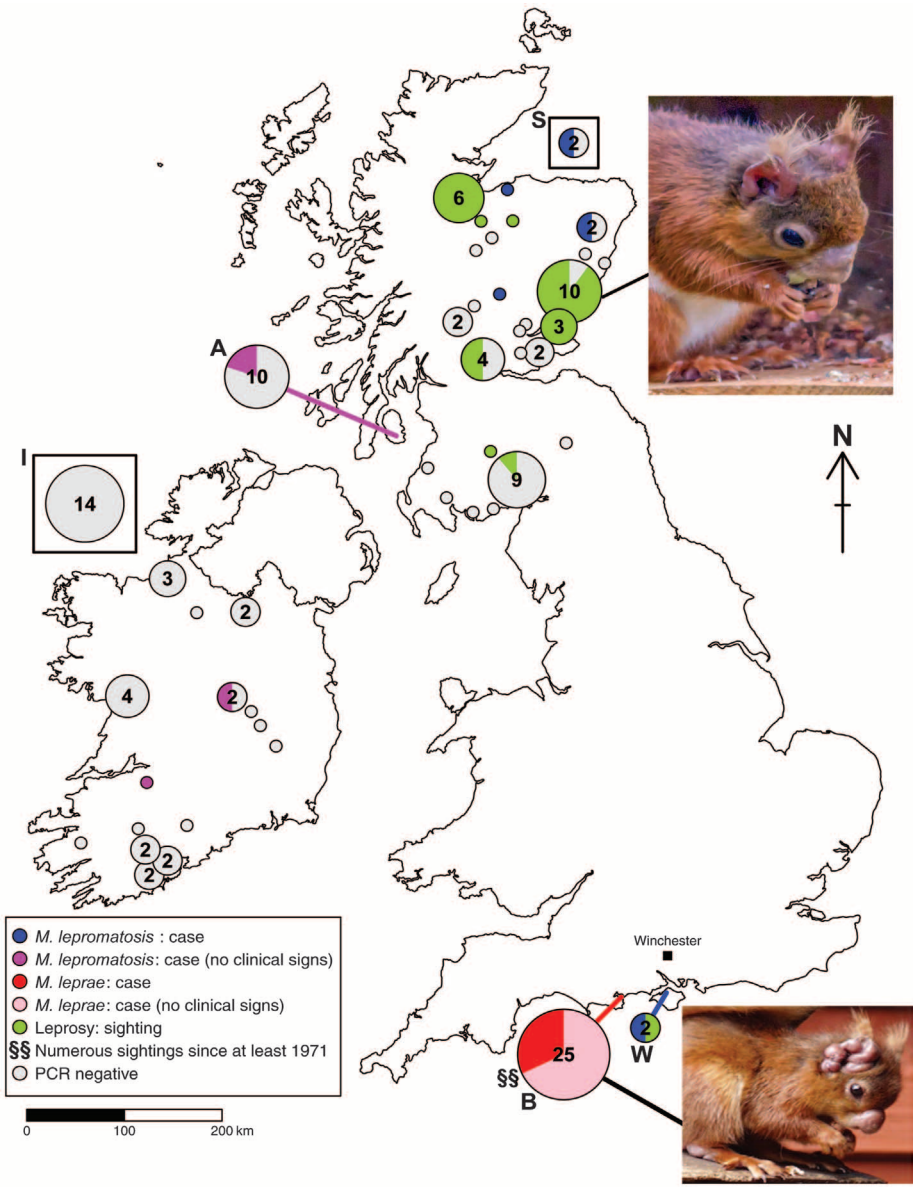

Fig. 1. Squirrel sampling sites in the British Isles. Pie charts indicate the location of sites where squirrels were sighted or found and are color-coded as indicated in the box; numbers within circles indicate different animals tested where $N > 1$. Boxed circles refer to squirrels of unknown location. I, Ireland; S, Scotland; A, Isle of Arran; B, Brownsea Island; W, Isle of Wight. The figure was drawn in R (v3.2.23) with the package *maps* (v3.1.0) using the *mapdata* (v2.2-6) "worldHiresMapEnv" and the package *plotrix* (v3.6-2) for pie charts.

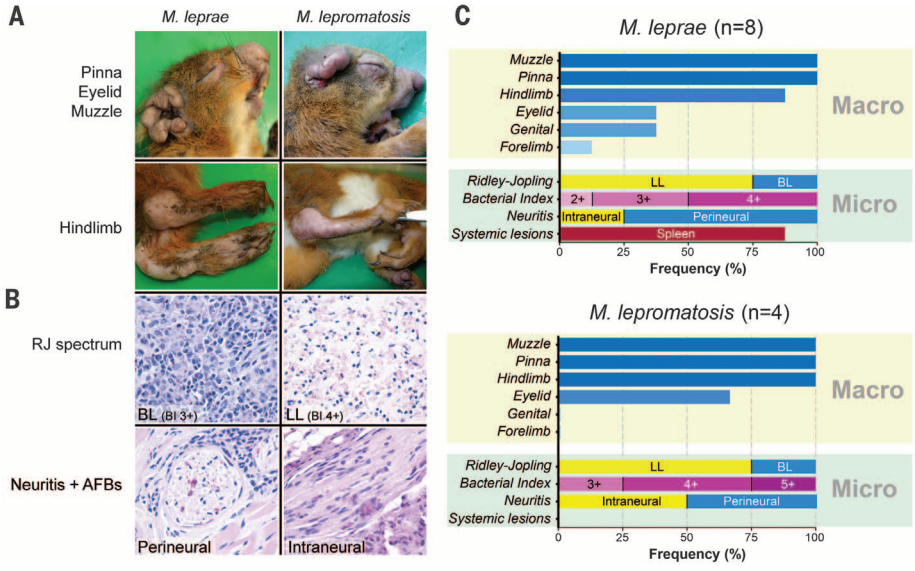

Fig. 2. Gross histopathological features of red squirrels with leprosy. (**A**) Macroscopic features of squirrels infected with *M. lepromatosis* or *M. leprae* are similar. (**B**) Histological examination of tissue sections from infected squirrels using the Ridley-Jopling (RJ) classification after Ziehl Neelsen staining (magnification 400×). LL, lepromatous leprosy; BL, borderline lepromatous leprosy. (**C**) Summary of main macroscopic and microscopic findings from squirrels infected with *M. leprae* (n = 8) or *M. lepromatosis* (n = 4).

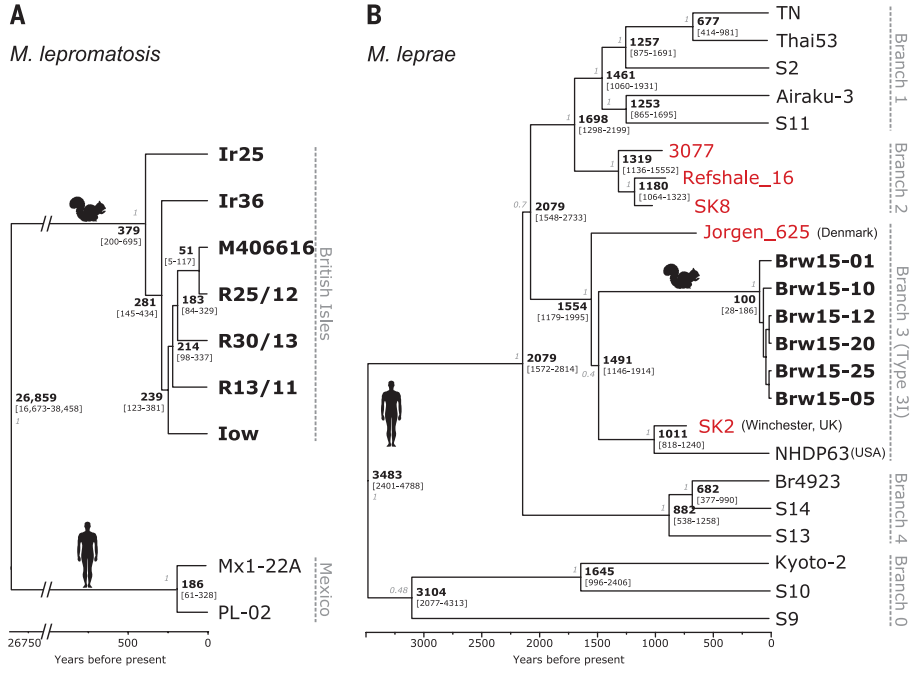

Fig. 3. Phylogeny of leprosy bacilli. (**A**) Bayesian phylogenetic tree representation of nine *M. lepromatosis* genome sequences obtained from squirrels (bold) or humans (upper and lower parts, respectively), calculated by BEAST 1.8.2 (*24*) using the mutation rate of *M. leprae* and inferred from 432 genome-wide variable positions. Squirrel sample prefixes: Ir, Ireland; Iow, Isle of Wight; all others from Scotland. Both human strains were from Mexico. (**B**) Bayesian phylogenetic tree representation of *M. leprae* inferred from 498 genome-wide variable positions, calculated as in (A). For squirrel samples (bold), Brw denotes Brownsea Island cluster; red labeling indicates ancient strains for which radiocarbon dating information was available (*3*). For both trees, divergence time intervals are shown on each node in years before present, with the 95% highest posterior density (HPD) range in brackets. Posterior probabilities for each node are shown in gray.

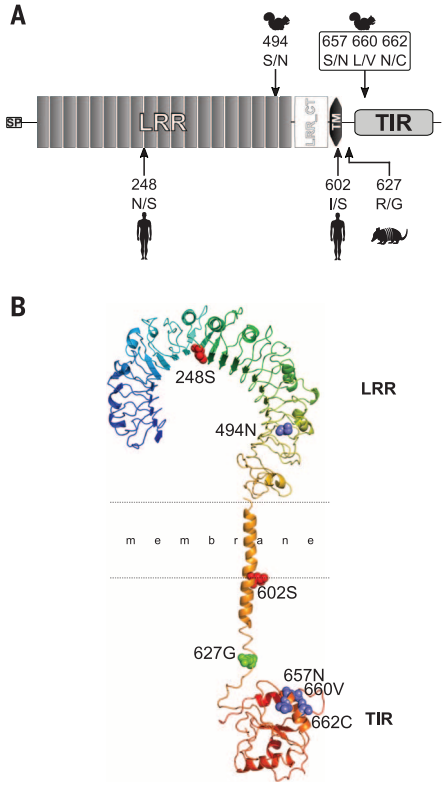

Fig. 4. Organization, structure, and polymorphisms in TLR1 associated with leprosy in humans, armadillos, and red squirrels. (**A**) Schematic representation of TLR1 and its domains (drawn to scale). SP, signal peptide; LRR, leucine-rich repeat; LRR_CT, leucine-rich repeat C-terminal; TM, transmembrane domain; TIR, Toll/interleukin-1 receptor. (**B**) Structural model of the red squirrel TLR1. Protein is colored in a rainbow spectrum from N terminus (blue) to C terminus (red). Amino acid abbreviations: C, Cys; G, Gly; I, Ile; L, Leu; N, Asn; R, Arg; S, Ser; V, Val.

P = 0.01; for S657N-L660V-N662C, odds ratio = 4.89; 95% CI, 0.98 to 24.53; P = 0.05).

It is unclear whether leprosy is contributing to the demise of the red squirrel population or how these animals became infected with *M. lepromatosis* or *M. leprae*. Because *M. lepromatosis* has only recently been discovered as a human pathogen (*10*) and few detailed case reports have been published (*10*, *11*, *21*, *29*), further investigation is required to establish its relative prevalence in wildlife compared to humans. *M. leprae* was long considered to be an obligate human pathogen that was introduced to the Americas by European settlers, prior to anthroponotic infection of armadillos, because there are no human skeletal remains with signs of leprosy from the pre-Columbian era (*9*). The discovery that the strain of *M. leprae* in red squirrels on Brownsea Island today is essentially the same as one that circulated in medieval England and Denmark, and is highly related to the extant North American armadillo strain, raises the possibility of a second anthroponotic introduction in Europe. If this were

the case, it must have occurred several centuries ago, as leprosy became increasingly scarce in the British Isles after the 17th century (*3*). It is also conceivable that humans may have been infected through contact with red squirrels bearing *M. leprae*, as these animals were prized for their fur and meat in former times (*30*). Our findings show that further surveys of animal reservoirs of leprosy bacilli are warranted, because zoonotic infection from such reservoirs may contribute to the inexplicably stubborn plateau in the incidence of the human leprosy epidemic despite effective and widespread treatment with multidrug therapy (*1*).

REFERENCES AND NOTES

1. World Health Organization, *Wkly. Epidemiol. Rec.* **88**, 365–379 (2013).
2. H. D. Donoghue *et al.*, *Infect. Genet. Evol.* **31**, 250–256 (2015).
3. V. J. Schuenemann *et al.*, *Science* **341**, 179–183 (2013).
4. A. Alter, A. Grant, L. Abel, A. Alcaïs, E. Schurr, *Mamm. Genome* **22**, 19–31 (2011).
5. S. H. Wong *et al.*, *PLOS Pathog.* **6**, e1000979 (2010).
6. N. Fulton, L. F. Anderson, J. M. Watson, I. Abubakar, *BMJ Open* **6**, e010608 (2016).
7. R. Sharma *et al.*, *Emerg. Infect. Dis.* **21**, 2127–2134 (2015).
8. R. Truman, *Lepr. Rev.* **76**, 198–208 (2005).
9. R. W. Truman *et al.*, *N. Engl. J. Med.* **364**, 1626–1633 (2011).
10. X. Y. Han *et al.*, *Am. J. Clin. Pathol.* **130**, 856–864 (2008).
11. P. Singh *et al.*, *Proc. Natl. Acad. Sci. U.S.A.* **112**, 4459–4464 (2015).
12. M. Carey, G. Hamilton, A. Poole, C. Lawton, *The Irish Squirrel Survey 2007* (COFORD, Dublin, 2007).
13. S. Harris, G. B. Corbet, *The Handbook of British Mammals* (Mammal Society/Blackwell Scientific, ed. 3, 1991).
14. D. M. Tompkins, A. W. Sainsbury, P. Nettleton, D. Buxton, J. Gurnell, *Proc. R. Soc. B* **269**, 529–533 (2002).
15. E. Stokstad, *Science* **352**, 1268–1271 (2016).
16. Council of Europe, Convention on the Conservation of European Wildlife and Natural Habitats (ETS No. 104), Appendix III (1979). https://rm.coe.int/CoERMPublicCommonSearchServices/DisplayDCTMContent?documentId=0900001680304356
17. A. Meredith *et al.*, *Vet. Rec.* **175**, 285–286 (2014).
18. V. Simpson *et al.*, *Vet. Rec.* **177**, 206–207 (2015).
19. See supplementary materials on *Science* Online.
20. J. S. Spencer, P. J. Brennan, *Lepr. Rev.* **82**, 344–357 (2011).
21. J. S. Velarde-Félix, G. Alvarado-Villa, L. Vera-Cabrera, *Am. J. Trop. Med. Hyg.* **94**, 483–484 (2016).
22. L. Vera-Cabrera *et al.*, *J. Clin. Microbiol.* **53**, 1945–1946 (2015).
23. M. Monot *et al.*, *Nat. Genet.* **41**, 1282–1289 (2009).
24. A. J. Drummond, A. Rambaut, *BMC Evol. Biol.* **7**, 214 (2007).
25. B. P. Vieira, C. Fonseca, R. G. Rocha, *Anim. Biodivers. Conserv.* **38**, 49–58 (2015).
26. S. R. Krutzik *et al.*, *Nat. Med.* **9**, 525–532 (2003).
27. C. de Sales Marques *et al.*, *J. Infect. Dis.* **208**, 120–129 (2013).
28. L. B. Adams *et al.*, *Mem. Inst. Oswaldo Cruz* **107** (suppl. 1), 197–208 (2012).
29. P. G. Jessamine *et al.*, *J. Drugs Dermatol.* **11**, 229–233 (2012).
30. P. Lurz, *Red Squirrel: Naturally Scottish* (Scottish Natural Heritage, 2010).

ACKNOWLEDGMENTS

We thank E. Sheehy, E. Goldstein, M. Flaherty, A. Zintl, the National Trust, Forestry Commission Scotland, and Saving Scotland's Red Squirrels for samples, help, and advice. We thank the Genomic Technologies Facility at the University of Lausanne for Illumina sequencing and technical support. Raw sequence read files have been deposited in the Sequence Read Archive of the National Center for Biotechnology Information under accession numbers SRR3672737 to SRR3672758 (NCBI BioProject PRJNA325727), SRR3674396 to SRR3674450 (NCBI BioProject PRJNA325827), SRR3674451 to SRR3674453 (NCBI BioProject PRJNA325856), and SRR3673933; representative TLR1 sequences have been deposited in GenBank under accession numbers KX388139, KX388140, and KX388141. Phylogenetic trees and SNP alignments have been deposited at Treebase under Study Accession URL http://purl.org/phylo/treebase/phylows/study/TB2:S19692. Supported by the Fondation Raoul Follereau and Swiss National Science Foundation grant IZRJZ3_164174 (S.T.C.), the Scottish Government Rural and Environment Science and Analytical Services Division (K.S.), and the Thomas O'Hanlon Memorial Award in Veterinary Medicine (F.McD.).

SUPPLEMENTARY MATERIALS

www.sciencemag.org/content/354/6313/744/suppl/DC1
Materials and Methods
Figs. S1 to S5
Tables S1 to S14
References (*31*–*51*)

21 June 2016; accepted 27 September 2016
10.1126/science.aah3783

ARCTIC SEA ICE

Observed Arctic sea-ice loss directly follows anthropogenic CO_2 emission

Dirk Notz[1]* and Julienne Stroeve[2,3]

Arctic sea ice is retreating rapidly, raising prospects of a future ice-free Arctic Ocean during summer. Because climate-model simulations of the sea-ice loss differ substantially, we used a robust linear relationship between monthly-mean September sea-ice area and cumulative carbon dioxide (CO_2) emissions to infer the future evolution of Arctic summer sea ice directly from the observational record. The observed linear relationship implies a sustained loss of 3 ± 0.3 square meters of September sea-ice area per metric ton of CO_2 emission. On the basis of this sensitivity, Arctic sea ice will be lost throughout September for an additional 1000 gigatons of CO_2 emissions. Most models show a lower sensitivity, which is possibly linked to an underestimation of the modeled increase in incoming longwave radiation and of the modeled transient climate response.

The ongoing rapid loss of Arctic sea ice has far-reaching consequences for climate, ecology, and human activities alike. These include amplified warming of the Arctic (*1*), possible linkages of sea-ice loss to mid-latitude weather patterns (*2*), changing habitat for flora and fauna (*3*), and changing prospects for human activities in the high north (*3*). To understand and manage these consequences and their possible future manifestation, we need to understand the sensitivity of Arctic sea-ice evolution to changes in the prevailing climate conditions. However, assessing this sensitivity has been challenging. For example, climate-model simulations differ widely in their timing of the loss of Arctic sea ice for a given trajectory of anthropogenic CO_2 emissions: Although in the most recent Climate Model Intercomparison Project 5 (CMIP5) (*4*), some models project a near ice-free Arctic during the summer minimum already toward the beginning of this century, other models keep a substantial amount of ice well into the next century even for an external forcing based on largely undamped anthropogenic CO_2 emissions as described by the Representative Concentration Pathway scenario RCP8.5 (*4*, *5*).

To robustly estimate the sensitivity of Arctic sea ice to changes in the external forcing, we identify and examine a fundamental relationship in which the CMIP5 models agree with the observational record: During the transition to a seasonally ice-free Arctic Ocean, the 30-year running mean of monthly mean September Arctic sea-ice area is almost linearly related to cumulative anthropogenic CO_2 emissions (Fig. 1). In the model simulations, the linear relationship holds until the 30-year running mean, which we analyze to reduce internal variability, samples more and more years of a seasonally ice-free Arctic Ocean, at which point the relationship levels off toward zero. For the first few decades of the simulations, a few models simulate a near-constant sea-ice cover despite slightly rising cumulative CO_2 emissions. This suggests that in these all-forcing simulations, greenhouse-gas emissions were initially not the dominant driver of sea-ice evolution. This notion is confirmed by the CMIP5 1% CO_2 simulations, where the initial near-constant sea-ice cover does not occur (fig. S3A). With rising greenhouse-gas emissions, the impact of CO_2 becomes dominating also in all all-forcing simulations, as evidenced by the robust linear trend that holds in all simulations throughout the transition period to seasonally ice-free conditions. We define this transition period as starting when the 30-year mean September Arctic sea-ice area in a particular simulation decreases for the first time to an area that is 10% or more below the simulation's minimum sea-ice cover during the period 1850 to 1900, and

[1]Max Planck Institute for Meteorology, Hamburg, Germany. [2]National Snow and Ice Data Center, Boulder, CO, USA. [3]University College, London, UK.
*Corresponding author. Email: dirk.notz@mpimet.mpg.de

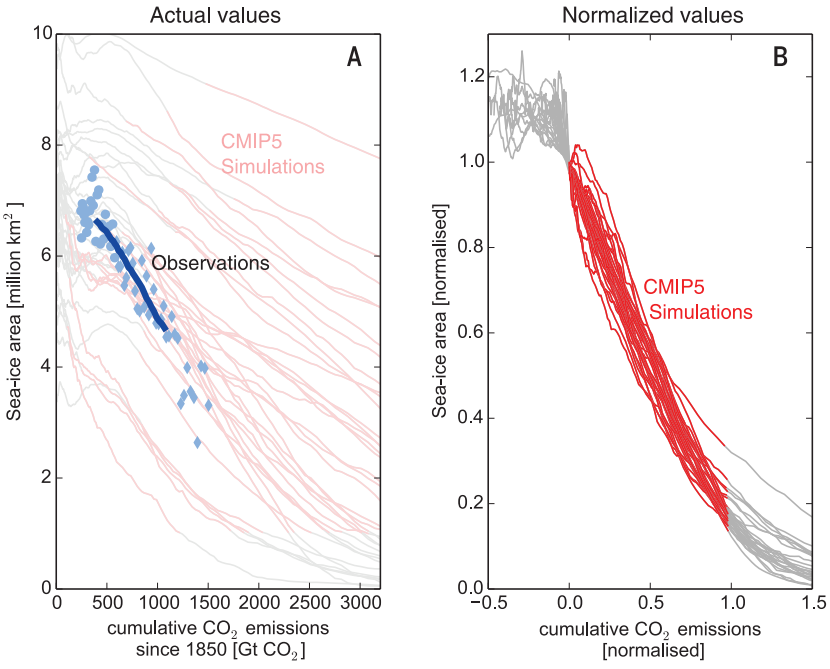

Fig. 1. Relationship between September Arctic sea-ice area and cumulative anthropogenic CO_2 emissions. (**A**) Actual values. The thick blue line shows the 30-year running mean of observed September sea-ice area, and the thinner red lines the 30-year running means from CMIP5 model simulations. For reference, we also show the annual values of observed September sea-ice area, based from 1953 to 1978 on HadISST (*31*) (circles) and from 1979 to 2015 on the NSIDC sea-ice index (*32*) (diamonds; see methods for details). (**B**) Normalized simulations. For this plot, the simulated CMIP5 sea-ice area is normalized by dividing by the simulated sea-ice area at the onset of the transition period as defined in the text. For each simulation, the cumulative emissions (*33*) are set to 0 at the onset of the transition period and then linearly scaled to reach 1 by the end of the transition period (compare table S1 for actual values). This linearization is only carried out to more explicitly visualize the linearity in the models. All analyses in the paper are based on the original data shown in (A).

as ending once the 30-year mean September Arctic sea-ice area drops for the first time below 1 million km^2 (see table S1 for specific numbers).

The existence of a robust, linear relationship between cumulative CO_2 emissions and Arctic sea-ice area in all CMIP5 models and in the observational record extends the findings of earlier studies that demonstrated such relationships for individual, sometimes more simplified models (*6*, *7*), and of studies that have demonstrated a linear relationship between Arctic sea-ice area and either global mean temperature (*5*, *8*–*12*) or atmospheric CO_2 concentration (*13*, *14*). These linear relationships are highly suggestive of a fundamental underlying mechanism, which has been elusive so far. We will later suggest a conceptual explanation of the linearity, but we begin by discussing two implications of the observed linear relationship that are independent of its underlying mechanism.

First, the observed linear relationship allows us to estimate a sensitivity of 3.0 ± 0.3 m^2 of September Arctic sea-ice loss per metric ton of anthropogenic CO_2 emissions during the observational period 1953 to 2015. This number is sufficiently intuitive to allow one to grasp the contribution of personal CO_2 emissions to the loss of Arctic sea ice. For example, on the basis of the observed sensitivity, the average personal CO_2 emissions of several metric tons per year can be directly linked to the loss of tens of square meters of Arctic sea ice in every year (fig. S1).

Second, the linear relationship allows for a robust evaluation of climate-model simulations. Although a number of previous studies have found that the observed sea-ice retreat has been faster than projected by most climate-model simulations (*15*, *16*), it has remained unclear whether these differences are primarily a manifestation of internal variability (*17*, *18*). The sensitivity that we estimate here is, in contrast, based on the average evolution over many decades, thus eliminating internal variability to a substantial degree. A mismatch between the observed and the simulated sensitivity hence robustly indicates a shortcoming either in the model or in the external forcing fields used for a simulation.

Evaluating the simulated sensitivity, we find that most CMIP5 models systematically underestimate the observed sensitivity of Arctic sea ice relative to anthropogenic CO_2 emissions of 3.0 ± 0.3 m^2 (see table S1 for details). Across the full

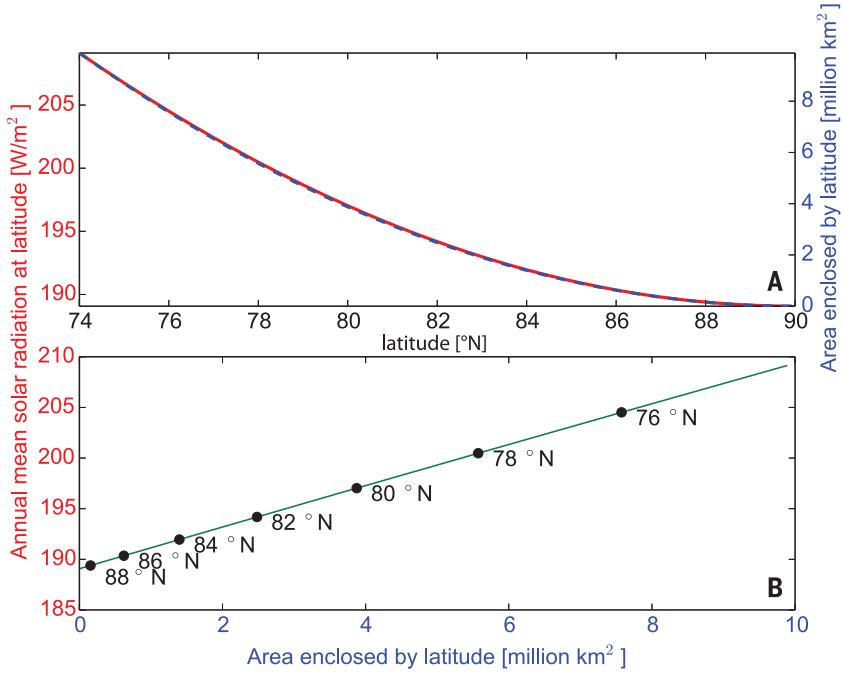

Fig. 2. Relationship between annual mean incoming shortwave radiation and sea-ice area. (**A**) Annual mean incoming top-of-the-atmosphere shortwave radiation at, and area within, a given latitude. The area within a given latitude band is calculated from simple spherical geometry. The latitudinal dependence of average daily incoming shortwave radiation at the top of the atmosphere is calculated from the very good approximation $S(\varphi) = 1 - 0.482P_2(\sin(\varphi))$, where P_2 is the second Legendre polynom (*34*). (**B**) As in (A), but with the *x* axis exchanged for clarity.

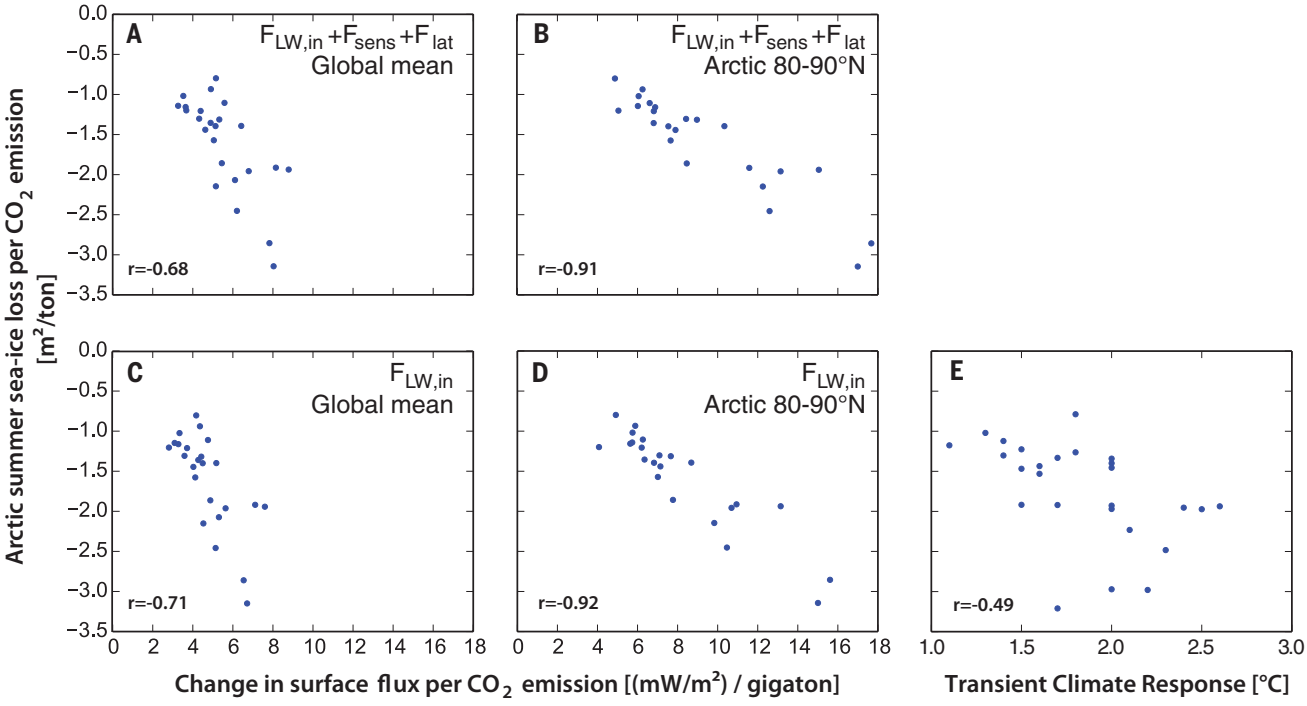

Fig. 3. Relationship between Arctic sea-ice loss and other metrics. (**A**) Each dot represents the sensitivity of Arctic sea-ice loss in a particular model as a function of the increase in global mean incoming nonshortwave fluxes per CO_2 emission in the same model. The latter was obtained from a linear fit of incoming nonshortwave fluxes as a function of cumulative anthropogenic CO_2 emissions during the transition period of each individual model. (**B**) Same as (A), but fluxes only evaluated in the Arctic. (**C** and **D**) Same as (A) and (B), but neglecting sensible and latent heat fluxes. (**E**) Each dot represents the sensitivity of Arctic sea-ice loss in a particular model as a function of the transient climate response (*24*) in the same model. [See table S1 for actual values and supplementary text for more discussion on (E).] All correlations given in the figure are significant at the 1% level.

transition range to near ice-free conditions, the multimodel mean sensitivity is only 1.75 ± 0.67 m^2 loss of Arctic sea ice per metric ton of anthropogenic CO_2 emissions. Because of the linear response, a similar sensitivity is obtained for subperiods of the transition period that have the same length as our observational record, with overall maximum sensitivities over such 61-year-long time periods from individual simulations of 1.95 ± 0.70 m^2/ton. These estimates of the models' sensitivity might be biased somewhat high, as previous studies found that the aerosol forcing of CMIP5 simulations might have been too weak in recent decades (*19*, *20*). This would give rise to artificially amplified warming and thus amplified sea-ice loss in these simulations, rendering the true sensitivity of the models to be even lower than the values that we estimate here.

The low sensitivity of the modeled sea-ice response can be understood through a conceptual model that explains the linearity. To derive such a conceptual model, we consider the annual mean surface energy balance at the ice edge, which describes the fact that the net incoming shortwave radiation $(1-\alpha)F_{SW}$ and the incoming nonshortwave flux $F_{nonSW,in}$ are balanced by the outgoing nonshortwave flux and the conductive heat flux at the surface of the ice.

With increasing atmospheric CO_2 concentration, the incoming nonshortwave flux increases at the ice edge in response to the rising atmospheric emissivity and related atmospheric feedbacks. However, neither the outgoing nonshortwave flux nor the conductive heat flux in the ice will change much, as the surface properties of sea ice at the ice edge are largely independent of its location. We conjecture that this also holds for total albedo α, because a possible rise in cloudiness caused by sea-ice loss (*21*) will primarily occur over the open water south of the moving ice edge, rather than at the ice edge itself. In addition, the albedo of clouds is comparable to that of the ice at the ice edge. Hence, it seems plausible to assume that the surface energy balance at the ice edge is primarily kept closed by a decrease in the incoming shortwave flux that compensates for the increase in incoming nonshortwave flux. Such decrease of the incoming shortwave radiation is obtained by the northward movement of the ice edge to a region with less annual mean solar irradiance. Equilibrium is reestablished at the ice edge when

$$\Delta F_{SW}(1-\alpha) = -\Delta F_{nonSW,in} \quad (1)$$

If, for simplicity, we assume a circular shape of the sea-ice cover centered at the North Pole, the sea-ice area that is enclosed by any given latitude has nearly the same latitudinal dependence as the annual mean incoming shortwave radiation at the top of the atmosphere (Fig. 2A). Hence, the change in area enclosed by the ice edge ΔA_{seaice} should be roughly proportional to the change in incoming annual mean shortwave radiation at the ice edge (Fig. 2B)

$$\Delta A_{seaice} \propto \Delta F_{SW}(1-\alpha) \quad (2)$$

We additionally find empirically that the incoming nonshortwave flux is fairly linearly related to anthropogenic CO_2 emissions E_{CO_2} across CMIP5 model simulations both in the Arctic, where the loss of sea ice might amplify the change in radiative forcing, and globally, where such amplification is small (fig. S2). The linearity arises because more of each ton of emitted CO_2 remains in the atmosphere as oceanic CO_2 uptake decreases in the future. This then roughly compensates for the logarithmic rather than linear change of atmospheric longwave emission with changes in atmospheric CO_2 concentration (*22*). It is hence a plausible assumption that the linearity of incoming longwave radiation with rising CO_2 emissions also holds at the ice edge, which we can express as

$$\Delta F_{nonSW,in} = \frac{dF_{nonSW,in}}{dE_{CO_2}} \Delta E_{CO_2} \quad (3)$$

Inserting Eqs. 2 and 3 into Eq. 1 then finally gives

$$\Delta A_{seaice} = \frac{dF_{nonSW,in}}{dE_{CO_2}} \Delta E_{CO_2} \quad (4)$$

which for constant $dF_{nonSW,in}/dE_{CO_2}$ is a possible explanation for the observed linear relationship

between Arctic sea-ice area and cumulative CO_2 emission.

On the basis of this expression, we can infer that most climate models underestimate the loss of Arctic sea ice because they underestimate the increase of incoming nonshortwave flux for a given increase of anthropogenic CO_2 emissions. An analysis of the available fields of surface heat fluxes in the CMIP5 archive confirms this notion, with high correlation between modeled sea-ice sensitivity and modeled changes in either incoming total nonshortwave flux or incoming longwave radiation, as the latter dominates the change in the nonshortwave flux (Fig. 3, A to D). Unfortunately, observational uncertainty is currently too large to test our finding of a lower-than-expected increase in incoming longwave radiation against independent records (*23*).

On a more regional scale, our conceptual explanation allows us to ascribe a minor role for the overall evolution of sea ice to processes that are unrelated to the large-scale change in atmospheric forcing. This includes a minor role of oceanic heat transport on the time scales that we consider here, because we can derive a linear relationship without considering these transports. Although it might alternatively be possible that the oceanic heat transports have changed monotonously in recent decades, we have no indication that this is the case from either observations or model simulations. The current minor role of oceanic heat transports implies that on time scales of several centuries, the linearity will most likely no longer hold, because sensitivity will increase once changes in oceanic heat content start measurably affecting Arctic sea-ice coverage (*12*).

Our results also suggest that regional differences in atmospheric heat-flux convergence or wind forcing do not appreciably affect the Arctic-wide mean energy balance on the time scales that we consider here. Furthermore, this also explains why the linear relationship does not hold in the Antarctic, where dynamical forcing from wind and oceanic heat transport are key drivers of the large-scale sea-ice evolution.

The apparent minor role of oceanic heat transport, and the correlation between the change in global surface fluxes and Arctic sea-ice loss, suggest that we can use the observed evolution of Arctic sea ice as an emergent constraint on transient climate response (TCR). This is commonly defined as the global-mean warming at the time of doubled atmospheric CO_2 concentration after a 1% CO_2 increase per year (*24*). Indeed, we find good correlation between the modeled sea-ice sensitivity and TCR both in the full-forcing simulations (Fig. 3E) and in the simulations with rising CO_2 only (fig. S3B).

Unfortunately, though indicative of a TCR at the higher end of simulated values, the correlation does not allow for a direct estimate of TCR for two reasons: (i) The loss of Arctic sea ice is more directly driven by the regional temperature rise in the Arctic than by the global temperature rise that is expressed by the TCR. Any failure of the models to realistically simulate the ratio between global and Arctic temperature rise, usually referred to as Arctic amplification, could hence lead to an erroneous quantitative estimate of the TCR based on the correlation that we identify. (ii) TCR is estimated from simulations where all non-CO_2 forcings are kept constant, whereas the non-CO_2 forcings change in the historical and RCP8.5 simulations that we consider here. This affects, at least to some degree, the robustness of the correlation (see supplementary text for details).

Previous studies that estimated climate sensitivity from emergent constraints have usually focused on the equilibrium climate sensitivity (ECS), which describes the equilibrium global-mean warming for a sustained doubling of atmospheric CO_2 concentration. They also come to the conclusion that the real sensitivity of the Earth climate system is at the higher end of simulated values, from analyzing either atmospheric convective mixing (*25*) or mid-troposphere relative humidity (*26*). By contrast, studies analyzing the Earth's energy budget, particularly after considering the recent slowing in atmospheric warming, find that the TCR should be at the lower end of simulated values (*27*, *28*). This result, however, might be biased by the different data coverage in models and observations (*29*).

Regarding the future evolution of sea ice, our analysis suggests that there is little reason to believe that the observed sensitivity of Arctic sea-ice loss will change substantially in the forseeable future. Hence, we can directly estimate that the remainder of Arctic summer sea ice will be lost for roughly an additional 1000 Gt of CO_2 emissions on the basis of the observed sensitivity of 3.0 ± 0.3 m^2 September sea-ice loss per ton of anthropogenic CO_2 emissions. Because this amount is based on the 30-year running mean of monthly averages, it is a very conservative estimate of the cumulative emissions at which the annual minimum sea-ice area drops below 1 million km^2 for the first time. In addition, internal variability causes an uncertainty of around 20 years as to the first year of a near-complete loss of Arctic sea ice (*18*, *30*). For current emissions of 35 Gt CO_2 per year, the limit of 1000 Gt will be reached before mid-century. However, our results also imply that any measure taken to mitigate CO_2 emissions will directly slow the ongoing loss of Arctic summer sea ice. In particular, for cumulative future total emissions compatible with reaching a 1.5°C global warming target—i.e., for cumulative future emissions appreciably below 1000 Gt—Arctic summer sea ice has a chance of long-term survival, at least in some parts of the Arctic Ocean.

REFERENCES AND NOTES

1. F. Pithan, T. Mauritsen, *Nat. Geosci.* **7**, 181–184 (2014).
2. T. Vihma, *Surv. Geophys.* **35**, 1175–1214 (2014).
3. W. N. Meier *et al.*, *Rev. Geophys.* **52**, 185–217 (2014).
4. K. E. Taylor, R. J. Stouffer, G. A. Meehl, *Bull. Am. Meteorol. Soc.* **93**, 485–498 (2012).
5. J. Stroeve, D. Notz, *Global Planet. Change* **135**, 119–132 (2015).
6. K. Zickfeld, V. K. Arora, N. P. Gillett, *Geophys. Res. Lett.* **39**, L05703 (2012).
7. T. Herrington, K. Zickfeld, *Earth Syst. Dyn.* **5**, 409–422 (2014).
8. J. M. Gregory *et al.*, *Geophys. Res. Lett.* **29**, 28-1–28-4 (2002).
9. M. Winton, *J. Clim.* **24**, 3924–3934 (2011).
10. I. Mahlstein, R. Knutti, *J. Geophys. Res.* **117**, D06104 (2012).
11. J. K. Ridley, J. A. Lowe, H. T. Hewitt, *Cryosphere* **6**, 193–198 (2012).
12. C. Li, D. Notz, S. Tietsche, J. Marotzke, *J. Clim.* **26**, 5624–5636 (2013).
13. O. Johannessen, *Atmos. Ocean. Sci. Lett.* **1**, 51 (2008).
14. D. Notz, J. Marotzke, *Geophys. Res. Lett.* **39**, L051094 (2012).
15. F. Massonnet *et al.*, *Cryosphere* **6**, 1383–1394 (2012).
16. J. C. Stroeve *et al.*, *Geophys. Res. Lett.* **39**, L16502 (2012).
17. G. Flato *et al.*, in *Climate Change 2013: The Physical Science Basis. Contribution of Working Group I to the Fifth Assessment Report of the Intergovernmental Panel on Climate Change*, T. Stocker *et al.*, Eds. (Cambridge Univ. Press, 2013), chap. 9, pp. 741–866.
18. D. Notz, *Philos. Trans. R. Soc. A* **373**, 20140164 (2015).
19. B. D. Santer *et al.*, *Nat. Geosci.* **7**, 185–189 (2014).
20. G. A. Schmidt, D. T. Shindell, K. Tsigaridis, *Nat. Geosci.* **7**, 158–160 (2014).
21. I. V. Gorodetskaya, L.-B. Tremblay, B. Liepert, M. A. Cane, R. I. Cullather, *J. Clim.* **21**, 866–882 (2008).
22. H. D. Matthews, N. P. Gillett, P. A. Stott, K. Zickfeld, *Nature* **459**, 829–832 (2009).
23. G. L. Stephens *et al.*, *Nat. Geosci.* **5**, 691–696 (2012).
24. U. Cubasch *et al.*, in *Climate Change 2001: The Scientific Basis*, J. T. Houghton *et al.*, Eds. (Cambridge Univ. Press, 2001), chap. 9, pp. 525–582.
25. S. C. Sherwood, S. Bony, J.-L. Dufresne, *Nature* **505**, 37–42 (2014).
26. J. T. Fasullo, K. E. Trenberth, *Science* **338**, 792–794 (2012).
27. A. Otto *et al.*, *Nat. Geosci.* **6**, 415–416 (2013).
28. N. P. Gillett, V. K. Arora, D. Matthews, M. R. Allen, *J. Clim.* **26**, 6844–6858 (2013).
29. M. Richardson, K. Cowtan, E. Hawkins, M. B. Stolpe, *Nat. Clim. Chang.* **6**, 931–935 (2016).
30. A. Jahn, J. E. Kay, M. M. Holland, D. M. Hall, *Geophys. Res. Lett.* **43**, 9113–9120 (2016).
31. Hadley Center for Climate Prediction and Research, Met Office, HadISST 1.1 - global sea-ice coverage and sea surface temperature (1870-2015); NCAS British Atmospheric Data Centre (2006); http://badc.nerc.ac.uk/data/hadisst/.
32. F. Fetterer, K. Knowles, W. Meier, M. Savoie, Sea ice index, Digital media, National Snow and Ice Data Center, Boulder, CO (2002, updated 2014).
33. M. Meinshausen *et al.*, *Clim. Change* **109**, 213–241 (2011).
34. G. R. North, *J. Atmos. Sci.* **32**, 2033–2043 (1975).

ACKNOWLEDGMENTS

We are grateful to J. Marotzke for the suggestion to analyze the TCR and for helpful comments on the manuscript. We are also grateful to two anonymous reviewers, whose insightful comments were essential for framing the final version of our study. We further thank B. Soden, D. Olonscheck, and C. Li for helpful feedback. D.N. acknowledges funding through a Max Planck Research Fellowship. J.S. acknowledges funding from NASA grant NNX12AB75G and NSF grant PLR 1304246. All primary data used for this study are based on publicly available output from CMIP5 models and are also available upon request from publications@mpimet.mpg.de.

SUPPLEMENTARY MATERIALS

www.sciencemag.org/content/354/6313/747/suppl/DC1
Materials and Methods
Supplementary Text
Figs. S1 to S3
Table S1
References (*35*–*37*)

27 May 2016; accepted 12 October 2016
Published online 3 November 2016
10.1126/science.aag2345

EMERGING INFECTIONS

Emergence and spread of a human-transmissible multidrug-resistant nontuberculous mycobacterium

Josephine M. Bryant,[1,2]* Dorothy M. Grogono,[2,3]* Daniela Rodriguez-Rincon,[2] Isobel Everall,[1] Karen P. Brown,[2,3] Pablo Moreno,[4] Deepshikha Verma,[5] Emily Hill,[5] Judith Drijkoningen,[2] Peter Gilligan,[6] Charles R. Esther,[6] Peadar G. Noone,[6] Olivia Giddings,[6] Scott C. Bell,[7,8,9] Rachel Thomson,[10] Claire E. Wainwright,[8,11] Chris Coulter,[12] Sushil Pandey,[12] Michelle E. Wood,[7,8,9] Rebecca E. Stockwell,[7,8] Kay A. Ramsay,[7,8] Laura J. Sherrard,[7] Timothy J. Kidd,[13,14] Nassib Jabbour,[15,16] Graham R. Johnson,[16] Luke D. Knibbs,[17] Lidia Morawska,[16] Peter D. Sly,[18] Andrew Jones,[19] Diana Bilton,[19] Ian Laurenson,[20] Michael Ruddy,[21] Stephen Bourke,[22] Ian C. J. W. Bowler,[23] Stephen J. Chapman,[23] Andrew Clayton,[24] Mairi Cullen,[25] Owen Dempsey,[26] Miles Denton,[27] Maya Desai,[28] Richard J. Drew,[29] Frank Edenborough,[30] Jason Evans,[21] Jonathan Folb,[31] Thomas Daniels,[32] Helen Humphrey,[32] Barbara Isalska,[25] Søren Jensen-Fangel,[33] Bodil Jönsson,[34] Andrew M. Jones,[25] Terese L. Katzenstein,[35] Troels Lillebaek,[36] Gordon MacGregor,[37] Sarah Mayell,[29] Michael Millar,[38] Deborah Modha,[39] Edward F. Nash,[40] Christopher O'Brien,[22] Deirdre O'Brien,[41] Chandra Ohri,[39] Caroline S. Pao,[38] Daniel Peckham,[27] Felicity Perrin,[42] Audrey Perry,[22] Tania Pressler,[35] Laura Prtak,[30] Tavs Qvist,[35] Ali Robb,[22] Helen Rodgers,[43] Kirsten Schaffer,[41] Nadia Shafi,[3] Jakko van Ingen,[44] Martin Walshaw,[45] Danie Watson,[38] Noreen West,[46] Joanna Whitehouse,[40] Charles S. Haworth,[3] Simon R. Harris,[1] Diane Ordway,[5] Julian Parkhill,[1]† R. Andres Floto[2,3]†

Lung infections with *Mycobacterium abscessus*, a species of multidrug-resistant nontuberculous mycobacteria, are emerging as an important global threat to individuals with cystic fibrosis (CF), in whom *M. abscessus* accelerates inflammatory lung damage, leading to increased morbidity and mortality. Previously, *M. abscessus* was thought to be independently acquired by susceptible individuals from the environment. However, using whole-genome analysis of a global collection of clinical isolates, we show that the majority of *M. abscessus* infections are acquired through transmission, potentially via fomites and aerosols, of recently emerged dominant circulating clones that have spread globally. We demonstrate that these clones are associated with worse clinical outcomes, show increased virulence in cell-based and mouse infection models, and thus represent an urgent international infection challenge.

Nontuberculous mycobacteria (NTM; referring to mycobacterial species other than *Mycobacterium tuberculosis* complex and *Mycobacterium leprae*) are ubiquitous environmental organisms that can cause chronic pulmonary infections in susceptible individuals (*1*, *2*), particularly those with preexisting inflammatory lung diseases such as cystic fibrosis (CF) (*3*). The major NTM infecting CF individuals around the world is *Mycobacterium abscessus*; this rapidly growing, intrinsically multidrug-resistant species, which can be impossible to treat despite prolonged combination antibiotic therapy (*1*, *3*–*5*), leads to accelerated decline in lung function (*6*, *7*) and remains a contraindication to lung transplantation in many centers (*3*, *8*, *9*).

Until recently, NTM infections were thought to be independently acquired by individuals through exposure to soil or water (*10*–*12*). As expected, previous analyses from the 1990s and 2000s (*13*–*16*) showed that CF patients were infected with genetically diverse strains of *M. abscessus*, presumably from environmental sources. We used whole-genome sequencing at a single UK CF center and identified two clusters of patients (11 individuals in total) infected with identical or near-identical *M. abscessus* isolates, which social network analysis suggested were acquired within the hospital via indirect transmission between patients (*17*)—a possibility further supported through the genomic sequencing (*18*) of a separate *M. abscessus* outbreak in a Seattle, Washington, CF center (*19*).

Given the increasing incidence of *M. abscessus* infections in CF and non-CF populations reported globally (*3*, *20*, *21*), we investigated whether cross-infection, rather than independent environmental acquisition, might be the major source of infection for this organism; we therefore undertook population-level, multinational, whole-genome sequencing of *M. abscessus* isolates from infected CF patients, correlating results with clinical metadata and phenotypic functional analysis of isolates.

We generated whole-genome sequences for 1080 clinical isolates of *M. abscessus* from 517 patients, obtained from UK CF clinics and their associated regional reference laboratories, as well as CF centers in the United States [University of North Carolina (UNC), Chapel Hill], the Republic of Ireland (Dublin), mainland Europe (Denmark, Sweden, and Netherlands), and Australia (Queensland). We identified 730 isolates as *M. a. abscessus*, 256 isolates as *M. a. massiliense*, and 91 isolates as *M. a. bolletii*, with three isolates (from three different patients) containing more than one subspecies.

Phylogenetic analysis of these sequences (using one isolate per patient)—supplemented by published genomes from the United States, France, Brazil, Malaysia, China, and South Korea (table S1)—was performed and analyzed in the context of the geographical provenance of isolates (Fig. 1 and fig. S1). As done previously (*17*), we obtained maximum-likelihood phylogenetic trees demonstrating separation of *M. abscessus* into three clearly divergent subspecies (*M. a. abscessus*, *M. a. bolletii*, and *M. a. massiliense*), challenging recent reclassifications of *M. abscessus* into only two subspecies (*22*).

[1]Wellcome Trust Sanger Institute, Hinxton, UK. [2]Molecular Immunity Unit, Department of Medicine, University of Cambridge, Medical Research Council (MRC)–Laboratory of Molecular Biology, Cambridge, UK. [3]Cambridge Centre for Lung Infection, Papworth Hospital, Cambridge, UK. [4]European Molecular Biology Laboratory (EMBL) European Bioinformatics Institute, Hinxton, UK. [5]Mycobacteria Research Laboratory, Department of Microbiology, Immunology, and Pathology, Colorado State University, Fort Collins CO, USA. [6]University of North Carolina School of Medicine, NC, USA. [7]Queensland Institute of Medical Research (QIMR) Berghofer Medical Research Institute, Brisbane, Australia. [8]School of Medicine, The University of Queensland, Australia. [9]The Prince Charles Hospital (TPCH), Brisbane, Australia. [10]Gallipoli Medical Research Centre, University of Queensland, Brisbane, Australia. [11]Lady Cilento Children's Hospital, Brisbane, Australia. [12]Queensland Mycobacterial Reference Laboratory, Brisbane, Australia. [13]Centre for Experimental Medicine, Queen's University Belfast, Belfast, UK. [14]School of Chemistry and Biomolecular Sciences, University of Queensland, Brisbane, Australia. [15]Queensland University of Technology, Brisbane, Australia. [16]International Laboratory for Air Quality and Health, Queensland University of Technology, Brisbane, Australia. [17]School of Public Health, University of Queensland, Brisbane, Australia. [18]Child Health Research Centre, University of Queensland, Brisbane, Australia. [19]Royal Brompton and Harefield National Health Service (NHS) Foundation Trust, London, UK. [20]Scottish Mycobacteria Reference Laboratory, Edinburgh, UK. [21]Wales Centre for Mycobacteria, Cardiff, UK. [22]The Newcastle upon Tyne Hospitals NHS Foundation Trust, Newcastle, UK. [23]Oxford University Hospitals NHS Foundation Trust, Oxford, UK. [24]Nottingham University Hospitals NHS Trust, Nottingham, UK. [25]University Hospital of South Manchester NHS Foundation Trust, Manchester, UK. [26]Aberdeen Royal Infirmary, NHS Grampian, Scotland, UK. [27]The Leeds Teaching Hospitals NHS Trust, Leeds, UK. [28]Birmingham Children's Hospital NHS Foundation Trust, Birmingham, UK. [29]Alder Hey Children's NHS Foundation Trust, Liverpool, UK. [30]Sheffield Teaching Hospitals NHS Foundation Trust, Sheffield, UK. [31]The Royal Liverpool and Broadgreen University Hospitals NHS Trust, Liverpool, UK. [32]University Hospital Southampton NHS Foundation Trust, Southampton, UK. [33]Department of Infectious Diseases, Aarhus University Hospital, Aarhus, Denmark. [34]Department of Infectious Medicine, Institute of Biomedicine, University of Gothenburg, Gothenburg, Sweden. [35]Copenhagen Cystic Fibrosis Center, Department of Infectious Diseases, Rigshospitalet, Copenhagen, Denmark. [36]International reference Laboratory of Mycobacteriology, Statens Serum Institut, Copenhagen, Denmark. [37]Gartnavel Hospital, Glasgow, NHS Greater Glasgow and Clyde, Scotland, UK. [38]Barts Health NHS Trust, London, UK. [39]University Hospitals of Leicester NHS Trust, Leicester, UK. [40]Heart of England NHS Foundation Trust, Birmingham, UK. [41]St Vincent's University Hospital, Dublin, Ireland. [42]King's College Hospital NHS Foundation Trust, London, UK. [43]Western General Hospital, NHS Lothian, Scotland, UK. [44]Department of Medical Microbiology, Radboud University Medical Centre, Nijmegen, Netherlands. [45]Liverpool Heart and Chest Hospital NHS Foundation Trust, Liverpool, UK. [46]Sheffield Children's NHS Foundation Trust, Sheffield, UK.
*These authors contributed equally to this work. †Corresponding author. Email: arf27@cam.ac.uk (R.A.F.); parkhill@sanger.ac.uk (J.P.)

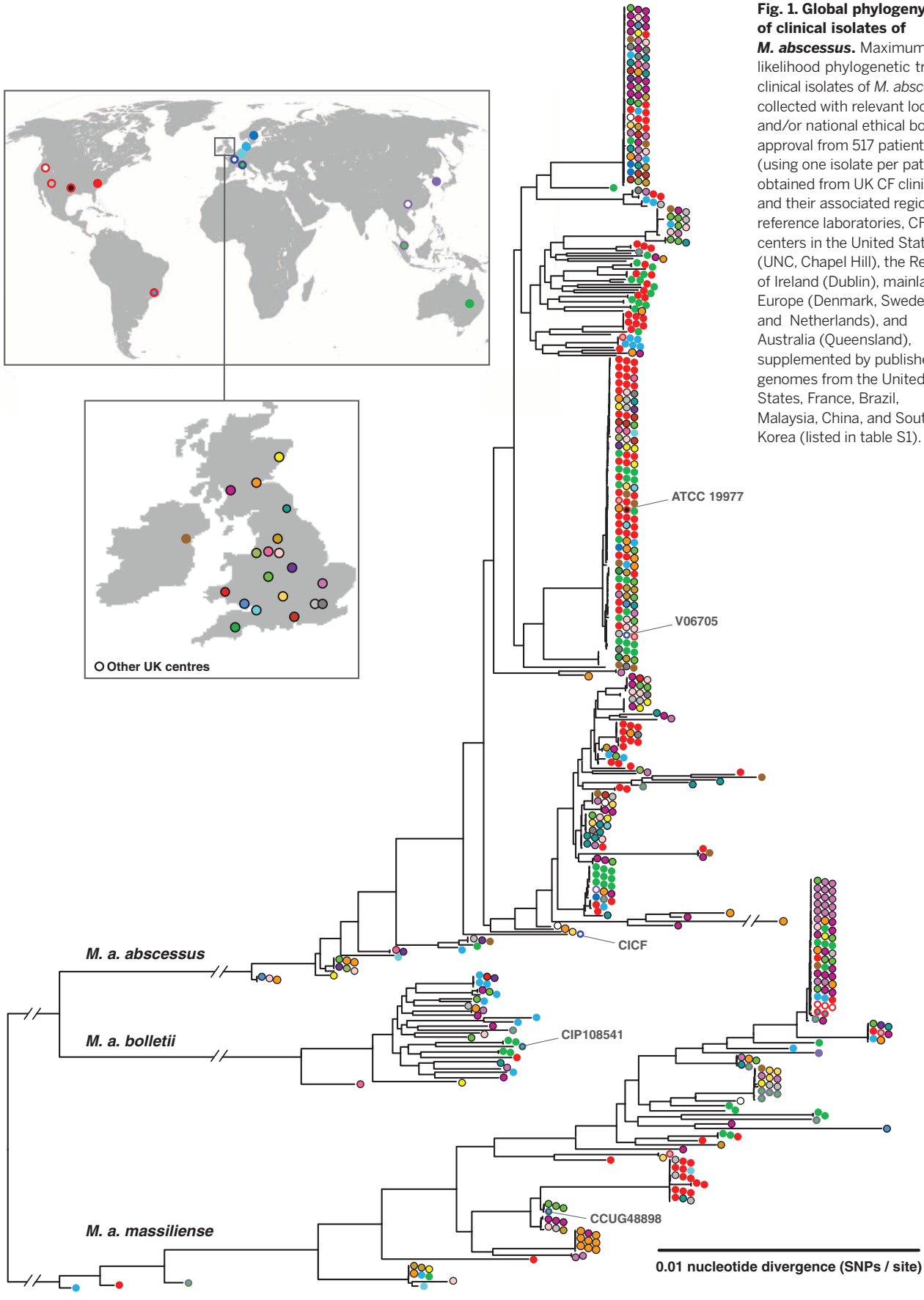

Fig. 1. Global phylogeny of clinical isolates of *M. abscessus*. Maximum likelihood phylogenetic tree of clinical isolates of *M. abscessus* collected with relevant local and/or national ethical board approval from 517 patients (using one isolate per patient), obtained from UK CF clinics and their associated regional reference laboratories, CF centers in the United States (UNC, Chapel Hill), the Republic of Ireland (Dublin), mainland Europe (Denmark, Sweden, and Netherlands), and Australia (Queensland), supplemented by published genomes from the United States, France, Brazil, Malaysia, China, and South Korea (listed in table S1).

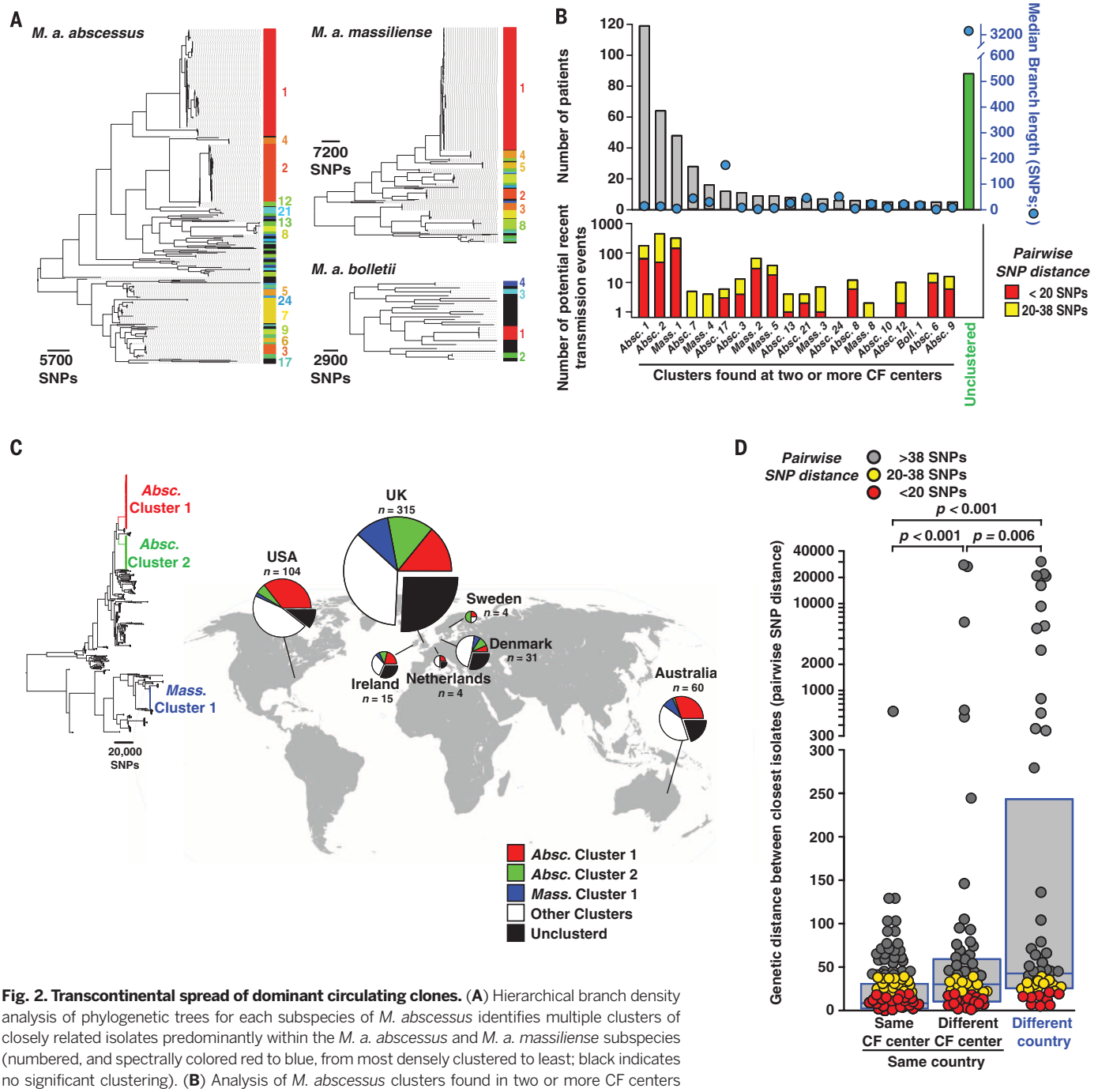

Fig. 2. Transcontinental spread of dominant circulating clones. (**A**) Hierarchical branch density analysis of phylogenetic trees for each subspecies of *M. abscessus* identifies multiple clusters of closely related isolates predominantly within the *M. a. abscessus* and *M. a. massiliense* subspecies (numbered, and spectrally colored red to blue, from most densely clustered to least; black indicates no significant clustering). (**B**) Analysis of *M. abscessus* clusters found in two or more CF centers showing (top) numbers of patients infected with each cluster (gray bars) or unclustered isolates (green) and median branch length (SNPs) of different patients' isolates within each cluster (blue circles). (Bottom) Numbers of potential recent transmission events with <20 SNPs (red) or 20 to 38 SNPs (yellow) difference between isolates from different patients. (**C**) Global distribution of clustered *M. abscessus* isolates showing *M. a. abscessus* cluster 1 (red) and cluster 2 (green), *M. a. massiliense* cluster 1 (blue), other clustered isolates (grouped together for clarity; white) and unclustered isolates (black) with numbers of patients (*n*) sampled per location. (**D**) Genetic differences between isolates (measured by pairwise SNP distance) from different patients attending the same CF center, different CF centers within the same country, or CF centers in different countries (boxes indicate median and interquartile range; *P* values were obtained from Mann Whitney Rank Sum tests). To exclude multiple highly distant comparisons, for each isolate only the smallest pairwise distance with an isolate from another patient is included. Color coding indicates whether there were <20 SNPs difference (red), 20 to 38 SNPs difference (yellow), or >38 SNPs difference (gray) between isolates from different patients.

Within each subspecies, we found multiple examples of deep branches (indicating large genetic differences) between isolates from different individuals, which is consistent with independent acquisition of unrelated environmental bacteria. However, we also identified multiple clades of near-identical isolates from geographically diverse locations (Fig. 1), suggesting widespread transmission of circulating clones within the global CF patient community.

To investigate further the relatedness of isolates from different individuals, we analyzed each subspecies phylogeny for the presence of high-density phylogenetic clusters (*23*). We identified multiple dense clusters of isolates, predominantly

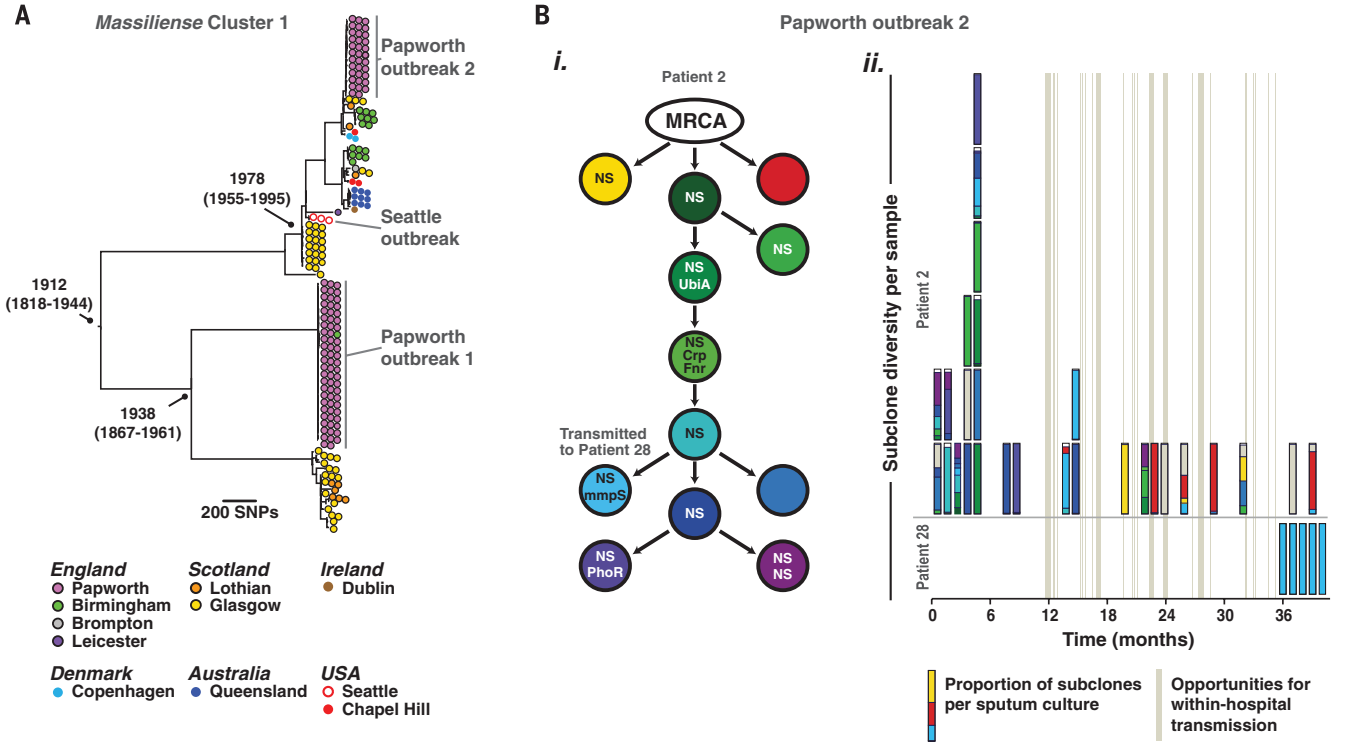

Fig. 3. Dating the emergence of dominant circulating clones. (**A**) Dating the emergence of the *M. a. massiliense* cluster 1 (responsible for the Papworth and Seattle CF center outbreaks), by using Bayesian analysis, with geographical annotation of isolates within the cluster. (**B**) Predicted evolution of subclones (identified through minority variant linkage) (*23*) within a single patient with CF [patient 2 from (*19*)] chronically infected with the dominant circulating clone *Massiliense* cluster 1 (representative of a total of 11 patients studied). (i) Analysis revealed successive acquisition of nonsynonymous polymorphisms (NS) by the most common recent ancestral clone (MRCA; white) in potential virulence genes (UBiA, MAB_0173; Crp/Fnr, MAB_0416c; mmpS, MAB_0477; and PhoR, MAB_0674) and then transmission of a single subclone to another patient from the same CF center [patient 28 from (*19*)]. (ii) Frequency of each subclone within longitudinal sputum isolates analyzed during the course of patient 2's infection and the subsequent transmission of a subclone to patient 28. We observed considerable heterogeneity in the detected repertoire of subclones within each sputum sample [vertical rectangles colored to illustrate the proportion of detected subclones coded as for (i) in each sputum sample], reflecting either temporal fluctuations in dominant sublineages or variable sampling of geographical diversity of subclones within the lung [as previously described for *P. aeruginosa* (*37*)]. Previously determined opportunities for hospital-based cross-infection between the two patients [using social network and epidemiologic analysis (*17*)] are shown in gray vertical bars.

within the *M. a. abscessus* and *M. a. massiliense* subspecies (Fig. 2A), indicating the presence of dominant circulating clones. We next excluded clusters found in only one CF center from further analysis so as to remove related isolates that might have been acquired from a local environmental point source. We found that most patients (74%) were infected with clustered, rather than unclustered, isolates, principally from *M. a. abscessus* cluster 1 and 2 and *M. a. massiliense* cluster 1 (Fig. 2B). The median branch lengths of almost all clusters found in two or more CF centers was less than 20 single-nucleotide polymorphisms (SNPs) (range of 1 to 175 SNPs), indicating a high frequency of identical or near identical isolates infecting geographically separate individuals.

To determine how much of the genetic relatedness found within clusters was attributable to recent transmission, we first examined the within-patient genetic diversity of *M. abscessus* isolates from single individuals. In keeping with our previously published results (*17*), we found that 90% of same-patient isolates differed by less than 20 SNPs, whereas 99% of same-patient isolates differed by less than 38 SNPs (fig. S2). We therefore classified isolates from different individuals varying by less than 20 SNPs as indicating "probable," and those varying by 20 to 38 SNPs as indicating "possible," recent transmission (whether direct or indirect). We thereby identified multiple likely recent transmission chains in virtually all multisite clusters of *M. abscessus* (Fig. 2B) and across the majority of CF centers (fig. S3).

We next examined the global distribution of clustered isolates and found that in all countries, the majority of patients were infected with clustered rather than unclustered isolates (Fig. 2C and table S2), suggesting frequent and widespread infection of patients with closely related isolates. Moreover, the three dominant circulating clones, *M. a. abscessus* clusters 1 and 2 and *M. a. massiliense* cluster 1, were all represented in the U.S., European, and Australian collections of clinical isolates, indicating transcontinental dissemination of these clades.

We then compared the genetic differences between isolates (measured by pairwise SNP distance) as a function of geography. As expected from our previous detection of hospital-based transmission of *M. abscessus* (*17*), average genetic distances were significantly shorter for *M. abscessus* isolates from the same CF center than those from different CF centers within the same country or from different countries (Fig. 2D). However, we also detected numerous examples of identical or near-identical isolates infecting groups of patients in different CF centers and, indeed, across different countries (Fig. 2D), indicating the recent global spread of *M. abscessus* clones throughout the international CF patient community.

We applied Bayesian analysis (*24*) to date the establishment and spread of dominant circulating clones (figs. S4 and S5), focusing on *M. a. massiliense* cluster 1, which includes isolates from both the Seattle (*19*) and Papworth (*17*) CF center outbreaks, as well as isolates from CF centers across England (Birmingham, London, and Leicester), Scotland (Lothian and Glasgow), Ireland (Dublin), Denmark (Copenhagen), Australia (Queensland), and the United States (Chapel Hill, North Carolina) (Fig. 3A). We estimate that the most recent common ancestor of isolates infecting patients from all these locations emerged around 1978

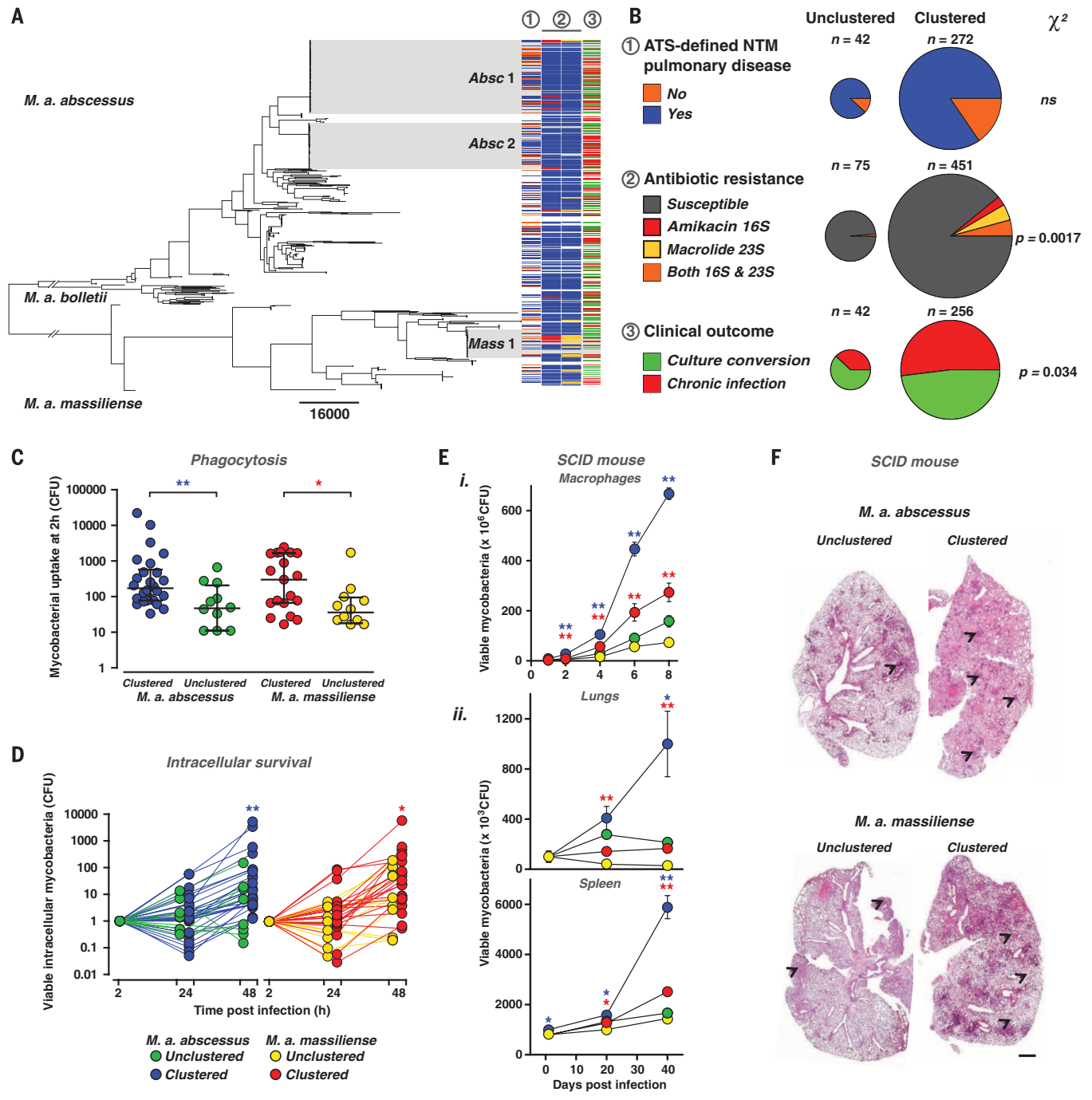

Fig. 4. Comparison of clinical outcomes and functional phenotyping of clustered and unclustered *M. abscessus* isolates. (**A** and **B**) Relationship of phylogeny with clinical metadata. (A) Phylogenetic tree of *M. abscessus* isolates (one isolate per patient) with dominant circulating clones *M. a. abscessus* 1 (Absc 1), *abscessus* 2 (Absc 2), and *M. a. massiliense* (Mass 1) highlighted (gray). (B) For each isolate, clinical data (where available) was used to determine whether (column 1) the infected patient fulfilled the ATS/Infectious Diseases Society of America (IDSA) criteria for NTM pulmonary disease, namely the presence of two or more culture-positive sputum samples with NTM-associated symptoms and radiological changes (*1*) (yes, blue; no, orange); whether (column 2) isolates have acquired amikacin resistance [through 16*S* ribosomal RNA (rRNA) mutations; red], macrolide resistance (through 23S rRNA mutations; yellow), or both [orange, (B) only]; and whether (column 3) patients culture converted (green) or remained chronically infected (red) with *M. abscessus*. (**C** and **D**). In vitro phenotyping of representative isolates of clustered (blue) and unclustered (green) *M. a. abscessus* and clustered (red) and unclustered (yellow) *M. a. massiliense*, comparing phagocytosis as shown in (C) and intracellular survival (normalized for uptake), as shown in (D), within differentiated THP1 cells. Data points represent averages of at least three independent replicates. (**E** and **F**) Using SCID mice, infection with clustered *M. a. abscessus* (blue) and *M. a. massiliense* (red) led to (E) greater intracellular survival within (i) bone marrow–derived macrophages in vitro and (ii) higher bacterial burdens in lung and spleen after in vivo inoculation with 1×10^7 bacilli per animal, with (F) worse granulomatous lung inflammation (arrowheads) than that of unclustered controls (*M. a. abscessus*, green; *M. a. massiliense*, yellow). Scale bar, 2 mm. Colony-forming unit (CFU) data are shown as mean ± SEM; $^*P < 0.05$; $^{**}P < 0.005$ (two-tailed unpaired Student's *t* test).

(95% confidence interval, 1955–1995), clearly indicating recent global dissemination of this dominant circulating clone among individuals with CF (Fig. 3A).

Furthermore, we were able to resolve individual transmission events between patients infected with dominant circulating clones through two orthogonal approaches. First, using high-depth genomic sequencing of colony sweeps, we were able to track changes in within-patient bacterial diversity in sputum cultures of a single individual over time. By linking the frequency of occurrence of minority variants in longitudinal samples, we were able to define the presence of particular subclones within infected individuals, assign their likely evolutionary development (involving the successive acquisition of nonsynonymous mutations in likely virulence genes) (Fig. 3B), monitor their relative frequencies over time, and demonstrate their transmission between patients (Fig. 3B). Second, through longitudinal whole-genome sequencing of isolates collected over time from individuals, we were able to find multiple examples of the complete nesting of one patient's sampled diversity within another's (fig. S6). Such paraphyletic relationships are strongly indicative of recent person-to-person transmission (*25*).

We next examined potential mechanisms of transmission of *M. abscessus* between individuals [which our previous epidemiological analysis had suggested was indirect rather than via direct contact between patients (*17*)]. We provide proof of concept for fomite spread of *M. abscessus* (detecting three separate transmission events associated with surface contamination of an inpatient room by an individual infected with a dominant circulating clone) (fig. S7) and also for potential airborne transmission (by experimentally demonstrating the generation of long-lived, potentially infectious cough aerosols by an infected CF patient) (fig. S8).

A potential explanation for the emergence of dominant clones of *M. abscessus* is that they are more efficient at infection and/or transmission. We therefore analyzed clinical metadata to establish whether outcomes were different for patients infected with clustered rather than unclustered isolates. We correlated clinical outcomes with bacterial phylogeny and the presence of constitutive resistance to two key NTM antibiotics, amikacin and macrolides (*26*, *27*), acquired through point mutations in the 16*S* and 23*S* ribosomal RNA, respectively (Fig. 4A). We found no differences in the proportions of *M. abscessus*–positive individuals diagnosed with American Thoracic Society (ATS)–defined NTM pulmonary disease (namely, the presence of two or more culture-positive sputum samples with NTM-associated symptoms and radiological changes) (*1*), but we did observe increased rates of chronic infection in individuals infected with clustered rather than unclustered isolates (Fig. 4B). As anticipated for transmissible clones exposed to multiple rounds of antibiotic therapy, we also found high rates of constitutive amikacin and/or macrolide resistance in clustered isolates (Fig. 4B). Resistance to these two antibiotics did not necessarily result in poor clinical outcomes (fig. S9), suggesting that additional bacterial factors might contribute to worse responses in patients infected with clustered isolates.

To explore differences in intrinsic virulence between clustered and unclustered *M. abscessus*, we subjected a panel of representative isolates (27 clustered and 17 unclustered *M. a. abscessus*; 25 clustered and 13 unclustered *M. a. massiliense*) to a series of in vitro phenotypic assays. Although we found no or only minor differences between groups in their colony morphotype, biofilm formation, ability to trigger cytokine release from macrophages (fig. S10), and their overall phenotypic profile (determined with multifactorial analysis) (fig. S11), we detected significantly increased phagocytic uptake (Fig. 4C) and intracellular survival in macrophages (Fig. 4D) of clustered isolates of both *M. a. abscessus* and *M. a. massiliense* as compared with unclustered controls, indicating clear differences in pathogenic potential. Moreover, infection of severe combined immunodeficient (SCID) mice revealed significantly greater bacterial burden (Fig. 4E) and granulomatous inflammation (Fig. 4F) after inoculation with clustered rather than unclustered isolates of *M. a. abscessus* and *M. a. massiliense*, confirming differences in virulence between these groups.

Our results reveal that the majority of *M. abscessus* infections of individuals with CF worldwide are caused by genetically clustered isolates, suggesting recent transmission rather than independent acquisition of genetically unrelated environmental organisms. Given the widespread implementation of individual and cohort segregation of patients in CF centers in Europe (*28*), the United States (*29*), and Australia (*30*) [which have led to falling levels of methicillin-resistant *Staphylococcus aureus* (MRSA), *Burkholderia*, and transmissible *Pseudomonas* infections (*31*–*33*)], we believe that the likely mechanism of local spread of *M. abscessus* is via fomite spread or potentially through the generation of long-lived infectious aerosols [as identified for other CF pathogens (*34*–*36*)]. Although further research is needed, both transmission routes are plausible given our findings (figs. S7 and S8) and would be potentially enhanced by the intrinsic desiccation resistance of *M. abscessus*. Such indirect transmission, involving environmental contamination by patients, is supported by our previous social network analysis of a UK outbreak of *M. abscessus* (*17*) in CF patients, which revealed hospital-based cross-infection without direct person-to-person contact, and by the termination of a Seattle *M. abscessus* outbreak associated with the introduction of clinic room negative pressure ventilation and double room cleaning (*19*). The long-distance spread of circulating clones is more difficult to explain. We found no evidence of CF patients or of equipment moving between CF centers in different countries, indicating that the global spread of *M. abscessus* may be driven by alternative human, zoonotic, or environmental vectors of transmission.

Our study illustrates the power of population-level genomics to uncover modes of transmission of emerging pathogens and has revealed the recent emergence of global dominant circulating clones of *M. abscessus* that have spread between continents. These clones are better able to survive within macrophages, cause more virulent infection in mice, and are associated with worse clinical outcomes, suggesting that the establishment of transmission chains may have permitted multiple rounds of within-host genetic adaptation to allow *M. abscessus* to evolve from an environmental organism to a true lung pathogen.

REFERENCES AND NOTES

1. D. E. Griffith *et al.*, *Am. J. Respir. Crit. Care Med.* **175**, 367–416 (2007).
2. K. L. Winthrop *et al.*, *Am. J. Respir. Crit. Care Med.* **182**, 977–982 (2010).
3. R. A. Floto *et al.*, *Thorax* **71** (suppl. 1), i1–i22 (2016).
4. K. Jeon *et al.*, *Am. J. Respir. Crit. Care Med.* **180**, 896–902 (2009).
5. J. Jarand *et al.*, *Clin. Infect. Dis.* **52**, 565–571 (2011).
6. C. R. Esther Jr., D. A. Esserman, P. Gilligan, A. Kerr, P. G. Noone, *J. Cyst. Fibros.* **9**, 117–123 (2010).
7. C. R. Esther Jr., M. M. Henry, P. L. Molina, M. W. Leigh, *Pediatr. Pulmonol.* **40**, 39–44 (2005).
8. M. Sanguinetti *et al.*, *J. Clin. Microbiol.* **39**, 816–819 (2001).
9. J. L. Taylor, S. M. Palmer, *J. Heart Lung Transplant.* **25**, 985–988 (2006).
10. J. O. Falkinham 3rd, *Clin. Chest Med.* **36**, 35–41 (2015).
11. J. van Ingen, M. J. Boeree, P. N. Dekhuijzen, D. van Soolingen, *Clin. Microbiol. Infect.* **15**, 888–893 (2009).
12. R. Thomson *et al.*, *J. Clin. Microbiol.* **51**, 3006–3011 (2013).
13. K. N. Olivier *et al.*, *Am. J. Respir. Crit. Care Med.* **167**, 828–834 (2003).
14. I. Sermet-Gaudelus *et al.*, *Emerg. Infect. Dis.* **9**, 1587–1591 (2003).
15. F. C. Bange, B. A. Brown, C. Smaczny, R. J. Wallace Jr., E. C. Böttger, *Clin. Infect. Dis.* **32**, 1648–1650 (2001).
16. B. E. Jönsson *et al.*, *J. Clin. Microbiol.* **45**, 1497–1504 (2007).
17. J. M. Bryant *et al.*, *Lancet* **381**, 1551–1560 (2013).
18. H. Tettelin *et al.*, *Emerg. Infect. Dis.* **20**, 364–371 (2014).
19. M. L. Aitken *et al.*, *Am. J. Respir. Crit. Care Med.* **185**, 231–232 (2012).
20. D. R. Prevots *et al.*, *Am. J. Respir. Crit. Care Med.* **182**, 970–976 (2010).
21. C. Pierre-Audigier *et al.*, *J. Clin. Microbiol.* **43**, 3467–3470 (2005).
22. S. C. Leao, E. Tortoli, J. P. Euzéby, M. J. Garcia, *Int. J. Syst. Evol. Microbiol.* **61**, 2311–2313 (2011).
23. Materials and methods are available as supplementary materials on *Science* Online.
24. A. J. Drummond, A. Rambaut, *BMC Evol. Biol.* **7**, 214 (2007).
25. E. O. Romero-Severson, I. Bulla, T. Leitner, *Proc. Natl. Acad. Sci. U.S.A.* **113**, 2690–2695 (2016).
26. T. Prammananan *et al.*, *J. Infect. Dis.* **177**, 1573–1581 (1998).
27. R. J. Wallace Jr. *et al.*, *Antimicrob. Agents Chemother.* **40**, 1676–1681 (1996).
28. S. Conway *et al.*, *J. Cyst. Fibros.* **13** (suppl. 1), S3–S22 (2014).
29. L. Saiman *et al.*, *Infect. Control Hosp. Epidemiol.* **35** (suppl. 1), S1–S67 (2014).
30. S. C. Bell, P. J. Robinson, Cystic Fibosis Standards of Care, Australia; www.rah.sa.gov.au/thoracic/whats_new/documents/CFA_Standards_of_Care_journal_31_Mar_08.pdf (2008).
31. S. J. Doe *et al.*, *J. Cyst. Fibros.* **9**, 104–109 (2010).
32. M. W. France *et al.*, *J. Cyst. Fibros.* **7**, 368–372 (2008).
33. A. M. Jones *et al.*, *Am. J. Respir. Crit. Care Med.* **171**, 257–260 (2005).
34. C. E. Wainwright *et al.*, *Thorax* **64**, 926–931 (2009).
35. L. D. Knibbs *et al.*, *Thorax* **69**, 740–745 (2014).
36. S. Panagea, C. Winstanley, M. J. Walshaw, M. J. Ledson, C. A. Hart, *J. Hosp. Infect.* **59**, 102–107 (2005).
37. P. Jorth *et al.*, *Cell Host Microbe* **18**, 307–319 (2015).

ACKNOWLEDGMENTS

This work was supported by The Wellcome Trust grants 098051 (J.M.B., S.H., and J.P.) and 107032AIA (R.A.F. and D.M.G.), The Medical Research Council (J.M.B.), The UK Cystic Fibrosis Trust (D.M.G., D.R.-R., I.E., J.P., and R.A.F.), Papworth Hospital (D.M.G., K.P.B., C.S.H., and R.A.F.), National Institute for Health Research (NIHR) Cambridge Biomedical Research Centre (R.A.F.), NIHR Specialist Respiratory Biomedical Research Unit, Imperial College London (D.B.), The UK Clinical Research Collaboration Translational Infection Research Initiative (J.P.), CF Foundation Therapeutics grant (S.B., T.K., C.W., L.M., and P.S.), the Australian National Health and Medical Research Council (L.K.) and The Prince Charles Hospital Foundation (S.B., T.K., C.C., R.T., L.K., L.M., and G.J.), and National Services Division, NHS Scotland (I.L.). We are grateful to the following for their assistance with microbiological culture, environmental sampling, and isolate retrieval: K. Ball (Aintree University Hospitals NHS Foundation Trust); M. Brodlie and M. Thomas (Newcastle upon Tyne Hospitals NHS Foundation Trust, UK); G. Smith (Regional Mycobacterial Reference Laboratory, Birmingham, UK); P. Fenton and K. Thickett (Sheffield Teaching Hospitals NHS Foundation Trust, UK); R. Williams (Wales Centre for Mycobacteria, UK); and V. Athithan and M. Gillham (Papworth Hospital NHS Foundation Trust). J. Corander (University of Oslo) assisted with BAPS clustering analysis. All sequence data associated with this study is deposited in the European Nucleotide Archive under project accession ERP001039. Ethical approval for the study was obtained nationally for centers in England and Wales from the National Research Ethics Service (NRES; REC reference: 12/EE/0158) and the National Information Governance Board (NIGB; ECC 3-03 (f)/2012), for Scottish centers from NHS Scotland Multiple Board Caldicott Guardian Approval (NHS Tayside AR/SW), and locally for other centers. Aerosol studies were approved by The Children's Health Queensland Hospital and Health Service Human Research Ethics Committee HREC/14/QRCH/88 and TPCH Research Governance Office SSA/14/QPCH/202.

SUPPLEMENTARY MATERIALS

www.sciencemag.org/content/354/6313/751/suppl/DC1
Materials and Methods
Figs. S1 to S12
Tables S1 and S2
References (*38*–*58*)

8 April 2016; accepted 23 September 2016
10.1126/science.aaf8156

NEUROSCIENCE

Neural correlates of ticklishness in the rat somatosensory cortex

S. Ishiyama[1] and M. Brecht[1,2]*

Rats emit ultrasonic vocalizations in response to tickling by humans. Tickling is rewarding through dopaminergic mechanisms, but the function and neural correlates of ticklishness are unknown. We confirmed that tickling of rats evoked vocalizations, approach, and unsolicited jumps (Freudensprünge). Recordings in the trunk region of the rat somatosensory cortex showed intense tickling-evoked activity in most neurons, whereas a minority of cells were suppressed by tickling. Tickling responses predicted nontactile neural responses to play behaviors, which suggests a neuronal link between tickling and play. Anxiogenic conditions suppressed tickling-evoked vocalizations and trunk cortex activity. Deep-layer trunk cortex neurons discharged during vocalizations, and deep-layer microstimulation evoked vocalizations. Our findings provide evidence for deep-layer trunk cortex activity as a neural correlate of ticklishness.

Tickling sensations can be differentiated into laughter-inducing "gargalesis" and non–laughter-inducing light touch, "knismesis" (*1*). The former is a peculiar, often funny form of social touch, which has been discussed for more than two millennia (*2*, *3*). Still, major questions remain unanswered: Why does tickling induce laughter? Why are tickling effects so mood-dependent (*4*)? Why do body parts differ in ticklishness (*1*)? Why can't we tickle ourselves (*2*)? Is ticklish laughter different from humorous laughter (*4*–*6*)? To address such questions, we need a better understanding of the neural correlates of ticklishness. We took advantage of groundbreaking advances that provided evidence for tickling-evoked 50-kHz vocalizations and primitive forms of joy in rats (*7*, *8*). On the basis of this work, we measured "rat ticklishness" in our work as the propensity to "laugh" (emit 50-kHz calls) upon being tickled. We focused on the somatosensory cortex because it is the largest tactile neural representation in mammals, because human imaging studies suggested this candidate region (*9*, *10*), and because work on somatosensory afferents provided no conclusive evidence for dedicated peripheral mechanisms of tickle.

We tickled and gently touched rats on different body parts (Fig. 1A, ventral tickling) and observed a variety of ultrasonic vocalizations (USVs; Fig. 1B), in particular during tickling (movie S1). Rat 50-kHz vocalizations indicate positive emotional valence (*11*). Consistent with earlier claims that tickling is rewarding through the dopaminergic system (*7*, *12*, *13*), rats rapidly approached the tickling hand, and tickling induced unsolicited jumps accompanied by 50-kHz USVs (Freudensprünge, "joy jumps"; movie S2), which can be seen in joyful subjects in various mammalian species (*14*–*16*). We visually categorized spectrograms of an extensive set of USVs (34,140 calls) into modulated, trill, combined, and miscellaneous call types (Fig. 1B and fig. S1). Both tickling and gentle touch evoked USVs (Fig. 1C), but tickling induced more USVs than did gentle touch (ventral tickling, 4.45 ± 0.28 Hz; ventral gentle touch, 2.58 ± 0.21 Hz; $n = 16$, $P < 0.001$; mean ± SEM, paired t test). Rats seemed to warm up to tickling and vocalized less before the initial interaction than during breaks between interaction episodes (Pre versus Break; Fig. 1, C and D). Tickling the ventral trunk evoked the largest number of USVs (Fig. 1D) and the largest fraction of combined USVs (Fig. 1E). Play behavior (rat chasing experimenter's hand; Fig. 1F) also evoked USVs (Fig. 1, G and H, and movie S3) (*17*). Consistent with our sense that rats experienced the experimental setting as emotionally positive, we did not observe 22-kHz alarm calls.

We simultaneously performed single-unit recordings in the trunk region of the somatosensory cortex (Fig. 2A). We obtained high-quality recordings of neuronal responses elicited by tickling and gentle touch (Fig. 2B and fig. S2A). Similar to USVs, activity in the trunk cortex was lower before initial tickling (Fig. 2, B and C, Pre) than during the short breaks between interactions (Fig. 2, B and C, Break). Remarkably, neuronal responses were also observed during hand-chasing phases, when rats were not touched by the experimenter (Fig. 2B and fig. S2E). Most cells increased their firing rate during trunk tickling, trunk gentle touch, and chasing hand (~77%, ~67%, and ~80% of the cells showed higher firing rates during interaction than during break, respectively; fig. S2B, top, and C to E), whereas a minority of cells were suppressed during interaction phases (fig. S2B, bottom, and C to E). Similar to USVs, neuronal firing rates increased more during tickling than during gentle touch on the trunk (Fig. 2D). As in the cells shown in fig. S2B, responses to tickling predicted play responses (chasing hand) across the population (Fig. 2E), which suggests a neural link between tickling and play behavior.

Anxiogenic conditions suppress tickling-evoked USVs in rats (*7*). To test whether neuronal responses to tickling are also modulated by such conditions, we tickled rats in both control (Fig. 3A, left) and anxiogenic settings, such as under bright illumination and on an elevated platform (Fig. 3A, right). Tickling-evoked USVs were significantly suppressed in the anxiogenic condition and recovered in control conditions (Fig. 3, B and C). Similarly, anxiogenic conditions suppressed neuronal response to tickling (Fig. 3D) and inverted the sign of response index to tickling (Fig. 3E).

Our recordings revealed that USVs and neuronal activity in the trunk cortex are modulated in a similar way by tickling and anxiogenic conditions. We wondered whether tickling-evoked USVs and neuronal responses to tickling are causally linked. We therefore aligned neuronal firing to the onsets of USVs (Fig. 4, A and B). To avoid a confounding effect of the coactivation of the trunk cortex and USVs by tickling and touch, we restricted this analysis to break periods. The activity of trunk somatosensory

[1]Bernstein Center for Computational Neuroscience Berlin, Institut für Biologie, Humboldt-Universität zu Berlin, 10115 Berlin, Germany. [2]NeuroCure Cluster of Excellence, Humboldt-Universität zu Berlin, Berlin, Germany.
*Corresponding author. Email: michael.brecht@bccn-berlin.de

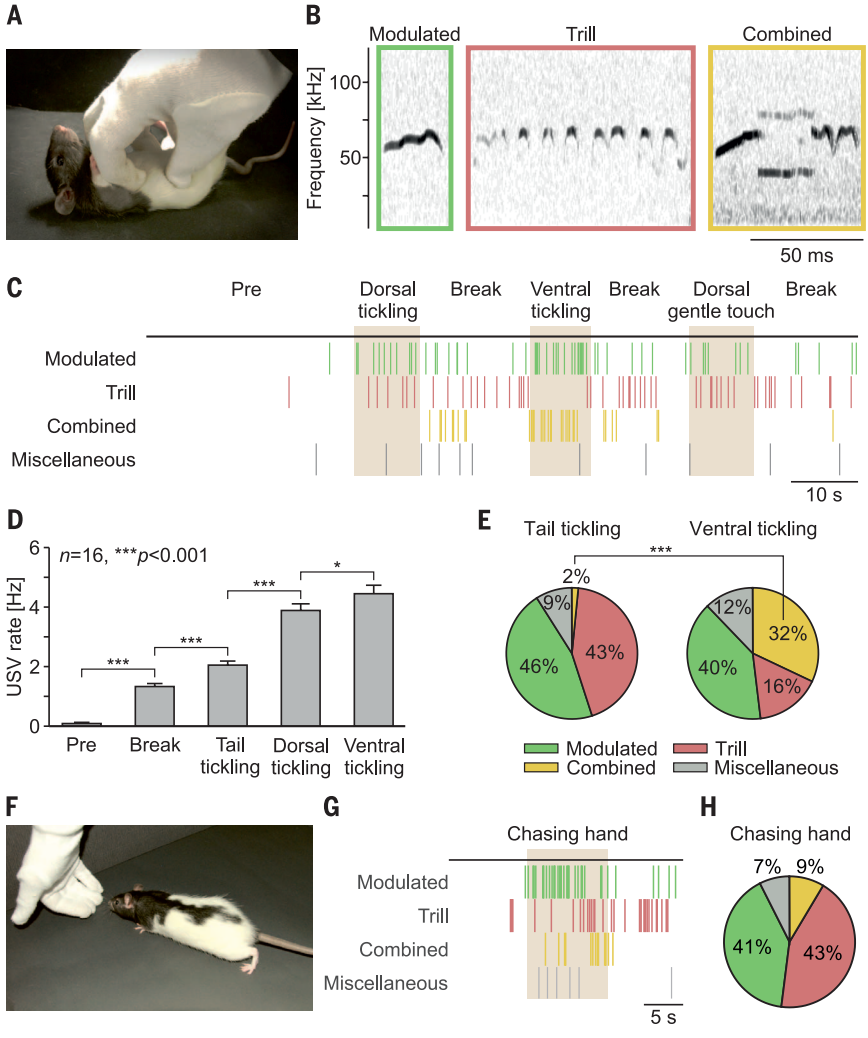

Fig. 1. Tickling and play behavior (chasing the experimenter's hand) evoke ultrasonic vocalizations. (**A**) Tickling of the ventral trunk of a rat. (**B**) Spectrograms of ultrasonic vocalizations (USVs). USVs were categorized into modulated (left), trill (middle), and combined (right) call types. (**C**) USVs during tickling and touch. Raster plots and beige boxes indicate USV onsets and interaction phases, respectively. (**D**) USV rate during different phases (n = 16 recordings from four animals). Data are means ± SEM. P value refers to analysis of variance (ANOVA); pairwise comparisons are denoted as ***P < 0.001 and *P = 0.014 (paired t test). (**E**) Fraction of USV types falling into the different categories [the same data from (D)] during tail tickling (1869 USVs) and ventral tickling (3380 USVs; combined, ***P < 0.001, Fisher exact test). (**F**) Play behavior: a rat chasing the experimenter's hand. (**G**) USVs during chasing hand. (**H**) Fraction of USV types during chasing hand [3181 USVs; 15 recordings from three animals; colors as in (E)].

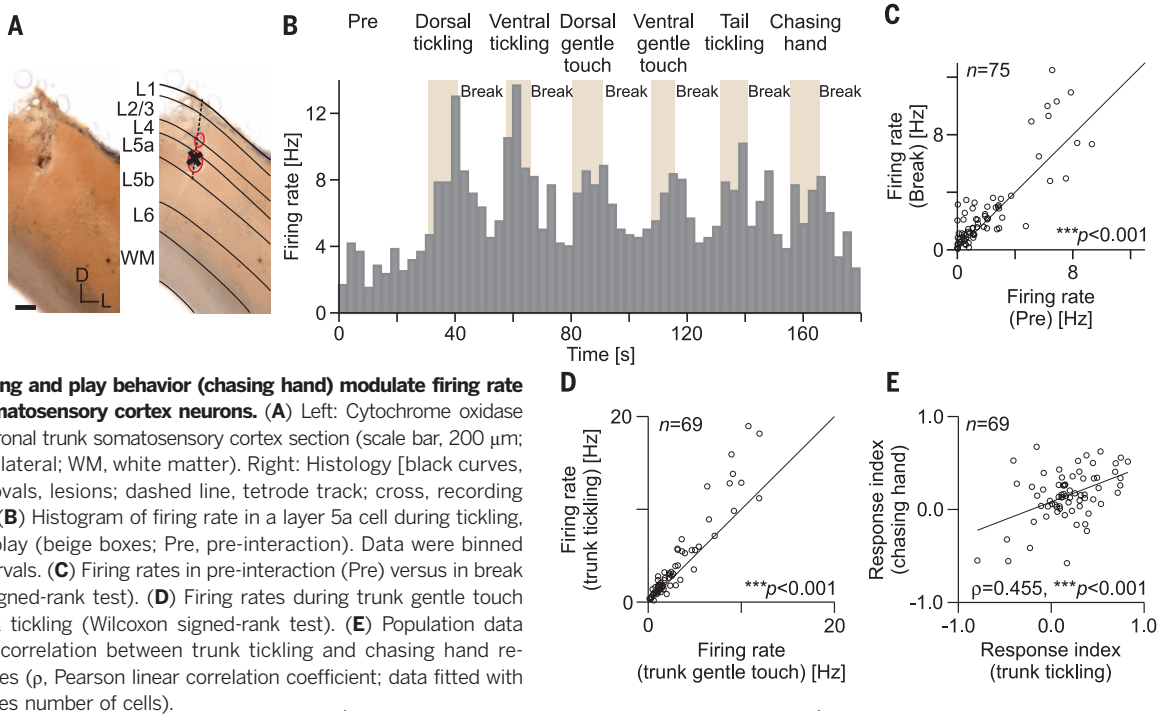

Fig. 2. Tickling and play behavior (chasing hand) modulate firing rate in trunk somatosensory cortex neurons. (**A**) Left: Cytochrome oxidase stain of a coronal trunk somatosensory cortex section (scale bar, 200 μm; D, dorsal; L, lateral; WM, white matter). Right: Histology [black curves, layers; red ovals, lesions; dashed line, tetrode track; cross, recording site of (B)]. (**B**) Histogram of firing rate in a layer 5a cell during tickling, touch, and play (beige boxes; Pre, pre-interaction). Data were binned into 3-s intervals. (**C**) Firing rates in pre-interaction (Pre) versus in break (Wilcoxon signed-rank test). (**D**) Firing rates during trunk gentle touch versus trunk tickling (Wilcoxon signed-rank test). (**E**) Population data indicating a correlation between trunk tickling and chasing hand response indices (ρ, Pearson linear correlation coefficient; data fitted with line; n denotes number of cells).

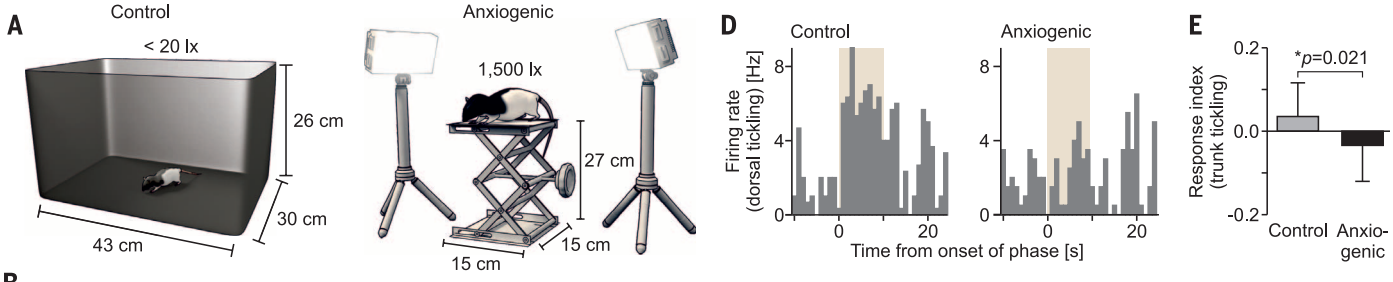

Fig. 3. Anxiogenic suppression of USVs and neuronal responses to tickling in trunk somatosensory cortex. (**A**) Control (left) and anxiogenic condition (right). (**B**) USVs in control and anxiogenic conditions. Black boxes, interaction phases; raster plots, USVs; D, dorsal tickling; V, ventral tickling; Dg, dorsal gentle touch; Vg, ventral gentle touch; T, tail tickling; Ch, chasing hand; Misc., miscellaneous. (**C**) USV rate during trunk tickling under control versus anxiogenic conditions; n = 6 recordings from four animals. Data are means ± SEM (paired t test). (**D**) Peristimulus time histograms (PSTHs) of firing in a cell during dorsal tickling (beige boxes) under control and anxiogenic conditions. (**E**) Response indices of cells for trunk tickling under control versus anxiogenic conditions (n = 27 cells, 6 recordings from four animals). Data are means ± SEM (paired t test).

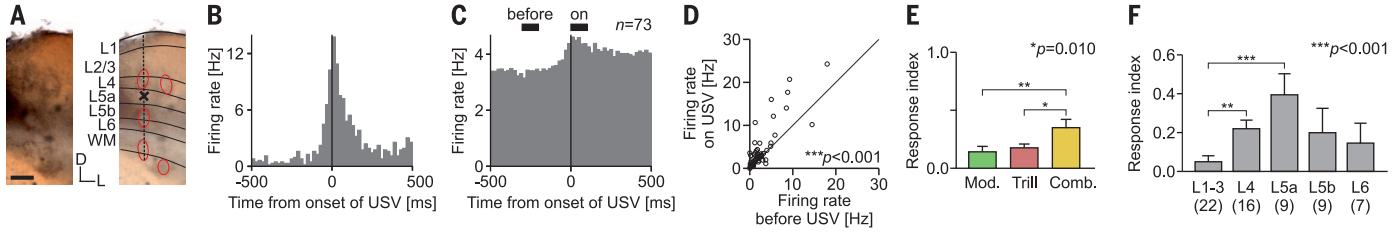

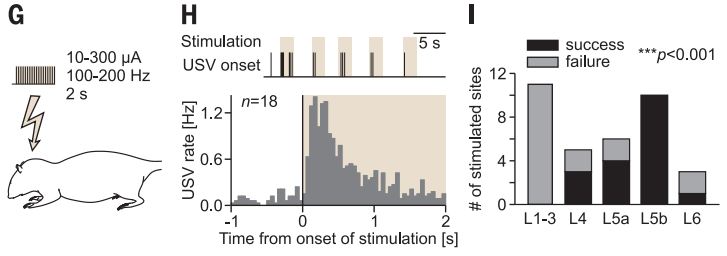

Fig. 4. Neuronal activity in deep layers of trunk somatosensory cortex is associated with USVs, and deep-layer microstimulation evokes USVs. (**A**) Left: Cytochrome oxidase stain of a coronal trunk somatosensory cortex section (scale bar, 200 µm; D, dorsal; L, lateral; WM, white matter). Right: Histology [black curves, layers; red ovals, lesions; dashed line, tetrode track; cross, recording site of (B)]. (**B**) PSTH of firing rate in a layer 5a cell aligned to USV onsets (in break phases with no previous USV onset within 500 ms). (**C**) PSTH of firing rate aligned to the onset of USV (n denotes number of cells). (**D**) Firing rate before USV [−300 to −200 ms from USV onset, Before in (C)] versus firing rate upon USV [0 to 100 ms from USV onset, On in (C)]. The same population data from (C) are plotted for each cell (Wilcoxon signed-rank test). (**E**) Response indices for each USV type, using the same data from (C) and (D). Mod., modulated; Comb., combined. Data are means ± SEM. P value refers to one-way ANOVA; pairwise comparisons are denoted as $^{**}P$ = 0.007 and $^{*}P$ = 0.010 (paired t test). (**F**) Average response indices in different cortical layers. Numbers of cells are shown in parentheses. Data are means ± SEM. P value refers to one-way ANOVA on ranks; pairwise comparisons are denoted as $^{***}P < 0.001$ and $^{**}P$ = 0.003 (t test). (**G**) Microstimulation in trunk somatosensory cortex. (**H**) Top: USVs during microstimulation (beige boxes; 200 µA, 100 Hz, 2 s). Raster plots indicate USV onsets. Bottom: Average PSTH of USV rate aligned to stimulation onsets (averaged over 278 stimulations that evoked USVs at 18 sites from three animals; data were binned into 50-ms intervals). (**I**) Number of sites in different layers of trunk somatosensory cortex, where microstimulation did ("success," black) or did not ("failure," gray) evoke USVs. P value refers to χ^2 statistics.

neurons was correlated with USV emissions: Neurons increased their firing rate before and during USV emissions (Fig. 4, C and D, Before versus On). This effect was strongest for combined USVs (Fig. 4E). Furthermore, the effect was more prominent in layers 4 and 5a than in the superficial layers (Fig. 4F). To test whether firing of somatosensory neurons causes USVs, we microstimulated the trunk cortex (Fig. 4G). Although rats had no interaction with the experimenter, they emitted USVs (Fig. 4H, top). Threshold amplitudes to trigger USVs varied between 50 and 300 µA. USVs were locked to microstimulation onset and were evoked after short latencies of 50 to 100 ms (Fig. 4H, bottom). When microstimulation was directly preceded by tickling, more USVs were evoked and current thresholds were lower. Microstimulation in the deep layers, but not in the superficial layers, evoked USVs (Fig. 4I).

Our findings confirm key conclusions of Panksepp and Burgdorf (*8*): Rats vocalize during tickling in a mood-dependent fashion. The increase of vocalizations after initial tickling (Fig. 1, C and D) and anxiogenic suppression of tickling-evoked calls (Fig. 3, B and C) support Darwin's idea that "the mind must be in a pleasurable condition" for ticklish laughter (*4*). Tickling-evoked calls are not simple reflexes in response to touch. Rats rarely emit combined calls during social facial touch with conspecifics (*18*, *19*). Rats emitted combined calls preferentially during tickling on the belly, the most ticklish body part (as assessed from calling rate). Combined calls might be a relatively tickle-specific vocalization in rats. Remarkably, similar call types have been described during conspecific play behavior (*20*). The numerous similarities between rat and human ticklishness, such as tickling-evoked vocalizations and anxiogenic modulation, suggest that tickling is a very old and conserved form of social physicality.

Peripheral mechanisms of pleasurable touch were first studied by Zotterman in cats and suggested that knismesis is carried in part by pain fibers (*21*). C-fibers, unmyelinated afferents, are putatively involved in pleasurable touch in rodents (*22*). Central mechanisms of tickling were investigated by functional magnetic resonance imaging (fMRI) in human brains (*9*); that study, which used tickling stimuli evoking knismesis and observed somatosensory cortex activation, suggested that self-tickle suppression might be mediated by the cerebellum. Recent human fMRI identified activation of the lateral hypothalamus, parietal operculum, amygdala, cerebellum, and somatosensory cortex by ticklish laughter (*10*).

Four of our results localize tickle processing to the somatosensory cortex: (i) We found that tickling can evoke intense neuronal activity in the somatosensory cortex (Fig. 2). Moreover, play behavior, which induces anticipatory vocalizations in rats (Fig. 1, F to H) (*17*) and humans (*23*), evoked neuronal activity similar to the activity evoked by tickling (fig. S2E). (ii) We observed "mood-dependent" alteration of activity in the trunk somatosensory cortex, specifically an activity increase after tickling phases (Fig. 2, B and C), anxiogenic suppression of responses (Fig. 3, D and E), and a reduction of microstimulation thresholds for evoking calls after tickling. Such "mood-dependent" modulation of the somatosensory cortex is unexpected, as it is nontactile and there is little evidence to date for mood effects in other cortical areas. (iii) The strong call-related activation of the trunk somatosensory cortex points to an involvement in tickling-evoked vocalizations. Call-related firing in the somatosensory cortex is much stronger than call-evoked activity in the auditory cortex (*18*). (iv) Microstimulation-evoked vocalizations suggest that deep-layer but not superficial-layer cortical activity is sufficient to trigger vocalizations. The short latencies of evoked calls indicate few intervening processing steps between trunk activity and calls. Electrical stimulation in various brain areas is known to evoke laughter with or without mirth (*24*–*27*), but stimulation-evoked ticklish laughter has not been reported so far, and our results might be different from previously reported laughter evoked by brain stimulation.

In line with lesion evidence, our observations suggest a neural link among tickling, play, and the somatosensory cortex (*28*). Other findings have implicated the somatosensory cortex in social information processing (*29*–*31*). The observation that the somatosensory cortex is involved in the generation of tickling responses suggests that this area might be more closely involved in emotional processing than previously thought. Identification of the neural correlates of ticklishness will allow us to frame questions about tickling in neural terms and thus help us to understand this mysterious sensation.

REFERENCES AND NOTES

1. G. S. Hall, A. Allin, *Am. J. Psychol.* **9**, 1–41 (1897).
2. Aristotle, *On the Parts of Animals*, W. Ogle, trans. (K. Paul, Trench & Co., London, 1882).
3. C. R. Harris, *Am. Sci.* **87**, 344–351 (1999).
4. C. Darwin, *The Expressions of the Emotions in Man and Animals* (John Murray, London, 1872).
5. E. Hecker, *Die Physiologie und Psychologie des Lachens und des Komischen* (Ferd. Dümmlers Verlags, Berlin, 1873).
6. C. R. Harris, N. Christenfeld, *Cogn. Emotion* **11**, 103–110 (1997).
7. J. Panksepp, J. Burgdorf, in *Toward a Science of Consciousness III*, S. R. Hameroff, D. Chalmers, A. W. Kaszniak, Eds. (MIT Press, 1999), pp. 231–244.
8. J. Panksepp, J. Burgdorf, *Physiol. Behav.* **79**, 533–547 (2003).
9. S. J. Blakemore, D. M. Wolpert, C. D. Frith, *Nat. Neurosci.* **1**, 635–640 (1998).
10. E. Wattendorf *et al.*, *Cereb. Cortex* **23**, 1280–1289 (2013).
11. B. Knutson, J. Burgdorf, J. Panksepp, *Psychol. Bull.* **128**, 961–977 (2002).
12. M. Hori *et al.*, *Neuroreport* **24**, 241–245 (2013).
13. J. Burgdorf, P. L. Wood, R. A. Kroes, J. R. Moskal, J. Panksepp, *Behav. Brain Res.* **182**, 274–283 (2007).
14. R. C. Newberry, D. G. M. Wood-Gush, J. W. Hall, *Behav. Processes* **17**, 205–216 (1988).
15. B. D. Sachs, V. S. Harris, *Anim. Behav.* **26**, 678–684 (1978).
16. M. Bekoff, *Am. Zool.* **14**, 323–340 (1974).
17. R. K. W. Schwarting, N. Jegan, M. Wöhr, *Behav. Brain Res.* **182**, 208–222 (2007).
18. R. P. Rao, F. Mielke, E. Bobrov, M. Brecht, *eLife* **3**, e03185 (2014).
19. J. M. Wright, J. C. Gourdon, P. B. Clarke, *Psychopharmacology* **211**, 1–13 (2010).
20. J. Burgdorf *et al.*, *J. Comp. Psychol.* **122**, 357–367 (2008).
21. Y. Zotterman, *J. Physiol.* **95**, 1–28 (1939).
22. S. Vrontou, A. M. Wong, K. K. Rau, H. R. Koerber, D. J. Anderson, *Nature* **493**, 669–673 (2013).
23. B. Newman, M. A. O'Grady, C. S. Ryan, N. S. Hemmes, *Percept. Mot. Skills* **77**, 779–785 (1993).
24. I. Fried, C. L. Wilson, K. A. MacDonald, E. J. Behnke, *Nature* **391**, 650 (1998).
25. G. Fernández-Baca Vaca, H. O. Lüders, M. M. Basha, J. P. Miller, *Epileptic Disord.* **13**, 435–440 (2011).
26. F. Caruana *et al.*, *Cortex* **71**, 323–331 (2015).
27. F. Caruana, F. Gozzo, V. Pelliccia, M. Cossu, P. Avanzini, *Neuropsychologia* **89**, 364–370 (2016).
28. J. Panksepp, L. Normansell, J. F. Cox, S. M. Siviy, *Physiol. Behav.* **56**, 429–443 (1994).
29. V. Gazzola *et al.*, *Proc. Natl. Acad. Sci. U.S.A.* **109**, E1657–E1666 (2012).
30. E. Bobrov, J. Wolfe, R. P. Rao, M. Brecht, *Curr. Biol.* **24**, 109–115 (2014).
31. C. Lenschow, M. Brecht, *Neuron* **85**, 718–725 (2015).

ACKNOWLEDGMENTS

Supported by BCCN Berlin, Humboldt-Universität zu Berlin, SFB665, and the Deutsche Forschungsgemeinschaft Leibniz Prize. We thank V. Bahr, T. Balmer, A. Clemens, R. de Filippo, J. Diederichs, C. Ebbesen, K. Hartmann, M. Kunert, C. Lenschow, F. Mielke, W. Muñoz-Miranda, A. Neukirchner, C. Posey, R. Rao, U. Schneeweiß, and A. Stern. All of the data are archived at the BCCN Berlin server and will be available for download upon request.

SUPPLEMENTARY MATERIALS

www.sciencemag.org/content/354/6313/757/suppl/DC1
Materials and Methods
Figs. S1 and S2
Movies S1 to S3
References (*32*–*34*)

7 July 2016; accepted 21 September 2016
10.1126/science.aah5114

EVOLUTIONARY GENOMICS

Detection of human adaptation during the past 2000 years

Yair Field,[1,2]*† Evan A Boyle,[1]* Natalie Telis,[3]* Ziyue Gao,[1,2] Kyle J. Gaulton,[1,4] David Golan,[1] Loic Yengo,[5,6] Ghislain Rocheleau,[5] Philippe Froguel,[5,7] Mark I. McCarthy,[4] Jonathan K. Pritchard[1,2,8]†

Detection of recent natural selection is a challenging problem in population genetics. Here we introduce the singleton density score (SDS), a method to infer very recent changes in allele frequencies from contemporary genome sequences. Applied to data from the UK10K Project, SDS reflects allele frequency changes in the ancestors of modern Britons during the past ~2000 to 3000 years. We see strong signals of selection at lactase and the major histocompatibility complex, and in favor of blond hair and blue eyes. For polygenic adaptation, we find that recent selection for increased height has driven allele frequency shifts across most of the genome. Moreover, we identify shifts associated with other complex traits, suggesting that polygenic adaptation has played a pervasive role in shaping genotypic and phenotypic variation in modern humans.

Understanding the genetic basis of adaptation is a central goal in evolutionary biology. Most work in humans and other species has focused on identifying signals of strong selection at individual loci (*1*). In humans, these methods have identified loci involved in adaptations to diet, altitude, and disease resistance, and lighter pigmentation in northern populations (*2*–*4*). Early methods for studying selection focused on detecting hard sweeps, in which new mutations under strong positive selection sweep through a population toward fixation (*5*). But selection often acts on preexisting variants, either in partial sweeps at individual loci (*6*, *7*), or through polygenic adaptation acting simultaneously on many variants across the genome (*8*, *9*).

However, it is difficult to measure recent selection on standing variation. In some cases this may be done by comparing closely related populations with divergent selective pressures (*4*, *10*),

[1]Department of Genetics, Stanford University, Stanford, CA 94305, USA. [2]Howard Hughes Medical Institute, Stanford University, Stanford, CA 94305, USA. [3]Program in Biomedical Informatics, Stanford University, Stanford, CA 94305, USA. [4]Wellcome Trust Center for Human Genetics, and Oxford Center for Diabetes Endocrinology and Metabolism, University of Oxford, Oxford, UK. [5]Univ. Lille, CNRS, Institut Pasteur de Lille, UMR 8199–EGID, F-59000 Lille, France. [6]Institute for Molecular Bioscience, The University of Queensland, Brisbane, Australia. [7]Imperial College, Department of Genomics of Common Disease, London Hammersmith Hospital, London, UK. [8]Department of Biology, Stanford University, Stanford, CA, USA. *These authors contributed equally to this work. **†Corresponding author. Email: yairf@stanford.edu (Y.F.); pritch@stanford.edu (J.K.P.)**

or by using ancient DNA when suitable ancestral samples are available (*11*, *12*), but a generally applicable method is lacking.

To tackle this challenge, we introduce the singleton density score (SDS). SDS uses whole-genome sequence data from contemporary samples to infer recent allele frequency changes at single-nucleotide polymorphisms (SNPs). Recent selection distorts the ancestral genealogy of sampled haplotypes, resulting in shorter terminal (tip) branches for the favored allele. Hence, haplotypes carrying the favored allele tend to carry fewer singleton mutations (Fig. 1, A to C, and fig. S1) (*13*). Following this intuition, we calculate the distance between the nearest singletons on either side of a test SNP as a summary statistic for each individual (Fig. 1D). The distributions of distances for the three genotypes at the test SNP are then used to compute a maximum likelihood estimate of the log-ratio of mean tip-branch lengths for the derived versus ancestral alleles (Fig. 1, E and F) (*13*). The two alleles act as natural controls for each other, correcting for local variation in mutation and recombination rates, or in the detection of singletons. The predictions are normalized within bins of derived allele frequency to have mean 0 and variance 1, where SDS > 0 corresponds to an increased frequency of the derived allele. In neutral simulations, SDS follows a standard normal distribution, even when considering

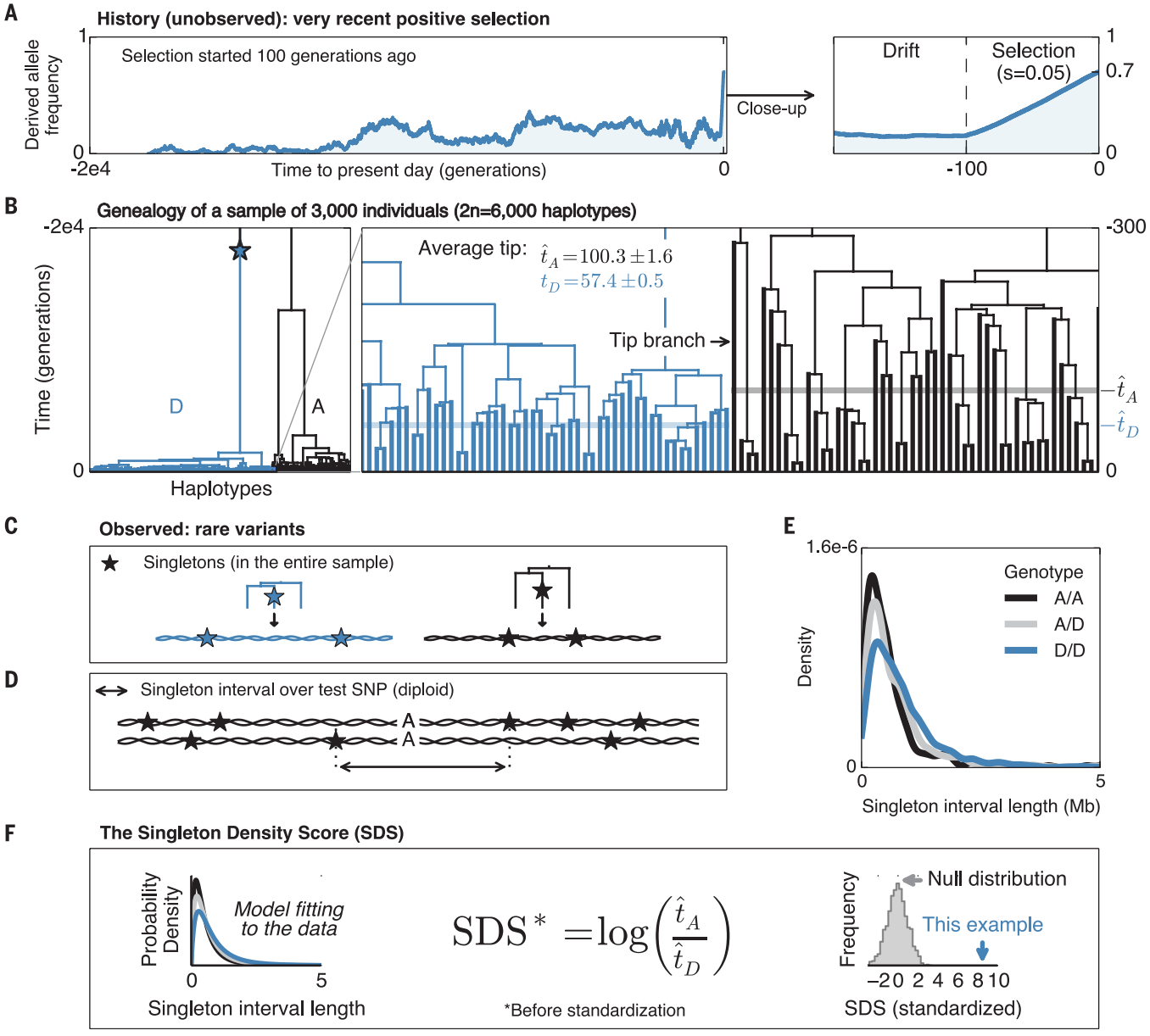

Fig. 1. Illustration of the SDS method. (**A**) Simulated frequency trajectory for a derived allele that was selected from standing variation starting 100 generations ago. (**B**) Corresponding genealogy of 3000 present-day genomes. Lineages carrying the derived allele (D) are in blue; ancestral (A) are in black. Enlargement of the genealogy illustrates that tip branches carrying the favored allele (blue) are on average shorter than those carrying the disfavored allele (black). (**C**) Because favored alleles (blue) tend to have shorter tip branches, their haplotypes tend to have lower singleton density. (**D**) For each individual, we compute the distance between nearest singletons around the test SNP. (**E**) Distribution of singleton distances as a function of genotype at the simulated test SNP. (**F**) Mean tip length t is estimated for each allele from a likelihood model. Unstandardized SDS is a log-ratio of estimated tip lengths; this is standardized to mean 0, variance 1 within bins of derived allele frequency. In this simulated example, SDS is highly significant ($P = 1 \times 10^{-17}$ in favor of the derived allele; relative to neutral simulations). Compare with illustration of drift simulation (fig. S1).

complex scenarios with recent admixture (figs. S2 and S3).

Because SDS measures changes in tip-branch lengths of the genealogy, it detects selection roughly within the timeframe of average tip lengths. For samples of 3000 individuals, this is ~75 generations, according to one recent demographic model (*14*) (Fig. 2A). At this sample size, SDS is powered to detect ~2% selection, with similar power for selection on standing variation and hard sweeps (Fig. 2, B and C, and fig. S4). Notably, SDS detects little or no signal for selection that stopped >100 generations before present (figs. S4 to S6). The time scale examined by SDS is roughly an order of magnitude shorter than the limits of sensitivity for previous methods that study hard sweeps (*13*). For example, the integrated haplotype score (iHS)—a commonly used test for hard sweeps (*5*)—integrates signal over >1000 generations, is generally less powerful, and has no specificity for recent selection (Fig. 2C and figs. S4 and S5).

To validate performance in real data, we analyzed 3195 individuals from the UK10K project (*15*) (fig. S7) (*13*). To model strong instantaneous selection, we performed biased subsampling of 1500 individuals (without replacement) to change allele frequencies at target SNPs by amounts ranging from 1% to 10% (Fig. 2D and figs. S8 and S9). Although iHS has no power in this test, each 1% change in allele frequency changes the mean SDS by ~0.3 to 0.4 standard deviations. Thus, we expect to have power to detect recent strong selection at individual loci, or weaker signals distributed across many alleles.

We used the set of 3195 genomes to compute SDS for 4.5 million autosomal SNPs with

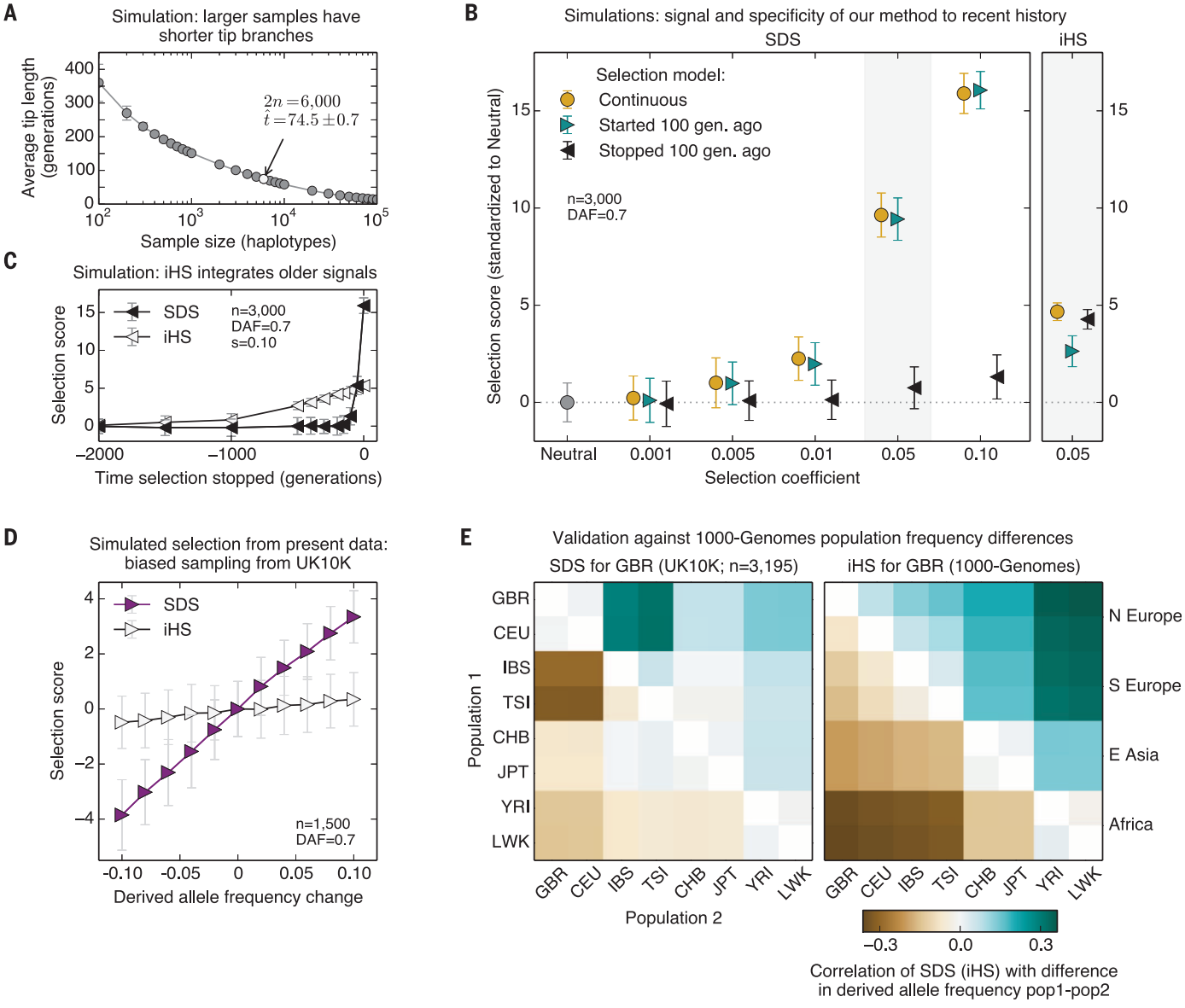

Fig. 2. Properties of SDS. (**A**) Mean tip length as a function of sample size, for a demographic model with strong recent growth (*14*) (additional models shown in fig. S10). (**B**) Power simulations for SDS (mean ± SD) under three models of selection with current derived allele frequency of 0.7: continuous hard sweep (orange); selection starting 100 generations ago (cyan); and hard sweep that stopped 100 generations ago (black). Right panel: corresponding simulations for iHS. (**C**) SDS and iHS, for sweeps that stopped in the past (s = 0.10), followed by neutral drift. (**D**) Power to detect simulated selection from present variation using half of the UK10K data. We biasedly sampled 1500 genomes out of 3195 without replacement so as to change the frequencies at randomly chosen SNPs. (**E**) Allele frequency differences between extant populations (1000-Genomes) versus SDS or iHS. SDS is most correlated with the difference between northern and southern Europe, whereas iHS reflects Europe versus Africa divergence. GBR, British; CEU, Utah residents (northwest European ancestry); IBS, Iberians (Spain); TSI, Tuscans (Italy); CHB, Han (China); JPT, Japanese; YRI, Yoruba (Nigeria); LWK, Luhya (Kenya).

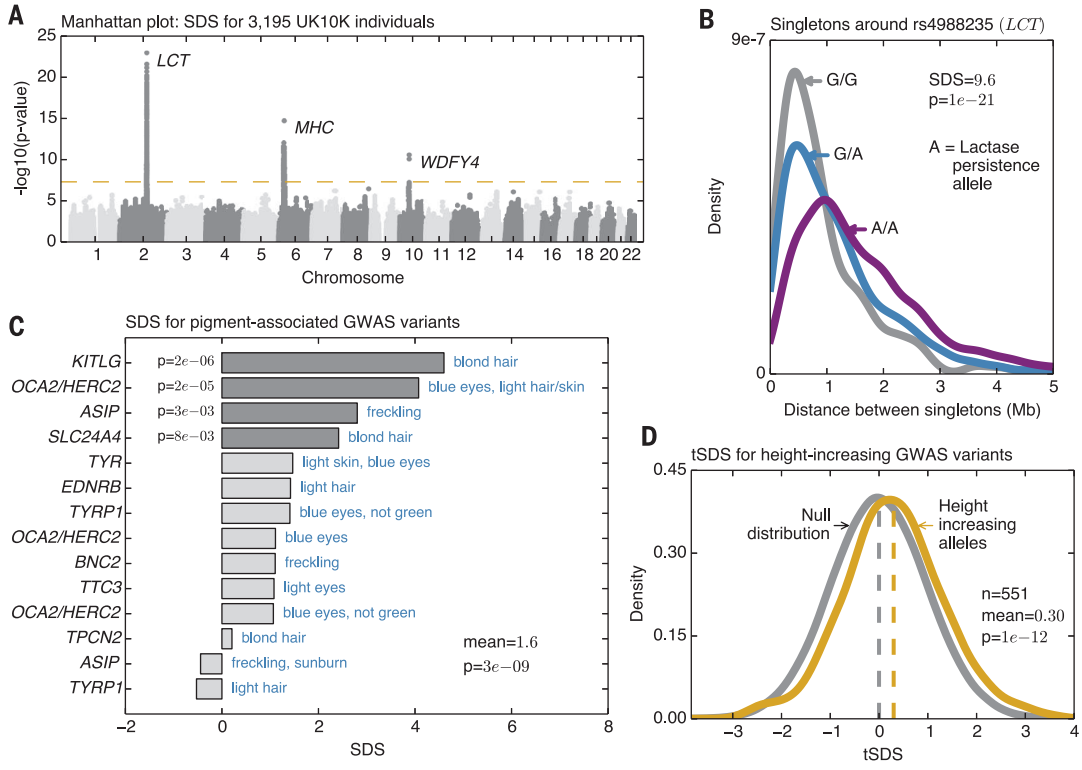

Fig. 3. Overview of signals. (**A**) Manhattan plot of SDS *P* values indicates regions of genome-wide significance ($P < 5 \times 10^{-8}$; *P* values are two-sided tail probabilities of standard normal). (**B**) Distributions of singleton distances at the lactase locus, partitioned by genotypes at the causal site. Compare to simulated signals (Fig. 1E). (**C**) SDS signals for a curated set of segregating variants with known effects on pigmentation shows overall increase in derived allele frequencies (one-sided *P* values). (**D**) Distribution of tSDS scores at 551 height-associated SNPs. tSDS is polarized so that tSDS > 0 implies increased frequency of the "tall" allele.

minor allele frequency >5%. We estimate the mean tip length to be 2000 to 3000 years [fig. S10; (*13*)]. Reassuringly, SDS predictions are correlated with allele-frequency differences between populations (Fig. 2E and fig. S11), and most strongly between southern and northern Europe (Spearman's ρ = 0.32 ± 0.005). In contrast, iHS measured in a British sample is most correlated with African-European differences. This provides empirical evidence that SDS captures historical frequency changes for times more recent than iHS.

Genome-wide, the largest values of SDS cluster at the lactase locus, a well-known target of selection in Europeans (*2*, *12*) ($P = 1 \times 10^{-23}$; Fig. 3, A and B, and figs. S12 and S13). Based on the magnitude of the signal, we infer that the selection almost certainly persisted into the last 2000 years (fig. S14) (*13*). The MHC (major histocompatibility complex) region, which has been subject to long-term balancing selection (*16*, *17*), includes the second-highest cluster, with high SDS values across most of the extended MHC region, and at least three independent signals (maximum SDS = 7.9; $P = 2 \times 10^{-15}$; figs. S15 and S16) (*13*). Curiously, SDS does not support the strongest hit reported from a study of European ancient DNA (*12*), suggesting complex dynamics of selection in this region (fig. S13). SNPs in the neighborhood of *WDFY4* also cross genome-wide significance ($P = 3 \times 10^{-11}$) (fig. S17), but the nature of selection is unclear (*13*).

We next considered GWAS-associated variants from the genome-wide association study (GWAS) catalog (*18*). Overall, these have significantly inflated SDS variance ($P = 5 \times 10^{-7}$ excluding lactase and MHC) (fig. S18) (*13*). Examining categories of related variants, we found a strong enrichment for variants associated with pigmentation (Fig. 3C and figs. S19 to S21) (*13*). Although the major determinants of light skin pigmentation in Europe are near fixation and thus not testable by SDS, there is a strong overall enrichment of selection in favor of derived variants associated with lighter pigmentation, especially of hair and eye color ($P = 3 \times 10^{-9}$ for mean SDS > 0).

It has been proposed that another major mechanism of adaptation may be through polygenic selection on complex traits (*8*). Polygenic adaptation can potentially change phenotypes rapidly, through small, directed allele frequency shifts at many loci, yet leave only weak signals at individual loci. Currently, the best candidate for polygenic selection in humans is height, as northern Europeans have come to possess more "tall" alleles than southern Europeans over the past ~5000 years (*9*, *12*, *19*, *20*).

We thus examined SDS for height-associated SNPs from a recent meta-analysis (*21*). To aid our analysis of height and other traits, we reset the sign of SDS scores for each trait such that positive values indicate increased frequency of the trait-increasing allele instead of the derived allele. We call these new metrics trait-SDS (tSDS) scores. The mean tSDS for 551 height-associated SNPs is significantly positive (mean = 0.30; $P = 4 \times 10^{-11}$), indicating that indeed, on average, "tall" alleles have been increasing in frequency within the past ~2000 to 3000 years in the ancestors of the British (Fig. 3D).

Because most complex-trait heritability is due to SNPs that do not reach GWAS significance (*22*), we hypothesized that we could increase power by including all SNPs, not just genome-wide significant hits. We thus used all SNPs to test for genome-wide rank correlation between tSDS and GWAS *Z* score [block-jackknife was used to account for linkage disequilibrium (LD)] (*13*). Notably, when testing height, mean tSDS is positive across nearly the entire range of *P* values, and the correlation is extremely significant (Spearman ρ = 0.078; $P = 9 \times 10^{-74}$; fig. S22A) (*13*). This is not an artifact of uncontrolled population structure in the GWAS, as the correlation is even stronger for a smaller family-based GWAS that provides stringent structure control (*20*) (Spearman ρ = 0.094; $P = 9 \times 10^{-163}$; Fig. 4A).

Our observation that the signal is stronger in the smaller family-based study may indicate that standard GWAS methods have overcorrected for population structure that pervasively correlates with the phenotypic signal. Further, it may seem counterintuitive that, in aggregate, even non-significant SNPs could have a detectable association with tSDS. However, we estimate that 85% of SNPs in this data set are associated with non-zero effects on height (including through LD tagging) and that the direction of effect is estimated correctly for 68% of all SNPs (*23*) (fig. S23) (*13*). Thus, our results indicate that polygenic selection on height has affected allele frequencies across most of the genome.

Aside from height and body mass index (BMI) (*19*), evidence for selection on other complex traits has generally been weak [e.g., (*12*, *19*)]. We expanded our test to consider 43 traits for which genome-wide GWAS data are available (tables S1 and S2). Notably, many traits show highly

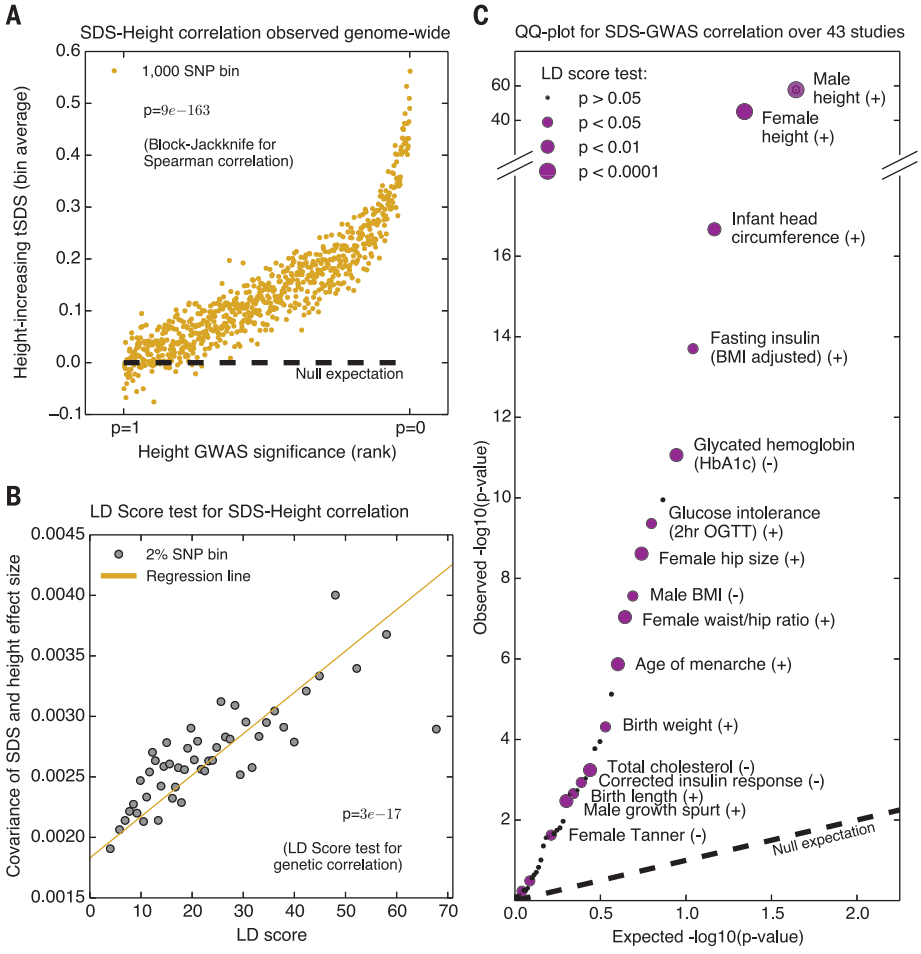

Fig. 4. Signals of polygenic adaptation. (**A**) Mean tSDS of SNPs, where tSDS > 0 implies increased frequency of the "tall" allele in a recent family-based study (*20*). The *x* axis is ordered from least significant SNPs ($P \sim 1$) to most significant ($P \sim 0$), and SNPs are placed into bins of 1000 consecutive SNPs for easier visualization. (**B**) Covariance of height *Z* score and SDS, as a function of LD score, provides evidence that selection on height is truly polygenic ($P = 2 \times 10^{-11}$; LD score regression). (**C**) QQ-plot testing for a correlation between GWAS *Z* score and tSDS for 43 traits. tSDS > 0 implies increased frequency of the "trait-increasing" allele. Significant traits that are also nominally significant by LD score regression ($P < 0.05$, one-sided test) are labeled.

significant associations between SDS and GWAS effect sizes (Fig. 4C). Because large-scale family studies are not available for most traits, we used LD score regression to verify these correlations (*24*, *25*). This method uses the property that the covariance between two correlated polygenic signals should increase with the amount of LD if they share an underlying genetic basis, but should be nearly independent of LD for spurious associations resulting from stratification (*13*). Indeed for height, LD score regression is highly significant ($P = 3 \times 10^{-17}$, family data; $P = 2 \times 10^{-11}$, meta-analysis; Fig. 4B and fig. S22B). Notably, most of the other significant traits are also nominally significant by this stringent test and persist in multiple genomic contexts (Fig. 4C and figs. S24 to S27).

Although height has the strongest signal, we also see signals for increased infant head circumference and birth weight, and increases in female hip size; as well as on variants underlying metabolic traits; male-specific signal for decreased BMI; and in favor of later sexual maturation in women, but not in men. Multiple regression analysis indicates that none of the examined traits, including height, uniquely underlies the top associations (fig. S28) (*13*). Although these signals are highly intriguing, and some match known phenotypes of modern Britons (*13*), the confounding role—if any—of population structure in contributing to these signals remains to be fully determined.

In this study, we have introduced a method for inferring very recent changes in allele frequencies that is widely applicable across human populations and other species. We found that human adaptation continued well into historical times, with polygenic adaptation being an important force shaping both genotypic and phenotypic variation.

REFERENCES AND NOTES

1. J. J. Vitti, S. R. Grossman, P. C. Sabeti, *Annu. Rev. Genet.* **47**, 97–120 (2013).
2. T. Bersaglieri *et al.*, *Am. J. Hum. Genet.* **74**, 1111–1120 (2004).
3. R. L. Lamason *et al.*, *Science* **310**, 1782–1786 (2005).
4. X. Yi *et al.*, *Science* **329**, 75–78 (2010).
5. B. F. Voight, S. Kudaravalli, X. Wen, J. K. Pritchard, *PLOS Biol.* **4**, e72 (2006).
6. J. Hermisson, P. S. Pennings, *Genetics* **169**, 2335–2352 (2005).
7. M. Przeworski, G. Coop, J. D. Wall, *Evolution* **59**, 2312–2323 (2005).
8. J. K. Pritchard, J. K. Pickrell, G. Coop, *Curr. Biol.* **20**, R208–R215 (2010).
9. M. C. Turchin *et al.*, *Nat. Genet.* **44**, 1015–1019 (2012).
10. G. Bhatia *et al.*, *Am. J. Hum. Genet.* **89**, 368–381 (2011).
11. S. Wilde *et al.*, *Proc. Natl. Acad. Sci. U.S.A.* **111**, 4832–4837 (2014).
12. I. Mathieson *et al.*, *Nature* **528**, 499–503 (2015).
13. Information on materials and methods is available on *Science* Online.
14. J. A. Tennessen *et al.*, *Science* **337**, 64–69 (2012).
15. K. Walter *et al.*, *Nature* **526**, 82–90 (2015).
16. P. I. W. de Bakker, S. Raychaudhuri, *Hum. Mol. Genet.* **21** (R1), R29–R36 (2012).
17. E. M. Leffler *et al.*, *Science* **339**, 1578–1582 (2013).
18. D. Welter *et al.*, *Nucleic Acids Res.* **42**, D1001–D1006 (2014).
19. J. J. Berg, G. Coop, *PLOS Genet.* **10**, e1004412 (2014).
20. M. R. Robinson *et al.*, *Nat. Genet.* **47**, 1357–1362 (2015).
21. A. R. Wood *et al.*, *Nat. Genet.* **46**, 1173–1186 (2014).
22. J. Yang *et al.*, *Nat. Genet.* **42**, 565–569 (2010).
23. M. Stephens, *bioRxiv* (2016).
24. B. K. Bulik-Sullivan *et al.*, *Nat. Genet.* **47**, 291–295 (2015).
25. B. Bulik-Sullivan *et al.*, *Nat. Genet.* **47**, 1236–1241 (2015).

ACKNOWLEDGMENTS

We thank G. Coop, R. Durbin, H. Fraser, N. Patterson, J. Pickrell, M. Przeworski, G. Sella, M. Robinson, P. Visscher, and the anonymous reviewers for comments; and A. Bhaskar for technical assistance. This work was supported by NIH grants ES025009, 5T32HG000044-19, and MH101825 and by the Howard Hughes Medical Institute. SDS scores and software are available through the Dryad Digital Repository at http://datadryad.org/resource/doi:10.5061/dryad.kd58f and GitHub at https://github.com/yairf/SDS, as well as through the authors' website at http://pritchardlab.stanford.edu.

SUPPLEMENTARY MATERIALS

www.sciencemag.org/content/354/6313/760/suppl/DC1
Materials and Methods
Figs. S1 to S28
Tables S1 and S2
References (*26*–*63*)

6 May 2016; accepted 3 October 2016
Published online 13 October 2016
10.1126/science.aag0776

RADIATION DAMAGE

The DNA-sensing AIM2 inflammasome controls radiation-induced cell death and tissue injury

Bo Hu,[1]* Chengcheng Jin,[1]* Hua-Bing Li,[1]* Jiyu Tong,[1,2] Xinshou Ouyang,[3] Naniye Malli Cetinbas,[4] Shu Zhu,[1] Till Strowig,[1]† Fred C. Lam,[4] Chen Zhao,[5] Jorge Henao-Mejia,[1]‡ Omer Yilmaz,[4] Katherine A. Fitzgerald,[6] Stephanie C. Eisenbarth,[1,7] Eran Elinav,[1]§ Richard A. Flavell[1,8]||

Acute exposure to ionizing radiation induces massive cell death and severe damage to tissues containing actively proliferating cells, including bone marrow and the gastrointestinal tract. However, the cellular and molecular mechanisms underlying this pathology remain controversial. Here, we show that mice deficient in the double-stranded DNA sensor AIM2 are protected from both subtotal body irradiation–induced gastrointestinal syndrome and total body irradiation–induced hematopoietic failure. AIM2 mediates the caspase-1–dependent death of intestinal epithelial cells and bone marrow cells in response to double-strand DNA breaks caused by ionizing radiation and chemotherapeutic agents. Mechanistically, we found that AIM2 senses radiation-induced DNA damage in the nucleus to mediate inflammasome activation and cell death. Our results suggest that AIM2 may be a new therapeutic target for ionizing radiation exposure.

Whole-body exposure to 2 Gy or higher radiation can induce hematopoietic syndrome, which might lead to death from infection or hemorrhage within 30 days (*1*). Higher doses of radiation cause severe damage to the gastrointestinal (GI) tract, resulting in diarrhea, malabsorption, and lethality within 10 days (*1*). However the cellular targets of GI syndrome and the mechanism of radiation-induced cell death remain controversial. Different forms of cell death have been implicated in radiation-induced GI syndrome, including apoptosis (*2*) or mitotic catastrophe (*3*) of intestinal epithelial cells (IECs), and apoptosis of endothelial cells in the intestinal vasculature (*4*). Although GI toxicity is a common complication in cancer patients undergoing radiotherapy or chemotherapy with DNA-damaging agents, there are currently no effective medical treatments to prevent or ameliorate GI syndrome. It is therefore important to gain a better understanding of the underlying mechanisms of cell death and tissue injury in response to double-strand DNA damage.

Several innate pattern recognition receptors (PRRs), including NLRP1, NLRP3, NLRC4, NLRP6, and Absent in melanoma 2 (AIM2), can drive the assembly of multiprotein complexes named inflammasomes to govern caspase-1 activation (*5*). Inflammasomes are critical regulators of intestinal tissue homeostasis through modulating intestinal microbial ecology, inflammation, and tissue repair (*6*). However, the role of inflammasomes in radiation-induced intestinal damage is unknown.

To investigate this, we used an established mouse model of radiation-induced small intestine syndrome in which mice are exposed to a lethal dose of subtotal body irradiation (SBI) with their limbs and head shielded to avoid hematopoietic damage (*3*). In this model, most wild-type (WT) mice died from severe intestinal damage within 10 days of radiation exposure. Notably, mice lacking caspase-1 were resistant to SBI-induced lethality (Fig. 1A), suggesting that inflammasome pathways play a critical role in controlling intestinal radiosensitivity. This commonly used caspase-1 knockout strain (*7*) was recently also found to be deficient in caspase-11 [here referred to as *Casp1(11)*$^{-/-}$]. Caspase-11 mediates noncanonical inflammasome activation in response to various Gram-negative bacterial infections, whereas caspase-1 is critical for the canonical inflammasome pathway downstream of several intracellular PRRs including NLRP3 and AIM2 (*8*). We therefore repeated the experiment and found that mice lacking only caspase-1 or the adapter protein ASC were also protected from SBI-induced lethality, indicating that a caspase-1–dependent, ASC-dependent canonical inflammasome pathway regulates intestinal radiosensitivity (Fig. 1, B and C).

AIM2 is an innate immune sensor that mediates assembly and activation of inflammasome in response to double-stranded DNA (dsDNA) (*9*, *10*). We found that AIM2-deficient mice were protected from SBI-induced lethality and intestinal damage (Fig. 1D). In accordance with previous observations (*11*–*13*), WT mice exhibited severe loss of crypts 3.5 days after SBI, whereas crypts of AIM2-deficient mice largely maintained their integrity (Fig. 1E). By contrast, no difference in survival from the GI syndrome was observed for mice lacking other inflammasome sensors including NLRP3 or NLRC4, indicating the specific role of the AIM2 inflammasome in controlling SBI-induced intestinal damage (fig. S1, A and B).

Upon binding to dsDNA via its HIN200 domain, AIM2 recruits the adapter protein ASC through its pyrin domain and assembles into an inflammasome to activate caspase-1, and thus maturation and secretion of proinflammatory cytokines interleukin-1β (IL-1β) and IL-18. In addition, activation of the AIM2 inflammasome in macrophages can induce caspase-1–dependent cell death known as pyroptosis (*5*, *9*). To elucidate the pathway downstream of the AIM2 inflammasome that might mediate intestinal radiosensitivity, we studied *Il1b*$^{-/-}$, *Il1r1*$^{-/-}$, and *Il18*$^{-/-}$ mice and found them to be equally susceptible to SBI-induced GI syndrome as WT controls (fig. S1, C to E). Therefore, AIM2 does not act through cytokine production to regulate intestinal damage in response to radiation. As IEC death plays a critical role in SBI-induced GI syndrome (*3*), we next examined the contribution of caspase-1–mediated cell death in this model. We selectively deleted caspase-1 in IECs by crossing mice carrying floxed caspase-1 alleles with mice expressing Cre under the control of Villin promoter (Villin-Cre). IEC-specific caspase-1 deletion protected mice from SBI-induced GI syndrome (Fig. 2A), suggesting that caspase-1–mediated pyroptosis of IECs is critical in controlling SBI sensitivity downstream of the AIM2 inflammasome. Consistently, fewer cells that stained positive for terminal deoxynucleotidyl transferase–mediated deoxyuridine triphosphate nick end labeling (TUNEL^{+}) were observed in the crypts of the jejunum of *Casp1(11)*$^{-/-}$ and *Aim2*$^{-/-}$ mice 24 hours after SBI (Fig. 2, B and C). In addition, the amounts of cleaved caspase-3 and caspase-7 were not decreased in intestines of *Aim2*$^{-/-}$ mice compared to WT (fig. S2, A and B), indicating that the reduction in the number of TUNEL^{+} cells in *Aim2*$^{-/-}$ mice was caused by abrogation of caspase-1–mediated pyroptosis (fig. S2C), not caspase-3/7–dependent apoptosis. AIM2 was suggested to inhibit AKT activation to suppress colorectal tumorigenesis (*14*, *15*). However, we did not observe any increase of AKT activity in *Aim2*$^{-/-}$ mice after radiation, implying that AKT might not be involved in AIM2 inflammasome signaling in response to radiation (fig. S2D). Mechanistically, loss of clonogenic (stem or progenitor) cells in the crypts has been suggested to be responsible for radiation-induced intestinal damage (*16*).

[1]Department of Immunobiology, Yale University School of Medicine, New Haven, CT 06520, USA. [2]Biomedical Translational Research Institute, Jinan University, Guangzhou 510632, China. [3]Section of Digestive Diseases, Yale University, New Haven, CT 06520, USA. [4]Koch Institute for Integrative Cancer Biology, Massachusetts Institute of Technology, 500 Main Street, Cambridge, MA 02139, USA. [5]Hematology Oncology Fellowship Program, National Institutes of Health, Bethesda, MD 20892, USA. [6]Division of Infectious Diseases and Immunology, Program in Innate Immunity, University of Massachusetts Medical School, Worcester, MA 01605, USA. [7]Department of Laboratory Medicine, Yale University School of Medicine, New Haven, CT 06520, USA. [8]Howard Hughes Medical Institute, Chevy Chase, MD 20815-6789, USA.

*These authors contributed equally to this work. †Present address: Helmholtz Centre for Infection Research, Inhoffenstrasse 7, 38124 Braunschweig, Germany. ‡Present address: Institute for Immunology, Perelman School of Medicine, University of Pennsylvania, Philadelphia, PA 19104, USA. §Present address: Immunology Department, Weizmann Institute of Science, Rehovot, Israel.
||Corresponding author. Email: richard.flavell@yale.edu

We performed the microcolony formation assay in vivo and found that AIM2 deficiency significantly enhanced crypt survival and regeneration in response to a range of radiation doses as assessed by histological analysis of hematoxylin and eosin (H&E) staining (fig. S3, A and B), as well as 5-bromo-2′-deoxyuridine (BrdU) incorporation (fig. S3C). Furthermore, intestinal organoids derived from AIM2-deficient crypts were more resistant to radiation (fig. S3, D and E). Taken together, our data suggest that the AIM2 inflammasome–mediated pyroptosis of clonogenic cells in the intestinal crypts plays a critical role in radiation-induced GI syndrome.

Mice deficient in inflammasome components, including ASC, caspase-1(11) (*17*), and AIM2 (*15*, *18*), can develop altered intestinal microbiota composition. Therefore, we cohoused WT controls used in these studies with the individual knockout strains at least 2 weeks before radiation in all of our experiments to equilibrate their gut microbiota (Figs. 1 and 2 and fig. S1), and thereby ruled out the contribution of dysbiosis in the AIM2 inflammasome–mediated regulation of radiation-induced intestinal injury. Taken together, our data demonstrated that the AIM2 inflammasome acts intrinsically in IECs to control intestinal radiosensitivity through caspase-1–mediated pyroptosis.

In addition to gastrointestinal toxicity (GI syndrome), acute irradiation can also induce bone marrow damage (hematopoietic syndrome), depending on the dose and route of radiation exposure (*1*, *19*, *20*). To further investigate whether the AIM2 inflammasome also contributes to radiosensitivity in the bone marrow compartment, we subjected mice to a lower dose (7 Gy) of total body irradiation (TBI). In this model, about 50% of WT mice died from hematopoietic syndrome starting around 2 weeks after irradiation; notably, *Aim2*$^{-/-}$ and *Casp1*$^{-/-}$ mice were resistant to TBI and survived beyond a month (Fig. 3, A and B, and fig. S4A).

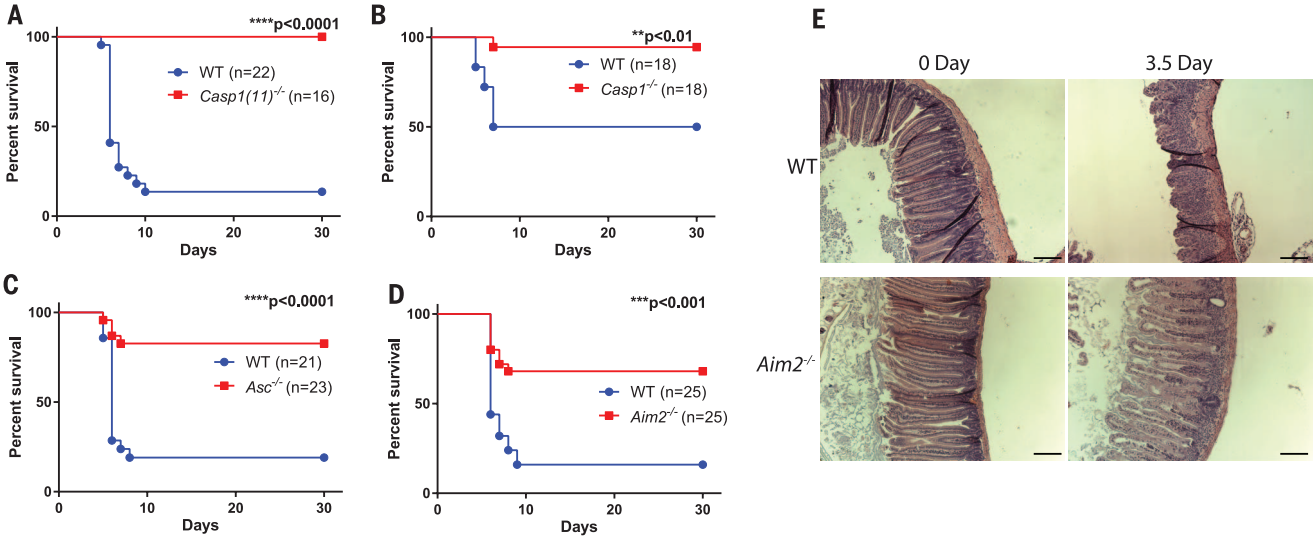

Fig. 1. AIM2 inflammasome deficiency protects mice from SBI-induced small intestine syndrome. (**A** to **D**) WT mice were cohoused with *Casp1(11)*$^{-/-}$, *Casp1*$^{-/-}$, *Asc*$^{-/-}$, or *Aim2*$^{-/-}$ mice for at least 2 weeks and then exposed to 14.2 Gy of subtotal-body irradiation (SBI). Kaplan-Meier survival analysis of *Casp1(11)*$^{-/-}$ mice (A), *Casp1*$^{-/-}$ mice (B), *Asc*$^{-/-}$, mice (C), *Aim2*$^{-/-}$ (D) mice and their cohabitated WT mice was performed. Each figure represents the pooled data from two to three independent experiments. The total number of mice in each group and the *P* value by log-rank comparison are indicated on the plots. (**E**) Representative pictures of H&E staining of the jejunum from *Aim2*$^{-/-}$ mice and their cohabitated WT mice at day 0 and day 3.5 after 14.2 Gy of SBI. Scale bars, 100 μm.

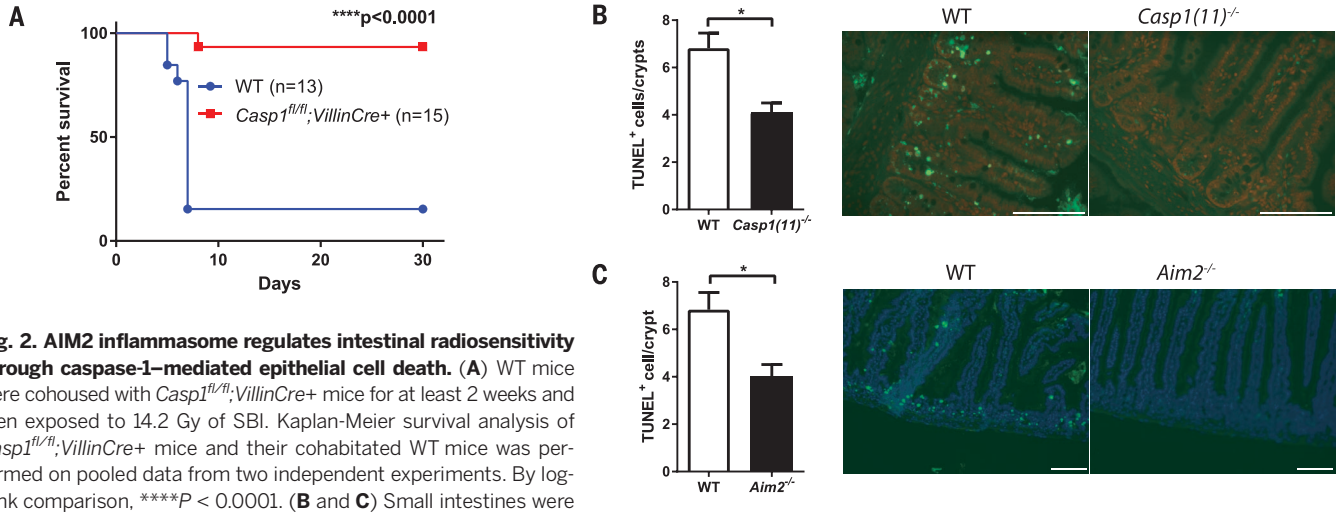

Fig. 2. AIM2 inflammasome regulates intestinal radiosensitivity through caspase-1–mediated epithelial cell death. (**A**) WT mice were cohoused with *Casp1*$^{fl/fl}$*;VillinCre*+ mice for at least 2 weeks and then exposed to 14.2 Gy of SBI. Kaplan-Meier survival analysis of *Casp1*$^{fl/fl}$*;VillinCre*+ mice and their cohabitated WT mice was performed on pooled data from two independent experiments. By log-rank comparison, ****$P < 0.0001$. (**B** and **C**) Small intestines were harvested from *Casp1(11)*$^{-/-}$, *Aim2*$^{-/-}$, and their cohabitated WT mice 24 hours after 14.2 Gy of SBI, and cell death was analyzed by TUNEL staining. Epithelial cells stained positively for TUNEL showed green fluorescence. Nuclei were stained with PI (propidium iodide, red) or DAPI (4′,6-diamidino-2-phenylindole, blue). Scale bars, 100 μm. Numbers of TUNEL-positive cells per crypts were quantified (n = 3 to 5 mice per group, at least 20 crypts of each mouse were counted), and representative images are shown. Results are expressed as mean ± SEM, *$P < 0.05$ by Student's t test.

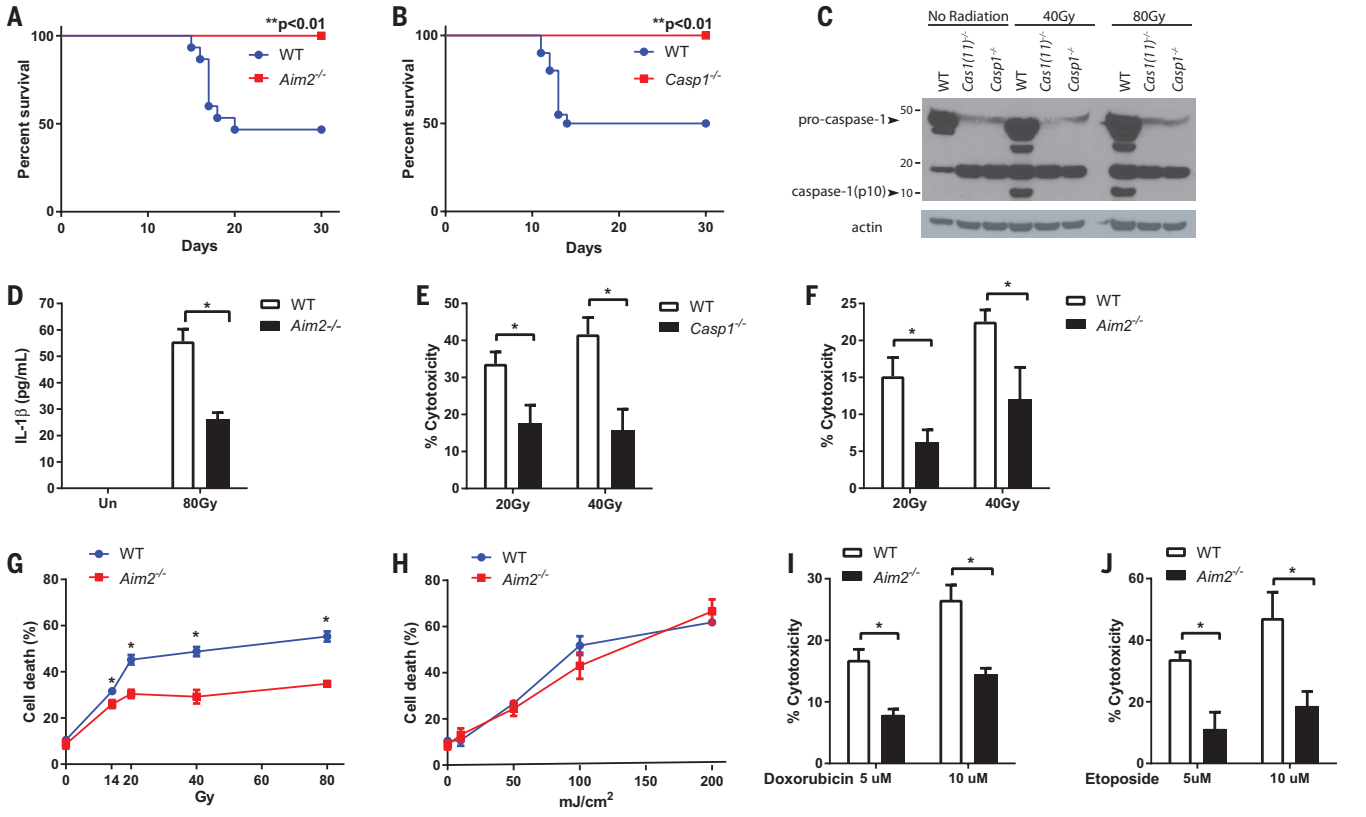

Fig. 3. AIM2 inflammasome mediates radiosensitivity of hematopoietic cells in response to dsDNA damage. (**A** and **B**) Kaplan-Meier survival analysis was performed on *Aim2*$^{-/-}$ mice (A), *Casp1*$^{-/-}$ mice (B), and their WT controls exposed to 7 Gy of total-body irradiation (TBI). Each figure represents the pooled data from two independent experiments (n = 10 to 20 mice per group). (**C**) Caspase-1 activation in WT and *Casp1*$^{-/-}$ BMDMs 4 hours after exposure to the indicated doses of radiation was assayed by immunoblotting of the cleaved form of caspase-1 (p10 subunit). (**D**) Supernatant was collected from unirradiated or 80 Gy–irradiated lipopolysaccharide (LPS)–primed WT and *Aim2*$^{-/-}$ BMDMs, and IL-1β concentration was measured by enzyme-linked immunosorbent assay. (**E**, **F**, **I**, and **J**) WT, *Casp1*$^{-/-}$, or *Aim2*$^{-/-}$ BMDMs were treated with different doses of ionizing radiation or drugs inducing dsDNA breaks, and cell death was measured by the amount of lactate dehydrogenase (LDH) released into the supernatant. (**G** and **H**) WT and *Aim2*$^{-/-}$ BMDMs were treated with different doses of ionizing radiation or UV radiation, and cell death was quantified by trypan blue staining. Determinations were performed in triplicate and expressed as the mean ± SEM. * $P < 0.05$ by Student's t test.

To investigate the cellular mechanism of AIM2-mediated radiosensitivity, we used primary bone marrow–derived macrophages (BMDMs). In WT cells, ionizing radiation activated the AIM2 inflammasome, as directly evidenced by the cleavage of caspase-1 to yield the p10 subunit and secretion of mature IL-1β, which were absent from *Casp1*$^{-/-}$ and *Aim2*$^{-/-}$ BMDMs (Fig. 3, C and D, and fig. S4B). Consistent with our in vivo findings, we observed a dose-dependent increase of cell death in response to ionizing radiation in WT BMDMs, which was significantly reduced in AIM2-deficient or caspase-1–deficient BMDMs (Fig. 3, E to G). As radiation-induced uric acid release from dead or damaged cells was previously suggested to activate caspase-1 in spleen cells (*21*), we harvested conditioned medium from irradiated bone marrow cells and found that it did not affect survival of either unirradiated WT or *Aim2*$^{-/-}$ bone marrow cells (fig. S4C). Our data suggest that the AIM2 inflammasome acts in a cell-autonomous manner in response to radiation, independently of soluble factors released from dead or injured cells. WT and *Aim2*$^{-/-}$ BMDMs were equally sensitive to ultraviolet (UV) radiation, which causes single-strand DNA breaks (Fig. 3H); however, *Aim2*$^{-/-}$ BMDMs showed significantly higher resistance to the commonly used chemotherapeutic agents doxorubicin and etoposide, which kill malignant cells by introducing DNA double-strand breaks (DSBs) (Fig. 3, I and J). In line with the in vitro data, *Aim2*$^{-/-}$ mice were also less sensitive to intestinal damage and lethality induced by high-dose doxorubicin treatment (fig. S4, D and E). Altogether, these findings suggested that the AIM2 inflammasome is specifically involved in mediating cell death in response to DSBs such as those caused by ionizing radiation and chemotherapeutic agents.

To further explore the molecular mechanism by which the AIM2 inflammasome responds to ionizing radiation, we reconstituted the AIM2 inflammasome in human embryonic kidney (HEK) 293T cells by overexpressing Flag-tagged AIM2, caspase-1, and ASC. Radiation induced the formation of AIM2-positive specks, a classical marker for inflammasome assembly, and resulted in cell death (fig. S5, A and B). In addition, we generated a Flag-tagged AIM2 mouse in which a Flag tag was knocked into the C terminus of AIM2 protein using the clustered regularly interspaced short palindromic repeats (CRISPR)–Cas9–based genome-editing system (here referred to as AIM2-Flag mice, fig. S5C), because highly specific antibodies against endogenous murine AIM2 are not available (*14*). As we found an important role of AIM2 in regulating cell death and tissue injury in immune cells and the small intestine, we first verified the steady-state expression of endogenous AIM2 protein in the spleen and small intestine using the AIM2-Flag mice (fig. S5D). Next, we analyzed irradiated primary macrophages from AIM2-Flag mice by immunofluorescence (IF) microscopy. Endogenous AIM2 showed very diffuse and weak staining before radiation exposure but formed puncta in the nucleus upon radiation exposure (Fig. 4, A and B, and fig. S5E). Moreover, considerable colocalization of AIM2-containing specks and gamma-H2AX–positive foci was observed in the nucleus, suggesting that AIM2 is recruited to sites of dsDNA breaks (Fig. 4C and fig. S5F). In support of our IF experimental observations, a strong interaction between Flag-tagged AIM2 and gamma-H2AX

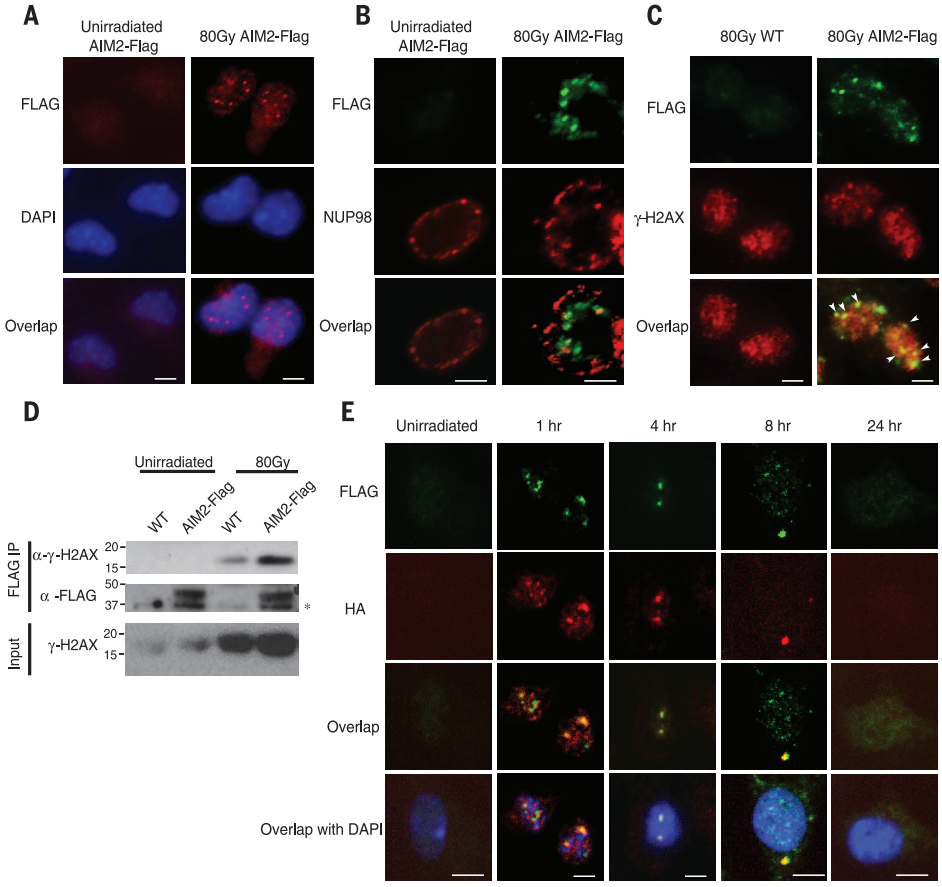

Fig. 4. Ionizing radiation induces the formation AIM2 specks in the nucleus. Primary macrophages from AIM2-Flag mice (**A** to **D**) or AIM2-Flag/ASC-HA double knockin mice (**E**) were left unirradiated or exposed to 80 Gy of ionizing radiation. For IF microscopy, cells were fixed at 4 hours [(A), (B), and (C)] or at indicated time points (E) after radiation. AIM2 was stained with antibody against Flag (anti-Flag) [red in (A); green in (B), (C), and (E)] and costained with nuclear envelope protein NUP98 [red, (B)] or gamma-H2AX [red, (C)] or ASC [using anti-HA, red, (E)]. Cell nuclei were visualized by DAPI (blue) in (A) and (E). Colocalization of AIM2-Flag specks and gamma-H2AX foci was indicated by white arrowheads in (C). Scale bars, 5 μm. Figures represent results from three independent experiments, and at least 100 cells were analyzed for each condition. (D) Coimmunoprecipitation (co-IP) of gamma-H2AX with AIM2-Flag in irradiated macrophages using anti-Flag M2 agarose beads. The immunoprecipitates (Flag IP) or the total lysates were analyzed by immunoblotting with antibodies against gamma-H2AX (Ser139) or the Flag tag. Samples from untagged WT mice were used as controls to determine the specificity of immunoblots. Nonspecific band is indicated with an asterisk. Data represent two independent experiments.

was detected by coimmunoprecipitation in irradiated cells (Fig. 4D). To further investigate the molecular mechanism of AIM2 inflammasome assembly, we also generated an ASC-HA knockin mouse to tag endogenous ASC protein with the human influenza hemagglutinin (HA) epitope using a similar strategy (fig. S5, G and H), and we crossed it to the AIM2-Flag mice to study the interaction between AIM2 and ASC. Notably, using AIM2-Flag/ASC-HA double knockin mice, we found that radiation induced AIM2 and ASC colocalization and speck formation in the nuclei after radiation exposure, and the speckles containing both AIM2 and ASC later accumulated in the perinuclear region (Fig. 4E). Together with the data showing robust caspase-1 processing in irradiated macrophages (Fig. 3C), these results provide strong evidence for the assembly and activation of an inflammasome in response to radiation. AIM2 was previously known as a cytoplasmic DNA sensor (*9*, *10*). Although its nuclear localization has been implicated in certain cell lines, the biological importance of nuclear AIM2 was not understood, and the subcellular distribution of endogenous AIM2 is unclear (*22*–*24*). Our results suggest that the recruitment of AIM2 to chromatin sites of radiation-induced DNA damage may be involved in mediating inflammasome activation and cell death.

Our present study demonstrates an unexpected role for AIM2 in sensing ionizing radiation–induced DNA damage in the nucleus. AIM2 acts thereby through the inflammasome pathway to trigger caspase-1–mediated cell death in intestinal epithelial cells and bone marrow cells. We show here that deficiency in the AIM2 inflammasome protects mice from radiation-induced small intestine syndrome as well as hematopoietic failure. Although the relative contribution of pyroptosis and other forms of cell death such as apoptosis to radiation-induced tissue damage merits further investigation, our findings may have important implications for development of therapy against radiation induced GI or hematopoietic toxicity. Drugs that block the activity of the AIM2 inflammasome may be effective in treating patients exposed to ionizing radiation, such as in radiation exposure via nuclear reactors or cancer patients suffering from hematopoietic or GI toxicity as a consequence of radiotherapy or chemotherapy.

REFERENCES AND NOTES

1. F. A. Mettler Jr., G. L. Voelz, *N. Engl. J. Med.* **346**, 1554–1561 (2002).
2. W. Qiu *et al.*, *Cell Stem Cell* **2**, 576–583 (2008).
3. D. G. Kirsch *et al.*, *Science* **327**, 593–596 (2010).
4. F. Paris *et al.*, *Science* **293**, 293–297 (2001).
5. M. Lamkanfi, V. M. Dixit, *Cell* **157**, 1013–1022 (2014).
6. T. Strowig, J. Henao-Mejia, E. Elinav, R. Flavell, *Nature* **481**, 278–286 (2012).
7. K. Kuida *et al.*, *Science* **267**, 2000–2003 (1995).
8. N. Kayagaki *et al.*, *Nature* **479**, 117–121 (2011).
9. T. Fernandes-Alnemri, J. W. Yu, P. Datta, J. Wu, E. S. Alnemri, *Nature* **458**, 509–513 (2009).
10. V. Hornung *et al.*, *Nature* **458**, 514–518 (2009).
11. E. A. Komarova, K. Christov, A. I. Faerman, A. V. Gudkov, *Oncogene* **19**, 3791–3798 (2000).
12. A. J. Merritt, T. D. Allen, C. S. Potten, J. A. Hickman, *Oncogene* **14**, 2759–2766 (1997).
13. A. J. Merritt *et al.*, *Cancer Res.* **54**, 614–617 (1994).
14. J. E. Wilson *et al.*, *Nat. Med.* **21**, 906–913 (2015).
15. S. M. Man *et al.*, *Cell* **162**, 45–58 (2015).
16. C. Booth, G. Tudor, J. Tudor, B. P. Katz, T. J. MacVittie, *Health Phys.* **103**, 383–399 (2012).
17. E. Elinav *et al.*, *Cell* **145**, 745–757 (2011).
18. S. Hu *et al.*, *Cell Reports* **13**, 1922–1936 (2015).
19. M. E. Berger, D. M. Christensen, P. C. Lowry, O. W. Jones, A. L. Wiley, *Occup. Med. (Lond.)* **56**, 162–172 (2006).
20. J. K. Waselenko *et al.*, *Ann. Intern. Med.* **140**, 1037–1051 (2004).
21. V. M. Stoecklein *et al.*, *J. Immunol.* **194**, 1178–1189 (2015).
22. K. S. Cresswell *et al.*, *Biochem. Biophys. Res. Commun.* **326**, 417–424 (2005).
23. B. A. Diner *et al.*, *Mol. Syst. Biol.* **11**, 787 (2015).
24. N. Kerur *et al.*, *Cell Host Microbe* **9**, 363–375 (2011).

ACKNOWLEDGMENTS

We thank V. M. Dixit, N. Kayagaki, and E. S. Alnemri for sharing materials and reagents, and V. A. Rathinam for technical advice. We thank P. Bongiorni for assistance with radiation experiments. The data presented in this manuscript are tabulated in the main paper and in the supplementary materials. H.-B.L. is supported by NIH T32 2T32DK007356. This work was supported by the Howard Hughes Medical Institute (R.A.F.).

SUPPLEMENTARY MATERIALS

www.sciencemag.org/content/354/6313/765/suppl/DC1
Materials and Methods
Figs. S1 to S5
References (*25*–*35*)

28 March 2016; accepted 16 September 2016
10.1126/science.aaf7532

ENHANCER FUNCTION

Systematic mapping of functional enhancer–promoter connections with CRISPR interference

Charles P. Fulco,[1,2] Mathias Munschauer,[1] Rockwell Anyoha,[1] Glen Munson,[1] Sharon R. Grossman,[1,3,4] Elizabeth M. Perez,[1] Michael Kane,[1] Brian Cleary,[1,5] Eric S. Lander,[1,2,4]*† Jesse M. Engreitz[1]*†

Gene expression in mammals is regulated by noncoding elements that can affect physiology and disease, yet the functions and target genes of most noncoding elements remain unknown. We present a high-throughput approach that uses clustered regularly interspaced short palindromic repeats (CRISPR) interference (CRISPRi) to discover regulatory elements and identify their target genes. We assess >1 megabase of sequence in the vicinity of two essential transcription factors, *MYC* and *GATA1*, and identify nine distal enhancers that control gene expression and cellular proliferation. Quantitative features of chromatin state and chromosome conformation distinguish the seven enhancers that regulate *MYC* from other elements that do not, suggesting a strategy for predicting enhancer–promoter connectivity. This CRISPRi-based approach can be applied to dissect transcriptional networks and interpret the contributions of noncoding genetic variation to human disease.

A fundamental goal in modern biology is to identify and characterize the noncoding regulatory elements that control gene expression in development and disease, yet we have lacked systematic approaches to do so. Studies of individual regulatory elements have revealed principles of their function, such as the ability of enhancers to recruit activating transcription factors, modify chromatin state, and physically interact with target genes (*1*, *2*). From these insights, systematic mapping of chromatin state and chromosome conformation across cell types has been used to identify putative regulatory elements (*3*–*6*). However, these measurements do not determine which (if any) genes are regulated or assess the quantitative effects on gene expression. Indeed, the rules that connect regulatory elements with their target genes in the genome appear to be complex. Regulatory elements do not necessarily affect the closest gene, but instead may act across long distances (*7*, *8*). It remains unclear how many regulatory elements control any given gene, or how many genes are regulated by any given element (*2*, *3*, *8*).

We developed a high-throughput approach that uses the programmable properties of clustered regularly interspaced short palindromic repeats (CRISPR)–Cas9 to characterize the regulatory functions of noncoding elements in their native contexts. We use pooled CRISPR screens in combination with CRISPR interference (CRISPRi)—which alters chromatin state at targeted loci through recruitment of a KRAB effector domain fused to catalytically dead Cas9 (dCas9) (*9*–*12*)—to simultaneously characterize the regulatory effects of up to 1 megabase (Mb) of sequence on a gene of interest (Fig. 1A) (*13*).

We studied two gene loci, *GATA1* and *MYC*, that affect proliferation of K562 erythroleukemia cells in a dose-dependent manner (fig. S1). This allowed us to search for regulatory elements that quantitatively tune *GATA1* or *MYC* expression using a proliferation-based pooled assay (Fig. 1A). *GATA1* and *MYC* are not located near other strongly essential genes (fig. S1); thus, proliferation defects caused by single guide RNAs (sgRNAs) targeted to sequences near these genes can be attributed to elements regulating *GATA1* or *MYC*. We designed a library containing 98,000 sgRNAs tiling across a total of 1.29 Mb of genomic sequence around *GATA1* and *MYC*, as well as 85 kb of control noncoding regions (*13*). We infected K562 cells expressing KRAB-dCas9 under a doxycycline-inducible promoter with a lentiviral sgRNA library and sequenced the representation of sgRNAs before and after growing cells in doxycycline for 14 population doublings (Fig. 1A). As expected, internal control sgRNAs targeting the promoters of known essential genes (*10*) were depleted (fig. S2A) and correlated across biological replicates (Pearson's $R = 0.91$, fig. S2B).

We examined the quantitative depletion of sgRNAs in a 74-kb region surrounding *GATA1*, which encodes a key erythroid transcription factor (Fig. 1B). Because the efficiency of different sgRNAs for CRISPRi can vary markedly (*10*), we used a sliding window approach, averaging the scores of 20 consecutive sgRNAs and assessing the false discovery rate (FDR) of this metric through comparison to negative control, nonessential regions (*13*) (fig. S3). Because the average spacing between consecutive sgRNAs was 16 base pairs (bp), the regions targeted by 20 consecutive sgRNAs spanned an average of 314 bp (fig. S3, C and D). With this approach, the window with the highest score (strongest depletion) overlapped the *GATA1* transcription start site (TSS) itself (Fig. 1B and fig. S3F). In addition, we identified three distal elements that significantly affected cellular proliferation (FDR < 0.05, Fig. 1B) (*13*). One such element (e-GATA1) is located ~3.6 kb upstream of *GATA1* and corresponds to a deoxyribonuclease I (DNase I) hypersensitive site (DHS) marked by acetylation of histone 3 at lysine-27 (H3K27ac) (Fig. 1C); notably, this element shows high sequence conservation among vertebrates, and the syntenic sequence in mouse is required for proper *Gata1* expression in murine erythroid progenitor cells (*14*). The second distal element (e-HDAC6) corresponds to a conserved DHS located ~1.5 kb upstream of *HDAC6* (Fig. 1C). The third significant element is located at a DHS near the promoter of *GLOD5*, which itself is not essential and only weakly expressed in K562 cells. The first two elements overlap GATA1 chromatin immunoprecipitation–sequencing (ChIP-seq) peaks and sequence motifs (Fig. 1C), consistent with known autoregulatory loops in which GATA1 activates its own expression (*15*). All three elements reside in close linear and spatial proximity to GATA1 (fig. S4A). Finally, multiple regions in the gene body of *GATA1* scored as significantly depleted in the screen (Fig. 1B), but, because recruitment of KRAB-dCas9 to these sites may directly interfere with transcription (*9*), we focused on distal regulatory elements in subsequent analysis.

To characterize these elements, we measured *GATA1* expression using quantitative PCR (qPCR) in cell lines stably expressing individual sgRNAs (*13*). As expected, targeting KRAB-dCas9 to the *GATA1* TSS reduced *GATA1* expression (76% reduction, Fig. 1D). sgRNAs targeting e-GATA1 or e-HDAC6 reduced *GATA1* expression by 44 and 33%, respectively (Fig. 1D), and affected the expression of genes known to be regulated by the GATA1 transcription factor (fig. S4B), confirming that these enhancers regulate *GATA1*. By contrast, sgRNAs targeting the *HDAC6* TSS did not reduce *GATA1* expression despite reducing *HDAC6* expression (Fig. 1D), indicating that (i) the pooled screen accurately predicted that this region does not reduce *GATA1* expression and (ii) the effects seen for the e-GATA1 and e-HDAC6 sgRNAs are not due to general effects of targeting KRAB-dCas9 to the gene neighborhood. Additionally, both e-GATA1 and e-HDAC6 can activate the expression of a plasmid-based reporter gene (fig. S4C) (*13*). Together, these results support the specificity of this CRISPRi-based approach and demonstrate that e-GATA1 and e-HDAC6 quantitatively control *GATA1* expression in K562 cells.

Considering the close proximity of *GATA1* to *HDAC6* (Fig. 1B and fig. S4A), we tested whether this pair of enhancers also regulates *HDAC6*. sgRNAs targeting e-GATA1 and e-HDAC6 reduced *HDAC6*

[1]Broad Institute of MIT and Harvard, Cambridge, MA 02142, USA. [2]Department of Systems Biology, Harvard Medical School, Boston, MA 02115, USA. [3]Division of Health Sciences and Technology, Massachusetts Institute of Technology (MIT), Cambridge, MA 02139, USA. [4]Department of Biology, MIT, Cambridge, MA 02139, USA. [5]Computational and Systems Biology Program, MIT, Cambridge, MA 02139, USA. *These authors contributed equally to this work. †Corresponding author. Email: engreitz@broadinstitute.org (J.M.E.); lander@broadinstitute.org (E.S.L.)

expression by 42 and 22%, respectively, comparable to their effects on *GATA1* (Fig. 1D). Intriguingly, inhibition of the *GATA1* promoter led to an increase in *HDAC6* expression (+47%, Fig. 1D), and inhibition of the *HDAC6* promoter modestly activated *GATA1* (+9%, Fig. 1D); this suggests that *GATA1* and *HDAC6* may compete for these shared enhancers, similar to observations for other pairs of neighboring genes (*16*, *17*). Histone deacetylases are required for erythropoiesis (*18*), and HDAC6 has been implicated in cellular proliferation in multiple cancers (*19*). Thus, although HDAC6 does not score as essential in proliferation assays in K562 cells, it is possible that proliferative defects observed upon inhibition of e-GATA1 or e-HDAC6 result from the combined effects on both *GATA1* and *HDAC6* expression (*13*), and the genomic proximity of these genes may be important for coordinating their expression in vivo. These observations indicate a complex connectivity between enhancers and promoters in their native genomic contexts (fig. S4D).

We next investigated the cis-regulatory architecture of *MYC*, a critical transcription factor encoded within a 3-Mb topological domain that contains hundreds of putative enhancers. Several enhancers in this domain are known to regulate *MYC* in other cell types (*13*), but chromatin state varies markedly across cell types, and it is unclear which of these elements regulate *MYC* in a given cell type. Notably, the domain contains more than 60 genetic haplotypes associated (through genome-wide association studies) with human phenotypes, including cancer susceptibility (*20*).

To identify elements that regulate *MYC* in K562 cells, we tiled sgRNAs across ~1.2 Mb of sequence in this topological domain (Fig. 2A). A sliding window analysis identified several regions whose inhibition reproducibly reduced cellular proliferation, including a known promoter-proximal element located 2 kb upstream of the *MYC* TSS (fig. S5A) (*21*), the transcribed region of the *MYC* gene body (fig. S5A), and seven distal regions (labeled e1 through e7) located between 0.16 and 1.9 Mb downstream of *MYC* (Fig. 2A and fig. S5, B and C). We also identified two regions that significantly increased cell proliferation (r1 and r2), and thus may repress *MYC* expression (Fig. 2A and fig. S5, D and E) (*13*).

Each of the seven putative activating elements is marked by high levels of DNase I hypersensitivity (Fig. 2A), is bound by multiple transcription factors (fig. S6A), and shows patches of sequence conservation across mammals (Fig. 2B). Each

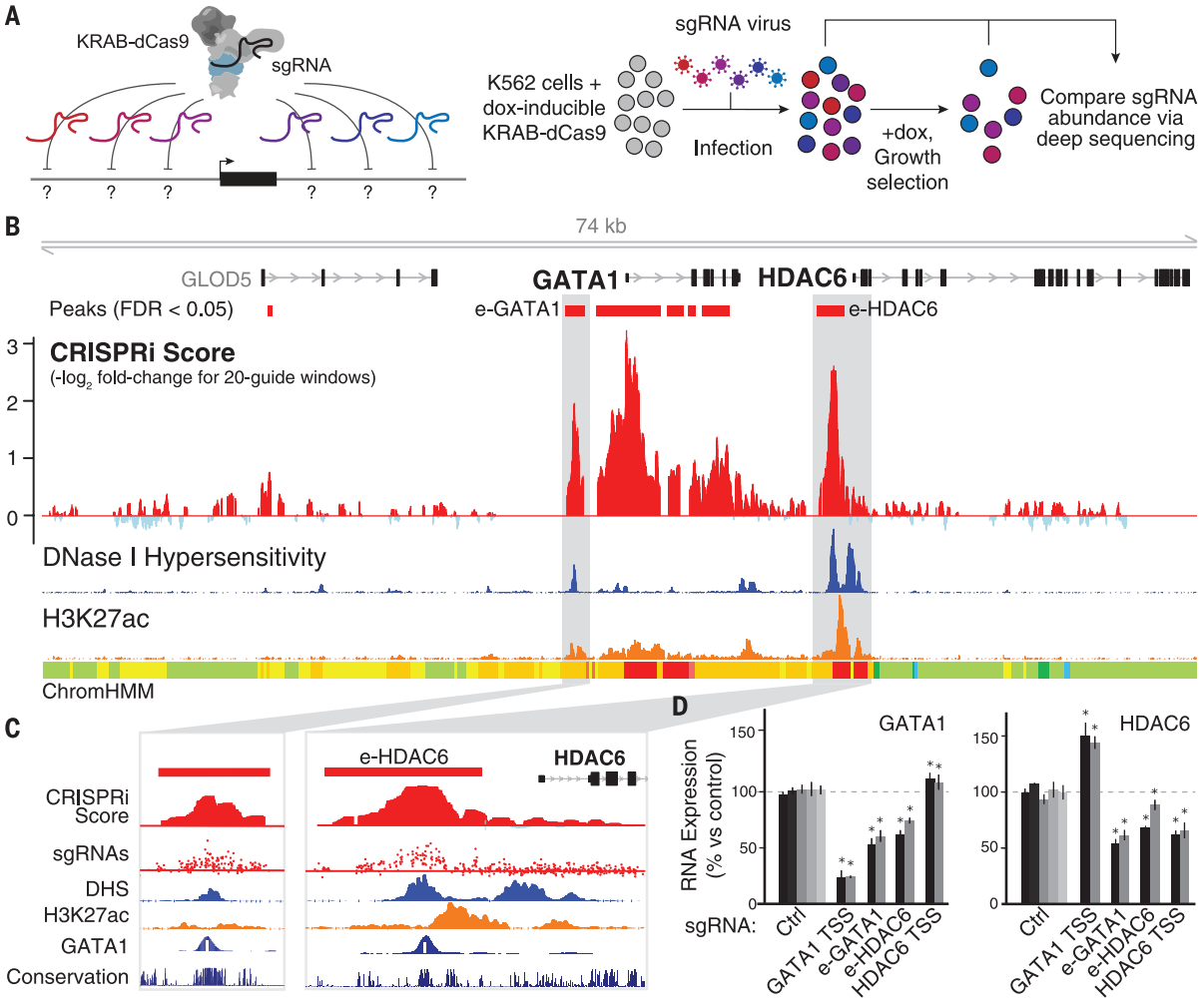

Fig. 1. Systematic mapping of noncoding elements that regulate *GATA1*. (**A**) CRISPRi method for identifying gene regulatory elements. Cells expressing KRAB-dCas9 from a dox-inducible promoter are infected with a pool of single guide RNAs (sgRNAs) targeting every possible site across a region of interest. In a proliferation-based screen, cells expressing sgRNAs that target essential regulatory elements are depleted in the final population. (**B**) CRISPRi screen results in the *GATA1* locus. A high CRISPRi score indicates strong depletion over the course of the screen. Red boxes: windows showing significant depletion compared to negative control sgRNAs (*13*). DNase I hypersensitivity, H3K27ac ChIP-seq, and histone modification annotations (ChromHMM) in K562 cells are from ENCODE (*4*). (**C**) Close-up of e-GATA1 and e-HDAC6. sgRNA track shows CRISPRi scores for each individual sgRNA in the region. White bar in GATA1 ChIP-seq track represents the GATA1 motif. (**D**) qPCR for GATA1 and HDAC6 mRNA in cells expressing individual sgRNAs. KRAB-dCas9 expression was activated for 24 hours before measurement. Gray bars: different sgRNAs for each target. Ctrl: negative control sgRNAs without a genomic target. Error bars: 95% confidence intervals (CI) for the mean of 3 biological replicates (*13*). *$P < 0.05$ in *t* test versus Ctrl.

enhancer frequently contacts the *MYC* promoter in three dimensions as assayed by Hi-C and chromatin interaction analysis with paired-end-tag sequencing (ChIA-PET) in K562 cells (Fig. 2A) (*3*, *6*); elements e5 and e6/7 form very long-range (>1.8 Mb) loops to the *MYC* promoter and are located within 10 kb of CCCTC-binding factor (CTCF) ChIP-seq peaks with motifs oriented toward *MYC* (fig. S5, B and C), consistent with the convergent rule for CTCF-mediated chromatin loops (*6*). Two elements (e3 and e4) correspond to alternative TSSs for the long noncoding RNA plasmacytoma variant translocation 1 (PVT1) (Fig. 2A); knockdown experiments indicate that the mature PVT1 RNA transcript itself is likely not

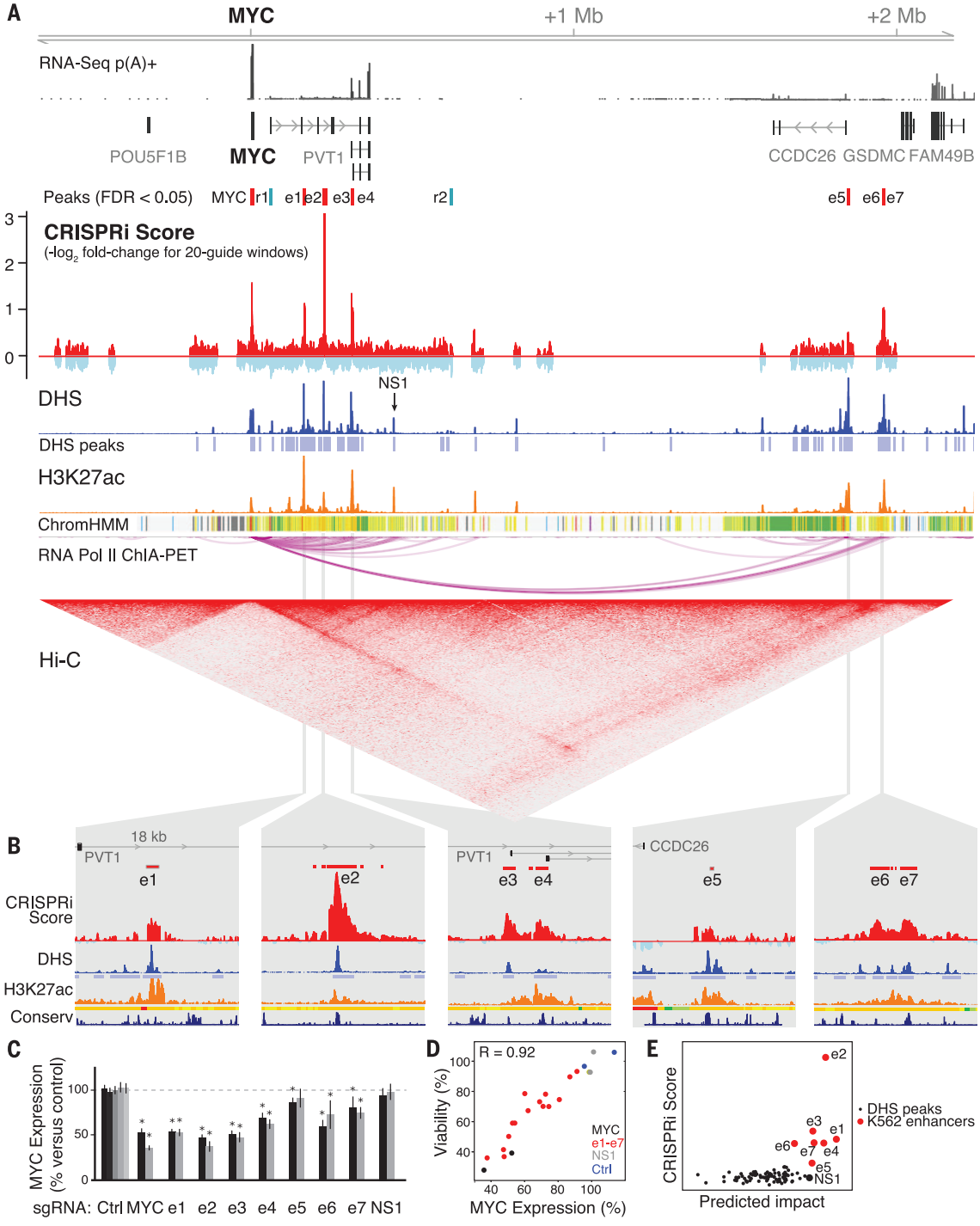

Fig. 2. Identification and prediction of elements that regulate *MYC*. (**A**) CRISPRi screening identifies seven distal enhancers (e1 to e7) that activate *MYC* and two repressive elements (r1, r2) that may act to repress *MYC*. NS1: an element that does not score in the screen. (**B**) Shown are 18-kb windows around each of the seven distal enhancers. *Y*-axis scales are equivalent between panels. (**C**) qPCR for MYC mRNA in cells expressing individual sgRNAs 24 hours after KRAB-dCas9 activation. Gray bars: two different sgRNAs per target, or five for nontargeting controls (Ctrl). Error bars: 95% CI for the mean of 12 biological replicates (*13*). *$P < 0.05$ in *t* test versus Ctrl. (**D**) Correlation between MYC expression and relative cell viability for e1 to e7, MYC TSS, NS1, and Ctrl sgRNAs (*13*). Pearson's $R = 0.92$ includes e1 to e7 sgRNAs only; with the others, $R = 0.95$. (**E**) Predicted impact of DHS elements on MYC expression (a function of quantitative DHS, H3K27ac, and Hi-C signal) versus their experimentally derived CRISPRi scores (*13*).

essential in K562 cells (fig. S1), and so e3 and e4 likely affect cellular proliferation through direct regulation of *MYC* (*13*).

We experimentally characterized these seven activating elements to test whether they regulate *MYC*. CRISPRi inhibition of each of these elements with individual sgRNAs led to proliferation defects in a competitive growth assay (fig. S6B) and resulted in a 9 to 62% reduction in *MYC* expression (Fig. 2C). The magnitude of the change in gene expression correlated with the proliferation defect, consistent with a quantitative relationship between cell growth and precise *MYC* expression levels (Pearson's R = 0.92, Fig. 2D). In a plasmid-based reporter assay, each putative regulatory element led to >5-fold up-regulation of a reporter gene relative to a control sequence (fig. S6C) (*13*). For a subset of the elements (e2, e3, and e4), we generated clonal cell lines containing genetic deletions on one or two of the three chromosome 8 alleles (K562 cells are triploid) and measured the expression of *MYC* from each allele (*13*). For each element, we found that genetic deletions reduced *MYC* expression from the corresponding allele(s), confirming our CRISPRi results (fig. S7). Together, these data support the hypothesis that these seven elements, spanning 1.6 Mb of noncoding sequence, act as enhancers to control *MYC* expression and cellular proliferation.

In addition to e1 to e7, we characterized one noncoding element (NS1) that did not score in the screen (Fig. 2A). In K562 cells, NS1 displays strong DHS and H3K27ac occupancy, binds to multiple transcription factors (fig. S6A), and participates in a long-range chromatin loop to the

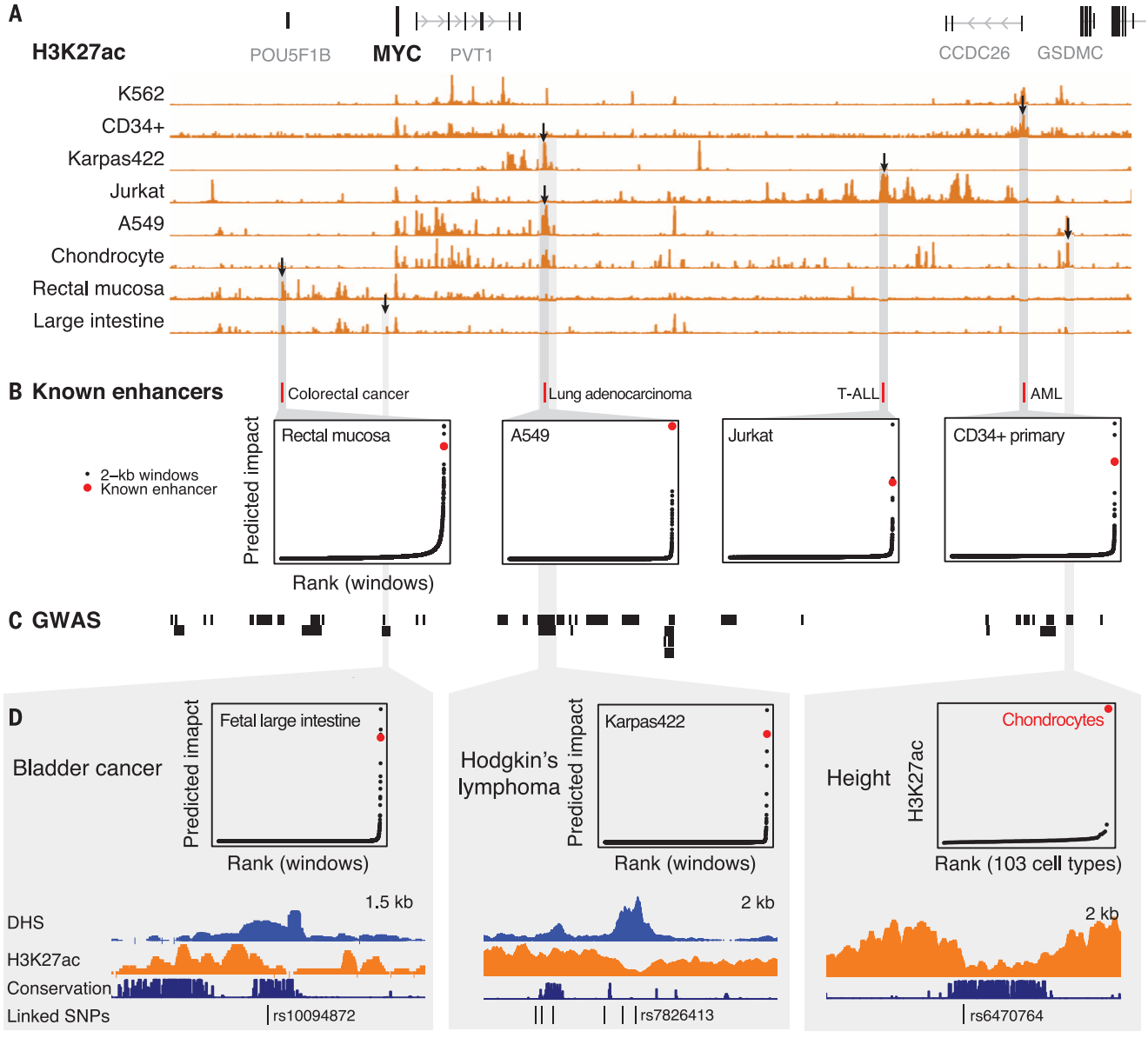

Fig. 3. A heuristic model predicts disease-associated *MYC* enhancers across cell types. (**A**) H3K27ac occupancy around *MYC* varies among eight cell types and primary tissues. Black arrows: elements highlighted in panels below. (**B**) Locations of four enhancers previously shown to regulate MYC expression in other cell types and their predicted impact in a corresponding cell type. Points show predicted impact of 2-kb windows tiled in 100-bp increments across the *MYC* locus (*13*). T-ALL, T-cell acute lymphoblastic leukemia; AML, acute myeloid leukemia. For each cell type, predicted impact is calculated on the basis of available data (*13*). (**C**) Haplotype blocks of SNPs linked to human diseases and phenotypes (R^2 > 0.8 with index SNP in genome-wide association study). (**D**) SNPs associated with bladder cancer and Hodgkin's lymphoma overlap regulatory elements predicted by our metric to regulate *MYC* in a corresponding cell type or tissue. A SNP associated with height overlaps a conserved element that is active only in chondrocytes. Karpas422, diffuse large B cell lymphoma cell line.

MYC promoter (Fig. 2A). In a lung adenocarcinoma cell line, NS1 regulates *MYC* as assayed by CRISPRi inhibition with individual sgRNAs (*22*). Accordingly, we wondered whether NS1 regulates *MYC* in K562 cells despite not being detected as such in our CRISPRi screen. To explore this possibility, we targeted KRAB-dCas9 to NS1 with individual sgRNAs in K562 cells and found that CRISPRi successfully reduced H3K27ac occupancy to an extent similar to that observed when targeting other *MYC* enhancers (fig. S6D). Despite affecting chromatin state at NS1 in K562 cells, these sgRNAs did not substantially affect cellular proliferation or *MYC* expression (Fig. 2, C and D), consistent with the results from the pooled screen. These observations support the ability of the CRISPRi screening approach to distinguish elements that do and do not regulate a given gene. However, we note that some regulatory elements, such as those that act redundantly with others in the locus, may not be discoverable by this method (*13*).

The ability to systematically test gene regulatory elements will help to train predictive models of functional enhancer-promoter connectivity. Notably, existing annotations and catalogs of enhancer-promoter predictions performed poorly at distinguishing e1 to e7 from enhancers that do not affect *MYC* expression (*13*). For example, ENCODE annotates 185 kb of sequence in this domain as putative "strong enhancer" in K562 cells (Fig. 2A), but only 8% of this sequence, corresponding to e1 to e7, appears to regulate *MYC*. We sought to improve the ability to predict enhancers and connect them with genes that they regulate. When we examined chromatin state maps (including DHS, H3K27ac, and Hi-C), we found that quantitative DHS or H3K27ac signal could distinguish most of the seven *MYC* enhancers but ranked them in the wrong order (fig. S8A): for example, e5 shows the strongest DHS signal, yet has the weakest effect on MYC expression (Fig. 2). Accordingly, we considered a framework (fig. S8B) wherein the impact of an enhancer on gene expression is determined both by its intrinsic activity level (for which we use quantitative DHS and H3K27ac levels as a proxy) and the frequency at which the enhancer contacts its target promoter (for which we use Hi-C data as a proxy) (*13*). This metric correctly ranked six of the seven distal enhancers as the most important of 93 DHS elements in K562 cells (Fig. 2E) and provided a reasonable ordering of their relative effects (Spearman correlation = 0.79). This approach did not perfectly distinguish between enhancers that do and do not regulate MYC: NS1 was ranked 7th and e6 was ranked 11th. Nonetheless, quantitative measures of chromatin state and chromosome conformation are strongly predictive of enhancers that regulate *MYC* in K562 cells.

To determine whether this approach might be applicable in other cellular contexts, we examined four *MYC* enhancers identified in other cell types (Fig. 3, A and B) (*13*). In each case, our metric ranked these known elements among the three most important in the corresponding cell type (Fig. 3B). We also identified multiple instances where elements predicted to regulate *MYC* in one or more cell types harbor single-nucleotide polymorphisms (SNPs) associated with human traits including cancer susceptibility and height (Fig. 3, C and D, and table S1). Additional CRISPRi-based functional mapping in other cell types and gene loci might allow the derivation of general models to predict functional enhancer–promoter connections and help to elucidate noncoding genetic variation.

In summary, CRISPRi screens can accurately identify and characterize the regulatory functions and connectivity of noncoding elements. In the *MYC* and *GATA1* loci, CRISPRi reveals complex and nonobvious dependencies between multiple genes and enhancers, including relationships that suggest regulation of multiple genes by the same enhancer, coordinated activity of multiple enhancers to control a single gene, and competition between neighboring promoters. Thus, learning the principles and connectivity of transcriptional networks requires dissecting putative regulatory elements in their native genomic contexts.

Although we used cellular proliferation as a readout to investigate two essential genes, this CRISPRi approach can be applied to identify regulatory elements that control an arbitrary gene or phenotype of interest through alternative assays—for example, by tagging an endogenous gene locus with green fluorescent protein (GFP) and sorting cells by GFP expression (*23*).

Together with complementary methods using catalytically active Cas9 (*13*, *23*–*25*), CRISPRi-based functional mapping provides a broadly applicable approach (*13*) to dissect transcriptional networks and interpret the contributions of noncoding genetic variation in gene regulatory elements to human disease.

REFERENCES AND NOTES

1. M. Bulger, M. Groudine, *Cell* **144**, 327–339 (2011).
2. F. Spitz, E. E. M. Furlong, *Nat. Rev. Genet.* **13**, 613–626 (2012).
3. G. Li *et al.*, *Cell* **148**, 84–98 (2012).
4. I. Dunham *et al.*, *Nature* **489**, 57–74 (2012).
5. A. Kundaje *et al.*, *Nature* **518**, 317–330 (2015).
6. S. S. P. Rao *et al.*, *Cell* **159**, 1665–1680 (2014).
7. D. Shlyueva, G. Stampfel, A. Stark, *Nat. Rev. Genet.* **15**, 272–286 (2014).
8. J. van Arensbergen, B. van Steensel, H. J. Bussemaker, *Trends Cell Biol.* **24**, 695–702 (2014).
9. L. A. Gilbert *et al.*, *Cell* **154**, 442–451 (2013).
10. L. A. Gilbert *et al.*, *Cell* **159**, 647–661 (2014).
11. N. A. Kearns *et al.*, *Development* **141**, 219–223 (2014).
12. P. I. Thakore *et al.*, *Nat. Methods* **12**, 1143–1149 (2015).
13. See supplementary materials on *Science* Online.
14. M. Suzuki, T. Moriguchi, K. Ohneda, M. Yamamoto, *Mol. Cell. Biol.* **29**, 1163–1175 (2009).
15. S. Nishimura *et al.*, *Mol. Cell. Biol.* **20**, 713–723 (2000).
16. O. R. Choi, J. D. Engel, *Cell* **55**, 17–26 (1988).
17. S. Ohtsuki, M. Levine, H. N. Cai, *Genes Dev.* **12**, 547–556 (1998).
18. A. Fujieda *et al.*, *Int. J. Oncol.* **27**, 743–748 (2005).
19. K. J. Falkenberg, R. W. Johnstone, *Nat. Rev. Drug Discov.* **14**, 219 (2015).
20. T. Burdett *et al.*, The NHGRI-EBI Catalog of published genome-wide association studies; www.ebi.ac.uk/gwas.
21. W. M. Gombert, A. Krumm, *PLOS ONE* **4**, e6109 (2009).
22. X. Zhang *et al.*, *Nat. Genet.* **48**, 176–182 (2016).
23. N. Rajagopal *et al.*, *Nat. Biotechnol.* **34**, 167–174 (2016).
24. M. C. Canver *et al.*, *Nature* **527**, 192–197 (2015).
25. G. Korkmaz *et al.*, *Nat. Biotechnol.* **34**, 192–198 (2016).

ACKNOWLEDGMENTS

We thank T. Wang and R. Issner for technical advice and reagents; and R. Ryan, B. Bernstein, N. Sanjana, J. Wright, and F. Zhang for discussions. This work was supported by funds from the Broad Institute (E.S.L.). C.P.F. is supported by the National Defense Science and Engineering Graduate Fellowship. J.M.E. is supported by the Fannie and John Hertz Foundation. M.M. is supported by a Deutsche Forschungsgemeinschaft Research Fellowship. S.R.G. is supported by National Institute of General Medical Sciences grant T32GM007753. The Broad Institute, which E.S.L. directs, holds patents and has filed patent applications on technologies related to other aspects of CRISPR. J.M.E., C.P.F., and E.S.L. are inventors on a patent application filed by the Broad Institute related to this work (U.S. no. 62/401,149). Data presented in this paper can be found in the supplementary materials and in GEO Accession GSE87257. J.M.E. conceived the study. J.M.E., C.P.F., M.M., and S.R.G. designed experiments. C.P.F., M.M., R.A., G.M., E.M.P., M.K., and J.M.E. performed experiments. C.P.F., J.M.E., and B.C. analyzed data. C.P.F., J.M.E., and E.S.L. wrote the manuscript with input from all authors.

SUPPLEMENTARY MATERIALS

www.sciencemag.org/content/354/6313/769/suppl/DC1
Materials and Methods
Supplementary Text
Figs. S1 to S9
Tables S1 to S3
References (*26*–*83*)

29 May 2016; accepted 21 September 2016
Published online 29 September 2016
10.1126/science.aag2445

sCMOS Microscope Camera

The Leica DFC9000, a monochrome microscope camera with a highly sensitive, third-generation scientific complementary metal-oxide semiconductor (sCMOS) sensor, enables researchers to image live cells under near-native conditions, and allows them to gain a better understanding of cellular processes and dynamics. The camera features an sCMOS sensor with superior quantum efficiency over the entire spectrum of light, which provides a high signal-to-noise ratio to securely detect even faint signals. A crisp fluorescence signal against a dark background is the end product—an effect very much desired in high-end fluorescence live-cell imaging. The sensitivity of the camera eliminates the need to monitor green fluorescent protein (GFP)-overexpressing specimens and protects cells from phototoxicity. The camera acquires full-frame images at a standard rate of 50 frames per second (fps) in the USB 3.0 interface version and at 90 fps with the Camera Link interface version. Researchers will not miss any fast cellular processes.

Leica Microsystems
For info: 800-248-0123
www.leica-microsystems.com

Translation Stages

A new line of XR-Series cross-roller bearing, aluminum-bodied translation stages is now available, including both rear- and side-actuated 1-in. travel stages and all components needed for left- or right-handed X, XY, XZ, YZ, and XYZ configurations. A dovetail feature is incorporated into the design for stacking; it could also be used to provide custom mounting options. When stacking two stages, coarse positional alignment in the axis perpendicular to stage travel is achieved by sliding the dovetail along the mating dovetail prior to lockdown. These products provide less than 150 microradians of angular deviation in pitch and yaw, with easy conversion between the two options, and deep and blind ¼ in.-20 (M6) tapped holes on the moving world. A 2-in. travel option is also available.

Thorlabs
For info: 973-300-3000
www.thorlabs.com

Biomolecular Imager

Amersham Typhoon biomolecular imagers are the next generation of Typhoon FLA scanners from GE Healthcare Life Sciences. Four instruments in one, these imagers offer versatility and precise quantitation of fluorescent, color-stained, and radiolabeled biomolecules such as proteins and nucleic acids. Featuring sensitive detection down to 3 picograms of protein, Typhoon delivers a combination of phosphor imaging, RGB fluorescence, near-infrared fluorescence, and optical density measurement in a single instrument. Its five-laser configuration option and advanced photomultiplier tubes offer a greater degree of fluorescent multiplexed detection, and its broad linear dynamic range provides the enhanced sensitivity and accuracy required to detect subtle differences in protein levels. Phosphor imaging allows for radiolabeled target detection with high sensitivity. Typhoon can image gels, membranes, multiwell plates, dishes, and tissue sections, and its modular configuration allows stages, detectors, and filters to be selected and updated as required.

GE Healthcare Life Sciences
For info: 800-526-3593
http://gelifesciences.com/Typhoon

Superresolution Microscopy Cubes

Commercially available microscope cubes with guaranteed λ/2 peak-to-valley (PV) per-inch flatness for super-resolution microscopy are now available. Conventional microscopy cubes can significantly compromise the flatness of the dichroic beamsplitters, thereby introducing aberrations. These cubes maximize signal-to-noise ratio and minimize artifacts in TIRF, confocal, PALM, STORM, SIM, and other superresolution techniques. Offered at attractive pricing, the assembled cubes are compatible with popular microscopes. Utilizing a 1-mm thick dichroic beamsplitter in the light path minimizes beam deviation, reduces light scatter in the emission path, and enables faster switching speed between different cubes. The beamsplitters are designed to minimize reflected wavefront distortion for even large-diameter illumination beams, and are readily available for the most popular microscopy cubes (e.g., Olympus U-MF2 and U-FF, Zeiss FL Cube EC P&C, and Nikon TE2000).

Semrock
For info: 866-736-7625
www.semrock.com

Filter Wheel

Filtering of excitation and emission light is vital in fluorescence microscopy. The HF110A/32 filter wheel offers a way to quickly and precisely change the wavelengths of light a sample is exposed to. It holds 10 32-mm diameter filters and fits on the excitation ports of a range of popular microscopes from manufacturers including Leica, Nikon, Olympus, and Zeiss. The filter wheel takes less than 95 milliseconds to move between adjacent positions—ideal for multifluorophore applications in which rapid imaging is essential. Both filter wheels and shutters can be easily controlled using the Prior Scientific ProScan III control system, which is compatible with a wide range of imaging software packages. The end user can therefore control all aspects of their microscope system from a single point, allowing precise coordination of illumination, stage movement, focus movement, shutter and filter wheel operation, and image capturing.

Prior Scientific
For info: +44-(0)-1223-881711
www.prior.com

Electronically submit your new product description or product literature information! Go to www.sciencemag.org/about/new-products-section for more information.

Newly offered instrumentation, apparatus, and laboratory materials of interest to researchers in all disciplines in academic, industrial, and governmental organizations are featured in this space. Emphasis is given to purpose, chief characteristics, and availability of products and materials. Endorsement by *Science* or AAAS of any products or materials mentioned is not implied. Additional information may be obtained from the manufacturer or supplier.

NEW ENGLAND BioLabs® Inc.

Migrate to Monarch®.

Environmentally-friendly Nucleic Acid Purification Kits from New England Biolabs

Want to feel good about your choice in DNA purification? With our fast and reliable Monarch Nucleic Acid Purification Kits, you can achieve optimal purification while creating less waste. Available for plasmid minipreps, DNA gel extraction and enzymatic cleanup (including PCR), our products use up to 44% less plastic and are packaged using responsibly-sourced, recyclable materials. Make the change and migrate to Monarch today.

> *These kits might be the best I have used for the price. The best part is that it uses less plastic for production!! Thank you for caring about our environmental impacts, NEB!!!*
>
> – NEB customer

Request your free sample at **www.NEBMonarch.com**

eppendorf

Eppendorf Consumables –
it´s your sample

Impress Yourself

Eppendorf Cell Culture Consumables
Proven Eppendorf quality brought to a new level. Premium in all aspects: Product, Performance and Packaging according to highest Eppendorf standards.

Find more information about our outstanding quality as a result of experience and constant development on www.eppendorf.com/ccc

www.eppendorf.com/consumables

Watch Video!

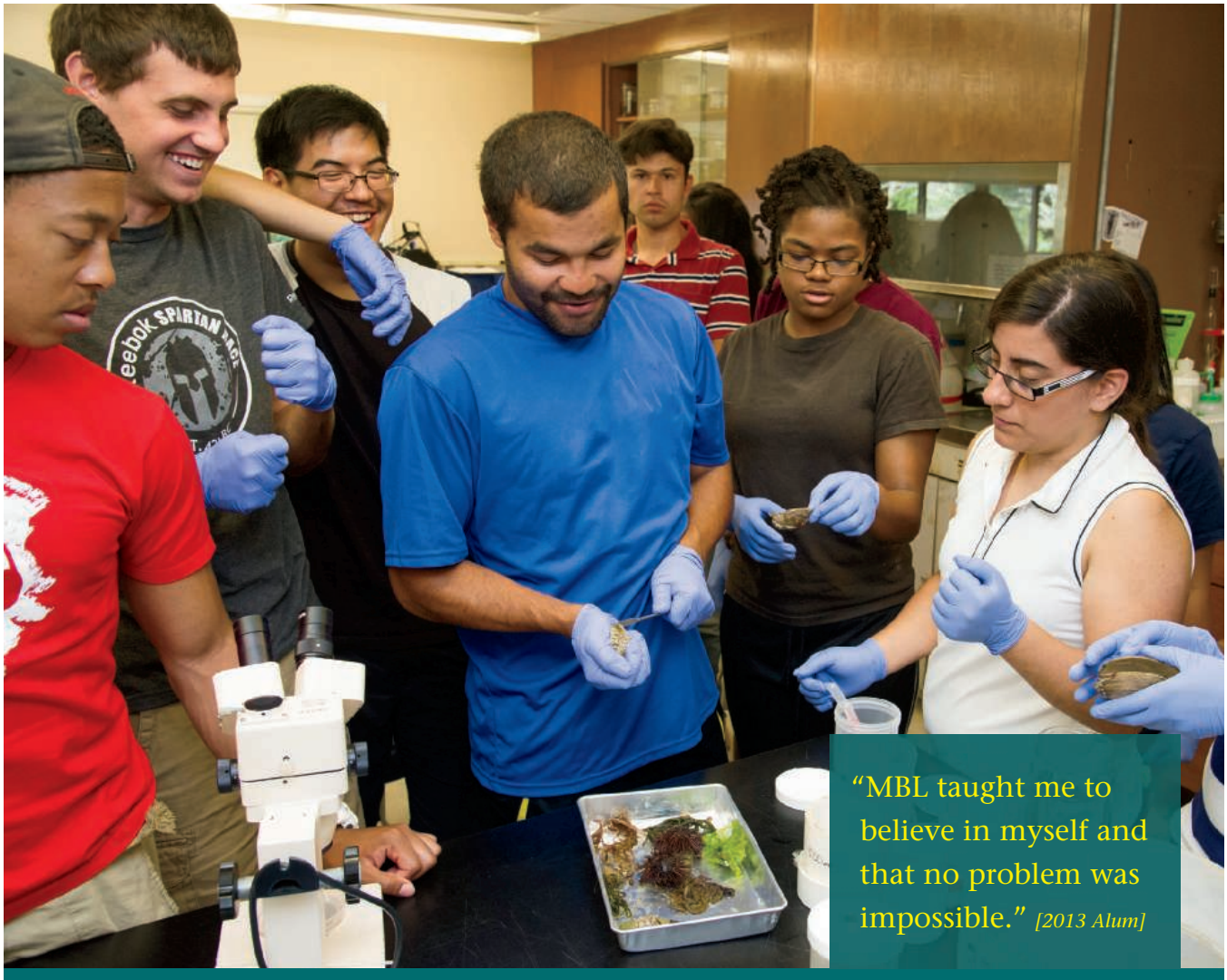

2017 Advanced Research Training Courses

on Cape Cod in Woods Hole, MA

Investigate contemporary research problems and learn cutting-edge approaches from an internationally renowned faculty.

Each year, MBL courses attract a diverse population of over 500 of the best and brightest students in the world, from more than 300 institutions and over 30 countries. Applicants must be in training for, or possess, a PhD or equivalent degree.

Discovery Courses are 6-8 week full immersion courses for those who seek advanced, hands-on training in pioneering research fields.

Special Topics Courses are 1-4 week long courses that provide intense training in specialized research areas.

Taking an MBL course is *transformative.*

Substantial financial assistance is available.

Marine Biological Laboratory | THE UNIVERSITY OF CHICAGO **mbl.edu/courses**

Eni Award 2016

Ideas for a brighter future

An award that attracts researchers from all over the world who share a common purpose: developing new technologies capable of producing more sustainable energy and helping to protect the environment. The Eni Award was established in 2007. It is given to outstanding researchers in the field of renewable energy, working on projects to safeguard the environment and pushing new frontiers in hydrocarbons. In 2017 a new prize will be introduced to mark the tenth anniversary of the Eni Award. Entitled "Research debut: new talents from Africa", it is reserved for recent graduates from African universities. Recognising excellent ideas today. Building a better tomorrow.

eni
eni.com

X Y ZOOM

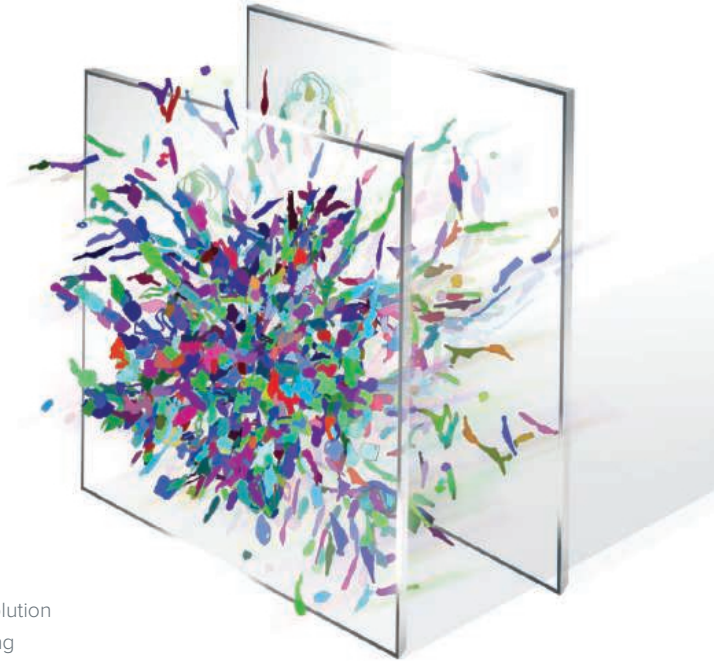

Position your research with our new ImageXpress® Micro 4 High-Content Imaging System

- Tackle your toughest assays with an imaging platform that adapts to your needs
- Image over 15 million cells per hour in a 3-color cell scoring assay
- Acquire and analyze in both 2D and 3D using our seamless, integrated end-to-end solution
- Drive your research with a system that builds on over 30 years of innovation in imaging

moleculardevices.com/ixm4

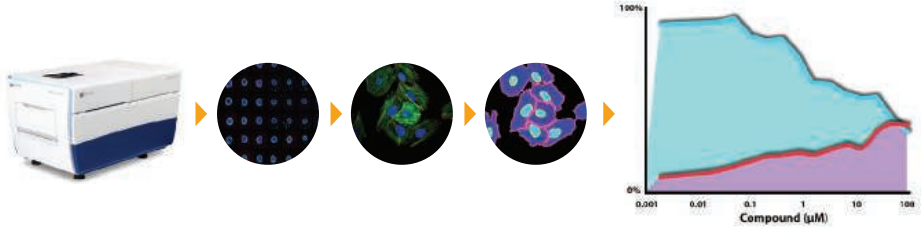

MOLECULAR DEVICES

www.moleculardevices.com | 800.635.5577

THE 2017 LASKER AWARDS

Call for Nominations

BASIC MEDICAL RESEARCH

CLINICAL RESEARCH

PUBLIC SERVICE

Recent Basic Awards

2016
Oxygen sensing–an essential process for survival

2015
DNA damage response

2014
Unfolded protein response

2013
Regulated neurotransmitter release

2012
Motor proteins that contract muscles and enable cell movements

Recent Clinical Awards

2016
Hepatitis C replicon system for drug discovery

2015
Checkpoint immunotherapy for cancer

2014
Deep brain stimulation for Parkinson's disease

2013
Cochlear implant for deafness

2012
Liver transplantation for end-stage liver disease

Submit a nomination online at **LASKERFOUNDATION.ORG**

DEADLINE: FEBRUARY 1, 2017

BUILD A BETTER FUTURE

WITH THE POWER OF SUREGUIDE CRISPR LIBRARIES

Empower your research with SureGuide CRISPR libraries. We provide complete, ultra-high quality CRISPR solutions for any gene, any species or any application. Harness the power of our fully customizable CRISPR offerings to unravel the cause of complex diseases and build a better future.

Learn more at **www.agilent.com/genomics/SureGuide**

For Research Use Only.
Not for use in diagnostic procedures.

Agilent Technologies

By **Maryam Zaringhalam**

The problem with 'alternative'

For years after I dissected a fetal pig in ninth grade, I identified as an aspiring scientist. I was enraptured by the way that anatomical parts, unimpressive on their own, came together to form a living creature. I wanted to devote my life to studying such marvels by becoming a professor at the helm of my own research laboratory. Every step I made was toward that goal—until my second year of graduate school. I still loved doing science. But, through launching a blog and salon series called ArtLab, I found that I loved thinking and talking about science—unfundable dream projects, happy lab accidents that became historical breakthroughs, the latest sci-fi fantasy and its implications—even more. I realized that a traditional professorship was not right for me. But I feared that pursuing my newfound interest would mean that I was settling for an "alternative" to my ninth grade dreams. I was stuck.

Talking with scientists who had gone on to careers in science communication, while inspiring, in some ways reinforced my hesitation. Watching them wield complex scientific concepts to provoke thought and excitement helped me envision a future outside academia. But from time to time, I picked up on a verbal tic that nagged at me: They'd jokingly refer to themselves as failed-scientists-turned-blank. How could I, a career overachiever, opt to fail? I recoiled at the idea of turning my back on the path a "successful" young scientist is meant to walk. The word "alternative," commonly applied to the types of careers that I was becoming more and more interested in, quietly rankled. I felt that to accept an "alternative" as my true aspiration would be to accept defeat and disappoint myself and all the mentors who had invested in my future as a scientist.

"I couldn't ignore my growing interest in nonacademic career options."

Nonetheless, I couldn't ignore my growing interest in nonacademic career options. I flirted with the idea of cutting my losses and leaving my Ph.D. program. As ArtLab gained steam, my peers would even stop me on campus and ask why I hadn't left already. But I didn't want to abort my education. I knew there would be no other time in my life when I would have the luxury of diving deep into a single biological question, no other place that would give me the freedom to follow my curiosity, and no other occasion to meet some of the greatest scientific minds.

As my identity crisis quietly brewed in the pit of my stomach, I began asking the communicators I so admired why they had finished graduate school only to leave research. Many of them noted that their scientific training gave them tools and insights that they took into their professional lives. I began to appreciate that graduate school isn't—and shouldn't be—vocational training. Through my time in the lab, I have learned how to deal with failure and frustration. I have translated the jargon of my field into plain and vivid English. I have collaborated with my peers in pursuit of a common goal. These skills, and the many others that I have developed, will serve me well regardless of which nonacademic path I choose. Moreover, my pursuit of an "alternative" path doesn't mean that the academic system has failed me. Instead, it has trained an ally.

Armed with this new perspective, I finally got up the courage to tell my adviser that my plans for the future did not involve a postdoctoral position. I readied myself for her disappointed speech about what a shame it was to see me go. Instead, she beamed and said, "If we're not sending our best and brightest out into the world beyond the bench, then there's no hope for us here in the lab."

Having defended my dissertation last month, I am now preparing to leave academia. Not for an alternative, nor to shed my identity as a scientist to become something less, but to pursue the path that is right for me. ■

Maryam Zaringhalam recently received her doctorate from The Rockefeller University in New York City. Send your career story to SciCareerEditor@aaas.org.

ILLUSTRATION: ROBERT NEUBECKER

Science Careers Advertising

For full advertising details, go to ScienceCareers.org and click For Employers, or call one of our representatives.

Tracy Holmes
Worldwide Associate Director
Science Careers
Phone: +44 (0) 1223 326525

THE AMERICAS

E-mail: advertise@sciencecareers.org
Fax: +1 (202) 289 6742

Tina Burks
Phone: +1 (202) 326 6577

Nancy Toema
Phone: +1 (202) 326 6578

Online Job Posting Questions
Phone: +1 (202) 312 6375

EUROPE / INDIA / AUSTRALIA / NEW ZEALAND / REST OF WORLD

E-mail: ads@science-int.co.uk
Fax: +44 (0) 1223 326532

Sarah Lelarge
Phone: +44 (0) 1223 326527

Kelly Grace
Phone: +44 (0) 1223 326528

Online Job Posting Questions
Phone: +44 (0) 1223 326528

JAPAN

Katsuyoshi Fukamizu (Tokyo)
E-mail: kfukamizu@aaas.org
Phone: +81 3 3219 5777

Hiroyuki Mashiki (Kyoto)
E-mail: hmashiki@aaas.org
Phone: +81 75 823 1109

CHINA / KOREA / SINGAPORE / TAIWAN / THAILAND

Danny Zhao
E-mail: dzhao@aaas.org
Phone: +86 131 4114 0012

ScienceCareers
FROM THE JOURNAL SCIENCE AAAS

ScienceCareers.org

UNIVERSITY OF MICHIGAN

The University of Michigan Division of Infectious Diseases and the Department of Computational Medicine and Bioinformatics invite applications for joint faculty positions at the rank of Assistant, Associate, or Full Professor, to develop and conduct independently funded basic and/or translational research programs. We are searching broadly for M.D. or Ph.D. scientists with an interest in infectious diseases that use combinations of molecular and computational approaches to understand pathogenesis, epidemiology and/or host- microbe interactions. Departmental placement, as well as teaching and clinical duties will be set by mutual agreement. To apply, please submit a statement of current and future research plans, a description of teaching and clinical experience (as appropriate), curriculum vitae and contact information for three references addressed to: **David Markovitz MD, Internal Medicine/ Infectious Diseases, 1150 W. Medical Center Drive, 5220 MSRB III, Ann Arbor, MI 48109-5640** or to **dmarkov@med.umich.edu**.

Review of applications will begin **December 1, 2016** and continue until suitable candidates are identified for both positions.

Women and minorities are encouraged to apply. The University of Michigan is an Equal Opportunity/Affirmative Action Employer and is supportive of the needs of

POSITIONS OPEN

ANATOMY AND CELL BIOLOGY EAST CAROLINA UNIVERSITY

The Department of Anatomy & Cell Biology, Brody School of Medicine at East Carolina University (ECU) is seeking applicants for a tenure track or fixed term **ASSISTANT/ ASSOCIATE PROFESSOR** position in Greenville, NC. Rank will be commensurate with qualifications. We are seeking applicants with a strong interest in graduate student education and enthusiasm for and experience in human gross anatomy with teaching responsibilities to a variety of professional students. The new faculty is expected to develop an extramurally funded research program that will compliment the strengths of ongoing research in the department. (http://www.ecu.edu/anatomy). Candidates must apply using the on-line application process to position #957502, website: **ecu.peopleadmin.com/applicants/Central?quickFind=83772**. Applicants should submit a complete application including a cover letter, statement of interest, curriculum vitae, statement of teaching philosophy, and statement of research plans including specific aims for a potential proposal.

ECU is a constituent institution of the University of North Carolina and an Equal Opportunity/Affirmative Action University that accommodates the needs of individuals with disabilities.

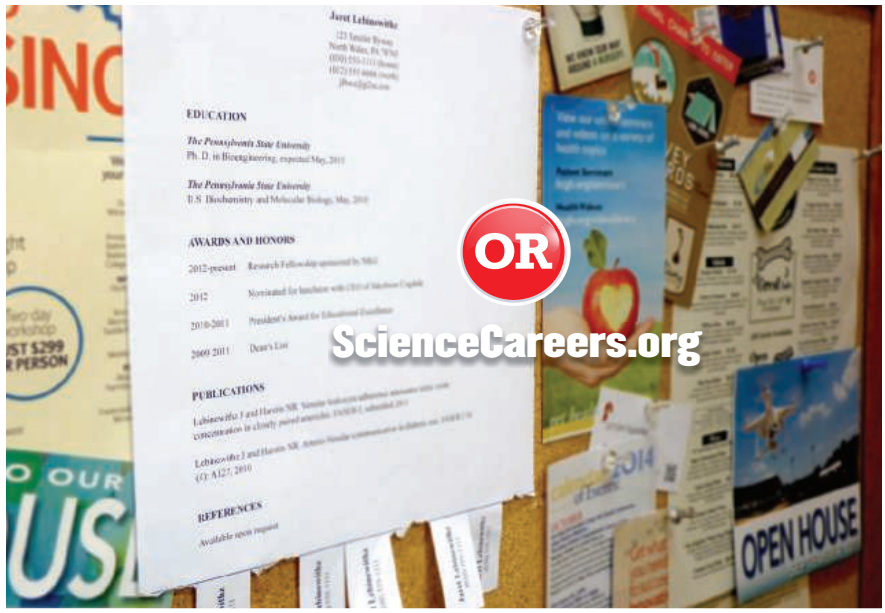

Conduct your job search the easy way.

Target your job search using relevant resources on **ScienceCareers.org**.

ScienceCareers
FROM THE JOURNAL SCIENCE AAAS

SANOFI IS ON A **MISSION**

COME BE A PART OF IT

Sanofi has shaped the future of medicine for over 100 years. Creating world-first therapies and vaccines is in our DNA. It's what we do.

We're looking for scientific talent to join us in our mission to discover and develop breakthrough medicines, cures and vaccines that could define human health in the 21st Century.

Are you up to the challenge?

We are building a world-class research team and seek outstanding scientists with significant track record. Global opportunities range at levels from Research Associate to Senior Director in the following focus areas:

IMMUNOLOGY & INFLAMMATION

Systems Immunology and Immunogenomics

Type 2 Inflammation and Fibrosis

Targeted Autoimmunity and Type 1 Diabetes

Innate Immunity

Checkpoint Immunology

RARE DISEASES

Inherited Metabolic Diseases

Rare Muscle, Renal and Bone Diseases

Nucleic Acids-Based Therapies

PRECLINICAL SAFETY

Investigative Toxicology

TRANSLATIONAL SCIENCES

Genomics

Bioinformatics

NEUROSCIENCE

Neurodegenerative Diseases

Neuroinflammation

Neuroprotection and Repair

Remyelination

Rare Genetic Diseases of the CNS

BIOLOGICS RESEARCH

Recombinant Protein Expression and Purification

Biophysical and Biochemical Analysis of Recombinant Proteins

Antibody Display Technologies

Visit www.sanofi.us and the "Career" tab, "Join Sanofi".

Search by one of the six areas listed above for positions. Locations of positions may be flexible.

Sanofi offers competitive benefits and we're one of the most highly rated companies to work for.

Sanofi is a global organization that employs over 115,000 employees worldwide. Sanofi US Services, Inc. and its U.S. affiliates are Equal Opportunity and Affirmative Action employers committed to a culturally diverse workforce. All qualified applicants will receive consideration for employment without regard to race; color; creed; religion; national origin; age; ancestry; nationality; marital, domestic partnership or civil union status; sex, gender, gender identity or expression; affectional or sexual orientation; disability; veteran or military status or liability for military status; domestic violence victim status; atypical cellular or blood trait; genetic information (including the refusal to submit to genetic testing) or any other characteristic protected by law.

SANOFI

PURDUE
UNIVERSITY

Faculty Opening in Industrial and Physical Pharmacy
Assistant Professor

The College of Pharmacy at Purdue University is seeking applications to fill a faculty position in the Department of Industrial and Physical Pharmacy in the general area of **Pharmaceutical Solids**.

The position is for a full-time tenure-track Assistant Professor. The faculty member is expected to establish an externally funded research program and will teach courses in the undergraduate, graduate and professional (PharmD) programs. It is expected that the individual will collaborate on various research activities within the department and in multidisciplinary, multi-institutional research throughout the University. This is a nine-month (academic year) appointment.

The candidate should have expertise in fundamental and applied research related to the development, design, analysis and manufacturing of drug products. Representative areas of expertise include:

- Pharmaceutical materials science
- Pharmaceutical engineering
- Crystallization and particle technology
- Solid state chemistry of pharmaceutical systems
- Unit operations/continuous manufacturing associated with drug substance and drug product

Established in 1869, Purdue is Indiana's land-grant university, a comprehensive educational and research institution which is a member of the prestigious American Association of Universities (AAU). The **Department of Industrial and Physical Pharmacy** encompasses multidisciplinary research and teaching in the areas of drug development, biotechnology, pharmacokinetics, drug delivery systems and manufacturing technologies. Purdue University offers a thriving interdisciplinary environment for education and research.

Qualifications: The candidate must hold a PhD degree or equivalent in a relevant discipline which would include pharmaceutical sciences, engineering, biochemistry, analytical chemistry and biophysics, and have an outstanding academic record, an exceptional potential for world-class research and a commitment to both undergraduate and graduate education. Postdoctoral and/or industrial experience is preferred but not required. Candidates with experience working with diverse groups of students, faculty, and staff and the ability to contribute to an inclusive climate are particularly encouraged to apply.

Application: For consideration, please submit a single PDF file electronically to mhurt@purdue.edu including:

- Candidate's curriculum vitae
- Letter of interest providing a summary of qualifications for the position
- Statement of research interests and goals
- Statement of teaching philosophy
- Names and contact information for three references

Incomplete applications will not be considered.

Review of applications will begin **October 24, 2016** and will continue until the position is filled. A background check will be required for employment in this position. The desired starting date is August 14, 2017, but flexible and negotiable.

For further information concerning the search please contact **Mary Ellen Hurt, Assistant Professor Search Committee, Department of Industrial and Physical Pharmacy, College of Pharmacy, Purdue University, West Lafayette, IN 47907-2091; mhurt@purdue.edu**.

Purdue University is an Equal Opportunity/Equal Access/Affirmative Action Employer. Purdue University is committed to maintaining a community which recognizes and values the inherent worth and dignity of every person. In pursuit of its goal of academic excellence, the University seeks to develop and nurture diversity. All qualified applicants for employment will receive consideration without regard to race, religion, color, sex, national origin or ancestry, genetic information, marital status, parental status, sexual orientation, gender identity and expression, disability or status as a veteran.

PURDUE
UNIVERSITY

Faculty Opening in Industrial and Physical Pharmacy
Assistant Professor

The College of Pharmacy at Purdue University is seeking applications to fill a faculty position in the Department of Industrial and Physical Pharmacy in the general area of **Pharmaceutical Biotechnology**.

The position is for a full-time tenure-track Assistant Professor. The faculty member is expected to establish an externally funded research program and will teach courses in the undergraduate, graduate and professional (PharmD) programs. It is expected that the individual will collaborate on various research activities within the department and in multidisciplinary, multi-institutional research throughout the University. This is a nine-month (academic year) appointment.

The candidate should have expertise in fundamental and applied research related to the development, design, evaluation and manufacturing of biopharmaceutical products. Representative areas of expertise include:

- Formulation and manufacturing of peptide, protein, and/or nucleic acid-based therapeutics
- Analysis, processing and engineering of therapeutic proteins
- Vaccine formulation development
- Formulation of immunotherapeutics
- Preclinical drug disposition (PKPD), in vitro in vivo correlations
- Gut pharmacomicrobiomics

Established in 1869, Purdue is Indiana's land-grant university, a comprehensive educational and research institution which is a member of the prestigious American Association of Universities (AAU). The **Department of Industrial and Physical Pharmacy** encompasses multidisciplinary research and teaching in the areas of drug development, biotechnology, pharmacokinetics, drug delivery systems and manufacturing technologies. Purdue University offers a thriving interdisciplinary environment for education and research.

Qualifications: The candidate must hold a PhD degree or equivalent in a relevant discipline which would include pharmaceutical sciences, engineering, biochemistry, analytical chemistry and biophysics, and have an outstanding academic record, an exceptional potential for world-class research and a commitment to both undergraduate and graduate education. Postdoctoral and/or industrial experience is preferred but not required. Candidates with experience working with diverse groups of students, faculty, and staff and the ability to contribute to an inclusive climate are particularly encouraged to apply.

Application: For consideration, please submit a single PDF file electronically to **mhurt@purdue.edu** including:

- Candidate's curriculum vitae
- Letter of interest providing a summary of qualifications for the position
- Statement of research interests and goals
- Statement of teaching philosophy
- Names and contact information for three references

Incomplete applications will not be considered.

Review of applications will begin **October 24, 2016** and will continue until the position is filled. A background check will be required for employment in this position. The desired starting date is August 14, 2017, but flexible and negotiable.

For further information concerning the search please contact **Mary Ellen Hurt, Assistant Professor Search Committee, Department of Industrial and Physical Pharmacy, College of Pharmacy, Purdue University, West Lafayette, IN 47907-2091; mhurt@purdue.edu**.

Purdue University is an Equal Opportunity/Equal Access/Affirmative Action Employer. Purdue University is committed to maintaining a community which recognizes and values the inherent worth and dignity of every person. In pursuit of its goal of academic excellence, the University seeks to develop and nurture diversity. All qualified applicants for employment will receive consideration without regard to race, religion, color, sex, national origin or ancestry, genetic information, marital status, parental status, sexual orientation, gender identity and expression, disability or status as a veteran.

10 ways that *Science* Careers can help advance your career

1. Register for a free online account on **ScienceCareers.org**.
2. Search thousands of job postings and find your perfect job.
3. Sign up to receive e-mail alerts about job postings that match your criteria.
4. Upload your resume into our database and connect with employers.
5. Watch one of our many webinars on different career topics such as job searching, networking, and more.
6. Download our career booklets, including Career Basics, Careers Beyond the Bench, and Developing Your Skills.
7. Complete an interactive, personalized career plan at "my IDP."
8. Visit our Career Forum and get advice from career experts and your peers.
9. Research graduate program information and find a program right for you.
10. Read relevant career advice articles from our library of thousands.

Visit **ScienceCareers.org** today — all resources are free

ScienceCareers

FROM THE JOURNAL SCIENCE AAAS

SCIENCECAREERS.ORG

The Yangtze River Delta:

"Double Tops" Universities in a World Class Urban Cluster

CHINA
聚焦"长三角"

The Yangtze River Delta, an alluvial plain at the mouth of the Yangtze River, boasts a dynamic economy, exceptional culture, and largest population in China. Dominant in China's strategy to modernize and strengthen its ties to the rest of the world, the Yangtze River Delta plays a pivotal role in fueling China's economic growth, with the economic aggregate of the Yangtze River Delta accounting for one fourth of the national economy, and its annual rate of growth well above average for China. By virtue of its powerful industrial base and advanced market economy, this area has become the largest export base in China. The cities clustered within the Yangtze River Delta boast modern river- and sea-ports, extensive networks of expressways, densely interconnected railway lines, and an advanced comprehensive transportation network. These features have propelled the Yangtze River Delta to a position of economic leadership worldwide.

As a result, the Yangtze River Delta has seen the healthiest growth in science and technology in China, bringing it in line with worldwide standards. The region's sound policies and regulations for science and technology have provided important institutional guarantees for innovation and entrepreneurialism, making this region a major hub for innovation throughout the world: a typical example is the Alibaba Group, a large-scale ecommerce company that launched in Hangzhou. Rich in human resources and technical prowess, the region boasts roughly 300 innovation platforms, such as the National Engineering Research Center and Engineering Laboratory, which in aggregate account for one third of the national total for R&D expenditure and patents.

Zhimin Li
Director of Center for Science and Technology Development Ministry of Education, People's Republic of China

The Yangtze River Delta has taken the nationwide lead in educational resources, and is home to approximately 400 colleges and universities, including Zhejiang, Nanjing, Shanghai Jiaotong, Fudan, Southwest, and Tongji Universities, and the University of Science and Technology of China, all of which are under the direct administration of the central government. Other renowned colleges and universities such as Soochow University are within the jurisdiction of local governments. Jiangsu province ranks the first in terms of total number of colleges and universities and the second for total 211 Project universities in China. The Yangtze River Delta is also home to the universities with the highest level and largest scale of international education in China. The University of Nottingham in Ningbo, the New York University in Shanghai, Duke University in Kunshan, and ShanghaiTech University have all played exemplary roles in internationalizing Chinese education, bringing many first-rate experts, scholars and teams to the Yangtze River Delta from throughout the world to play roles in scientific teaching, research, and management.

The "Double Tops" proposal (Top Universities and Top Disciplines in the world) for education reform has extolled the quality of colleges and universities in the Yangtze River Delta region throughout the world, and has hastened the optimization of local college and discipline distribution in the region, streamlining the administration of local colleges and universities. Recently, the Education Department of Jiangsu Province issued the *Construction Program of Jiangsu High-level University*, a document that provides provinces and cities in the region clear measures and methods to implement the central spirit of *The Overall Construction Plan of Integrating Development of Double Tops* proposed by the central government of China.

At the top echelon of Chinese domestic higher education, the Yangtze River Delta has a running start to the construction and development of higher education, with each region having their own characteristics in "Double Tops" construction program. Colleges and universities in the Yangtze River Delta region are, however, in urgent need of high-level talents to provide a steady driving force for innovation of colleges and universities and to continue to propel Chinese higher education to a world-class level.

To this end, university presidents in the Yangtze River Delta region send this invitation to overseas talents:

Jun Chen

President of Nanjing University

As one of the leading institutions of higher learning in China, Nanjing University regards the "Double Top" Program as a critical catalyst for its further development. I cordially invite global talents to make their academic breakthroughs and develop their careers at Nanjing University. With a dynamic environment that nurtures learning, creativity, and discovery, we are committed to constructing a world-class university with first-class disciplines here in the near future.

Guangjun Zhang

President of Southeast University

The national "double first rate" strategic plan in China provides an opportunity as well as a challenge for our university to greatly raise of capabilities in innovations, in fostering first-rate talents, in yielding first-rate achievements in all research fields, at the same time to make it a first-rate university in the world. Making it among the world top universities is not only a vision, not a long-term goal for future, but it is a real test of our wisdom and our spirits of taking actions, showing our ambitions and courage, it even is a test of our willpowers and strengths. The Southeast University will continue the principles of "aiming at the foremost developments, following the strategy, depending on both bodies of teachers and students, placing priorities on the outstanding people", to maintain the theme of strengthening the status of the university by using capable people, deepening the structural reforming so that we could be able to raise the quality of our teaching, to expand the research fields, encouraging the collaborations among different fields, among the people in teaching and research, among science and technology people with those in humanity and medical fields, and encouraging the collaborations with top universities of the world, following the "four-collaborations" plans. We will put a lot efforts to make four major breakthroughs in teaching, research, faculty and international exchanges, so our goal of making the Southeast University a first rate university in the world will be achieved soon.

Hong Nie

President of Nanjing University of Aeronautics and Astronautics

Nanjing University of Aeronautics and Astronautics will embrace the construction goal of "Double Tops" Program and stick to the development strategy of "strengthening university via talents", gathering outstanding talents and making marvelous achievements to commonly develop itself to be a high-level research university.

Hui Xu

President of Hohai University

Our vision is to cultivate outstanding talents with a global view, an appreciation for things Chinese, and Hohai's high standards. We aim to develop Hohai University into a distinctive and world-class research university by the middle of the 21st century.

Maode Lai

President of China Pharmaceutical University

China Pharmaceutical University adheres to the motto of "Committed to Academic Excellence & Devoted to Public Health" and the mission of "cultivating elites of the pharmaceutical industry, developing good medicine that benefits the public and contributing to a happy life", whist striving to turn itself into a world-famous, high-level research-oriented university.

Guihong Hua

President of Jiangsu Normal University

Gathering first-rate talents is a prominent mark of "Double-First-Class" universities, and it is a booster for key projects, broad platform, brilliant achievements and significant awards. By taking it as the University's strategic stronghold, Jiangsu Normal University will set up an ecological environment for attraction, aggregation, cultivation, utilization and appreciation of talents. The University will try all her efforts on building brand recognition of education, science, technology and culture with the aim of constructing a comprehensive university of high quality, refined taste and unique feature.

Yukun Sun

President of Nanjing Institute of Technology

Our university is an application-based university that boasts a history of one hundred years and is empowered to award engineering master degree. We will uphold the philosophy of "Strengthening our university with talents" and gather all elites from around the world, thus jointly building a high-level application-based engineering university.

Hongbing Shen

President of Nanjing Medical University

Nanjing Medical University is committed to its primary goal of developing into an outstanding institute of medical education and research in China. In an effort to build a contingent of accomplished scientists as well as encourage independent innovation, we will stick to the principle of training our faculty members and at the same time recruiting talents from overseas, while providing them with an atmosphere in which everyone dreams to be, has the opportunity to be, and strives to be a talent. We warmly welcome preeminent talents from all over the world to join us in establishing a high-level research-oriented medical university.

Kuiyang Zheng

President of Xuzhou Medical University

Xuzhou Medical University, honored as the cradle of Anesthesiology talents cultivation in China, endeavors to advance academic level and to build an innovative high-quality faculty team. In an effort to complete the present mission of accelerating the introduction of high-level talents, increasing the internationalization of faculty team and strengthening the assembling of a high-level innovation team, we are committed to providing the opportunity and atmosphere to train and improve our faculty members and recruiting outstanding domestic and overseas talents from all the world. We welcome advanced talents from around the world to engage in the development of Xuzhou Medical University.

Xinke Zhang

President of Xuzhou University of Technology

A qualified college student is similar to a car in that knowledge and skills are his/her rear wheels while the love for live and the passions about occupation are his/her front wheels.

Donghan Jin

President of Shanghai University

The mission of Shanghai University is to constantly innovate the whole-person mode of talent training so as to cultivate various kinds of talent with a global vision, civic consciousness, humanitarian sentiments, innovative spirit and practical skill capable of coping with future challenges.

Changjun Jiang

President of Donghua University

Donghua University, as a key university directly affiliated to Education of Ministry, China, will firmly embrace the national construction goal of "Double Tops" Program, focus on improving the level of talents cultivation and innovation, and adhere to the core strategy of strengthening universities via talents. We warmly welcome excellent talents all over the world, especially youth ones, to join us to create an exquisite Donghua University.

Jing Lu

President of Shanghai Institute of Technology

Shanghai Institute of Technology is driving for a high-level university of applied sciences with great-international-influence on the basis of enhancing its advantages of application-oriented disciplines, taking a leading role in industrial development and adhering to the particular talent-training principles of cultivating talents with undergraduate level and technical skills.

Hexing Li

President of Shanghai University of Electric Power

Surrounding the "Double Tops" Program, Shanghai University of Electric Power will rapidly construct new energy, electric power security, smart grid and other innovation centers as well as the strategic thinkbank of electric power and energy development, vigorously introduce high-end talents at home and abroad and endeavor to be a high-level application-oriented university of technology with distinct characterisitics of energy and electricity.

Liang Liang

President of Hefei University of Technology

Excellent teachers are the key factor in the development of our university, and that whether our young teachers can become outstanding determines how high HFUT can reach in the future. HFUT pays high attention to the introduction and training of our young talents while it is moving ahead to construct a world-class university and build first-class disciplines. Excellent young scholars at home and abroad are warmly welcome to join HFUT to compose a mutual glorious future.

Manhong Shen

President of Ningbo University

"Double Tops" Program provides a valuable opportunity for Ningbo University to construct first-class disciplines. Ningbo University will endeavor to vigorously introduce top-notch talents all over the world, construct its three key discipline groups, namely, "Modern Marine Sciences", "Electronics and Communication", and "Life & Health" and strive for being a comprehensive research university in the near future.

Lihong Guo

President of Northwest University

Northwest University sincerely invites talents from China and abroad. With a history of over one hundred years, Northwest University takes the opportunity of One Belt, One Road Initiative, aiming at to construct a world-class university and first-class disciplines. We will spare no efforts to put up a platform for talents development and realize your dreams. Let's make a concerted effort for our splendid future!

"In May 2016, the State Council proposed to cultivate a higher level of economic growth in the Yangtze River Delta through the *Urban Agglomeration Development Plan*. By 2030, a world-class urban agglomeration incorporating global influences will have been fully completed. This resource will be built at the center of the most dynamic regions in China in terms of economic development, science and technology, and global interconnectedness. In addition the resource will host the world's most advanced modern service industry and manufacturing center, and largest international gateway in the Asia Pacific region. Thus the Yangtze River Delta will be an international pacesetter in the latest round of national reform and in opening up and demonstration area of Beauty China construction."

This land is a spiritual place with a deeply cultivated foundation of knowledge that naturally makes it as an ideal setting for world-class universities. The "Double Tops" program of colleges and universities in the Yangtze River Delta is looking forward to having you join us!

To help China's top-ranked universities attract high-level talent from overseas, CERNET has partnered with Science to launch a print and online media campaign. Many of China's top universities are recognized as world-class and are doing first-class research but the aim is to build on this and establish worldwide acclaim for all of China's top universities in both institute and discipline rankings.

Researchers, interested in working in China, are invited to consider applying for jobs published in the following special section "Opportunities in China" and online at **http://jobs.sciencecareers.org/**.

Further information can also be located at **www.edu.cn/jjcsj**.

Academic Openings

Nanjing University (NJU) has a broad range of academic disciplines, covering natural sciences, applied sciences and engineering, social sciences, arts and humanities, management and some newly emerging inter-disciplines. All fields of study are open to applicants.

- The 1000 Talents Plan (Full-time) for Innovative Talents, Young Professionals and Foreign Experts
- The 1000 Talents Plan (Part-time) for Innovative Talents and Foreign Experts
- The Chang Jiang Scholars Program for Distinguished Professorship and Young Talents Professor
- **The Nanjing University "Deng Feng" Distinguished Scholars Program for Level A (Distinguished Professorship) / Level B (Young Talents)**

Note: Please kindly scan the QR code on the bottom for detailed information on these programs.

Remuneration

Nanjing University will provide comprehensive and competitive support for the appointees. The benefits include start-up research funds, salaries, accommodation benefits, offices, laboratories, research assistants and graduate students.

Qualifications

Candidates should have:

- ✓ A demonstrated commitment to excellence in teaching and research
- ✓ A proven track record of academic achievement, comparable to those of full professors or associate/assistant professors in world-renowned universities
- ✓ A doctoral degree from a world-renowned university, preferably with postdoctoral experience

Young and mid-career researchers are particularly encouraged to apply.

Qualified candidates are cordially invited to send a copy of job intention letter together with curriculum vitae to *rcb@nju.edu.cn*. Applications are accepted all year round.

Contact: Mr. Li Sijia **+86-25-89686783** *rcb@nju.edu.cn*

宁波大学
NINGBO UNIVERSITY

Faculty Positions Available in Ningbo University

◆ Seeking bright minds

Located in the historical port city of Ningbo in eastern China, Ningbo University is a burgeoning comprehensive university co-established by the Chinese Ministry of Education, Zhejiang provincial government and Ningbo municipal government. It is among the first five provincially governed key universities designated by the Zhejiang provincial government. Young and dynamic, Ningbo University is already ranked among the top 100 universities in China.

Ningbo University is actively seeking talented researchers to strengthen its faculty team.

Openings for academic leaders

Requirements:

- A doctoral degree from an overseas institution is expected, along with at least three years of work experience conducting research overseas; for those who have obtained their doctoral degree from a domestic institution, at least three years of overseas teaching or research experience is a must
- Experience working as a tenured professor or equivalent in a well-known university or research institution overseas (associate professor experience is fine for young candidates from top universities or institutions); generally, candidates should qualify for the national Thousand Talents Program
- A proven track record of achievements in a specialized research field, with the potential to become an academic or technical leader in the field
- Ability to work full-time on site, and preferably under 50 years old

Openings for top young scientists

Requirements:

- A doctoral degree from an overseas institution is preferred, along with at least three years post-graduate research experience overseas; those with doctoral degrees from domestic institutions must have at least three years of experience conducting research or teaching overseas
- Experience working full-time in a well-known university or research institution overseas, conducting research or teaching; generally, candidates should qualify for the national Thousand Young Talents Program or the provincial Thousand Talents Program
- Ability to work full-time on site, and preferably under 45 years old

Openings for excellent doctoral researchers

Requirements:

- A doctoral degree from an overseas institution is preferred, along with at least three years of work experience conducting research overseas; those with doctoral degrees from domestic institutions should have at least three years of experience conducting research or teaching overseas
- A track record of publication experience, with at least one paper published in Social Sciences Citation Index or Arts & Humanities Citation Index journals for candidates in humanities and social sciences fields; two or more papers published in Science Citation Index-listed journals or at least one publication in a top journal for candidates in natural sciences fields
- Ability to work full-time at the university

◆ Compensation

Generous compensation packages will be available. For excellent doctoral researchers, the successful candidate will receive a settling-in allowance of 600,000 (180,000+420,000) RMB. Those with four or more publications in top journals are eligible to be hired as associate professors, and will receive a settling-in allowance of 800,000 (600,000+200,000) RMB.

◆ Application procedure

Please submit a completed application form, a curriculum vitae and a cover letter, along with other relevant supporting materials via e-mail to: **rsc@nbu.edu.cn**.

For additional information regarding the application, such as the number of openings, please visit: **http://www.nbu.edu.cn/shizi**.

Recruitment of Hefei University of Technology for Talents

I. Profile

Hefei University of Technology(HFUT), a key university under the direct administration of the Ministry of Education, is situated in Hefei, the provincial capital of Anhui, which is one of Four National-Level Science and Technology Bases. Hefei University of Technology is a key base for talent cultivation, scientific research and social services, supported by the government under the State 211 Project and 985 Project for key construction and the construction of preponderant disciplines innovation platform.

The University has 3,705 staffs and 2,004 full-time teachers. It also boasts 1 academician of the China Academy of Engineering, 2 foreign academicians, 8 distinguished experts of the national "Thousand Talents Program", 14 professors of "Yangtze River Scholars", 7 granted with funds from the National Outstanding Youth Science Foundation, 4 granted with funds from the Outstanding Youth Natural Science Foundation, 1 member of Academic Degrees Committee of the State Council and 21 members of the advisor committee of national basic course and professional teaching. The University has more than 30450 full time undergraduate students and more than 10780 graduates and doctors.

The University has 3 national key disciplines, 1 national key cultivating discipline, 28 provincial-level key disciplines, 12 post-doctoral research stations, 12 authorized first-level disciplines of doctoral degree, 32 authorized first-level disciplines of master degree; 11 professional degree authorizations; 86 undergraduate majors. The University has formed coordinated development of multi-discipline structure, which emphasizes on engineering, combines engineering with science and focuses on the permeation of humanities and science

HFUT is actively pursuing connections with leading institutions through academic partnerships with top universities worldwide. By supporting a wide range of collaborative activities, it has established academic links with more than 30 prestigious universities around the world. HFUT with its 70-year achievements in several key disciplines, is now striving for even greater success with the ultimate goal of becoming a top innovative university with international prestige and distinctive features. We invite outstanding talents from home and abroad to join Hefei University of Technology and to polish your performance. Hefei University of Technology will cooperate with you to create a glorious future!

II. Disciplines

All discipline about natural sciences, engineering, management and new interdiscipline can be applied.

III. Candidates

- △ Doctors, Post-doctors;
- △ Associate professors and above;
- △ Senior engineers and technicians from large enterprises or research institutes
- ▲ **PS: All posts recruit doctors and post-doctors.**

IV. Contact

If interested in the post of talents, please contact as follows:

Contacts: Mr. Zhang, Mr. Meng, Mr. Sun
E-mail: rcb@hfut.edu.cn
Phone: 86-551-62901630; 86-551-62901353; 86-551-62901122
Fax: 86-551-62901353
Postcode: 230009
Site: No.9,Hefei University of Technology, No.193 Tunxi Road, Hefei, Anhui
Website of School: **http://www.hfut.edu.cn**
Website of Talent Recruitment Office: **http://rcb.hfut.edu.cn**

上海交通大學
SHANGHAI JIAO TONG UNIVERSITY

MULTIPLE FACULTY POSITIONS IN ULTRAFAST SCIENCES / ELECTRON MICROSCOPY SHANGHAI JIAO TONG UNIVERSITY, SHANGHAI, CHINA

Shanghai Jiao Tong University is establishing a world-class research Center for Ultrafast Sciences in physics, chemistry, materials and biology with integration of both experimental and theoretical efforts. The Center will provide state-of-the-art ultrafast laser spectroscopy, electron diffraction and microscopy, and excellent multi-disciplinary environment for cutting-edge research.

The Center invites applications for a number of open-rank faculty positions to begin in the spring of 2017 (or earlier). Applicants should have a Ph.D. degree, preferably with postdoctoral experience in a closely related field, and a strong record of research accomplishments. Previous experimental and/or theoretical experience in electron microscopy and ultrafast sciences is favorable. The successful candidates will be expected to develop world-class research programs and teach classes at both undergraduate and graduate levels. The University will provide competitive annual salary, start-up fund, housing allowance and other benefits.

All applicants should send a cover letter, a curriculum vitae with a publication list, a research proposal (3-4 pages) and a statement of teaching interest in a single pdf file by Dec. 31, 2016 to Dr. Jie Chen, Shanghai Jiao Tong University, Shanghai 200240, China through e-mail to ultrafast@sjtu.edu.cn. Please also arrange three reference letters directly to the above e-mail address. Applications after the deadline could be reviewed until the positions are filled.

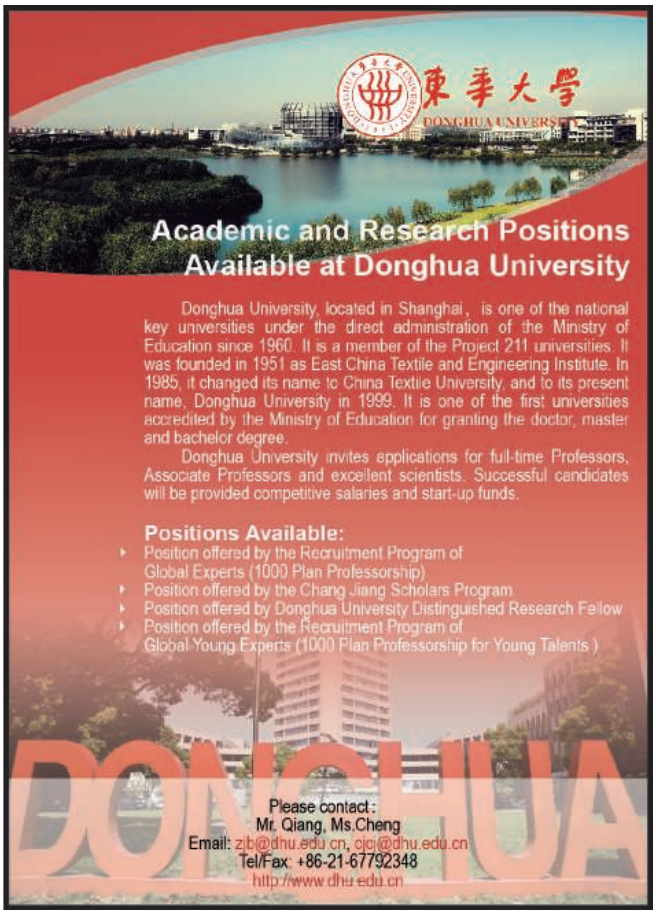

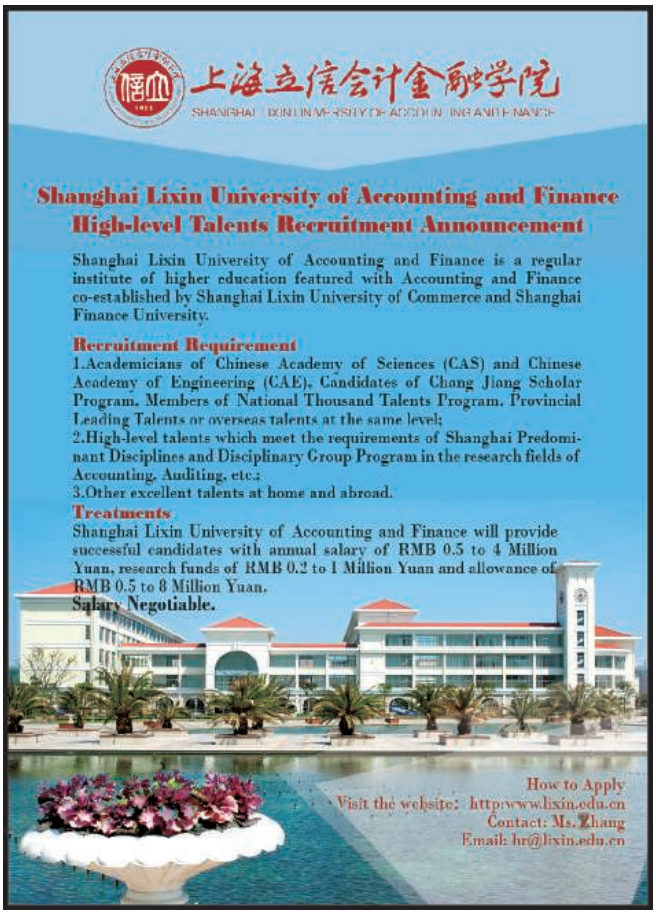

Northwest University
Calls for Talents All Over the World

Established in 1902 and located in Xi'an, China, Northwest University (NWU) currently has been selected as one of the leading universities sponsored by the national "211 Project" and under the joint administration of the Ministry of Education and Shaanxi province. NWU sincerely invites talents home and abroad to join us, and warmly welcome distinguished talents declare the talents programme, for instance, the national "Thousand Talents Plan", "Changjiang Scholars Program" and Shannxi"Excellent One Hundred Talents" Project.

Requirements:

A. Academic Leading Talents:

1. Under the Age of 55.
2a. Full Professor in Overseas University.
2b.Candidates should be qualified to be listed in talents programs such as "Thousand Talents Plan", "Tens of Thousands of People Plan", "Changjiang Scholars Program", "The National Distinguished Young Scholars", etc.

B. Youth Top-notch Talents:

1. Under the age of 45;
2a. In the formal position for teaching and scientific research overseas, or the PHD graduates from international top universities, with excellent achievements;
2b. Candidates are preferable to be listed or qualified for the following programs: "Youth Thousand Talents Plan", "Ten Thousand Distinguished Young Talents", "Youth Yangtze River Scholar", "Outstanding Youth" or published papers in top academic journals (like Science). Scientists with outstanding achievements.

C. Youth Academic Backbone Talents:

1. Under the age of 35;
2a. Overseas post-doctor or excellent PHD graduates;
2b. Domestic excellent scientific research personnel, PHD graduates, with outstanding research achievement or achieved important awards for teaching and scientific research.

D. Chair Professor Position for Level-A Part-time Candidates:

We sincerely welcome excellent talents home and abroad to join us and salary negotiate.

Website: http://www.nwu.edu.cn/
Email: rcb@nwu.edu.cn
Contact Person: Yibo Shen
Tel: (86) 29-88305288
Address: High-level talent project office, Northwest University, 229 North Taibai Road, Beilin District, Xi'an, 710069,Shaanxi Province, China

---

上海理工大學
University of Shanghai for Science and Technology

High-end Talents Recruitment in University of Shanghai for Science and Technology

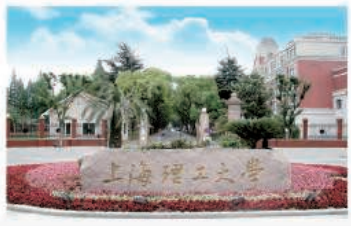

1. Introduction

University of Shanghai for Science and Technology (USST), with a long history of over one hundred years, is a key municipal research-oriented university specializing in engineering, focusing on interdisciplinary integration of engineering, science, management, economics, arts, laws and so on.

2. Recruitment Disciplines

Optical Engineering, System Science, Power Engineering and Engineering Thermophysics, Management Science and Engineering, Biomedical Engineering, Mechanical Engineering or other related interdiscipline.

3. Scope of Talents Recruitment

(1)**Level One**: Academicians of the Chinese Academy of Sciences and Chinese Academy of Engineering.
(2)**Level Two**: Distinguished professor of Changjiang Scholars Program; Selected candidate of innovation project of National "1000 Talents Plan"; Winner of National Science Fund for Outstanding Young Scholars; Outstanding talents of Thousands Talents Program; Selected candidate of Leading Talents, etc.
(3)**Level Three**: Selected candidate of Thousands Talents Program for Young Top-notch Talent; Winner of "Top University Teacher in Teaching Award" issued by Chinese Ministry of Education.
(4)**Level Four**: Selected candidate and young selected candidate of "1000 Talents Plan" issued by the Organization Department of the Central Committee of the CPC; Candidate from the "National Millions of Talents Projects".
(5)**Level Five**: Selected candidate of Shanghai "1000 Talents Plan" (Innovation Project); Selected candidate of "Hundred Talent Plan" of Chinese Academy of Sciences; Shanghai Leading Talents; Distinguished Professor of Shanghai "Orientalist".

4. Treatment

(1)USST will provide competitive salaries, house purchase and renting subsidies and settlement allowance (one-off payment).
Talents of Level One: Salary negotiable according to personal details;
Talents of Level Two:
Annual salary: RMB700,000-800,000Yuan,
House Purchase and Renting Subsidies: RMB1,200,000-2,400,000Yuan

Talents of Level Three:
Annual salary: RMB500,000-600,000Yuan,
House Purchase and Renting Subsidies: RMB600,000-1,200,000Yuan.

Talents of Level Four:
Annual salary: RMB400,000-500,000Yuan,
House Purchase and Renting Subsidies: RMB400,000-800,000Yuan.

Talents of Level Five:
Annual salary: RMB300,000-400,000Yuan,
House Purchase and Renting Subsidies: RMB300,000-600,000Yuan.

(2)Besides the above treatment, USST will also provide makeshift shelter and corresponding scientific research allowance (RMB200,000-2,000,000Yuan)

5. Contact:

Contact Person: Weijia Li, Dong An
Phone: 86-21-55271605
E-mail: liweijia@usst.edu.cn
andong@usst.edu.cn
Address: Room 207, Gezhi Hall, University of Shanghai for Science and Technology, No. 516 Jungong Road, Shanghai, China
Zip code: 200093

Effective Connection Full Service 三城三校高效联动 人才顾问全程陪同

Endorsed by 中国教育在线 www.eol.cn Organizers 暨南大學 JINAN UNIVERSITY 東南大學 SOUTHEAST UNIVERSITY 北京理工大學 BEIJING INSTITUTE OF TECHNOLOGY

海外学者中国行

Overseas Chinese Scholars' Visit to Top Chinese Universities

Date:
Dec. 21st to 29th, 2016;
Universities:
Jinan University (Guangdong);
Southeast University (Nanjing);
Beijing Institute of Technology (Beijing)

The sponsors will cover all costs during this activity and provide high subsidies of international flight for successful candidates.

FULL SERVICE & SUPPORT FOR YOU!

Jinan University

It is a multi-disciplinary university with a special emphasis on Life Science, Medicine, Pharmacy, Environmental Science, Information Science, Applied Economics and Journalism and Communication.

Southeast University

It is a comprehensive and research-oriented university featuring the coordinated development of multi-disciplines with engineering as its focus. Among it, 9 disciplines including Engineering, Computer Science, and Material Science, etc. rank among the first 1% of global ESI database.

Beijing Institute of Technology

BIT is the first university of science and engineering established by the Communist Party of China (CPC). Its disciplines are colored with peculiar characteristics, especially Aerospace Engineering, Mechanical Engineering, Optoelectronics and Informatics.

Applications

Requirements:
Applicants should have a doctoral degree in the relevant research field and have at least 3-year overseas working experience in overseas universities and institutes. The restrictions can be relaxed for extraordinary excellent ones.

Methods:
Please refer to the website www.edu.cn/zgx to apply and send your CV directly to consultant@acabridge.edu.cn.

Deadline:
Nov. 20th, 2016. Please apply early as seats are limited. We will officially send successful candidates Invitation Letters via email.

Contacts

Jia Zhao	zhaojia@eol.cn	+86-10-62603373	Bei Jiang	jiangbei@eol.cn	+86-10-62603770
Lu Zhang	zhanglu@eol.cn	+86-10-62603334	Pingping Ma	mapingping@eol.cn	+86-10-62603667

The Big Data Decision Institute (BDDI) of Jinan University Recruitment of Scholars (Second half of 2016)

暨南大學 JINAN UNIVERSITY

Jinan University is one of China's "One Hundred Key Universities of 21st Century"(the "211 Project") and is operated under the leadership of the Overseas Chinese Affairs Office of State Council. As the first university established by the State for overseas Chinese students, JNU currently has the largest number of overseas and foreign students and is honored as the "top university for overseas Chinese".

The Big Data Decision Institute (BDDI) is directly affiliated to Jinan University (JNU), engaged in research on big data-based Precision Health and Financial Quantitative Investment. The BDDI has integrated institution resources from School of Finance, School of Medical, School of Life Science, School of Medicine, and more than 20 affiliated hospitals of JNU, as well as JNU's national key discipline resources of the finance, clinical medicine, pharmacology and other disciplines that enter the ESI top 1%.

In the second half of 2016, we invite global applications for the following posts.

► Open Positions

1. BDDI: 10 or more full-time teachers (no restricted proportion between professors, associate professors, and assistant professors), and unlimited number of high-level talents and post-doctors.
2. Sino-US Joint research team: 1-2 post-doctors working at University of Kansas, US.

The BDDI combines the cutting-edge scientific research and industrial application together, forge the productive power of science and technology and accelerates the transformation of achievements. We attach importance to meritocracy and give priority to those who match the conditions of the Double Hundred Talents Program of JNU and the Implementing Measures of Talent Introduction of JNU ([2014] no. 34). For more information, please visit the web site of the department of human resources development and management (***http://personal.-jnu.edu.cn***).

► Basic Requirements

1.Professional Requirements:

- Big data-based Precision Health direction: network medicine, electronic medical record mining, drug side effects mining, bioinformatics, mobile medical, slow disease precise management, etc.
- Big data-based Financial Quantitative Investment direction: intelligent investment consulting, financial intelligent computing, programming trading, etc.
- Data Mining and Quantitative Modeling Method direction: data mining and machine learning, complex systems, natural language processing, artificial intelligence, robot and automatic control, computational mathematics, etc.
- Other relevant research directions.

2.Doctorate degree in related areas;

3.Meeting the team value "team working, innovation, dedication, integrity and modesty".

Materials Required

1.Detailed resume and 5 representative papers;

2.After the preliminary examination, applicants need to provide documentary evidence such as academic and degree certificate, copies of ID card, etc.

Contact Us

- The Big Data Decision Institute (BDDI) of Jinan University (JNU)
- TEL: 020-85223261 (The BDDI Human Resource Office), Prof. Hu and Assistant Chen, Assistant Mo 13632313877 (Chen) /15920168867 (Mo)
- E-mail: **bddi.jnu@foxmail.com** (directly managed by the director of BDDI)

Guangdong-Hongkong-Macau Institute of CNS Regeneration is Recruiting Postdoctors

Founded in 2012, Guangdong-Hongkong-Macau Institute of CNS Regeneration is based on Jinan University- The University of Hong Kong BFAH, directly under the administration of Jinan University. The Institute enjoys the advantages such as it is the university for Overseas Chinese and it has geographical advantage, stimulating international cooperation by Guangdong-Hongkong-Macau regional cooperation , striving to be a center for Neuroscience Research, base for talent cultivation, platform for basic research and clinical application with distinctive characteristics and advantages, leading in home and abroad.

Payment: Jinan University implements a performance-based pay system for postdoctors. The basic pay divides into three level: annual salary for Level 1 is 130 thousand, for level 2 is 180 thousand and for level 3 is 280 thousand. Those who publish papers at JCR-I or take charge of national programs in post-doctoral research station will provide annual salary at level 3. Housing or renting subsidies will be offered, and children education will be given special help. The postdoctor achieved level 3 can be given the priority to stay to work in school. The treatment for detail can be checked from No 61. 2015 Jinan University Research Paper.

The Period in Station: Generally for three years, the outstanding one can be out of station ahead of time.

The Applicants can send CV to Teacher Zhou (**tlibingzh@jnu.edu.cn**) We will contact you ASAP.

For more information, please check the website: **http://ghmicr.jnu.edu.cn/index.asp?index.html**

北京航空航天大學
BEIHANG UNIVERSITY

Beihang University

Beihang University, abbreviated as BUAA, was founded in 1952 through the merging of the aeronautical departments from eight top Chinese universities. Today it is one of China's foremost research universities supported by China's Project 211, Project 985 and Project 2011.

BUAA has an enrollment of more than 29,000 students, attending 28 schools in two campuses in Beijing and many going on exchange in partner universities across Europe, Asia, the Americas and Oceania. Among the first Chinese universities to offer postgraduate programs in English for international students, BUAA annually attracts over 1,700 foreign students from 90 countries.

The faculty has over 2,100 members whose research and teaching encompasses science, engineering, economics, management science, literature, law, philosophy, education, medicine, art, etc. A strong body of accomplished professors has formed, which includes 22 Academicians of Chinese Academy of Science and Chinese Academy of Engineering, 26 recipients of the Recruitment Program of Global Experts (1000 Talents Plan), 55 Chang Jiang Scholars and 42 winners of the National Science Fund for Distinguished Young Scholars. The newly founded International Research Institute for Multidisciplinary Science has established a world-class, cutting-edge research platform for outstanding overseas scientists, including 2 Nobel laureates, 8 overseas Academicians, 43 recipients of the Recruitment Program of Young Professionals (1000 Young Talents Plan) and about 100 'Zhuoyue' full and associate professors.

The University offers 189 academic programs, of which 61 are undergraduate programs and 128 are postgraduate programs. BUAA has been renowned for its competitive edge in disciplines such as aeronautics and astronautics; instrument science and technology; computer science and technology; management science and engineering; and materials science and engineering.

As a powerhouse of research and innovation, BUAA has earned 1,264 awards for achievements at national or ministerial level, including three First Prizes of National Science & Technology Progress Awards and six First Prizes of National Technological Innovation Awards. BUAA also has strong links with the industrial sector, which contributes to more than 50 percent of the University's research projects.

BUAA has also grown to be a university of global outreach, with a recently inaugurated Europe Office in Brussels and visibility in several global consortia, including Top Industrial Managers for Europe (T.I.M.E). The University maintains partnerships with 185 universities, research institutions and companies in over 30 countries. The cooperation covers faculty and student exchanges, joint workshops and publications, joint research endeavors and international educational projects. The Sino-French Engineer School (or, Ecole Centrale de Pekin), established by Beihang and the Groupe des Ecoles Centrales in 2005, has won international recognition for its excellence in international engineering education. BUAA is also home to the U.N. Regional Center for Space Science and Technology Education in Asia and the Pacific (China) established in November 2014.

The center of BUAA is its Xueyuan Road campus in the heart of "China's Silicon Valley" – Zhongguancun Science Park. The Park is one of the technology centres in the world and is growing fast into a high and new-tech industrial cluster. In addition to its Xueyuan Road Campus, the University is also located in northwest Beijing's Changping District with a newly developed campus and has comprehensive research facilities, notably the National Laboratory of Aeronautics and Astronautics (NLAA).

BUAA pursues excellence in research and education with an emphasis on innovation and internationalization. We sincerely invite global elites to join us at levels of full, associate and assistant professors and postdoctoral fellows.

诚邀海外优秀人才加盟北京航空航天大学

Interested individuals should send their CV to:
rsc@buaa.edu.cn or call **(0086) 010-82317779** for more information.